Electrical conductivity from first principles

Dissertation

zur Erlangung des akademischen Grades

doctor rerum naturalium
(Dr. rer. nat.)

im Fach: Physik
Spezialisierung: Theoretische Physik

eingereicht an der Mathematisch-Naturwissenschaftlichen Fakultät
Humboldt-Universität zu Berlin

von

M. Sc. Zhenkun Yuan

Präsidentin der Humboldt-Universität zu Berlin:
Prof. Dr.-Ing. Dr. Sabine Kunst

Dekan der Mathematisch-Naturwissenschaftlichen Fakultät:
Prof. Dr. Elmar Kulke

Gutachter/innen:	1. Prof. Dr. Matthias Scheffler
	2. Prof. Dr. Claudia Draxl
	3. Prof. Dr. Andreas Knorr

Tag der mündlichen Prüfung: 22.02.2022

Abstract

The reliable prediction of the electrical conductivity from first-principles is important for computationally guided discovery of novel materials with desired electrical properties. Recent studies suggest that improving the accuracy of electrical conductivity calculations in many materials requires accounting for the typically ignored lattice anharmonicity by higher-order electron-phonon interactions. First-principles supercell calculations of the electrical conductivity based on a combination of the Kubo-Greenwood (KG) formula and *ab initio* molecular dynamics (*ai*MD) appear to be a promising approach because they naturally include these interactions. However, the application of this approach to crystalline materials has so far received very little attention. This thesis describes the *ab initio* KG approach, the difficulties of a numerical implementation for crystalline solids, and it demonstrates the problems with two very different systems.

The first case study for silicon (Si), which is a very harmonic material, reveals that the *ab initio* KG calculations place a high demand on computational resources, and identifies the considerable numerical difficulties. In particular, the KG calculation requires a dense **k**-point sampling, which hinders supercell-size convergence and makes the calculation only feasible with (semi)local density functional approximations (e.g., LDA and GGA). Besides, the necessary introduction of a broadening parameter (η) introduces a significant uncertainty in the quantitative determination of the electrical conductivity. Computationally efficient strategies are discussed in this thesis to address these problems, including: (i) the "scissor operator" approach to correct the LDA band-gap problem; (ii) the “optimal-η scheme" to choose an appropriate value of η; and (iii) the finite-size scaling method to deduce the electrical conductivity in the limit of an infinitely large supercell. With these strategies, it is found that while our calculations at the LDA level yield electrical conductivities in reasonable agreement with experiment, our results do not agree well with those of previous *ab initio* calculations using the Boltzmann transport equation (BTE) at the LDA level. This comparison suggests that the η problem and the issue of supercell-size convergence still require improved concepts.

The second case study for SnSe, which is a highly anharmonic material, shows very similar numerical difficulties as in the case of Si. For SnSe, it is rather challenging to address the issue of supercell-size convergence, because of the anisotropic electrical conductivity and that the supercell size quickly becomes computationally unfeasible. By choosing appropriate supercell sizes and using the defined strategies, the x and z components of the electrical conductivity in p-doped SnSe at 300 K and 523 K are computed. It is found that at the GGA-PBEsol level the calculated results are in reasonable agreement with experiment. However, the large uncertainties due to the η problem and the issue of supercell-size convergence remain. Comparison with previous *ab initio* BTE calculations and discussion of the influence of lattice anharmonicity on the supercell-size convergence are presented.

It is concluded that more expertise needs to be acquired on how to deal with the η problem and the issue of supercell-size convergence before the *ab initio* KG approach can be used to predict the electrical conductivity of crystalline materials.

Zusammenfassung

Die zuverlässige Vorhersage der elektrischen Leitfähigkeit ausgehend von ersten Prinzipien ist wichtig für die rechnerisch gestützte Entdeckung neuer Materialien mit erwünschten elektrischen Eigenschaften. Jüngste Studien legen nahe, dass die Verbesserung der Genauigkeit von Berechnungen der elektrischen Leitfähigkeit in vielen Materialien die Berücksichtigung der typischerweise ignorierten Gitteranharmonizität durch Elektron-Phonon-Wechselwirkungen höherer Ordnung erfordert. Superzellenberechnungen der elektrischen Leitfähigkeit aus ersten Prinzipien, die auf einer Kombination aus der Kubo-Greenwood-Formel (KG) und der *ab initio* Molekulardynamik (*ai*MD) beruhen, scheinen ein vielversprechender Ansatz zu sein, da sie diese Wechselwirkungen auf natürliche Weise berücksichtigen. Die Anwendung dieses Ansatzes auf kristalline Materialien hat jedoch bisher nur sehr wenig Aufmerksamkeit erhalten. In dieser Arbeit werden der *ab initio* KG-Ansatz und die Schwierigkeiten einer numerischen Umsetzung für kristalline Festkörper beschrieben und die Probleme anhand zweier sehr unterschiedlicher Systeme demonstriert.

Die erste Fallstudie für Silizium (Si), das ein sehr harmonisches Material ist, zeigt, dass die *ab initio* KG-Berechnungen eine hohe Anforderung an die Rechenressourcen stellen, und zeigt die erheblichen numerischen Schwierigkeiten auf. Insbesondere erfordert die KG-Berechnung eine dichte **k**-Punktabtastung, was die Konvergenz in Superzellengröße behindert und die Berechnung nur mit (halb)lokalen Dichtefunktionalapproximationen (z.B. LDA und GGA) durchführbar macht. Außerdem führt die notwendige Einführung eines Verbreiterungsparameters (η) zu einer erheblichen Unsicherheit bei der quantitativen Bestimmung der elektrischen Leitfähigkeit. In dieser Arbeit werden rechnerisch effiziente Strategien diskutiert, um diese Probleme zu lösen, darunter: (i) der Scherenoperator-Ansatz zur Korrektur des LDA-Bandlückenproblems; (ii) das Öptimal-η-Schemaßur Wahl eines geeigneten Wertes für η; und (iii) die Finite-Size-Scaling-Methode zur Ableitung der elektrischen Leitfähigkeit im Grenzfall einer unendlich großen Superzelle. Mit diesen Strategien zeigt sich, dass unsere Berechnungen auf LDA-Ebene zwar elektrische Leitfähigkeiten in angemessener Übereinstimmung mit Experimenten ergeben, unsere Ergebnisse jedoch nicht gut mit denen früherer *ab initio*-Berechnungen unter Verwendung der Boltzmann-Transportgleichung (BTE) auf LDA-Ebene übereinstimmen. Dieser Vergleich deutet darauf hin, dass das η-Problem und die Frage der Konvergenz in Superzellengröße weiter verbesserte Konzepte erfordern.

Die zweite Fallstudie für SnSe, ein stark anharmonisches Material, zeigt sehr ähnliche numerische Schwierigkeiten wie im Fall von Si. Bei SnSe ist die Frage der Konvergenz der Superzellengröße aufgrund der anisotropen elektrischen Leitfähigkeit und der Tatsache, dass die Größe der Superzellen schnell rechnerisch nicht mehr machbar ist, recht schwierig zu lösen. Durch die Wahl geeigneter Superzellengrößen und die Anwendung der definierten Strategien werden die x- und z-Komponenten der elektrischen Leitfähigkeit in p-dotiertem SnSe bei 300 K und 523 K berechnet. Es zeigt sich, dass die berechneten Ergebnisse auf der GGA-PBEsol-Ebene in angemessener Übereinstimmung mit dem Experiment sind. Allerdings bleiben die großen Unsicherheiten aufgrund des η-Problems und das Problem der Konvergenz in Superzellengröße bestehen. Vergleich mit früheren *ab initio* BTE-Berechnungen und die Diskussion des Einflusses der Gitteranharmonizität auf die Konvergenz der Superzellengröße werden vorgestellt.

Man kommt zu dem Schluss, dass mehr Fachwissen über den Umgang mit dem η-Problem und die Frage der Konvergenz der Superzellengröße erworben werden muss, bevor der *ab initio* KG-Ansatz zur Vorhersage der elektrischen Leitfähigkeit von kristallinen Materialien verwendet werden kann.

Acknowledgement

First and foremost, I would like to express my sincere gratitude to my supervisor Prof. Dr. Matthias Scheffler, who offered me the opportunity to work in his world-leading lab at FHI Berlin and brought me to the challenging and exciting research topic. This thesis is not possible without his generous support, precious time, insightful advice, and great patience throughout my PhD project. In my future academic career, I will be guided by his hard-working and excellent academic attitude. I would also like to thank my second supervisor Prof. Dr. Claudia Draxl at HU Berlin for her kind support.

I would like to thank all the colleagues I have met at FHI Berlin, and will keep in mind their friendships. My special thanks go to Florian Knoop and Sheng Bi who are always willing to help me and to share me their expertise. I want to extend many thanks to Olle Hellman, Sebastian Matera, Chuan-Ding Dong, Yue-Yu Zhang, Honghui Shang, and Zhenglu Li for the fruitful discussions. I am indebted to Yuanyuan Zhou and Jinkai Quan for their proof-reading part of the thesis. I would also like to mention Christian Carbogno who offered some help at the initial stage of my PhD study. Thanks to my officemates Nathaniel Raimbault, Maria Dragoumi, and Alaa Akkoush for creating a great working atmosphere.

I am deeply grateful to the support, understanding, and encouragement from my family. Friendship is so valuable (especially during the Corona lockdown), and I want to thank all my old and new friends.

I will miss Berlin deeply, for this city's freedom and open-mindedness that are very precious during the pandemic time.

Contents

1 Introduction

The electrical conductivity, referred to as σ in this thesis, describes the ability of a material to conduct charge carriers. According to Ohm's law $\mathbf{J} = \sigma\mathbf{E}$, it is the proportionality between the electric current density $\mathbf{J}$ and the applied electric field $\mathbf{E}$. Its value can vary by more than a factor of 10^{20} from one material to another [1, 2], leading to the traditional classification of materials as metals, semiconductors, and insulators. Figure 1.1 shows the electrical conductivities of some common materials at room temperature. Metals such as Cu are good electrical conductors with high electrical conductivities of the order of $10^4 - 10^5\ \Omega^{-1}\text{cm}^{-1}$ [3]. Intrinsic semiconductors such as pure Si are rather electrically resistive with electrical conductivities of the order of $10^{-8} - 10^{-2}\ \Omega^{-1}\text{cm}^{-1}$ [4]. Depending on doping and temperature, the electrical conductivity of a semiconductor can usually be varied in a wide range. For example, heavily phosphorus (P)-doped Si can have significantly enhanced electrical conductivity up to the order of $10^3\ \Omega^{-1}\text{cm}^{-1}$ [5]. Such a wide tunability of the electrical conductivity of semiconductors is the basis for (opto)electronic applications.

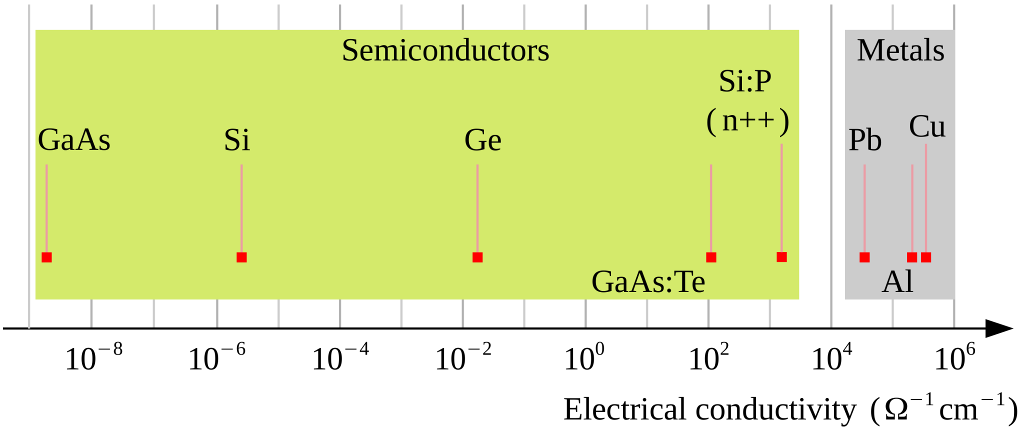

Figure 1.1: Electrical conductivities (in units of $\Omega^{-1}\text{cm}^{-1}$) of some common materials at room temperature: high-purity single-crystal semiconductors: GaAs, Si, and Ge [4]; Te-doped (*n*-type) GaAs [6]; heavily P-doped (*n*-type) Si [5]; high-purity metals: Cu, Al, and Pb [3]. Note that data for semiconductors depend sensitively on doping and temperature. Adapted from Refs. [1, 2].

Assessing the electrical conductivity of materials is typically done by experimental measurements and/or semi-empirical calculations [7]. These approaches are now being expanded by a new research paradigm: the big-data driven materials science [8, 9]. A prominent example [10] in this direction is the development of high-performance thermoelectric materials — materials in which a temperature difference converts heat into electricity, in order to help today's demand for waste heat management and generation of clean electricity. The electrical conductivity is a factor entering the thermoelectric figure of merit, $zT = \sigma S^2 T/\kappa$. Ideally, a high value of zT is realized by a large electrical conductivity (σ), a large Seebeck coefficient (S), and a small thermal conductivity (κ) at the temperature T. However, these are a set of properties that nature is not likely to provide in a single material [11]. Fortunately, the periodic table of elements offers immense possibilities of: (i) discovering novel thermoelectric materials where large σ and S and small κ manifest simultaneously, and (ii) defining strategies to optimize the known thermoelectric materials, such as through doping, alloying, and nano-structuring [10]. For such a huge search space, it is crucial to develop methods that can reliably and efficiently determine the electrical conductivity of materials.

First-principles calculations have emerged as a powerful approach to address the above challenge. Over the last decade, predictive non-empirical calculations of electrical conductivities and carrier mobilities using the Boltzmann transport equation (BTE) became feasible [12, 13], owing to advances in: (i) density-functional theory (DFT) calculations of total energies, structural properties, and electronic band structures of solids, (ii) the development of density-functional perturbation theory (DFPT) for lattice dynamics and electron-phonon (e-ph) interactions, and (iii) the rapid growth and broad availability of supercomputing power for overcoming size and time constraints as well as numerical complexities. The *ab initio* BTE approach to the calculation of electronic transport coefficients has been successfully applied to a variety of materials, from simple materials (e.g., Si) to complex materials (e.g., metal-halide perovskites) and two-dimensional materials (e.g., MoS_2) [12, 13].

In many *ab initio* BTE calculations[1], the description of electron-phonon scattering by perturbation theory relies on the harmonic approximation to lattice dynamics [14, 12]. In the harmonic approximation, the potential-energy surface (PES) is expanded to second order in the atomic displacements, and the third- and higher-order terms, i.e., lattice anharmonicity, are neglected. Thus, the reliability of the BTE calculations depend on the validity of the harmonic approximation. This is material dependent, and in general materials tend to be anharmonic at high temperature. For instance, Si is a highly harmonic material even at temperatures well above room temperature [15, 16]; the thermoelectric material SnSe and the photovoltaic materials metal-halide perovskites are anharmonic in nature, and are already highly anharmonic at room temperature (see, e.g., Ref. [17, 18] for SnSe and Ref. [19, 20] for metal-halide perovskites). In state-of-the-art *ab initio* BTE calculations, the role of lattice anharmonicity has largely been ignored

---

[1] In this thesis, the BTE calculation is only about the calculation of electronic transport coefficients.

[21, 22, 23]. This is mainly because when going beyond the harmonic approximation, the resulting e-ph coupling formalism is exceedingly complex (let alone computation) [14]. However, for anharmonic materials, there are growing evidences showing that inclusion of anharmonic effects on both the phonon dynamics and e-ph coupling is required to get the correct electronic transport coefficients. The BTE calculation of the electrical conductivity of SnSe by Caruso *et al.* [24] showed that a good quantitative agreement with experiment requires accounting simultaneously for the thermal lattice expansion (which is an anharmonic effect) and thermal enhancement of the e-ph interaction. Failure of the *ab initio* BTE approach may occur when calculations of e-ph coupling matrix elements break down due to the presence of soft phonon modes in the harmonic approximation (e.g., $SrTiO_3$ [25, 26] and metal-halide perovskites [22]). In this case, self-consistent phonon calculations [27, 28, 29], which approximately account for lattice anharmonicity at finite temperature, can be performed to stabilize the soft phonon modes; if this method works, the e-ph matrix elements and scattering rates are then computed using the anharmonic phonons [25, 26]. Besides, the e-ph scattering rates are usually evaluated at the lowest order of perturbation theory, and the inclusion of higher-order e-ph coupling effects constitutes a pressing challenge [12, 30, 31].

As an alternative, first-principles supercell calculations based on a combination of the Kubo-Greenwood (KG) formula [32] and *ab initio* molecular dynamics provide a non-perturbative, fully-anharmonic approach for calculating the electrical conductivity of materials. In this approach, *ai*MD simulations at finite temperature are used to generate atomic trajectories on the *ab initio* PES, naturally accounting for lattice anharmonicity to all orders [33, 27]. A sufficiently large number of MD samples (i.e., atomic configurations) is generated from these trajectories to represent the typical distribution of the nuclei on the PES at the temperature of interest. The electrical conductivity for each of the samples collected is determined from a KG calculation, which requires only a standard DFT calculation and does not involve any perturbative treatment. The final electrical conductivity is evaluated as an average over the collected samples. The calculated results naturally contain information on the dynamics of the system, i.e., on lattice vibrations and the coupling between electrons and lattice vibrations. While the *ab initio* KG approach is clearly promising, to date, its application is largely limited to warm dense matter and disordered solids and has received very little attention regarding crystalline materials (see Section 3.3.4). Previous studies [34, 35] showed that the KG calculations on crystalline solids are prone to numerical problems, e.g., the issue of supercell-size convergence. It is necessary to carry out a thorough test of this approach and its numerical implementation for crystalline solids.

This thesis is motivated by the quest for a first-principles approach to reliably predict the electrical conductivity in anharmonic materials, and is devoted to the *ab initio* KG approach. Our goals are to (1) describe the *ab initio* KG approach and the difficulties of a numerical implementation of this approach for crystalline solids; (2) explore a numerical implementation of the *ab initio* KG approach for two very different systems (the harmonic crystal Si and anharmonic crystal SnSe), demonstrate the problems, and discuss the solutions; and (3) assess the predictive power of the *ab initio* KG approach to the calculation of the electrical conductivity of crystalline materials. We hope that our work will serve as (i) a useful guide to the application of the *ab initio* KG approach to calculate the electrical conductivity of crystalline solids, and (ii) a valuable starting point towards a reliable numerical implementation of this approach for crystalline materials. The thesis is structured as follows:

Chapter 2 reviews the relevant concepts and methods in modern electronic-structure theory of solids. This gives the theoretical foundation of DFT calculations by which *ab initio* material parameters required for the KG calculations are provided.

Chapter 3 gives an overview on the theory of electronic transport in solids, from the Boltzmann transport theory to the Kubo's theory of linear response. It provides a detailed introduction of the KG formula, and establishes the connection with electronic-structure calculations including *ai*MD simulations of lattice vibrations. Practical aspects of the *ab initio* KG approach such as the broadening of the Dirac delta function, the methods to describe free-carrier doping, and our computer code implementation of the KG formula are also discussed.

In Chapter 4 we apply the *ab initio* KG approach to calculate the electrical conductivity of Si at 300 K. With a focus on intrinsic Si, we provide a detailed convergence study for the relevant computational parameters, including **k**-point sampling, broadening parameter, basis-set size, number of MD samples, and supercell size. Computationally efficient strategies are discussed to deal with the identified problems, including the choice of broadening parameter, the DFT band-gap problem, and the issue of supercell-size convergence. We also compute the electrical conductivities of both p- and n-doped Si at different doping levels, and compare our calculations with experiment and with previous *ab initio* calculations using the BTE approach. The latter comparison allows for assessing the convergence of our calculations.

In Chapter 5 we apply the *ab initio* KG approach and the strategies defined in Chapter 4 to calculate the anisotropic electrical conductivity of the layered semiconductor SnSe at 300 K. This case study is partly motivated by the question whether the numerical difficulties identified in the case of Si is less severe for anharmonic crystals. We consider the x (i.e., interlayer) and z (i.e., in-plane) components of the electrical conductivity of SnSe, and present a detailed convergence study for **k**-point sampling, broadening parameter, number of *ai*MD samples, and supercell size. The calculated electrical conductivities are compared with experiment and with previous *ab initio* BTE calculations. The calculated results for SnSe 523 K are also reported.

Finally, Chapter 6 summarizes this work, and gives an outlook that may help future developments of the *ab initio* KG approach.

2 *Ab initio* electronic-structure theory

The insights of materials ultimately rest on understanding their electronic structure [36]. This chapter reviews the basic concepts and standard formalism that have enabled first-principles density-functional theory (DFT) calculations of the electronic structure of crystalline solids. Emphasis is laid on how the material parameters, such as equilibrium structure, electronic band structure, lattice dynamics, and more, for assessing the electrical conductivity of real materials at finite temperature can be obtained from solid-state DFT calculations.

2.1 Many-body Schrödinger equation

Consider a system of interacting particles, which can be either an atom, molecule or solid, consisting of N electrons and N_n nuclei. The coordinates of the electrons are denoted as $\{\mathbf{r}_i\} = \{\mathbf{r}_1, \mathbf{r}_2, \ldots, \mathbf{r}_N\}$ (spin is omitted for simplicity), and the coordinates of the nuclei are denoted as $\{\mathbf{R}_I\} = \{\mathbf{R}_1, \mathbf{R}_2, \ldots, \mathbf{R}_{N_\mathrm{n}}\}$, which sum up to a total of $3N + 3N_\mathrm{n}$ degrees of freedom. To treat this many-body system, the starting point is the time-independent Schrödinger equation:

$$H\Psi(\{\mathbf{r}_i\}, \{\mathbf{R}_I\}) = E\Psi(\{\mathbf{r}_i\}, \{\mathbf{R}_I\}). \tag{2.1}$$

In the absence of external field, the non-relativistic Hamiltonian H of the system comprises the following terms:

$$H = T^\mathrm{n} + T^\mathrm{e} + V^\text{n-n} + V^\text{e-e} + V^\text{e-n} \tag{2.2}$$

with (i) the kinetic energy of the nuclei:

$$T^\mathrm{n} = -\sum_{I=1}^{N_\mathrm{n}} \frac{\hbar^2}{2M_I} \nabla^2_{\mathbf{R}_I}, \tag{2.3}$$

(ii) the kinetic energy of the electrons:

$$T^\mathrm{e} = -\frac{\hbar^2}{2m} \sum_{i=1}^{N} \nabla^2_i, \tag{2.4}$$

(ii) the Coulomb interactions between the nuclei:

$$V^{\text{n-n}} = \frac{e^2}{2} \sum_{I=1}^{N_\text{n}} \sum_{\substack{J=1 \\ (J \neq I)}}^{N_\text{n}} \frac{Z_I Z_J}{|\mathbf{R}_I - \mathbf{R}_J|}, \tag{2.5}$$

(iv) the Coulomb interactions between the electrons:

$$V^{\text{e-e}} = \frac{e^2}{2} \sum_{i=1}^{N} \sum_{\substack{j=1 \\ (j \neq i)}}^{N} \frac{1}{|\mathbf{r}_i - \mathbf{r}_j|}, \tag{2.6}$$

and (v) the Coulomb interactions between the electrons and the nuclei:

$$V^{\text{e-n}} = -\sum_{i=1}^{N} \sum_{I=1}^{N_\text{n}} \frac{Z_I e^2}{|\mathbf{r}_i - \mathbf{R}_I|}. \tag{2.7}$$

In these equations, m and e are the electron mass and charge, M_I and Z_I are the mass and charge of the I-th nucleus, and $\hbar = h/2\pi$ the reduced Planck constant.

Equation (2.1) constitutes a complex quantum-mechanical many-body problem, of which the exact solution is well beyond existing computing and data-storage capacities (except for a few very simple systems) [37]. This is even more obvious for solids which consist of $\sim 10^{23}$ particles per cm^3. Thus, reducing the degrees of freedom in Equation (2.1) is essential to make it numerically solvable, which is achieved by the physical approximations on the many-body problem, as introduced in the following sections.

2.2 Born-Oppenheimer approximation and potential-energy surface

In order to find an approximate solution of Equation (2.1), one begins by making the Born-Oppenheimer (BO) approximation [38]. Because the nuclei are much heavier than the electrons (e.g., for hydrogen, $M_{\mathrm{H}}/m \approx 1836$) and the forces on the particles are the same, the electrons instantaneously and adiabatically follow the motion of the nuclei. Thus, one can assume that the nuclei are stationary and solves first for the motion of the electrons, then computes the energy of the system in that nuclear configuration, and finally solves for the motion of the nuclei, as outlined below.

For a system of interacting electrons moving in the field of the stationary nuclei, the electronic Hamiltonian is given by:

$$H^{\mathrm{e}}(\{\mathbf{R}_I\}) = T^{\mathrm{e}} + V^{\text{e-e}} + V^{\text{e-n}}(\{\mathbf{R}_I\}), \tag{2.8}$$

which acts on the electronic variables and depends parametrically on the coordinates of the nuclei $\{\mathbf{R}_I\}$. The time-independent Schrödinger equation for this electronic problem reads:

$$H^{\mathrm{e}}(\{\mathbf{R}_I\})\Phi_\nu(\{\mathbf{r}_i\};\{\mathbf{R}_I\}) = E^{\mathrm{e}}_\nu(\{\mathbf{R}_I\})\Phi_\nu(\{\mathbf{r}_i\};\{\mathbf{R}_I\}), \tag{2.9}$$

where $E^{\mathrm{e}}_\nu(\{\mathbf{R}_I\})$ and $\Phi_\nu(\{\mathbf{r}_i\};\{\mathbf{R}_I\})$ are the energy and wave function of the electronic system in the ν-th eigenstate. Note that in Equations (2.8) and (2.9), the nuclear coordinates $\{\mathbf{R}_I\}$ are only parameters that label or classify the H^{e}, E^{e}_ν, and Φ_ν. Accordingly, $V^{\text{e-n}}(\{\mathbf{R}_I\})$ describes the potential energy of the electrons in the so-called external field of the nuclei.

For a given nuclear configuration $\{\mathbf{R}_I\}$, the eigenfunctions $\Phi_\nu(\{\mathbf{r}_i\};\{\mathbf{R}_I\})$ of the electronic system form a complete basis. The wave function of the total system as the solution of Equation (2.1) can be expanded as:

$$\Psi(\{\mathbf{r}_i\},\{\mathbf{R}_I\}) = \sum_\nu \chi_\nu(\{\mathbf{R}_I\})\Phi_\nu(\{\mathbf{r}_i\};\{\mathbf{R}_I\}), \tag{2.10}$$

where $\chi_\nu(\{\mathbf{R}_I\})$ are the expansion coefficients. Inserting Equation (2.10) into Equation (2.1) and multiplying $\Phi^*_\mu(\{\mathbf{r}_i\};\{\mathbf{R}_I\})$ from the left lead to:

$$\begin{aligned}&[T^{\mathrm{n}} + V^{\text{n-n}}(\{\mathbf{R}_I\}) + E^{\mathrm{e}}_\mu(\{\mathbf{R}_I\})]\chi_\mu(\{\mathbf{R}_I\})\\ &+\sum_\nu\sum_{I=1}^{N_{\mathrm{n}}} -\frac{\hbar^2}{2M_I}[(\langle\Phi_\mu|\nabla^2_{\mathbf{R}_I}|\Phi_\nu\rangle)\chi_\nu + 2\langle\Phi_\mu|\nabla_{\mathbf{R}_I}|\Phi_\nu\rangle(\nabla_{\mathbf{R}_I}\chi_\nu)] = E\chi_\mu(\{\mathbf{R}_I\}).\end{aligned} \tag{2.11}$$

The second term on the left-hand side of Equation (2.11) describes the electronic transition from Φ_ν to Φ_μ if there exists nuclear motion (the $\nabla_{\mathbf{R}_I}$ and $\nabla^2_{\mathbf{R}_I}$ operators), which is known as the electron-vibrational coupling. This term contributes typically very little to the energy of the system compared to $E^{\mathrm{e}}_{\mu}(\{\mathbf{R}_I\})$ [39], and is neglected in the BO approximation, thus allowing for a separated treatment of the dynamics of the electrons and nuclei. Equation (2.11) then becomes:

$$[T^{\mathrm{n}} + V^{\mathrm{n\text{-}n}}(\{\mathbf{R}_I\}) + E^{\mathrm{e}}_{\mu}(\{\mathbf{R}_I\})]\chi_{\mu}(\{\mathbf{R}_I\}) = E\chi_{\mu}(\{\mathbf{R}_I\}), \tag{2.12}$$

which describes the motion of the nuclei, and the wave function of the system is:

$$\Psi_{\mu}(\{\mathbf{r}_i\}, \{\mathbf{R}_I\}) = \chi_{\mu}(\{\mathbf{R}_I\})\Phi_{\mu}(\{\mathbf{r}_i\}; \{\mathbf{R}_I\}). \tag{2.13}$$

Equation (2.12) defines a so-called BO potential-energy surface (PES) [33]:

$$U_{\mu}(\{\mathbf{R}_I\}) = V^{\mathrm{n\text{-}n}}(\{\mathbf{R}_I\}) + E^{\mathrm{e}}_{\mu}(\{\mathbf{R}_I\}), \tag{2.14}$$

which is the total energy of the system in the μ-th electronic eigenstate, as a function of nuclear coordinates. Therefore, in the BO approximation, the motion of the nuclei is on a BO PES which is a solution to the electronic Schrödinger equation. Note that for a given nuclear configuration $\{\mathbf{R}_I\}$, the $V^{\mathrm{n\text{-}n}}(\{\mathbf{R}_I\})$ is a constant.

When the nuclei are fixed at positions $\{\mathbf{R}_I\}$, which corresponds to zero temperature (neglecting nuclear quantum effects), the ground-state wave function is given by:

$$\Psi_0(\{\mathbf{R}_I\}) = \chi_0(\{\mathbf{R}_I\})\Phi_0(\{\mathbf{r}_i\}; \{\mathbf{R}_I\}), \tag{2.15}$$

and the total energy of the system is:

$$E_0 = U_0(\{\mathbf{R}_I\}) = V^{\mathrm{n\text{-}n}}(\{\mathbf{R}_I\}) + E^{\mathrm{e}}_0(\{\mathbf{R}_I\}). \tag{2.16}$$

The force acting on the I-th nucleus in the electronic ground state is defined as:

$$\mathbf{F}_I = -\frac{\partial E_0(\{\mathbf{R}_I\})}{\partial \mathbf{R}_I}. \tag{2.17}$$

The calculation of atomic forces enables one to [38]: (i) relax the system to find the ground-state equilibrium geometry, $\{\mathbf{R}^0_I\}$, which corresponds to the global minimum of the BO PES and at which the atomic forces vanish for all the nuclei; and (ii) perform *ab initio* molecular dynamics (*ai*MD) simulations to sample the BO PES for studying the equilibrium properties of the system at finite temperature (see Section 2.5.2).

However, the calculation of the electronic ground state for a static nuclear configuration by solving Equation (2.9) remains a complex many-body problem and requires further simplifications. Since this is purely an electronic problem, from this point on the parametric dependence of the electronic quantities on the nuclear coordinates will be suppressed.

2.3 Density-functional theory

Density-functional theory (DFT) introduced in this section reduces the complexity in solving for the electronic ground state for a static nuclear configuration, by using the electron density instead of the many-body wave function as the basic variable. It provides a computationally practical way to calculate the ground-state properties of a many-electron system.

2.3.1 Hohenberg-Kohn theorems

The Hohenberg-Kohn (HK) theorems [40], which are the foundation of DFT, state that the (electron) density $n(\mathbf{r})$ is the basic variable that determines the ground-state properties of a system of interacting electrons in an external potential. This is a significant simplification of the many-body electronic problem as one then only needs to deal with 3 instead of $3N$ degrees of freedom [via $\mathbf{r} = (x, y, z)$, spin is omitted for simplicity]. The HK theorems consist of two theorems:

Theorem 1. The external potential $V_{\text{ext}}(\mathbf{r})$ (apart from a trivially additive constant), and hence the total energy, is a unique functional of the density $n(\mathbf{r})$.

Theorem 2. For a static external potential $V_{\text{ext}}(\mathbf{r})$, there exists a universal functional of $n(\mathbf{r})$, $F[n(\mathbf{r})]$, which is independent of $V_{\text{ext}}(\mathbf{r})$, such that the energy functional

$$E[n(\mathbf{r})] \equiv F[n(\mathbf{r})] + \int n(\mathbf{r}) V_{\text{ext}}(\mathbf{r}) d\mathbf{r} \tag{2.18}$$

has as its minimum value the correct ground-state energy associated with $V_{\text{ext}}(\mathbf{r})$.

The HK theorems apply to the ground state of any electronic system, irrespective of the detail of the external potential. Often the external potential is provided by the stationary nuclei, which is the case here. However, the $F[n(\mathbf{r})]$ is unknown. Further, additional theory is required to compute the ground-state density in practice. This has been achieved by Kohn-Sham DFT.

2.3.2 Kohn-Sham DFT

In order to use the variational principle to find the electronic ground state, Kohn and Sham [41] considered an auxiliary, fictitious system of N non-interacting electrons with the same density $n(\mathbf{r})$ as that of the real system of N interacting electrons. With this, the universal functional $F[n(\mathbf{r})]$ for the interacting electrons is cast into the form,

$$F[n(\mathbf{r})] = T_{\text{s}}[n(\mathbf{r})] + V_{\text{H}}[n(\mathbf{r})] + E_{\text{xc}}[n(\mathbf{r})]. \tag{2.19}$$

In this equation, $T_{\rm s}[n(\mathbf{r})]$ is the kinetic energy of the non-interacting electrons:

$$T_{\rm s}[n(\mathbf{r})] = -\frac{\hbar^2}{2m}\sum_{i=1}^{N}\int \psi_i^*(\mathbf{r})\nabla^2\psi_i(\mathbf{r})d\mathbf{r}, \tag{2.20}$$

where $\psi_i(\mathbf{r})$ are auxiliary one-electron orbitals which are orthonormal. $T_{\rm s}$ is of comparable magnitude to the true kinetic energy and is treated exactly [37]. $E_{\rm H}[n(\mathbf{r})]$ is the classical electrostatic energy (Hartree energy) of the electrons:

$$E_{\rm H}[n(\mathbf{r})] = \frac{e^2}{2}\int d\mathbf{r}\int d\mathbf{r}'\frac{n(\mathbf{r})n(\mathbf{r}')}{|\mathbf{r}-\mathbf{r}'|}. \tag{2.21}$$

$E_{\rm xc}[n(\mathbf{r})]$ is the exchange-correlation (xc) energy, which by construction includes two contributions [41]: (i) the difference between $T_{\rm s}$ and the true kinetic energy, and (ii) the non-classical electron-electron interaction energy. The energy functional $E[n(\mathbf{r})]$ of the real, interacting system then reads:

$$E[n(\mathbf{r})] = T_{\rm s}[n(\mathbf{r})] + E_{\rm H}[n(\mathbf{r})] + E_{\rm xc}[n(\mathbf{r})] + \int n(\mathbf{r})V_{\rm ext}(\mathbf{r})d\mathbf{r}, \tag{2.22}$$

which assumes its minimum value at the ground-state density. The Euler-Lagrange equation for this variational-principle problem is given by [42, 43]:

$$\delta\{E[n(\mathbf{r})] - \sum_{i=1}^{N}\epsilon_i\int \psi_i^*(\mathbf{r})\psi_i(\mathbf{r})d\mathbf{r}\} = 0, \tag{2.23}$$

where ϵ_i are Lagrange multipliers ensuring that the N one-electron orbitals ψ_i are orthonormal. The minimization:

$$\frac{\delta}{\delta\psi_i^*}\{E[n(\mathbf{r})] - \sum_i\epsilon_i\int \psi_i^*(\mathbf{r})\psi_i(\mathbf{r})d\mathbf{r}\} = 0,\ \forall i \tag{2.24}$$

leads to a single-particle Schrödinger equation:

$$[-\frac{\hbar^2}{2m}\nabla^2 + V_{\rm eff}(\mathbf{r})]\psi_i(\mathbf{r}) = \epsilon_i\psi_i(\mathbf{r}), \tag{2.25}$$

with an effective potential:

$$\begin{aligned} V_{\rm eff}(\mathbf{r}) &= V_{\rm ext}(\mathbf{r}) + V_{\rm H}(\mathbf{r}) + V_{\rm xc}(\mathbf{r}) \\ &= V_{\rm ext}(\mathbf{r}) + e^2\int\frac{n(\mathbf{r}')}{|\mathbf{r}-\mathbf{r}'|}d\mathbf{r}' + \frac{\delta E_{\rm xc}[n(\mathbf{r})]}{\delta n(\mathbf{r})}, \end{aligned} \tag{2.26}$$

which yields the exact ground-state density:

$$n(\mathbf{r}) = \sum_{i=1}^{N} |\psi_i(\mathbf{r})|^2. \tag{2.27}$$

The ground-state energy of the system is expressed as:

$$E_0 = \sum_{i=1}^{N} \epsilon_i - \frac{e^2}{2} \int \int \frac{n(\mathbf{r})n(\mathbf{r}')}{|\mathbf{r}-\mathbf{r}'|} d\mathbf{r}d\mathbf{r}' + E_{\mathrm{xc}}[n(\mathbf{r})] - \int n(\mathbf{r})V_{\mathrm{xc}}(\mathbf{r})d\mathbf{r}. \tag{2.28}$$

where the single-particle eigenvalues are labeled such that $\epsilon_1 \leq \epsilon_2 \leq \ldots$. Equation (2.25)-(2.28) are called Kohn-Sham self-consistent equations, which are the basis of Kohn-Sham DFT. The solution of the Kohn-Sham equation needs to be self-consistent because $V_{\mathrm{eff}}(\mathbf{r})$ is a functional of $n(\mathbf{r})$.

Kohn-Sham DFT demonstrates that for a system of N interacting electrons in an external potential, the exact ground-state density and energy can be found by solving self-consistently the Kohn-Sham equation for N one-electron orbitals $\psi_i(\mathbf{r})$, each of which is a function of only three arguments $\mathbf{r} = (x, y, z)$. Such an exact mapping provides a practical way of computing the ground-state density and energy. Yet, the exact xc energy $E_{\mathrm{xc}}[n]$ and potential $V_{\mathrm{xc}}(\mathbf{r}) = \delta E_{\mathrm{xc}}/\delta n$ are not known [44]. Therefore, in practical DFT calculations $E_{\mathrm{xc}}[n]$ must be approximated by some known functionals of $n(\mathbf{r})$, as introduced in Section 2.3.3.

The meaning of the Kohn-Sham eigenvalues

The eigenvalues of the Kohn-Sham equation (2.25) enter the formalism as Lagrange multipliers. They cannot be identified with the excitation energies of the interacting many-electron system. This is evident from that the total energy is not equal to $\sum_{i=1}^{N} \epsilon_i$. Rather, the eigenvalues are interpreted according to Janak's theorem [45] as derivatives of the total energy with respect to occupation numbers:

$$\epsilon_i = \frac{\partial \tilde{E}}{\partial f_i}, \tag{2.29}$$

where $\tilde{E}$ is the generalized energy functional:

$$\tilde{E} = -\frac{\hbar^2}{2m} \sum_i f_i \int \psi_i^*(\mathbf{r}) \nabla^2 \psi_i(\mathbf{r}) d\mathbf{r} + E_{\mathrm{H}}[n(\mathbf{r})] + E_{\mathrm{xc}}[n(\mathbf{r})] + \int n(\mathbf{r}) V_{\mathrm{ext}}(\mathbf{r}) d\mathbf{r}, \tag{2.30}$$

and

$$n(\mathbf{r}) = \sum_i f_i |\psi_i(\mathbf{r})|^2, \tag{2.31}$$

where f_i denotes the occupation number of the one-electron orbital ψ_i. Equation (2.29) holds for any choice of the $\{f_i\}$, including fractional occupations ($0 \leq f_i \leq 1$ with $\sum_i f_i = N$) [45]. The $\tilde{E}$ at its minimum is just the ground-state energy E_0 that corresponds to the occupation of the N lowest orbitals.

By integration of Equation (2.29) one connects the ground-state energies of the systems with N and $(N-1)$ electrons, i.e.,

$$I(N) = E_0(N-1) - E_0(N) = -\int_0^1 \epsilon_i(f)df. \tag{2.32}$$

where $I(N)$ is the ionization energy of the N-electron system. Equation (2.32) has a formal justification only if ϵ_i refers to the highest occupied eigenstate in the N-electron system. However, it has been used with success for calculating the ionization energy of localized states (e.g., core levels [46]):

$$I_i(N) = -\int_0^1 \epsilon_i(f)df \approx -\epsilon_i(f_i = \frac{1}{2}). \tag{2.33}$$

This approach is called the Slater's transition-state method [47] (earlier than Janak's theorem and DFT). When the eigenvalue ϵ_i is approximately constant as a function of f_i, then $-\epsilon_i$ predicts well the ionization energy of this level of the real system. This is the analog of Koopmans' theorem[1] of Hartree-Fock theory.

Extension to finite temperatures

For a system of interacting electrons in thermal equilibrium in contact with a heat bath at temperature T, the state of the system should be described by a statistical ensemble. Within the framework of DFT, this can be done using the Mermin free-energy functional or Mermin-Kohn-Sham self-consistent equation [48, 49], which is formally similar to the Kohn-Sham equation (the zero-T case). In this case, the density is given by:

$$n(\mathbf{r}) = \sum_i f_i |\psi_i(\mathbf{r})|^2, \tag{2.34}$$

where f_i is a Fermi-Dirac distribution:

$$f_i = f(\frac{\epsilon_i - \mu}{T}) = \frac{1}{1 + e^{\frac{\epsilon_i - \mu}{k_B T}}}, \tag{2.35}$$

---

[1] In the Hartree-Fock theory, the Koopmans' theorem states that the change in total energy due to the removal of an electron from an unrelaxed orbital ψ_i^{HF} is simply related to the eigenvalue of this orbital, i.e., $E(N-1; f_i = 0) - E_0(N) = -\epsilon_i^{\mathrm{HF}}$ [43]. This theorem requires that all the orbitals do not relax when the occupancy f_i is reduced.

where μ is the chemical potential (or Fermi level) of the electrons, and k_B the Boltzmann constant. For a canonical ensemble, the μ is determined by:

$$\sum_i f(\frac{\epsilon_i - \mu}{T}) = N. \tag{2.36}$$

The finite-temperature extension of Kohn-Sham DFT is useful for studying systems at finite temperature.

2.3.3 Exchange-correlation approximations

Kohn-Sham DFT provides a practical way to determine the ground state of an interacting many-electron system by self-consistent solution of the Kohn-Sham equation. The only problem is that in practice the xc energy $E_{\text{xc}}[n(\mathbf{r})]$ has to be approximated by some known functionals of $n(\mathbf{r})$. In the same work of Kohn-Sham DFT [41], the $E_{\text{xc}}[n(\mathbf{r})]$ is approximated with the local-density approximation (LDA). Following the LDA, many density functional approximations (DFAs) have been developed or are under development [50]. Each of them can be assigned to a certain rung in Perdew's "Jacob's ladder" of DFAs [51], with increasing complexity and numerical accuracy as well as computational cost from lower to higher rungs. The LDA is at the lowest rung, and the generalized gradient approximations (GGAs), which introduce also the density gradient, are at the next higher rung of the ladder. The numerical accuracy of a DFT calculation depends to a large extent on the chosen DFA, and there is no universally good approximation. In practice, one may need to find a compromise between accuracy and computational cost, especially when performing solid-state calculations with simulation cells containing more than a few hundred atoms [52].

In this subsection, we review the most widely used DFAs, including LDA, GGAs (PBE and PBEsol as examples), and hybrid functionals (HSE06 as an example), together with a discussion of their performance in solid-state calculations.

Local-density approximation

In the LDA [41], it is assumed that the $E_{\text{xc}}[n(\mathbf{r})]$ is entirely local, and that the xc energy per electron at point $\mathbf{r}$ is equal to the xc energy per electron of a homogeneous electron gas (HEG) at this point with the same density; i.e.,

$$E_{\text{xc}}[n(\mathbf{r})] \approx E_{\text{xc}}^{\text{LDA}}[n(\mathbf{r})] = \int n(\mathbf{r}) \epsilon_{\text{xc}}^{\text{HEG}}[n(\mathbf{r})] d\mathbf{r}. \tag{2.37}$$

The $\epsilon_{\text{xc}}^{\text{HEG}}[n(\mathbf{r})]$ is commonly decomposed into exchange and correlation terms:

$$\epsilon_{\text{xc}}^{\text{HEG}}[n(\mathbf{r})] = \epsilon_{\text{x}}^{\text{HEG}}[n(\mathbf{r})] + \epsilon_{\text{c}}^{\text{HEG}}[n(\mathbf{r})]. \tag{2.38}$$

The $\epsilon_{\mathrm{x}}^{\mathrm{HEG}}$ is known analytically:

$$\epsilon_{\mathrm{x}}^{\mathrm{HEG}}[n(\mathbf{r})] = -\frac{3}{4}(\frac{3}{\pi})^{1/3} n(\mathbf{r})^{1/3}. \tag{2.39}$$

For $\epsilon_{\mathrm{c}}^{\mathrm{HEG}}$, analytic expressions are known only in the high- and low-density limits. For several intermediate values of $n(\mathbf{r})$, numerical results for $\epsilon_{\mathrm{c}}^{\mathrm{HEG}}$ have been calculated from nearly accurate Quantum Monte Carlo (QMC) simulations [53]. Several approximate analytic forms for $\epsilon_{\mathrm{c}}^{\mathrm{HEG}}$ exist; they are parametrized using the QMC data and meanwhile reproduce the known limiting behavior, and yield very similar results [38]. In our later study of Si, we will use the analytic form given by Perdew and Wang [54],

$$\epsilon_{\mathrm{c}}^{\mathrm{HEG}}[n(\mathbf{r})] = -2A(1+\alpha_1 r_{\mathrm{s}}) \ln[1 + \frac{1}{2A(\beta_1 r_{\mathrm{s}}^{1/2} + \beta_2 r_{\mathrm{s}} + \beta_3 r_{\mathrm{s}}^{3/2} + \beta_4 r_{\mathrm{s}}^{p+1})}], \tag{2.40}$$

where $r_{\mathrm{s}} \equiv r_{\mathrm{s}}(\mathbf{r}) = [\frac{3}{4\pi n(\mathbf{r})}]^{1/3}$ is the dimensionless Wigner-Seitz radius. The detailed value of the parameters in Equation (2.40) can be found in Ref. [54].

In principle the LDA is only valid for systems with uniform or slowly-varying density. However, this approximation has turned out to work surprisingly well in predicting the ground-state properties of atoms, molecules, and solids, in which the electron density is far from homogeneous [37]. For weakly correlated solids, such as simple metals and semiconductors, the LDA reliably describes structural and vibrational properties [33]. The success of this approximation has been partly attributed to the fact that it gives the correct sum rule for the xc hole[2] [55]. The LDA also has some well-known deficiencies: (i) It tends to overestimate the binding energies of solids and hence often underestimates the lattice constants [56, 57]; (ii) It systematically underestimates the band gaps of semiconductors and insulators (by about $40-50\%$) [58]. The band-gap problem will be discussed later.

Generalized Gradient Approximations

In order to account for density inhomogeneity, GGAs extend LDA by introducing an additional dependence on the gradients of the density [59]; i.e.,

$$E_{\mathrm{xc}}[n(\mathbf{r})] \approx E_{\mathrm{xc}}^{\mathrm{GGA}}[n(\mathbf{r})] = \int n(\mathbf{r}) \epsilon_{\mathrm{xc}}^{\mathrm{HEG}}[n(\mathbf{r})] F_{\mathrm{xc}}[n(\mathbf{r}), \nabla n(\mathbf{r})] d\mathbf{r}. \tag{2.41}$$

The $F_{\mathrm{xc}}[n, \nabla n]$ is the xc-enhancement factor, a dimensionless parameter that describes the deviation from $\epsilon_{\mathrm{xc}}^{\mathrm{HEG}}[n]$ (inherited from the LDA). Due to the density gradient ∇n, GGAs are semilocal functionals. Since there is no unique recipe for F_{xc}, various GGA

---

[2] The xc hole describes the depletion of electron density in the vicinity of each electron due to the exchange and Coulomb interactions. The sum rule states that this hole should contain only one charge unit [55].

functionals are available; they are different in which and how many exact physical constraints (limits, bounds, asymptotics, etc.) for E_{xc} are satisfied [60].

The PBE functional, developed by Perdew, Burke, and Ernzerhof [61], is the most widely used GGA in the physics community. It is nonempirical; that is, the numerical parameters in this functional are set solely by imposing several exact physical constraints on the energy functional. The PBE exchange is expressed as:

$$E_{\text{x}}^{\text{PBE}}[n] = \int n(\mathbf{r})\epsilon_{\text{x}}^{\text{HEG}}[n]F_{\text{x}}^{\text{PBE}}(s)d\mathbf{r}, \tag{2.42}$$

where the $F_{\text{x}}^{\text{PBE}}(s)$ takes a simple analytic form:

$$F_{\text{x}}^{\text{PBE}}(s) = 1 + \kappa(1 - \frac{1}{1 + \mu^{\text{PBE}}s^2/\kappa}), \tag{2.43}$$

where: (i) $s = |\nabla n|/(2k_{\text{F}}n(\mathbf{r}))$ is the reduced density-gradient, a dimensionless parameter measuring the local density inhomogeneity over a Fermi wavelength $\lambda_{\text{F}} = 2\pi/k_{\text{F}}$ with $k_{\text{F}} = [3\pi^2 n(\mathbf{r})]^{1/3}$; (ii) $\kappa = 0.804$ is set to the maximum value allowed by the Lieb-Oxford bound (a lower bound on E_{xc}) [62]; (iii) $\mu^{\text{PBE}} = 0.21951$ is set to reproduce the slowly varying limit ($s \to 0$), in which the gradient correction for exchange cancels that for correlation. The correlation component of PBE has a relatively complex analytic expression and is not detailed here. As a minor modification of PBE, PBEsol [63] is specifically parameterized to the physical constraints that are relevant to solids, and it differs from PBE only in two parameters.

When used in solid-state calculations, the PBE functional provides a good balance between numerical accuracy and computational cost. While PBE reduces the overbinding of the LDA, it often overestimates the lattice constants [56, 57]. This deficiency is generally improved by PBEsol [63, 56, 57]. For the band gaps, all GGAs show no significant improvement over LDA [64].

Hybrid functionals

Hybrid functionals [65], which are at the fourth rung of Perdew's "Jacob's ladder" of DFAs, replace a fraction of GGA exchange with that of Hartree-Fock:

$$E_{\text{xc}}[n] \approx E_{\text{xc}}^{\text{hybrid}} = \alpha E_{\text{x}}^{\text{HF}} + (1-\alpha)E_{\text{x}}^{\text{GGA}}[n] + E_{\text{c}}^{\text{GGA}}[n], \tag{2.44}$$

where E_{x}^{HF} is the exact (Hartree-Fock) exchange, and $\alpha \approx 1/4$. The exact exchange has an explicit dependence on the occupied one-electron orbitals:

$$E_{\text{x}}^{\text{HF}}[\{\psi_i\}] = -\frac{e^2}{2}\sum_{i,j}^{N}\int\int \psi_i^*(\mathbf{r}_1)\psi_j^*(\mathbf{r}_2)\frac{1}{|\mathbf{r}_1 - \mathbf{r}_2|}\psi_j(\mathbf{r}_1)\psi_i(\mathbf{r}_2)d\mathbf{r}_1 d\mathbf{r}_2, \tag{2.45}$$

which is a nonlocal functional. The one-electron orbitals are now solutions of the generalized Kohn-Sham equation [66, 67]:

$$[-\frac{\hbar^2}{2m}\nabla^2 + V_{\text{loc}}(\mathbf{r})]\psi_i(\mathbf{r}) + \int V_{\text{x}}^{\text{HF}}(\mathbf{r},\mathbf{r}')\psi_i(\mathbf{r}')d\mathbf{r}' = \epsilon_i\psi_i(\mathbf{r}), \tag{2.46}$$

where $V_{\text{loc}}(\mathbf{r})$ is the usual GGA potential, and a fraction α of the GGA exchange potential is replaced with the Hartree-Fock exchange potential (V_{x}^{HF}). Due to the nonlocal nature of the Hartree-Fock exchange potential, the numerical solution of Equation (2.46) is computationally costly.

Considering that the electron-electron Coulomb interaction is screened in solids, Heyd-Scuseria-Ernzerhof (HSE) screened hybrid functional [68] introduces an additional screening for the exact exchange, by partitioning the Coulomb operator $1/r = 1/|\mathbf{r}_1 - \mathbf{r}_2|$ into short-range (SR) and long-range (LR) components:

$$\frac{1}{r} = \underbrace{\frac{\text{erfc}(\omega r)}{r}}_{\text{SR}} + \underbrace{\frac{\text{erf}(\omega r)}{r}}_{\text{LR}}, \tag{2.47}$$

where ω is an adjustable parameter. With such a treatment, the decay of the exact exchange interaction in real space is accelerated [68], enabling a substantial lowering of the computational cost (though still much more costly than LDA and GGAs). Furthermore, the HSE functional considers only a screened short-range exchange, i.e.,

$$E_{\text{xc}}^{\text{HSE}} = \alpha E_{\text{x}}^{\text{HF, SR}}(\omega) + (1-\alpha)E_{\text{x}}^{\text{PBE,SR}}(\omega) + E_{\text{x}}^{\text{PBE,LR}}(\omega) + E_{\text{c}}^{\text{PBE}}. \tag{2.48}$$

The HSE06 [69] with the parameters $\omega = 0.11$ bohr^{-1} and $\alpha = 0.25$ has proven to be very successful in reasonably predicting the band gaps of many semiconductors. However, it does not provide general solutions [64].

DFT-LDA/GGA band-gap problem

As mentioned above, LDA and GGAs systematically and severely underestimate the band gaps of semiconductors and insulators. This problem has long been discussed since the 1980s [58, 70, 71, 43], and there is still ongoing effort to elucidate it [72, 42]. These works are reviewed as follows, and our focus is on the relation between the fundamental band gap (E_G) and the gap of Kohn-Sham band structure (E_g) for both the exact Kohn-Sham DFT and the (semi)local approximations.

For a neutral solid of N electrons, the fundamental gap E_G is defined as the difference between the electron ionization energy $I(N)$, which is the energy required to remove an electron from the neutral solid, and electron affinity $A(N)$, which is the energy gained by adding an electron:

$$\begin{aligned} E_G &= I(N) - A(N), \\ &= [E_0(N-1) - E_0(N)] - [E_0(N) - E_0(N+1)], \end{aligned} \tag{2.49}$$

where $E_0(N)$ is the ground-state energy of the N-electron system.

Consider first Kohn-Sham DFT with the exact functional and its extension to fractional electron numbers. It has been shown that the ground-state energy as a function of electron number is a set of straight-line segments connecting the total energies for consecutive integer electron numbers [44]:

$$\begin{aligned} \delta \times I(N) &= E_0(N-\delta) - E_0(N), \\ \delta \times A(N) &= E_0(N) - E_0(N+\delta), \end{aligned} \tag{2.50}$$

where $0 \leq \delta \leq 1$. Based on this linear behavior, E_G can be expressed in terms of a difference of derivatives at N [70]:

$$E_G = \lim_{\delta \to 0^+} \{ \frac{\partial E_0}{\partial N}|_{N+\delta} - \frac{\partial E_0}{\partial N}|_{N-\delta} \}, \tag{2.51}$$

where the first (second) derivative is carried out from the right (left). According to Janak's theorem, Equation (2.51) leads to [70]:

$$\begin{aligned} E_G &= \lim_{\delta \to 0^+} \{\epsilon_{\text{LUMO}}(N+\delta) - \epsilon_{\text{HOMO}}(N-\delta)\} \\ &= \lim_{\delta \to 0^+} \{\epsilon_{\text{LUMO}}(N-\delta) + C - \epsilon_{\text{HOMO}}(N-\delta)\} \\ &= \epsilon_{\text{LUMO}}(N) - \epsilon_{\text{HOMO}}(N) + C \\ &= E_g + C, \end{aligned} \tag{2.52}$$

where E_g is a nonzero gap[3] separating the highest occupied orbital (HOMO) and the lowest unoccupied orbital (LUMO) of Kohn-Sham band structure, and C is the derivative discontinuity of the xc energy:

$$C = \lim_{\delta \to 0^+} \{ \frac{\partial E_{\text{xc}}}{\partial N}|_{N+\delta} - \frac{\partial E_{\text{xc}}}{\partial N}|_{N-\delta} \}. \tag{2.53}$$

The understanding of Equation (2.51)-(2.53) is as follows [58, 42, 73]: First, it is worth noting that when the electron number is increased from N to $N+\delta$ and decreased from N to $N-\delta$, the HOMO and LUMO is "probed", respectively (this holds for the ground state). The HOMO and LUMO, which are separated by the E_g, correspond to distinct parts of the Kohn-Sham band structure. The gap E_g implies no orbital relaxations when

---

[3] Semiconductors and insulators.

an electron is lifted in energy from the HOMO to LUMO, i.e., both the density and E_{xc} are fixed to those of the N-electron ground state. This means that the E_g of the exact Kohn-Sham DFT is contributed solely by a derivative discontinuity in the kinetic energy $T_{\mathrm{s}}[n]$ of the Kohn-Sham electrons, while the difference between E_G and E_g stems from the xc discontinuity as the LUMO begins to fill. Equation (2.52) suggests that even the band gap for the exact functional underestimates the fundamental band gap.

For LDA and GGAs to DFT, the xc discontinuity is absent [58, 42]. As a result, the fundamental gap equals the gap of Kohn-Sham band structure:

$$E_G^{\mathrm{LDA/GGA}} = E_g^{\mathrm{LDA/GGA}}. \tag{2.54}$$

Equations (2.52)-(2.54) have explained the deficiency of (semi)local functionals in predicting the band gaps.

The band-gap problem can be traced back to the self-interaction error [43, 74] (or localization and delocalization errors [72]) in the (semi)local functionals, as briefed as follows. The electronic self-interaction describes the unphysical interaction of an electron with the Coulomb potential generated by its own charge. There is no self-interaction error in the exact Kohn-Sham DFT, where the xc energy of a single, fully occupied Kohn-Sham orbital cancels exactly its self-direct Coulomb energy. Such an exact cancellation no longer holds in the LDA and GGA functionals which are (semi)local, leading to underestimation of the band gap of semiconductors and insulators. Since the Hartree-Fock theory is self-interaction-free, hybrids of GGA with exact exchange can largely reduce the self-interaction error and give substantial improvement over LDA and GGAs for the band gaps.

To partially overcome the band-gap problem, one usually resorts to the HSE06 functional or, in particular, GW methods (introduced in Section 3.3.2). In this thesis, it is not possible to use these advanced methods for electrical conductivity calculations, due to the high computational cost. Thus, as in many state-of-the-art studies of real materials [75], in the present work we have to address the DFT band-gap problem with computationally less expensive alternatives.

2.4 DFT calculations with the FHI-aims code

The numerical solution of the Kohn-Sham equation is found by expanding the Kohn-Sham eigenfunctions in a basis set [38]:

$$\psi_n(\mathbf{r}) = \sum_{i=1}^{N_\mathrm{b}} C_{in}\varphi_i(\mathbf{r}), \tag{2.55}$$

i.e., each unknown $\psi_n(\mathbf{r})$ is expressed into a linear combination of N_b predefined functions $\varphi_i(\mathbf{r})$ with coefficients C_{in} associated with ψ_n. The basis functions specify the potential field of the nuclei. Further, with Equation (2.55), the Kohn-Sham equation reduces to a matrix equation of the coefficients C_{in}, and the resultant algebraic eigenvalue problem is routinely solved using standard iterative matrix diagonalization technique on a supercomputer. For having good flexibility in the self-consistent procedure, N_b should be reasonably larger than the number of ψ_n to be computed.

Kohn-Sham DFT has been implemented in various DFT computer codes which enable practical electronic-structure calculations. A key difference between these DFT codes is that they employ different types of basis functions. Common choices of basis functions include plane waves [38, 76], Gaussians [77], numeric atom-centered orbitals [78, 79], and their combinations as well [80, 81].

Numeric atom-centered orbitals as basis set in FHI-aims

Here we introduce the FHI-aims code, according to Refs. [78, 82]. FHI-aims uses numeric atom-centered orbitals (NAOs) as the basis functions. The NAO basis functions take the form:

$$\varphi_i(\mathbf{r}) = \frac{u_i(r)}{r} Y_{lm}(\Omega), \tag{2.56}$$

where $u_i(r)$ is a radial function specifying the radial shape and $Y_{lm}(\Omega)$ is a spherical harmonic. The NAO basis functions in the FHI-aims code have the following important features. (i) First, they are real-valued by construction. This is enabled by making $Y_{lm}(\Omega)$ comprise both the real parts ($m = 0, 1, \ldots, l$) and imaginary parts ($m = -l, \ldots, -1$) of the complex spherical harmonics (l and m are implicit functions of the basis index i). (ii) Second, the $u_i(r)$ are taken to be numerical solutions of Schrödinger-like radial equations:

$$[-\frac{1}{2}\frac{d^2}{dr^2} + \frac{l(l+1)}{r^2} + v_i(r) + v_\mathrm{cut}(r)]u_i(r) = \epsilon_i u_i(r). \tag{2.57}$$

The shape of $u_i(r)$ is mainly defined by the potential $v_i(r)$, but when r is far away from the (atomic) center, the steeply rising (yet smooth) confining potential $v_\mathrm{cut}(r)$ ensures that each $u_i(r)$ decays smoothly to zero for $r > r_\mathrm{cut}$. Owing to this, basis functions from well separated spatial regions of a large system do not overlap with each other. This is essential to form sparse matrices and to enable Kohn-Sham DFT implementation with near-$O(N)$ [instead of $O(N^3)$] scaling for all integrals (see below; N denotes system size). (iii) Third, each chemical element has a minimal basis set comprising the radial functions of occupied free-atom orbitals of this element. This is achieved by simply setting the $v_i(r)$ in Equation (2.57) to the self-consistent free-atom radial potential $v_{\mathrm{at}}^{\mathrm{free}}(r)$. This feature significantly improves both the numerical accuracy and convergence of all-electron full-potential calculations, as it naturally accounts for wave-function oscillations near the nucleus (the deep nuclear potential Z/r).

With the NAO basis functions entering Equation (2.55), one obtains a generalized eigenvalue problem:

$$\begin{aligned} \sum_j (h_{ij} - \epsilon_n s_{ij}) C_{jn} &= 0, \\ h_{ij} = \langle \varphi_i | \hat{h}^{\mathrm{KS}} | \varphi_j \rangle &= \int \varphi_i(\mathbf{r}) \hat{h}^{\mathrm{KS}} \varphi_j(\mathbf{r}) d\mathbf{r}, \\ s_{ij} = \langle \varphi_i | \varphi_j \rangle &= \int \varphi_i(\mathbf{r}) \varphi_j(\mathbf{r}) d\mathbf{r}, \end{aligned} \tag{2.58}$$

where h_{ij} and s_{ij} are the Hamiltonian and overlap matrix elements, respectively. Note that the FHI-aims NAO basis functions are nonorthogonal, which renders the overlap matrix. These real-space integrals are computed numerically using Lebedev grids [83, 84] which are overlapping atomic-centered grid points distributed in a set of radial shells for each atomic center. The basis functions are numerically tabulated with respect to both the basis index i and integration point. This allows for matrix operations in performing the real-space integration.

Equation (2.58) is solved using iterative matrix diagonalization algorithms in the standard self-consistent field (SCF) method [85]. The SCF cycle begins with an initial guess for the density. A trial h_{ij} is then constructed and used to solve Equation (2.58). The resulted coefficients C_{in} update the density and thus h_{ij}, and so forth. The convergence of the SCF iterations is monitored by keeping a track of the changes in density and total energy as well as other quantities between two consecutive SCF steps. Once these changes become smaller than the given thresholds, the numerical convergence is reached, and the SCF cycle is then finished. Note that the overlap matrix elements s_{ij} are computed only once and do not change during a SCF cycle (during which the nuclear positions are kept fixed). This is the reason why a SCF cycle is usually referred to as a static DFT calculation.

The numerical accuracy and computational cost of FHI-aims calculations depend critically on basis-set settings: (i) basis-set size (N_{b}), (ii) cutoff radius r_{cut}, and (iii) density of integration points. For each chemical element, besides the aforementioned free-atom minimal basis, there is a list of additional basis functions to be included in

FHI-aims calculations. In this list, the ordering of basis functions is exactly the output sequence of the basis-function construction process, and the additional basis functions are grouped into different *tiers*, e.g., for Si, $spdf$ (*tier* 1)-$spdg$ (*tier* 2)-... (Each tier includes the basis functions of lower tiers). There are three predefined default basis-set settings: "light", "tight", and "really_tight". As their names suggest, N_b, r_{cut}, and the density of integration points are all increased from "light" to "tight" and to "really_tight" settings. When it comes to total-energy calculations, the "light" settings usually provide a satisfactory convergence of total-energy differences, while the "tight" settings usually provide a satisfactory convergence of total energies [86]. Recently, a simple analytic model was proposed to estimate the numerical error associated with basis-set settings [87]. The "tight" settings are recommended for production calculations. However, when dealing with large-scale periodic systems using the "tight" settings, the computational effort can be enormous [88]. In this case, the cheaper "light" settings are usually used, but careful basis-set convergence test is necessary. In this thesis, our electrical conductivity calculations will be carried out using the "light" basis sets, and we will provide test calculations using the “tight" basis sets.

2.5 DFT in the solid state

From now on our discussion will be focused on crystalline solids which are infinitely extended systems. This section describes the electronic structure, lattice vibrations, and their interactions in crystalline solids.

2.5.1 Periodic boundary conditions

In a crystalline solid, any nucleus can be found by the position vector in the form:

$$\boldsymbol{\tau}_{\kappa p} = \mathbf{R}_p + \boldsymbol{\tau}_\kappa, \tag{2.59}$$

where: (i) $\mathbf{R}_p = \sum_i n_i \mathbf{a}_i$ is the lattice vector identifying the p-th primitive cell which is the smallest structural unit spanned by the primitive lattice vectors $\mathbf{a}_i$ with $i = 1, 2, 3$; (ii) $\boldsymbol{\tau}_\kappa$ is the position vector of the κ-th nucleus in the primitive cell.

The simulation of crystalline solids, in which an infinite number of electrons moving in the field of infinite number of nuclei, relies on using the Born-von Kármán (BvK) supercell [14]: a cell compromises $N_1 \times N_2 \times N_3$ primitive cells and is imposed with periodic boundary conditions (PBCs). The p-th primitive cell in the BvK supercell is identified by the lattice vector $\mathbf{R}_p = \sum_i n_i \mathbf{a}_i$ $(n_i = 0, 1, \ldots, N_i - 1)$ which is restricted in the BvK supercell. Starting from any point in the BvK supercell and translating $\sum_i l_i (N_i \mathbf{a}_i)$ (l_i are arbitrary integers) will trivially find the same point. Although still periodic, the BvK supercell no longer extends into the space outside itself.

For the BvK supercell, the Kohn-Sham Hamiltonian is given by $h_{\text{KS}} = -\frac{\hbar^2}{2m^2}\nabla^2 + V_{\text{eff}}(\mathbf{r}; \{\boldsymbol{\tau}_{\kappa p}\})$. The effective potential $V_{\text{eff}}(\mathbf{r}; \{\boldsymbol{\tau}_{\kappa p}\})$ takes the same form as Equation (2.26), but is now a periodic potential. According to Bloch's theorem, the Kohn-Sham eigenfunctions are Bloch functions [89]:

$$\psi_{n\mathbf{k}}(\mathbf{r}) = \frac{1}{\sqrt{N_{\text{cell}}}} e^{i\mathbf{k}\cdot\mathbf{r}} u_{n\mathbf{k}}(\mathbf{r}), \tag{2.60}$$

where $u_{n\mathbf{k}}(\mathbf{r}) = u_{n\mathbf{k}}(\mathbf{r} + \mathbf{R}_p)$ is a lattice-periodic function. By definition, $\psi_{n\mathbf{k}}$ and $u_{n\mathbf{k}}$ are normalized to one in the BvK supercell and primitive cell, respectively. The eigenfunctions $\psi_{n\mathbf{k}}(\mathbf{r})$ and eigenvalues $\epsilon_{n\mathbf{k}}$ are now labeled by two quantum numbers: band index n and wave vector $\mathbf{k}$. The $\mathbf{k}$ points allowed by the BvK supercell are:

$$\mathbf{k}_p = \sum_{i=1}^{3} \frac{n_i}{N_i} \mathbf{b}_i,\ n_i = 0, 1, \ldots, N_i - 1. \tag{2.61}$$

This relation indicates that a $N_1 \times N_2 \times N_3$ BvK supercell corresponds to a regularly spaced grid of $N_1 \times N_2 \times N_3$ points in the BZ of the primitive cell and vice versa. The electron density is now computed with an additional sum of $\mathbf{k}$ points:

$$n(\mathbf{r}) = \sum_{\mathbf{k}} \sum_{n=1}^{N} |\psi_{n\mathbf{k}}(\mathbf{r})|^2, \tag{2.62}$$

where N is the number of electrons in the primitive cell (instead of the BvK supercell).

Equation (2.62) indicates that by using a BvK supercell, the problem of calculating an infinite number of one-electron orbitals in an infinitely extended solid is changed to the one of calculating a finite number of one-electron orbitals at a finite number of $\mathbf{k}$ points. This mapping becomes exact when the number of $\mathbf{k}$ points is infinite, corresponding to an infinitely large BvK supercell. In practical calculations, fully converged electron density and total energy can be obtained by using a finite, yet sufficiently large number of $\mathbf{k}$ points, due to the fact that the electronic wave functions are almost identical for $\mathbf{k}$ points that are very close to each other [38]. The $\mathbf{k}$-point sampling is usually generated using the Monkhorst-Pack scheme [90], which leads to a regularly spaced grid of $N_1 \times N_2 \times N_3$ points in the BZ of the primitive cell[4]. In principle, the magnitude of any numerical error in the total energy due to incompletely converged $\mathbf{k}$-point sampling can always be reduced by using a denser set of $\mathbf{k}$ points [38], provided that the computational resources allow.

Solid-state calculations with FHI-aims

In FHI-aims, the PBCs are implemented by defining the Bloch-like generalized basis functions [78, 91]:

$$\chi_{i\mathbf{k}}(\mathbf{r}) = \frac{1}{\sqrt{N_{\text{cell}}}} \sum_{\mathbf{R}_p} e^{i\mathbf{k}\cdot\mathbf{R}_p} \varphi_i(\mathbf{r} - \boldsymbol{\tau}_\kappa - \mathbf{R}_p), \tag{2.63}$$

where $\varphi_i(\mathbf{r} - \boldsymbol{\tau}_\kappa - \mathbf{R}_p)$ denotes the i-th basis function which is centered at the κ-th atom belonging to the p-th primitive cell within the BvK supercell. It is easy to verify that $\chi_{i\mathbf{k}}(\mathbf{r} + \mathbf{R}_p) = e^{i\mathbf{k}\cdot\mathbf{R}_p}\chi_{i\mathbf{k}}(\mathbf{r})$. The Kohn-Sham eigenfunctions $\psi_{n\mathbf{k}}(\mathbf{r})$ are then expressed as a linear combination of $\chi_{i\mathbf{k}}(\mathbf{r})$:

$$\begin{aligned}\psi_{n\mathbf{k}}(\mathbf{r}) &= \sum_i C_{in}(\mathbf{k})\chi_{i\mathbf{k}}(\mathbf{r}) \\ &= \frac{1}{\sqrt{N_{\text{cell}}}} \sum_i C_{in}(\mathbf{k}) \sum_{\mathbf{R}_p} e^{i\mathbf{k}\cdot\mathbf{R}_p} \varphi_i(\mathbf{r} - \boldsymbol{\tau}_\kappa - \mathbf{R}_p),\end{aligned} \tag{2.64}$$

which are Bloch functions by construction.

---

[4] In practical DFT calculations, one provides a "simulation cell", which is the structural model, as the input. In FHI-aims calculations, the “simulation cell" is specified in the "geometry.in" file. Any “simulation cell" is treated as a primitive cell by solid-state DFT codes.

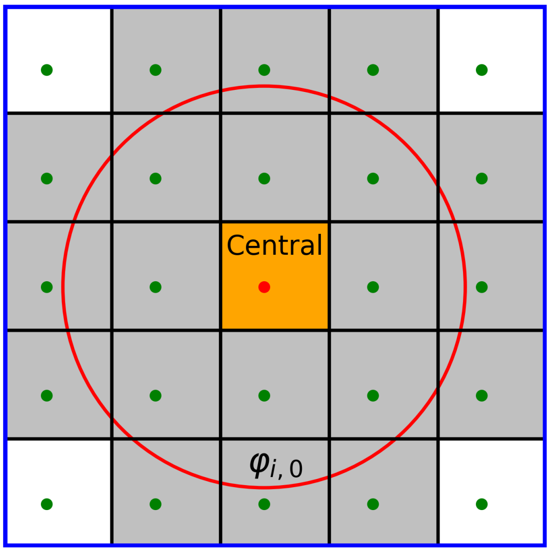

Figure 2.1: Schematic illustration of the central unit cell (orange area), the DFT supercluster (grey and orange area), and the implicit BvK supercell (all the blocks). The dots denote atomic centers, and $\varphi_{i,0}$ denotes the most extended basis function from the central unit cell. Adapted from Refs. [91, 92].

In FHI-aims, the so-called “supercluster" instead of the BvK supercell is actually used in solid-state calculations [91, 92]. As shown schematically in Figure 2.1, a central unit cell is defined, and has the lattice vector $\mathbf{R}_p = (0, 0, 0)$. The basis functions from the central unit cell extend into other unit cells (the so-called image unit cells), but since the basis functions are strictly localized within a certain range, they can only touch the nearby unit cells. Equivalently speaking, only those unit cells whose basis functions can touch the central unit cell can have nonzero basis functions in the central unit cell and contribute to the real-space integrals (which are carried out in the central unit cell). These unit cells, including the central unit cell, forms the supercluster. The supercluster can be viewed as the BvK supercell excluding the unit cells whose basis functions cannot touch the central unit cell (see Figure 2.1). It is of fixed size, regardless of the **k**-point sampling. The use of supercluster enables limiting the computational cost when using a dense **k**-point sampling and/or a large simulation cell [78], and it is the key to enable near-$O(N)$ scaling in FHI-aims calculations.

The matrix elements of electron momentum operator, i.e., $\langle\psi_{m\mathbf{k}}|\mathbf{p}|\psi_{n\mathbf{k}}\rangle$, are one of the main quantities needed in electrical conductivity calculations. In the semi-classical theory, the diagonal elements of momentum matrix are called the electron group velocities, i.e., $\mathbf{v}_{n\mathbf{k}} = \langle\psi_{n\mathbf{k}}|\mathbf{p}|\psi_{n\mathbf{k}}\rangle/m$ [7]. The non-diagonal elements ($m \neq n$) represent electronic inter-band transitions. In FHI-aims, the computation of $\langle\psi_{m\mathbf{k}}|\mathbf{p}|\psi_{n\mathbf{k}}\rangle$ is straightforward by using the definition of the electron momentum operator $\mathbf{p} = -i\hbar\nabla$, i.e.,

$$\begin{aligned}\langle\psi_{m\mathbf{k}}|\mathbf{p}|\psi_{n\mathbf{k}}\rangle &= -i\hbar\sum_{i,j} C^*_{jm}(\mathbf{k})C_{in}(\mathbf{k})\int \chi^*_{j\mathbf{k}}(\mathbf{r})\nabla\chi_{i\mathbf{k}}(\mathbf{r})d\mathbf{r} \\ &= -i\hbar\sum_{i,j} C^*_{jm}(\mathbf{k})C_{in}(\mathbf{k}) \\ &\times \frac{1}{N_{\text{cell}}}\sum_{p,q} e^{i\mathbf{k}\cdot(\mathbf{R}_p-\mathbf{R}_q)}\int \varphi_j(\mathbf{r}-\boldsymbol{\tau}_\kappa-\mathbf{R}_q)\nabla\varphi_i(\mathbf{r}-\boldsymbol{\tau}_\kappa-\mathbf{R}_p)d\mathbf{r} \\ &= -i\hbar\sum_{i,j} C^*_{jm}(\mathbf{k})C_{in}(\mathbf{k})\frac{1}{N_{\text{cell}}}\sum_{p,q} e^{i\mathbf{k}\cdot(\mathbf{R}_p-\mathbf{R}_q)}\langle\varphi_j;\mathbf{R}_q|\nabla|\varphi_i;\mathbf{R}_p\rangle,\end{aligned} \tag{2.65}$$

where the basis gradient elements $\langle\varphi_j;\mathbf{R}_q|\nabla|\varphi_i;\mathbf{R}_p\rangle$ can be conveniently computed in the spherical coordinates. Detailed derivation of the atomic-sphere contribution to $\langle\varphi_j;\mathbf{R}_q|\nabla|\varphi_i;\mathbf{R}_p\rangle$ can be found in the work of Draxl *et al.* [93]. The computation of the momentum-matrix elements is a post-SCF calculation.

2.5.2 Interactions between electrons and lattice vibrations

Having outlined the key elements in DFT calculations of the electronic structure of crystalline solids with static nuclei, we now proceed to describe lattice vibrations and coupling between electrons and lattice vibrations in crystalline solids at finite temperature. Two established methods are introduced and compared: the first (also *de facto* standard) is based on approximate models; the second is based on *ai*MD simulations.

Supercell calculations

Lattice vibrations in crystalline solids are characterized by collective atomic displacements. For this long-range behavior, the theoretical description can use a large simulation cell with PBCs. The allowed lattice-vibrational modes are determined by the size of the simulation cell, which can be understood as follows. Consider a simulation cell consisting of $N_1 \times N_2 \times N_3$ primitive cells. The BZ of the simulation cell can be obtained by folding (towards the zone center) the BZ of the primitive cell N_i times along the $\mathbf{b}_i$ (the reciprocal-space lattice vector of the primitive cell) for the i-th direction. Let's sample the BZ of the simulation cell by a single $\boldsymbol{\Gamma}$ point. Due to the periodicity of the reciprocal lattice, the $\boldsymbol{\Gamma}$ point can be mapped to its periodic images by the lattice vector $\sum_i \mathbf{b}_i/N_i$. This is equivalent to sampling the BZ of the primitive cell with a $N_1 \times N_2 \times N_3$ $\mathbf{q}$-point grid[5], and the set of $\mathbf{q}$ points is given by Equation (2.61). Such an effective $\mathbf{q}$-point grid is considered to be commensurate with the simulation cell [94]. Thus, in order to allow

---

[5] Following the convention, $\mathbf{q}$ instead of $\mathbf{k}$ is used when discussing the lattice dynamics.

for a fine sampling of the BZ of the primitive cell, or in other words, to access the long-wavelength vibrational modes (characterized by small **q** in the BZ of the primitive cell), a large simulation cell has to be used.

The above "large simulation cell" is called “supercell" in literature (also in this thesis), and it is conceptually the same as the "BvK supercell", though the former serves as an input structural model in DFT calculations and is always treated as a “primitive" cell by DFT codes. When the BZ of the supercell is sampled with a $M_1 \times M_2 \times M_3$ **k**-point grid, a BvK supercell of size $M_1 \times M_2 \times M_3$ will be constructed out of the supercell. Therefore, when performing supercell calculations using a dense **k**-point sampling, the calculations would be costly, especially for large supercells.

The DFT calculations based on a supercell model are known as the "supercell approach". This approach is widely used in studying crystalline solids when the lattice-translational symmetry is broken due to e.g. lattice vibrations [95] or point defects [52].

Phonons: Lattice vibrations in the harmonic approximation

Within the BO approximation, the motion of the nuclei is on the ground-state BO PES $U(\{\boldsymbol{\tau}_{\kappa p}\})$, i.e., the total potential energy of the system which depends parametrically on the instantaneous coordinates $\boldsymbol{\tau}_{\kappa p}$ of all the nuclei (see Section 2.2). The lattice vibrations are usually treated in the harmonic approximation [33, 14]; in this approximation, the total potential energy is expanded to second order in the atomic displacement $\Delta\tau_{\kappa\alpha p} = \tau_{\kappa\alpha p} - \tau^0_{\kappa\alpha p}$ ($\alpha = 1, 2, 3$) of atom κ in the p-th unit cell:

$$U = U_0 + \frac{1}{2} \sum_{\substack{\kappa\alpha p \\ \kappa'\alpha' p'}} \frac{\partial^2 U}{\partial\tau_{\kappa\alpha p}\partial\tau_{\kappa'\alpha' p'}} \Delta\tau_{\kappa\alpha p}\Delta\tau_{\kappa'\alpha' p'}, \tag{2.66}$$

where: (i) $U_0 = U(\{\boldsymbol{\tau}^0_{\kappa p}\})$ denotes the total energy calculated for the nuclei at their ground-state equilibrium positions, at which the atomic forces $\partial U/\partial\tau_{\kappa\alpha p}$ vanish; (ii) The interatomic force constants $\partial^2 U/\partial\tau_{\kappa\alpha p}\partial\tau_{\kappa'\alpha' p'}$ are evaluated for the equilibrium nuclear configuration; (iii) The third- and higher-order terms, which are called *lattice anharmonicity*, have been discarded. Equation (2.66) defines a so-called harmonic PES [96], as schematically shown in Figure 2.2. The lattice vibrations are then described by a set of independent harmonic oscillators, i.e., the phonons. For a given wave vector **q** in the BZ of the primitive cell, there are $3N_\mathrm{a}$ branches (labeled by index ν) of phonons with frequencies $\omega_{\mathbf{q}\nu}$ and polarization vectors $e_\nu(\mathbf{q})$.

There are two commonly used approaches by which to obtain the interatomic force constants from first-principles calculations [33]: (i) the frozen-phonon method on a reasonably sized supercell; (ii) the density-functional perturbation theory (DFPT) method on the primitive cell of the perfect crystal.

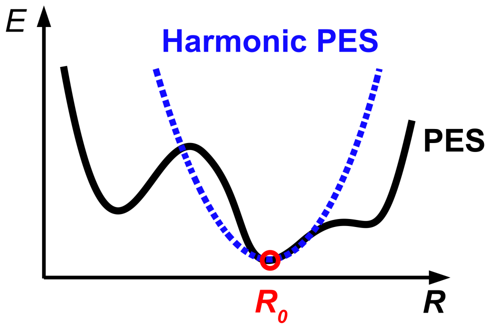

Figure 2.2: Schematic illustration of the potential-energy surface (PES) (black) and its harmonic approximation (blue). The minimum of the PES corresponds to the ground-state equilibrium geometry.

Electron-phonon interactions

As a consequence of lattice vibrations, the crystal potential seen by the electrons fluctuates and perturbs the electronic structure. Such a coupling between the electrons and lattice vibrations in crystalline solids is known as the electron-phonon (e-ph) interaction, which plays a key role in understanding the finite-temperature properties of crystals. In fact, in the very same work [97] where Bloch presented the formal solution of the Schrödinger equation in a periodic potential, the first quantum-mechanical description of temperature dependence of the electrical conductivity in metals was also provided based on a discussion of the e-ph interaction.

In the theoretical description of the e-ph interaction, the key is to express the e-ph coupling matrix elements. For this, the Kohn-Sham effective potential $V_{\text{eff}}(\mathbf{r};\{\boldsymbol{\tau}_{\kappa p}\})$ is usually expanded to first order in the atomic displacements $\Delta\tau_{\kappa\alpha p}$ [14, 12]:

$$V_{\text{eff}}(\mathbf{r};\{\boldsymbol{\tau}_{\kappa p}\}) = V_{\text{eff}}(\mathbf{r};\{\boldsymbol{\tau}^0_{\kappa p}\}) + \sum_{\kappa\alpha p} \frac{\partial V_{\text{eff}}}{\partial \tau_{\kappa\alpha p}} \Delta\tau_{\kappa\alpha p}, \tag{2.67}$$

where $V_{\text{eff}}(\mathbf{r};\{\boldsymbol{\tau}^0_{\kappa p}\})$ is calculated for the nuclei in their equilibrium positions, and the first-order derivatives are evaluated for the equilibrium geometry.

In the phonon representation, the e-ph matrix elements are expressed as [14, 12]:

$$g_{mn\nu}(\mathbf{k},\mathbf{q}) = \sum_{\kappa\alpha} \sqrt{\frac{\hbar}{2M_\kappa \omega_{\mathbf{q}\nu}}} [e_\nu(\mathbf{q})]_{\kappa\alpha} \sum_p \langle \psi_{m\mathbf{k}+\mathbf{q}} | \frac{\partial V_{\text{eff}}}{\partial \tau_{\kappa\alpha p}} | \psi_{n\mathbf{k}} \rangle e^{i\mathbf{q}\cdot\mathbf{R}_p}, \tag{2.68}$$

where $\psi_{n\mathbf{k}}$ and $\psi_{m\mathbf{k}+\mathbf{q}}$ are the Kohn-Sham eigenstates for the equilibrium geometry $\{\boldsymbol{\tau}^0_{\kappa p}\}$. The $g_{mn\nu}(\mathbf{k},\mathbf{q})$ describes the probability amplitude of the electronic scattering between the states $\psi_{n\mathbf{k}}$ and $\psi_{m\mathbf{k}+\mathbf{q}}$ by emitting or absorbing a phonon in the mode with frequency $\omega_{\mathbf{q}\nu}$, due to the collective atomic motion along the phonon polarization vector $e_\nu(\mathbf{q})$. It should be emphasized that the e-ph matrix elements defined by Equation (2.68) are based on the approximation of first-order e-ph interaction considering only electron-one-phonon processes.

The $g_{mn\nu}(\mathbf{k},\mathbf{q})$ can be computed by using either the frozen-phonon method [94, 98] or the DFPT method [14, 33, 99]. In the frozen-phonon method, the derivatives of the Kohn-Sham potential are evaluated by finite differences as:

$$\frac{\partial V_{\text{eff}}}{\partial \tau_{\kappa\alpha p}} \simeq \frac{V_{\text{eff}}(\mathbf{r};\{\boldsymbol{\tau}_{\kappa p}+\Delta\}) - V_{\text{eff}}(\mathbf{r};\{\boldsymbol{\tau}_{\kappa p}\})}{\Delta}, \tag{2.69}$$

where Δ denotes a small displacement. This method is limited to the phonon wavevectors that are commensurate with the supercell, and it is computationally prohibitive to access long-wavelength phonons (those with small $\mathbf{q}$ in the BZ of the primitive cell). This difficulty can be circumvented by performing DFPT calculations, which employ the primitive cell of the perfect crystal and can provide $g_{mn\nu}(\mathbf{k},\mathbf{q})$ at arbitrary $\mathbf{q}$ points in the BZ. Within DFPT, the evaluation of $g_{mn\nu}(\mathbf{k},\mathbf{q})$ goes through the self-consistent calculation of the linear response of the electron density to phonon perturbations, by evaluating the variation of the Kohn-Sham wavefunctions to first order in perturbation theory. Since DFPT calculations for a large number of $\mathbf{q}$ points are computationally prohibitive, $g_{mn\nu}(\mathbf{k},\mathbf{q})$ are usually computed on a coarse grid of $\mathbf{q}$ (as well as of $\mathbf{k}$), and are then interpolated onto arbitrarily dense grids for calculating materials properties related to the e-ph interaction [100]. DFPT has become the prevailing and most efficient *ab initio* method to calculate e-ph interactions.

Ab initio molecular dynamics

The approximate models in the above treatment of lattice vibrations and the coupling between electrons and lattice vibrations can be avoided altogether by performing *ai*MD simulations at finite temperature, as introduced below.

The *ai*MD is a conceptually simple yet powerful computational technique [101, 102, 103], which can generate atomic trajectories on the BO PES according to the equations of motion for the nuclei in the supercell[6]:

$$M_I \ddot{\mathbf{R}}_I(t) = -\frac{\partial U(\{\mathbf{R}_I\})}{\partial \mathbf{R}_I}, \tag{2.70}$$

where $U(\{\mathbf{R}_I\})$ is the total potential energy of the supercell in the atomic configuration $\{\mathbf{R}_I\}$. Equation (2.70) relates the acceleration of the nuclei to the *ab initio* forces acting on them. For *ai*MD simulations in a canonical ensemble (NVT), the temperature can

---

[6] We follow the convention of the MD community using $\{\mathbf{R}_I\}$ to denote the atomic configurations.

be controlled via e.g. a Langevin thermostat [103]. A MD run starts from an initial condition, i.e., initial atomic positions and velocities $\{\mathbf{R}_I(t_0), \dot{\mathbf{R}}_I(t_0)\}$. By performing a SCF calculation on $\{\mathbf{R}_I(t_0)\}$, the atomic forces obtained are used to solve Equation (2.70) via numerical time-integration method (e.g., the velocity Verlet algorithm) with a reasonable time step Δt, leading to $\{\mathbf{R}_I(t_1), \dot{\mathbf{R}}_I(t_1)\}$ ($t_1 = t_0 + \Delta t$), and so forth, generating a trajectory on the PES. After sufficiently many time steps for equilibrating the system (e.g., when the temperature becomes stable), one starts collecting samples (i.e., atomic configurations) as the MD trajectory is generated. The sampling time interval (i.e., number of time steps for regularly selecting one sample) should be large enough in order to create a set of uncorrelated samples. Due to numerical noise in the integration of the equations of motion, i.e., truncation error in the Verlet integrator and round-off error, many correlations are lost very fast. However, because of long-wavelength phonons, some correlations may stay for very long times [104, 105], which defines the lower bound of the allowed sampling time interval. On the other hand, one must not use a too large sampling time interval, because this means a very long MD trajectory to achieve a representative set of samples. These point to the subtleties involved in choosing a reasonable sampling time interval. The practice is to estimate the correlation for the physical quantity of interest (see the test in Section 4.1).

By creating a sufficiently large number of samples from MD trajectories, equilibrium properties at the temperature T, in terms of thermodynamic expectation value $\langle O\rangle_T$ of a physical observable O (for example, the electronic band gap [106]), can be obtained by averaging over the samples collected:

$$\langle O\rangle_T \simeq \langle O\rangle_{N_s} = \frac{1}{N_s}\sum_{i=1}^{N_s} O(\{\mathbf{R}_I\}_i), \tag{2.71}$$

where $O(\{\mathbf{R}_I\}_i)$ denotes the calculated value of observable O for the i-th sample $\{\mathbf{R}_I\}_i$, and $\langle O\rangle_{N_s}$ is the average over N_s samples. The results, evaluated as the sample mean, naturally contain information on the dynamics of the system including the fully anharmonic lattice dynamics [33, 27].

Equation (2.71) holds for ergodic systems; that is to say, one is capable of creating a set of samples to represent the typical distribution of the nuclei on the BO PES at the temperature of interest. In general, crystalline materials at low temperature (e.g. below the Debye temperature) tend to be strongly harmonic and, hence, poorly ergodic [33]. This is understood as follows: In a harmonic system, phonons generally have a long lifetime such that the system is prone to spend a long period of time in each of its lattice-vibrational modes, thus requiring long MD trajectories to describe the typical distribution of the nuclei. Besides, the fluctuation of a physical observable in the canonical ensemble is roughly proportional to $1/\sqrt{N_\text{atom}}$ (N_atom denotes the number of atoms in the system) [107], so one can expect that the smaller the system size, the larger the N_s required (in order for a good statistical convergence).

Summary of the methods

We summarize the pros and cons of the two methods introduced in this subsection for treating lattice vibrations and the coupling between electrons and lattice vibrations.

Phonons and e-ph interactions: In this method, finite-temperature properties can be understood in terms of individual phonon modes and e-ph scattering events, by which rich microscopic insights can be obtained. When e-ph matrix elements are evaluated from DFPT, the calculation involves only a single unit cell and is allowed for arbitrary $\mathbf{q}$ points. Regarding the weaknesses, this method relies on two key assumptions: harmonic phonons and first-order e-ph interaction. The harmonic approximation to lattice dynamics is known to be inaccurate in many modern functional materials [15], and even breaks down completely when applied to crystal structures which are dynamically unstable at 0 K (i.e., soft phonon modes are found). In the latter case, self-consistent phonon calculations [27, 28, 29], which construct an effective harmonic PES by accounting for lattice anharmonicity at finite temperature, are usually performed to stabilize the soft phonon modes; the e-ph matrix elements are then computed using the anharmonic phonons [25, 26]. It should be noted that the self-consistent phonon method is still an approximate model accounting only partially for lattice anharmonicity [27]. We also briefly note that: (i) The phonon picture may be invalid for e.g. soft systems; (ii) It could be complicated to represent the lattice distortion induced by point defects[7] in the phonon picture (in this case defect supercells are also needed). Besides, including higher-order terms, notably anharmonic terms and multiphonon terms, in the e-ph interaction is a challenging task. Studies by means of frozen-phonon calculations [29, 108] or perturbative calculations [30, 31, 109] were both found.

AiMD simulations: This method naturally accounts for lattice anharmonicity to all orders and does not require perturbation theory to treat the coupling between electrons and lattice vibrations. It is versatile, i.e., solids being ideally crystalline, doped, or disordered, and, with weak or strong lattice anharmonicity can in principle be treated with this method on the same footing. This method has two major limitations. First, it lacks microscopic insights into the dynamics of the system, and hence cannot provide a detailed understanding of the physical properties studied. Second, the system size may prevent achieving meaningful results [33, 94]. In principle, an infinitely large supercell (corresponding to the thermodynamic limit) should be used in *ai*MD simulations, but in practice, the supercells allowed by current computational resources are of limited size (typically a few hundred atoms). The use of finite supercells neglects entirely long-wavelength phonons which are relevant in semiconductors at typical operating temperature, leading to finite-size errors.

In this thesis, we choose to use *ai*MD simulations, as its combination with the Kubo-Greenwood formula constitutes a promising approach for studying the electrical conductivity of anharmonic materials (see next chapter).

---

[7] Point defects cannot be ignored in real materials for their large influence on the electrical properties.

3 Electrical conductivity and the *ab initio* approaches

Electrical transport phenomena occur when materials are subjected to an applied electric field[1]. Such nonequilibrium dynamic states in the linear regime[2] obey the Ohm's law (1860s), which states that the macroscopic, steady-state electric current density **J** in the system is proportional to the external electric field **E**:

$$\mathbf{J} = \sigma \mathbf{E}, \tag{3.1}$$

where the constant of proportionality σ is the electrical conductivity, which is a scalar for an isotropic system. The electrical conductivity is an intrinsic material property that quantifies the ability of a material to conduct charge carriers (free electrons and free holes). In the literature, the electrical resistivity $\rho = 1/\sigma$ is also often used. Once the electrical conductivity is determined, other electrical transport coefficients, such as the electrical mobility, can be obtained.

Historically, understanding the electrical conductivity has played a central role in the development of the theory of electrons in solids [111]. There are two most celebrated theories of the electrical conductivity: Boltzmann transport theory (established by Boltzmann 1872, Drude 1900, Sommerfeld 1928, Bloch 1929, and others) and Kubo's theory of linear response (established by Onsager 1931, Green 1954, Kubo 1957, and others). Over the past decades, the theoretical description of electronic transport in solids[3] has mostly been based on the Boltzmann transport equation (BTE) and evolved from early semi-empirical calculations [7] to fully *ab initio* calculations [12, 13].

This chapter reviews these two theories and their *ab initio* implementations for calculating the electrical conductivity of real materials from first principles. Despite of the remarkable success of the *ab initio* BTE approach to the electronic-transport problem, the current challenge in studying materials with strong lattice anharmonicity calls for developing new computational approaches and leads us to explore the *ab initio* Kubo-Greenwood (KG) approach.

---

[1] Or other external driving forces, e.g., temperature difference across the system (thermoelectric effect) [1].

[2] Where the fluxes (charge, heat, mass, etc.) depend linearly on the external driving forces [110].

[3] In most crystalline solids, electrical transport properties are associated with electronic transport.

3.1 Boltzmann theory of electronic transport

In the Boltzmann transport theory, the kinetic motion of a classical ideal gas under a uniform applied electric field **E** is described by the BTE [112]:

$$\begin{aligned}\frac{\partial f}{\partial t} &\equiv (\frac{\partial f}{\partial t})_{\text{diff}} + (\frac{\partial f}{\partial t})_{\text{drift}} + (\frac{\partial f}{\partial t})_{\text{scatt}} \\ &= -\frac{\mathbf{p}}{m} \cdot \nabla_{\mathbf{r}} f - \mathbf{E} \cdot \frac{\partial f}{\partial \mathbf{p}} + (\frac{\partial f}{\partial t})_{\text{scatt}},\end{aligned} \tag{3.2}$$

where $f = f(\mathbf{r}, \mathbf{p}, t)$ is the non-equilibrium phase-space distribution function. The quantity $f(\mathbf{r}, \mathbf{p}, t) d\mathbf{r} d\mathbf{p}$ term gives the number of particles found at time t in the phase-space elementary volume $d\mathbf{r}d\mathbf{p}$ at the point $(\mathbf{r}, \mathbf{p})$. The three terms on the right-hand side of Equation (3.2) are called the diffusion, drift, and scattering (or collision) terms, respectively. The diffusion term vanishes for spatially uniform systems which are usually assumed. When $\partial f / \partial t = 0$, a steady state is reached.

The modern theory of electrical conduction in solids began with the Drude model [113], thirteen years after Thomson (1897) discovered the electron. By treating metals as a classical free-electron gas plus ions, Drude model provides the following microscopic picture of electron motion in metals: (i) In the absence of an external electric field, the electrons are in thermal motion due to collisions with the ions. (ii) In the presence of an electric field, the electrons acquire a drift motion, which is opposite the direction of the applied electric field and superimposed on the thermal motion. The drift velocity is typically much smaller than the thermal velocity [114]. (iii) The electron-ion collisions are assumed as instantaneous events, which randomize completely the motion of the electrons and dissipate the energy gained by the electrons from the external electric field into heat (i.e., lattice vibrations). In the Drude model, the electrical conductivity reads [115]:

$$\sigma = \frac{ne^2\tau}{m}, \tag{3.3}$$

where e (< 0), m, and n are the electron charge, electron mass, and number density of the electrons, respectively. The phenomenological parameter τ is called the relaxation time, which is understood as the average time spent by an electron between two successive electron-ion collisions. The value of τ can be estimated by fitting the experimental data, and it is typically a few tens fs at room temperature [116, 117]. A related important concept is the mean free path $l = u\tau$ (u denotes the thermal velocity).

Drude model unveils the fundamental microscopic mechanism underlying the electrical conductivity of metals: (i) The electrons are responsible for the electrical conduction, and (ii) scattering of the electrons gives rise to resistance. Despite of simplicity, these notions remain at the heart of the modern theory of the electrical conductivity. Sommerfeld (1928) [118] extended the Drude model by applying the Fermi-Dirac statistics to the electrons, and attempted to solve the failure of the Drude model in explaining temperature dependence of the electrical conductivity in metals, which, however, was not successful.

Ab initio BTE approach

A milestone was reached in 1929 when Bloch presented the theory of electrons in a periodic potential [97]. In the very same work, Bloch improved Sommerfeld's treatment of temperature dependence of the electrical conductivity of metals by considering the motion of crystal electrons. He discussed the scattering of electrons by the fluctuations of crystal potential due to thermally induced lattice vibrations (in modern language, e-ph interactions), and derived the first expression of the e-ph matrix element. Further, Bloch identified a semiclassical, linearized BTE where the drift term is given by [119],

$$(\frac{\partial f_{n\mathbf{k}}}{\partial t})_{\text{drift}} = -e\mathbf{E}\cdot\mathbf{v}_{n\mathbf{k}}\frac{\partial f^0_{n\mathbf{k}}}{\partial \epsilon_{n\mathbf{k}}}, \tag{3.4}$$

where $\mathbf{v}_{n\mathbf{k}} = \frac{1}{\hbar}\frac{\partial \epsilon_{n\mathbf{k}}}{\partial \mathbf{k}}$ and $f^0_{n\mathbf{k}}$ are the band velocity and Fermi-Dirac distribution (i.e., the distribution function in thermal equilibrium) associated with the single-particle state $|n\mathbf{k}\rangle$, respectively. Note that Bloch's linearized BTE is still founded on the electron-gas model, but the equilibrium states of the electrons are described by Bloch states. For a comprehensive historical perspective of the Boltzmann transport theory of electrical conductivity in solids, the reader is referred to Bardeen [120], Allen and Butler [119], and Allen [121, 122].

Bloch's work includes all the key elements of *ab initio* BTE calculations of the electrical conductivity of solids. However, for many years, due to the lack of first-principles approaches to systematic calculations of e-ph interactions, the relaxation-time approximation (RTA) with a constant relaxation time τ (an empirical parameter) was usually employed [7]. In this approximation, the scattering term can be written as [12]:

$$(\frac{\partial f_{n\mathbf{k}}}{\partial t})_{\text{scatt}} = -\frac{\delta f_{n\mathbf{k}}}{\tau}, \tag{3.5}$$

where $\delta f_{n\mathbf{k}} = f_{n\mathbf{k}} - f^0_{n\mathbf{k}}$ is the deviation from the Fermi-Dirac distribution. Solving $(\partial f_{n\mathbf{k}}/\partial t)_{\text{drift}} + (\partial f_{n\mathbf{k}}/\partial t)_{\text{scatt}} = 0$ with Equations (3.4) and (3.5) gives rise to a steady-state current $\mathbf{J} = \frac{e}{V}\sum_{n\mathbf{k}}\delta f_{n\mathbf{k}}\mathbf{v}_{n\mathbf{k}}$ with $\delta f_{n\mathbf{k}} = e\mathbf{E}\cdot(-\frac{\partial f^0_{n\mathbf{k}}}{\partial \epsilon_{n\mathbf{k}}})\mathbf{v}_{n\mathbf{k}}\tau$. The electrical conductivity is then given by:

$$\sigma = \frac{e^2}{3V}\sum_{n\mathbf{k}}(-\frac{\partial f^0_{n\mathbf{k}}}{\partial \epsilon_{n\mathbf{k}}})\mathbf{v}_{n\mathbf{k}}\cdot\mathbf{v}_{n\mathbf{k}}\tau. \tag{3.6}$$

Within band theory, Bardeen [120] provided an intuitive understanding of the electrical conductivity of metals: (i) A perfectly periodic lattice has an infinite electrical conductivity, because Bloch states are eigenfunctions having a infinite lifetime; but (ii) thermally induced lattice vibrations (as well as other imperfections like point defects) destroy the periodicity of the lattice and lead to scattering of the electrons, resulting in finite relaxation times $\tau_{n\mathbf{k}}$ and a finite electrical conductivity.

Today, owing to the development of the DFPT method for *ab initio* calculations of e-ph interactions, it has become common practice to compute the state-resolved relaxation times $\tau_{n\mathbf{k}}$ [123, 124, 125]:

$$\begin{aligned}\tau_{n\mathbf{k}}^{-1} = \frac{2\pi}{\hbar}\sum_{\mathbf{q}m\nu}|g_{nm\nu}(\mathbf{k},\mathbf{q})|^2 \\ \times [(1 - f^0_{m\mathbf{k}+\mathbf{q}} + n_{-\mathbf{q}\nu})\delta(\epsilon_{n\mathbf{k}} - \hbar\omega_{-\mathbf{q}\nu} - \epsilon_{m\mathbf{k}+\mathbf{q}}) + \\ (f^0_{m\mathbf{k}+\mathbf{q}} + n_{\mathbf{q}\nu})\delta(\epsilon_{n\mathbf{k}} + \hbar\omega_{\mathbf{q}\nu} - \epsilon_{m\mathbf{k}+\mathbf{q}})],\end{aligned} \tag{3.7}$$

where $g_{nm\nu}(\mathbf{k},\mathbf{q})$ are the e-ph matrix elements (defined in Section 2.5.2), and $n_{\mathbf{q}\nu}$ is the Bose-Einstein occupation of the phonon mode $(\mathbf{q},\nu)$. Equation (3.7) indicates that the e-ph interaction leads to energy- and crystal-momentum-conserving inelastic scattering of the electrons. The e-ph scattering rates $\tau_{n\mathbf{k}}^{-1}$ given by Equation (3.7) are derived in the lowest order of perturbation theory [12, 31] and are for the electron-one-phonon scattering processes. We also note the relation $\tau_{n\mathbf{k}}^{-1} = \frac{2}{\hbar}\mathrm{Im}\Sigma_{n\mathbf{k}}$, where $\Sigma_{n\mathbf{k}}$ is the e-ph self-energy [14]. The solution of the linearized BTE using iterative method (without assuming the RTA) can also be found (see, e.g., Refs. [124, 126]).

Examples of BTE studies

Since the early 2010s, *ab initio* BTE calculations of electronic transport coefficients have been successfully carried out for a variety of materials, from simple materials (e.g., Si and GaAs [124, 127, 125]) to modern functional materials [e.g., metal-halide perovskites [22, 23], SnSe [21, 24], β-Ga$_2$O$_3$ [128], and two-dimensional materials (e.g., MoS$_2$ [123, 129])]. The *ab initio* BTE approach has become the *de facto* standard for calculating electronic transport coefficients in crystalline materials. Comprehensive and up-to-date reviews of this approach and its applications can be found in Refs. [12, 13].

While the e-ph scattering rates are usually calculated with Equation (3.7) and with harmonic phonons, recent *ab initio* BTE studies revealed the important role of lattice anharmonicity and higher-order e-ph interactions in obtaining reliable results. In the following, we briefly review some of them.

Caruso *et al.* [24] studied the temperature dependence of the electrical conductivity of the highly anharmonic material SnSe. The authors found that obtaining a good quantitative agreement with experiment requires accounting simultaneously for (i) the thermal lattice expansion and (ii) the temperature-dependent renormalization of the relaxation times. This work of Caruso *et al.* will be further discussed in Chapter 5 of this thesis.

Brown-Altvater *et al.* [31] studied the organic molecular crystal naphthalene. The authors computed the e-ph self-energy self-consistently, by which the temperature-dependent renormalization of both the electronic band structure and the e-ph scattering rates was given. By including these higher-order electron-phonon coupling effects in the BTE calculations, the mobilities of electrons and holes calculated at 300 K are in good agreement with experimental values.

Zhou *et al.* [25] computed the electron mobility of $SrTiO_3$. For this material, the calculation of the e-ph interaction is complicated by the presence of soft phonon modes (resulting from 0 K harmonic calculations). The authors used the temperature-dependent effective potential (TDEP) method [28], which describes approximately the anharmonic BO PES at finite temperature T, to stabilize the soft phonon modes. Then, the e-ph matrix elements were computed using the anharmonic phonons. In the TDEP calculations (which employ a supercell), the authors created a number of atomic configurations with random thermal displacements corresponding to a canonical ensemble at temperature T. In a more recent study of $SrTiO_3$, for the TDEP calculations, Antonius *et al.* [26] generated the atomic configurations from *ai*MD simulations which directly sample the anharmonic BO PES.

For metal-halide perovskites, which feature strongly anharmonic lattice dynamics, the effect of lattice anharmonicity on the electronic transport has not been addressed in existing BTE studies [22, 23]. For this class of materials, the e-ph calculations are challenging due to structural instabilities and large unit cells [130].

Given the important role of lattice anharmonicity and higher-order e-ph interactions in many materials of current interest and the challenge to address this role by approximate, perturbative models, it is worth developing new computational methods for the electronic transport problem. This motivates us to explore approaches within the Kubo's theory of linear response.

3.2 Kubo's theory of linear response

Compared to Boltzmann transport theory, the Kubo's theory of linear response [131] introduced in this section provides a different perspective on the electrical conductivity of macroscopic systems. It gives a general expression of the electrical conductivity, the Kubo formula, which expresses the electrical conductivity in terms of electric current-current correlation function in thermal equilibrium.

3.2.1 Fluctuation-dissipation theorem

Consider an electrical conductor in thermal equilibrium in contact with a heat bath at finite temperature T. According to Ohm's law, the electric current should vanish exactly in the absence of external driving forces, but in fact there always exists spontaneous current fluctuations in the conductor. This phenomenon is known as Johnson-Nyquist noise or thermal noise [132, 133], which exists in all electrical conductors at finite T.

The thermal noise is understood as follows [132, 133]: At finite T, the atoms of an electrical conductor are always in thermal motion around their equilibrium positions[4]. In response to this, the charge carriers are in a state of thermal agitation, in thermodynamic equilibrium with the thermal motion of the atoms. The charge carriers are thus in incessant random motion (i.e., Brownian motion) producing a random electric current in the conductor.

As discussed in Section 3.1, the thermal motion of charge carriers leads to dissipation of the energy gained from external electric field into heat. It is therefore clear that in an electrical conductor, the thermal motion of the atoms causes two kinds of effect [135]: On one hand, it acts as an electromotive force on the charge carriers to carry out thermal motion, leading to the electric current fluctuations in thermal equilibrium; on the other hand, it acts as a frictional force impeding the drift motion of charge carriers in the presence of an external electric field, leading to the energy dissipation. Thus, fluctuation and dissipation are two aspects of the same phenomenon and are necessarily related to each other [112]. This important relation is called fluctuation-dissipation theorem [135, 136]: Irreversible processes in nonequilibrium are necessarily related to thermal fluctuations in equilibrium. This theorem is at the heart of Kubo's theory of linear response.

3.2.2 Kubo formula

In this subsection, we follow the work of Kubo [131] to prove the fluctuation-dissipation theorem. The proof itself constitutes the Kubo's theory of linear response, and most

---

[4] There is zero-point motion at $T = 0$ K, but its effects on the thermal noise is under debate (see Ref. [134] and references therein) and is not considered here.

importantly, it gives the Kubo formula of electrical conductivity. The present derivation is a synthesis of the works of Kubo [131], Kohn [137], Zwanzig [138], and Mahan [139].

Consider, in the very remote past ($t = -\infty$), an electrical conductor in thermal equilibrium in contact with a heat bath at finite T. The many-body Hamiltonian H_0 of the system, as given by Equation (2.1), includes the kinetic energy of electrons and nuclei, electron-electron, electron-nuclei, and nuclei-nuclei Coulomb interactions. For the initial thermal equilibrium, the system is statistically represented by the canonical density operator ϱ_0:

$$\varrho_0 = \frac{1}{Z} e^{-\beta H_0}, \tag{3.8}$$

where $Z = \mathrm{Tr}\{\exp(-\beta H_0)\}$ is the canonical partition function, and $\beta = 1/k_{\mathrm{B}}T$.

At this very moment ($t = -\infty$), an external electric field is turned on according to the formula [137]:

$$E_\alpha(t) = E_\alpha^0 e^{st}, \tag{3.9}$$

where s is a positive infinitesimal (in unit of inverse of time) which ensures an adiabatic switching-on of the electric field. The electric field is assumed to be uniform in space and, for convenience, directed along one of the spatial direction (labeled by $\alpha = 1,\ 2,$ or 3). The effect of the external electric field is represented by an additional term to the Hamiltonian [138]:

$$H_{\mathrm{F}}(t) = -M_\alpha E_\alpha(t), \tag{3.10}$$

where $M_\alpha = e \sum_i x_{i\alpha}$ is the dipole moment, e the electron charge, and $x_{i\alpha}$ the position of the i-th electron. The total Hamiltonian is given by

$$H(t) = H_0 + H_{\mathrm{F}}(t), \tag{3.11}$$

and the equation of motion of the density operator is:

$$\frac{\partial \varrho(t)}{\partial t} = \frac{1}{i\hbar}[H(t), \varrho(t)], \tag{3.12}$$

with the initial condition $\varrho(t = -\infty) = \varrho_0$.

In the following, the aim is to solve Equation (3.12) to first order in the electric field and to compute the expectation value of the electric current-density operator J_α at $t = 0$ when the electric field reaches its full strength. The density operator is now written as:

$$\varrho(t) = \varrho_0 + \varrho_{\mathrm{F}}(t), \tag{3.13}$$

where ϱ_F represents the correction which is linear in E_α^0. By inserting Equation (3.13) into Equation (3.12), one gets:

$$\begin{aligned} i\hbar\frac{\partial \varrho_{\mathrm{F}}}{\partial t} &= [H_0 + H_{\mathrm{F}}, \varrho_0 + \varrho_{\mathrm{F}}] \\ &\approx [H_0, \varrho_{\mathrm{F}}] + [H_{\mathrm{F}}, \varrho_0], \end{aligned} \tag{3.14}$$

where the term $[H_{\mathrm{F}}, \varrho_{\mathrm{F}}]$, which is of the second order in E_α^0, has been neglected (the validity will be discussed later). By observing the identity:

$$i\hbar\frac{\partial \varrho_{\mathrm{F}}}{\partial t} - [H_0, \varrho_{\mathrm{F}}] = e^{-iH_0t/\hbar}[i\hbar\frac{d}{dt}(e^{iH_0t/\hbar}\varrho_{\mathrm{F}}e^{-iH_0t/\hbar})]e^{iH_0t/\hbar}, \tag{3.15}$$

the $\varrho_{\mathrm{F}}(t)$ can be written as:

$$\varrho_{\mathrm{F}}(t) = \frac{1}{i\hbar}\int_{-\infty}^{t} e^{-i(t-t')H_0/\hbar}[H_{\mathrm{F}}(t'), \varrho_0]e^{i(t-t')H_0/\hbar}dt'. \tag{3.16}$$

Since ϱ_F satisfies the initial condition $\varrho_F(t = -\infty) = 0$, one can introduce the ansatz [137, 139]:

$$\varrho_F = fe^{st}, \tag{3.17}$$

where f is independent of time. This leads to:

$$f = \frac{-E_\alpha^0}{i\hbar}\int_{-\infty}^{t} e^{-i(t-t')H_0/\hbar}e^{-s(t-t')}[M_\alpha, \varrho_0]e^{i(t-t')H_0/\hbar}dt'. \tag{3.18}$$

By changing integration variable with $t' - t \Longrightarrow -t$:

$$f = \frac{-E_\alpha^0}{i\hbar}\int_{0}^{\infty} e^{-st}e^{-iH_0t/\hbar}[M_\alpha, \varrho_0]e^{iH_0t/\hbar}dt. \tag{3.19}$$

In this equation, f is proportional to E_α^0, thus describing the linear response. The further derivations rely on the Kubo's identity [131] of an arbitrary physical operator O (detailed in Appendix A.1):

$$[O, \varrho_0] = -i\hbar\varrho_0\int_0^{\beta}\dot{O}(-i\hbar\lambda)d\lambda. \tag{3.20}$$

where $\dot{O}$ is the time derivative of O at $t = 0$ and $\dot{O}(-i\hbar\lambda)$ is a Heisenberg operator as a function of the imaginary time $t = i\hbar\lambda$ $(0 \leq \lambda \leq \beta)$:

$$\dot{O}(-i\hbar\lambda) = e^{\lambda H}\dot{O}e^{-\lambda H}. \tag{3.21}$$

Using the Kubo's identity, f can be written as:

$$f = E_\alpha^0 \int_0^\infty dt e^{-st} e^{-iH_0 t/\hbar} \int_0^\beta \varrho_0 \dot{M}_\alpha(-i\hbar\lambda) e^{iH_0 t/\hbar} d\lambda. \tag{3.22}$$

On the other hand, the electric current-density operator of the whole system in the α-th direction is given by:

$$J_\alpha = \frac{e}{V}\sum_i v_{i\alpha}, \tag{3.23}$$

which is simply $\dot{M}_\alpha/V$ (V denotes the volume of the system). The final expression of f then reads:

$$f = \frac{E_\alpha^0}{V} \int_0^\infty dt e^{-st} e^{-iH_0 t/\hbar} \int_0^\beta \varrho_0 J_\alpha(-i\hbar\lambda) e^{iH_0 t/\hbar} d\lambda. \tag{3.24}$$

The expectation value of the electric current-density operator is obtained by calculating the trace of the operator product:

$$\begin{aligned} \langle J_\alpha \rangle &\equiv \mathrm{Tr}\{f J_\alpha\} \\ &= \frac{E_\alpha^0}{V} \mathrm{Tr}\{\int_0^\infty dt e^{-st} e^{-iH_0 t/\hbar} \int_0^\beta \varrho_0 J_\alpha(-i\hbar\lambda) e^{iH_0 t/\hbar} J_\alpha d\lambda\} \\ &= \frac{E_\alpha^0}{V} \int_0^\infty dt e^{-st} \int_0^\beta \mathrm{Tr}\{\varrho_0 J_\alpha(-i\hbar\lambda) J_\alpha(t)\} d\lambda, \end{aligned} \tag{3.25}$$

where $J_\alpha(t) = e^{iH_0 t/\hbar} J_\alpha e^{-iH_0 t/\hbar}$ is the Heisenberg motion of the electric current-density operator governed by the equilibrium Hamiltonian H_0 (instead of H). Finally, a comparison with the Ohm's law leads to the Kubo formula, which expresses the electrical conductivity in terms of electric current-current correlation function:

$$\sigma = \frac{1}{3V} \lim_{s\to 0^+} \int_0^\infty dt e^{-st} \int_0^\beta \mathrm{Tr}\{\varrho_0 \mathbf{J}(t - i\hbar\lambda) \cdot \mathbf{J}\} d\lambda, \tag{3.26}$$

where the electrical conductivity has been averaged over the three spatial directions, and the time-translation symmetry has been used to make the expression compact [140]. The mathematical convergence factor e^{-st} with the limit $s \to 0^+$ allows the upper limit of the t-integration to be infinity [131].

Since the ϱ_0 in Equation (3.26) is the equilibrium density operator, the Kubo formula is indeed an example of the fluctuation-dissipation theorem: A measure of the electric current fluctuations in thermal equilibrium (the right hand side of Kubo formula) is related to the electrical conductivity (the left hand side of Kubo formula) which is a nonequilibrium property.

Discussion

The Kubo's theory of linear response is restricted to nonequilibrium states near equilibrium. In the above derivation of Kubo formula the terms that are of second order in E_α^0 are consistently neglected: (i) In Equation (3.13), the ϱ_F, i.e., the deviation of the density operator from equilibrium, is taken to be linear in E_α^0; (ii) In Equation (3.14), the term $[H_\mathrm{F}, \varrho_\mathrm{F}]$, which is of second order in E_α^0, is discarded. These first-order treatments are needed in order to get a steady-state electrical current that is linear in E_α^0. They hold for weak E_α^0. Experimentally it was found that for most semiconductors, Ohm's law breaks down at electric fields exceeding $\sim 10^3 - 10^4$ V/cm [117, 141]. By contrast, the "internal electric field" of a solid can be estimated by $k_B T / e a_0 \approx 10^6$ V/cm (a_0 is the Bohr radius, T is e.g. 300 K). Therefore, in the linear regime where the Ohm's law is respected, the interaction energy with the external electric field, i.e., H_F as given by Equation (3.10), is small compared to H_0, and the first-order correction ϱ_F is the dominant correction to the density operator.

The Kubo formula (or more generally, Green-Kubo formula) is a general expression of linear transport coefficients in macroscopic systems, and has been used for computing different types of transport coefficients [142, 143]. A general extension of the fluctuation-dissipation theorem to far-from-equilibrium situations is so far unsuccessful [144, 145], and this is not the topic of this thesis.

3.3 *Ab initio* Kubo-Greenwood approach

For solid-state systems, the density operator and current-density operator in the Kubo formula are abstract many-body operators. Thus, it is difficult to directly evaluate the Kubo formula. In practice, the Kubo-Greenwood (KG) formula is used for *ab initio* calculations of the electrical conductivity of real materials. This section establishes the connection between the Kubo formula and KG formula, and describes an *ab initio* KG approach, which combines the KG formula and *ai*MD, to calculating the electrical conductivity of crystalline materials.

3.3.1 Kubo formula in the Born-Oppenheimer approximation

Consider a crystalline solid in thermal equilibrium in contact with a heat bath at finite T. The first approximation made to simplify the Kubo formula is the BO approximation in which the equilibrium density operator ϱ_0 can be written as [146, 147, 148]:

$$\varrho_0 = \varrho_0^{\mathrm{n}} \varrho_0^{\mathrm{e}}, \tag{3.27}$$

where ϱ_0^{n} and ϱ_0^{e} are the canonical density operators for the nuclei and electrons, respectively. The ϱ_0^{n} is considered as the classical distribution function of the nuclei on the BO PES. The ϱ_0^{e}, which depends parametrically on the nuclei coordinates $\{\mathbf{R}_I\}$, contains the electronic Hamiltonian $H^{\mathrm{e}}(\{\mathbf{r}_i\};\{\mathbf{R}_I\})$ for this atomic configuration [see Equation (2.8)]. By inserting Equation (3.27) into the Kubo formula, one obtains:

$$\sigma(T) = \mathrm{Tr}^{(\mathrm{n})}\{\varrho_0^{\mathrm{n}} \sigma(\{\mathbf{R}_I\})\}, \tag{3.28}$$

where $\sigma(\{\mathbf{R}_I\})$ is the electrical conductivity for the atomic configuration $\{\mathbf{R}_I\}$:

$$\sigma(\{\mathbf{R}_I\}) = \lim_{s\to 0^+} \frac{1}{3V} \int_0^\infty dt e^{-st} \int_0^\beta \mathrm{Tr}^{(\mathrm{e})}\{\varrho_0^{\mathrm{e}} \mathbf{J}(t - i\hbar\lambda)\cdot \mathbf{J}\} d\lambda, \tag{3.29}$$

where $\mathrm{Tr}^{(\mathrm{n})}$ and $\mathrm{Tr}^{(\mathrm{e})}$ denote the traces for the nuclei and electrons, respectively.

The right-hand side of Equation (3.29) describes the thermal agitation of the electrons and corresponds to the instantaneous atomic configuration $\{\mathbf{R}_I\}$. At the moment (defined as $t = 0$) when the nuclei move into their positions $\{\mathbf{R}_I\}$, the electrons respond instantaneously with random motion governed by $H^{\mathrm{e}}(\{\mathbf{r}\};\{\mathbf{R}_I\})$, leading to electric current fluctuations. When the nuclei adopt a new configuration $\{\mathbf{R}'_I\}$, the corresponding $\sigma(\{\mathbf{R}'_I\})$ is understood in the same manner. The validity of the BO approximation in simplifying the Kubo formula is under discussion (see Ref. [148]). In Equation (3.29), infinity is used as the upper limit of the t-integration. This makes sense given that the time scale of the electronic motion is much shorter than that of the nuclei.

3.3.2 Kubo-Greenwood formula

To further simplify the Kubo formula, let us consider an electronic Hamiltonian for which the eigenstates can be computed. The simplest case is the Hamiltonian $H_0^{\mathrm{e}} = \sum_{i=1}^{N_{\mathrm{e}}} \hat{h}_0$ for non-interacting electrons, where $\hat{h}_0(\mathbf{r}) = -\frac{1}{2}\nabla^2 + v_{\mathrm{ext}}(\mathbf{r}; \{\mathbf{R}_I\})$ is the single-particle Hamiltonian. In this case, the many-body operators in Equation (3.29) can be conveniently expressed in second-quantization notation using the single-particle eigenstates of $\hat{h}_0|n\mathbf{k}\rangle = \epsilon_{n\mathbf{k}}|n\mathbf{k}\rangle$ as a complete basis set. In this representation, the electrical current density reads[5] [149]:

$$\mathbf{J} = \frac{e}{m} \sum_{\mathbf{k}} \sum_{nm} \langle m\mathbf{k}|\mathbf{p}|n\mathbf{k}\rangle c_{m\mathbf{k}}^{\dagger} c_{n\mathbf{k}}, \tag{3.30}$$

where e (< 0) is the electron charge, $c_{n\mathbf{k}}^{\dagger}$ $(c_{n\mathbf{k}})$ is the creation (annihilation) operator of an electron in the single-particle eigenstate $|n\mathbf{k}\rangle$, and $\langle m\mathbf{k}|\mathbf{p}|n\mathbf{k}\rangle$ is the matrix element of the momentum operator. Accordingly, the Heisenberg operator $\mathbf{J}(t - i\hbar\lambda)$ in Equation (3.29) is given by:

$$\mathbf{J}(t - i\hbar\lambda) = \frac{e}{m} \sum_{\mathbf{k}} \sum_{nm} \langle m\mathbf{k}|\mathbf{p}|n\mathbf{k}\rangle c_{m\mathbf{k}}^{\dagger} c_{n\mathbf{k}} e^{\frac{i(\epsilon_{m\mathbf{k}} - \epsilon_{n\mathbf{k}})}{\hbar}(t - i\hbar\lambda)}. \tag{3.31}$$

The electric current-current correlation function then reads,

$$\begin{aligned} &\mathrm{Tr}\{\varrho_0 \mathbf{J}(t - i\hbar\lambda) \cdot \mathbf{J}\} \\ &= \frac{e^2}{m^2} \sum_{\mathbf{k}} \sum_{nm} e^{\frac{i(\epsilon_{m\mathbf{k}} - \epsilon_{n\mathbf{k}})}{\hbar}(t - i\hbar\lambda)} \langle m\mathbf{k}|\mathbf{p}|n\mathbf{k}\rangle \cdot \sum_{\mathbf{k}'} \sum_{n'm'} \langle m'\mathbf{k}'|\mathbf{p}|n'\mathbf{k}'\rangle \\ &\quad \times \mathrm{Tr}\{\varrho_0 c_{m\mathbf{k}}^{\dagger} c_{n\mathbf{k}} c_{m'\mathbf{k}'}^{\dagger} c_{n'\mathbf{k}'}\}. \end{aligned} \tag{3.32}$$

The trace can be evaluated using Wick's theorem [150]:

$$\mathrm{Tr}\{\varrho_0 c_{m\mathbf{k}}^{\dagger} c_{n\mathbf{k}} c_{m'\mathbf{k}'}^{\dagger} c_{n'\mathbf{k}'}\} = \delta_{mn}\delta_{m'n'} f_{m\mathbf{k}} f_{m'\mathbf{k}'} + \delta_{\mathbf{k}\mathbf{k}'}\delta_{mn'}\delta_{m'n} f_{m\mathbf{k}}(1 - f_{n\mathbf{k}'}), \tag{3.33}$$

where

$$f_{n\mathbf{k}} \equiv f(\epsilon_{n\mathbf{k}}) = \frac{1}{1 + \exp(\frac{\epsilon_{n\mathbf{k}} - E_F}{k_{\mathrm{B}}T})}, \tag{3.34}$$

is the Fermi-Dirac distribution function for the Fermi level E_F and temperature T. The first term on the right-hand side of Equation (3.33) gives rise to $\frac{e}{m}\sum_{n\mathbf{k}} \langle n\mathbf{k}|\hat{\mathbf{p}}|n\mathbf{k}\rangle f_{n\mathbf{k}}$, which is zero (regardless of the temperature; as clear from the time-reversal symmetry); that is to say, there is no electric current in the (exact) state of thermal equilibrium.

---

[5] The sum of $\mathbf{k}$ is implicitly associated with the weight of each $\mathbf{k}$ point.

Equation (3.32) can be written as

$$Tr\{\varrho_0 \mathbf{J}(t-i\hbar\lambda)\cdot\mathbf{J}\} = \frac{e^2}{m^2}\sum_{\mathbf{k}}\sum_{nm} e^{\frac{i(\epsilon_{m\mathbf{k}}-\epsilon_{n\mathbf{k}})}{\hbar}(t-i\hbar\lambda)} f_{m\mathbf{k}}(1-f_{n\mathbf{k}})|\langle m\mathbf{k}|\mathbf{p}|n\mathbf{k}\rangle|^2. \tag{3.35}$$

The two integrals in Equation (3.29) can now be derived. The λ integral reads:

$$\int_0^\beta e^{\lambda(\epsilon_{m\mathbf{k}}-\epsilon_{n\mathbf{k}})}d\lambda = \frac{e^{\beta(\epsilon_{m\mathbf{k}}-\epsilon_{n\mathbf{k}})}-1}{\epsilon_{m\mathbf{k}}-\epsilon_{n\mathbf{k}}}, \tag{3.36}$$

which, together with $f_{m\mathbf{k}}(1-f_{n\mathbf{k}})$, leads to,

$$\frac{e^{\beta(\epsilon_{m\mathbf{k}}-\epsilon_{n\mathbf{k}})}-1}{\epsilon_{m\mathbf{k}}-\epsilon_{n\mathbf{k}}} f_{m\mathbf{k}}(1-f_{n\mathbf{k}}) = \frac{f_{n\mathbf{k}}-f_{m\mathbf{k}}}{\epsilon_{m\mathbf{k}}-\epsilon_{n\mathbf{k}}}. \tag{3.37}$$

The time integral reads,

$$\lim_{s\to 0^+}\int_0^\infty e^{-st}e^{\frac{i}{\hbar}(\epsilon_{m\mathbf{k}}-\epsilon_{n\mathbf{k}})t}dt = \lim_{s\to 0^+}\frac{i\hbar}{(\epsilon_{m\mathbf{k}}-\epsilon_{n\mathbf{k}})+i\hbar s}. \tag{3.38}$$

With these, Equation (3.29) can be expressed as

$$\sigma = \lim_{\eta\to 0^+}\frac{ie^2\hbar}{3Vm^2}\sum_{\mathbf{k}}\sum_{nm}\frac{f_{n\mathbf{k}}-f_{m\mathbf{k}}}{\epsilon_{m\mathbf{k}}-\epsilon_{n\mathbf{k}}}|\langle m\mathbf{k}|\mathbf{p}|n\mathbf{k}\rangle|^2\frac{1}{(\epsilon_{m\mathbf{k}}-\epsilon_{n\mathbf{k}})+i\eta}, \tag{3.39}$$

where $\hbar s$ has been replaced by η. The real part of Equation (3.39) is,

$$\sigma = \lim_{\eta\to 0^+}\frac{\pi e^2\hbar}{3Vm^2}\sum_{\mathbf{k}}\sum_{nm}\frac{f_{n\mathbf{k}}-f_{m\mathbf{k}}}{\epsilon_{m\mathbf{k}}-\epsilon_{n\mathbf{k}}}|\langle m\mathbf{k}|\mathbf{p}|n\mathbf{k}\rangle|^2\frac{1}{\pi\eta}\frac{\eta^2}{(\epsilon_{m\mathbf{k}}-\epsilon_{n\mathbf{k}})^2+\eta^2}. \tag{3.40}$$

The $\frac{1}{\pi\eta}\frac{\eta^2}{(\epsilon_{m\mathbf{k}}-\epsilon_{n\mathbf{k}})^2+\eta^2}$ is a nascent Dirac delta function, and hence approaches a Dirac delta function in the limit $\eta\to 0^+$, by which one gets,

$$\sigma = \frac{\pi e^2\hbar}{3Vm^2}\sum_{\mathbf{k}}\sum_{nm}|\langle m\mathbf{k}|\mathbf{p}|n\mathbf{k}\rangle|^2\left(-\frac{\partial f}{\partial\epsilon}\right)_{\epsilon_{n\mathbf{k}}}\delta(\epsilon_{m\mathbf{k}}-\epsilon_{n\mathbf{k}}). \tag{3.41}$$

Equation (3.41) is called the Kubo-Greenwood (KG) formula, which was derived by Greenwood [151] and later rewritten using contemporary notation by Allen [122] and Holst *et al.* [152]. It turns out that for a system of non-interacting electrons, the Kubo formula reduces to the KG formula. Note that since the $\epsilon_{n\mathbf{k}}$ and $|n\mathbf{k}\rangle$ are solved for a given atomic configuration $\{\mathbf{R}_I\}$, the electrical conductivity given by Equation (3.41) is for this atomic configuration.

Interacting electrons in real materials

The KG formula can be directly used for the fictitious, non-interacting Kohn-Sham electrons of DFT, i.e., the single-particle eigenvalues $\epsilon_{n\mathbf{k}}$ and eigenfunctions $|\psi_{n\mathbf{k}}\rangle$ entering the KG formula can be determined from a Kohn-Sham DFT calculation.

Since electronic transport in crystalline solids is electronic quasiparticle propagation involving excited states of the system, its reliable description requires the concept of the quasiparticles (i.e., single-particle-like excitations) of the system [153, 122]. The *GW* method [154] can accurately predict the quasiparticle energies $\epsilon^{\mathrm{QP}}_{n\mathbf{k}}$ and wavefunctions $\psi^{\mathrm{QP}}_{n\mathbf{k}}$ by solving the quasiparticle equation,

$$[\hat{h}_0(\mathbf{r}) + v_{\mathrm{H}}(\mathbf{r})]\psi^{\mathrm{QP}}_{n\mathbf{k}}(\mathbf{r}) + \int d\mathbf{r}'\Sigma^{GW}_{\mathrm{xc}}(\mathbf{r},\mathbf{r}';\epsilon^{\mathrm{QP}}_{n\mathbf{k}})\psi^{\mathrm{QP}}_{n\mathbf{k}}(\mathbf{r}') = \epsilon^{\mathrm{QP}}_{n\mathbf{k}}\psi^{\mathrm{QP}}_{n\mathbf{k}}(\mathbf{r}), \tag{3.42}$$

where $\Sigma^{GW}_{\mathrm{xc}}$ is the *GW* approximation to the nonlocal energy-dependent self-energy $\Sigma(\mathbf{r},\mathbf{r}';\epsilon)$ that includes all the electron-electron interactions (beyond the Hartree term v_{H}). By capturing the many-body correlation effects of the electrons in the evaluation of the quasiparticle energies, the *GW* method has proven, for many materials, to describe accurately the band gap and band-edge dispersion which are essential for the reliable description of the electronic transport [155].

In the widely used G_0W_0 method [156], the quasiparticle wave functions are approximated with the Kohn-Sham eigenfunctions $|\psi_{n\mathbf{k}}\rangle$, and the quasiparticle energies are obtained as the first-order correction to the Kohn-Sham eigenvalues,

$$\epsilon^{\mathrm{QP}}_{n\mathbf{k}} = \epsilon_{n\mathbf{k}} + \langle\psi_{n\mathbf{k}}|\Sigma^{GW}_{\mathrm{xc}}(\epsilon^{\mathrm{QP}}_{n\mathbf{k}}) - v^{\mathrm{DFT}}_{\mathrm{xc}}|\psi_{n\mathbf{k}}\rangle. \tag{3.43}$$

The G_0W_0 quasiparticle correction is becoming increasingly popular in *ab initio* BTE calculations of electronic transport coefficients [21, 157, 158, 159].

3.3.3 Combination with *ai*MD simulations

Finally, the electrical conductivity by Equation (3.28) is evaluated as an arithmetic average over a sufficiently large number of uncorrelated atomic configurations generated from *ai*MD simulations in the canonical ensemble (NVT) at finite T [147, 148]:

$$\sigma(T) = \frac{1}{N_{\mathrm{s}}}\sum_{i=1}^{N_{\mathrm{s}}}\sigma(\{\mathbf{R}_I\}_i), \tag{3.44}$$

where $\sigma(\{\mathbf{R}_I\}_i)$ is the electrical conductivity of the i-th sample, and N_{s} the number of samples collected. Note that the *ai*MD simulations are based on the supercell approach and so does the evaluation of the KG formula. A discussion of computing equilibrium properties from *ai*MD simulations can be found in Section 2.5.2.

3.3.4 Summary of the approach

Taken together, Equations (3.41) and (3.44) constitute a promising first-principles approach to the calculation of the electrical conductivity of solids. This approach, referred to as the *ab initio* KG approach in this thesis, naturally accounts for all the anharmonic effects and does not require perturbation theory to treat the coupling between electrons and lattice vibrations. This is understood as follows. First, the material parameters entering the KG formula for determining the $\sigma(\{\mathbf{R}_I\})$ for the atomic configuration $\{\mathbf{R}_I\}$ are the $\epsilon_{n\mathbf{k}}$ and $\psi_{n\mathbf{k}}$ that are calculated for this atomic configuration. These material parameters inherently include a portion of information on the dynamics of the system, i.e., lattice vibrations and the coupling between electrons and lattice vibrations. Second, this information is fully captured by averaging over a sufficiently large number of *ai*MD samples. In light of these, the *ab initio* KG approach is ideally suited for studying the electrical conductivity of anharmonic crystals.

Practical *ab initio* KG calculations employ a supercell containing a large number of atoms and are of three steps: (i) First, perform *ai*MD simulations to generate a sufficiently large number of samples; (ii) Second, for each of the samples collected, compute the eigenvalues $\epsilon_{n\mathbf{k}}$ and momentum-matrix elements $\langle m\mathbf{k}|\mathbf{p}|n\mathbf{k}\rangle$, and subsequently input these quantities into the KG formula to evaluate the electrical conductivity for this sample; (iii) Third, compute the expectation value of the electrical conductivity as the sample mean.

The *ai*MD simulations can be performed at the DFT level of theory using LDA/GGAs, while the $\epsilon_{n\mathbf{k}}$ and $\langle m\mathbf{k}|\mathbf{p}|n\mathbf{k}\rangle$ should in principle be evaluated at the GW level. Since the focus of this thesis is on exploring the KG method and that the supercell calculations are computationally demanding (even at the DFT level), we will approximate both the $\epsilon_{n\mathbf{k}}$ and $\langle m\mathbf{k}|\mathbf{p}|n\mathbf{k}\rangle$ by DFT values. As a result, the predictive power of our calculations will be limited by (i) the approximate nature of DFT xc functionals and (ii) the approximate meaning of the Kohn-Sham eigenvalues and eigenfunctions.

Examples of KG studies

Owing to its computational simplicity, the *ab initio* KG approach has been widely used to study the electrical conductivity of non-crystalline systems: (i) warm dense matter and plasmas [160, 161, 162]; and (ii) alloys and disordered materials [163, 164, 165].

However, the application of this approach to crystalline solids is rarely found in the literature. To our knowledge, there are only three previous works on crystalline solids, and all the systems studied exhibit metallic electrical conductivity. Alfè *et al.* [34] calculated the electrical conductivity of bcc iron at ambient pressure and two temperatures (300 and 500 K). The authors paid special attention to the numerical convergence of their KG calculations with respect to supercell size and **k**-point sampling of the Brillouin zone, and found that obtaining converged electrical conductivities requires using large supercells, especially for the lower temperature (i.e., 300 K). Their calculated results fall within the experimental range at 500 K, and are slightly overestimated at 300 K. French *et al*. [35] studied molybdenum at 1000 K, and found that supercells containing at least 250 atoms are needed to converge the electrical conductivity. Recently, noticing that the *ab initio* KG approach can conveniently capture strong lattice anharmonicity, Paola *et al*. [166] applied this approach to $Cu_{12}Sb_4S_{13}$, which is an unintentionally heavily-doped semiconductor for thermoelectric applications. In this work, the authors employed a $2 \times 2 \times 1$ (232-atom) supercell and a $3 \times 3 \times 6$ **k**-mesh. The electrical conductivities calculated at $300 - 700$ K are about two times larger than the upper range of the experimental values.

For crystalline semiconductors with a moderate doping level and at typical device operating temperatures (e.g., room temperature), the KG calculations are likely to suffer from convergence problems. For example, in this case the Fermi level lies within the band gap, so a dense **k**-point sampling is required to describe the Fermi-Dirac tail. It is necessary to conduct a systematic test of the *ab initio* KG approach to see whether it can provide reliable results for the electrical conductivity of crystalline solids.

3.4 Computational implementations

In this section, we discuss the practical aspects of a numerical implementation of the *ab initio* KG approach for crystalline solids, and introduce our FHI-kubo code that allows for an integrated workflow of KG calculations.

3.4.1 Thermodynamic limit and broadening parameter

Special care must be taken with regard to the limit $\eta \to 0^+$ in going from Equation (3.40) to (3.41). This limit makes sense only in the thermodynamic limit of a macroscopic system where the single-particle energy spectrum is quasi-continuous[6]; it has to be taken after the thermodynamic limit [167, 168, 169].

However, in practical KG calculations, η has to be kept finite and exists as a numerical parameter. This is because one can only deal with finite-size supercells (i.e., large yet finite systems with periodic boundary conditions), whose single-particle energy spectrum is inevitably discrete. Accordingly, one should instead use

$$\sigma = \frac{\pi e^2 \hbar}{3Vm^2} \sum_{\mathbf{k}} \sum_{n,m} \frac{f_{n\mathbf{k}} - f_{m\mathbf{k}}}{\epsilon_{m\mathbf{k}} - \epsilon_{n\mathbf{k}}} |\langle m\mathbf{k}|\mathbf{p}|n\mathbf{k}\rangle|^2 \frac{1}{\pi\eta} \frac{\eta^2}{(\epsilon_{m\mathbf{k}} - \epsilon_{n\mathbf{k}})^2 + \eta^2}, \tag{3.45}$$

by keeping η finite[7]. A nonzero η is referred to as broadening parameter. The appropriate choice of η is very important: On one hand, η should be large compared to the average level spacing, in order to recover the thermodynamic limit [167]; on the other hand, η should be as small as possible to reflect the limit $\eta \to 0^+$. For a given supercell size, using either a too large or a too small η will lead to incorrect results.

Besides the above numerical consideration, the physical origin of η is clear [137, 171]. In the derivation of the Kubo formula, the limit $\eta \to 0^+$ (in its original form $\eta = \hbar s$ and $s \to 0^+$; the inverse $1/s$ is in unit of time, and $\eta = \hbar s$ is in unit of energy) guarantees that the external electric field (in the form of $E_0 e^{st}$) is slowly turned on starting from the remote past $t = -\infty$, such that the system can at all times adjust itself to the instantaneous strength of the external electric field, and reaches a steady state at $t = 0$ when the electric field reaches its full strength. The switch-on time $1/s$ should be large compared to the time necessary for the system to relax [137]: (i) $1/s \gg t_\mathrm{r}$, where t_r is of the order of the relaxation time; (ii) $1/s \gg t_\mathrm{a}$, where t_a is an “internal" time associated with the dynamics of the electrons (as discussed in the BO approximation) and and has

---

[6] Single-particle eigenvalues $\epsilon_{n\mathbf{k}}$ as a function of band index n. “Quasi-continuous" instead of “continuous" considering gapped systems.

[7] This is identical to Equation (3.41) by replacing the δ function in this equation with Lorentzian. The use of Lorentzian instead of Gaussian makes more sense from a theoretical perspective because in Equation (3.41) the delta function is derived from the Lorentzian function in the limit $\eta \to 0^+$. Similar argument can be found in Ref. [170].

nothing to do with t_r. It was argued that there exists a tremendous range of s for which the electrical conductivity is practically independent of s [137]. We suspect that this argument is valid for a sufficiently large system.

In short, the bulk value of the electrical conductivity can be determined using Equation (3.45) with the limit process: The system size first approaches infinity (thus $\delta E \to 0$) and then η approaches zero; at each stage of this process for a given system size, the value of η is larger than δE [172].

Practice in the literature

Desjarlais *et al*. [173] proposed that for a finite-size supercell, η can be chosen to be roughly the average level spacing of the Kohn-Sham energy levels. This has been followed by several authors [34, 174, 175]. For example, in the study of Alfè *et al*. [34], η was set to 16, 8, 4, 2.4, 2, and 1.4 meV for the 64-, 128-, 250-, 432-, 686-, and 1024-atom supercells of bcc iron, respectively. The main drawback of this method is that the level spacings are difficult to estimate [176].

A simpler strategy for choosing an appropriate value of η may be drawn from the work of Nomura and MacDonald [177], who studied the quantum transport of disordered 2D massless Dirac fermions (i.e., disordered graphene) at $T = 0$ K. In this work, the systems are of finite size L with periodic boundary conditions, and the electrical conductivity has only the inter-band contribution[8]. For a given system size L, the authors computed the electrical conductivity σ at a large number of η values. It was found that σ is a maximum when η corresponds to $\sim \delta E$ (which is the level spacing at the Fermi level), and vanishes for both small and large η. Finally, the electrical conductivity at a given system size L was estimated by the maximum of σ vs η.

3.4.2 Simulation of doping

For semiconductors, the electrical conductivity is largely influenced by doping (i.e., creation of native point defects and/or incorporation of impurities into the crystal lattice) and temperature. Under thermal equilibrium conditions, free charge carriers (free electrons and free holes) arise from two mechanisms [117]: (i) thermal excitation of electrons from upper valence bands to lower conduction bands, leaving holes in the upper valence bands (this is the only source of free charge carriers in intrinsic semiconductors that are free of native point defects and impurities); and (ii) thermal ionization of dopants releasing charge carriers into the host material. The band states (i.e., single-particle energy levels) are populated by electrons according to the Fermi-Dirac

---

[8] See definitions of the intra-band, degenerate-state, and inter-band contributions to the electrical conductivity in Subsection 3.4.3.

distribution function:

$$f_{n\mathbf{k}} \equiv f(\epsilon_{n\mathbf{k}}) = \frac{1}{1+\exp(\frac{\epsilon_{n\mathbf{k}}-E_F}{k_{\mathrm{B}}T})}. \tag{3.46}$$

E_F is the electron chemical potential (known as Fermi level), which is determined by that the system has a fixed number of electrons. The (free) electron concentration n_{e} and hole concentration n_{h} are given by:

$$n_{\mathrm{e}} = \frac{1}{V}\sum_{\mathbf{k}}\sum_{n\in\mathrm{CB}} f_{n\mathbf{k}}, \tag{3.47}$$

$$n_{\mathrm{h}} = \frac{1}{V}\sum_{\mathbf{k}}\sum_{n\in\mathrm{VB}} (1-f_{n\mathbf{k}}), \tag{3.48}$$

where VB (CB) denotes the valence (conduction) bands. In an intrinsic (undoped) semiconductor, $n_{\mathrm{h}} = n_{\mathrm{e}} = n_{\mathrm{i}}$, where n_{i} denotes the intrinsic carrier concentration.

In the following, we introduce three different approaches that can be used for modeling free-carrier doping in *ab initio* KG calculations, two of which are self-consistent and the third of which is non-self-consistent.

Realistic point defects

A general approach to treat doping is to introduce a dopant into the supercell [52] used for *ab initio* KG calculations (as early as when performing *ai*MD simulations).

This approach would lead to unrealistically high dopant concentration, given that in first-principles solid-state calculations the supercell size is typically $100-1000$ atoms. For example, replacing a Si atom with a boron (B) atom in the cubic supercell of 1000 Si atoms will result in 5×10^{19} cm^{-3} $\mathrm{B_{Si}}$ (Boron-on-Si antisite). In order to realize a typical dopant concentration on the order of 10^{18} cm^{-3}, a supercell of around $20,000$ atoms will have to be used [178]. Nevertheless, this approach is suited for studying e.g. thermoelectric materials and transparent conductive oxides, where the doping level can be as high as $\sim 10^{20}$ cm^{-3} [179, 180, 181]. As mentioned before, Paola *et al.* [166] computed the electrical conductivity of $\mathrm{Cu_{12}Sb_4S_{13}}$ using a 232-atom supercell. This material can be viewed as $\mathrm{Cu_3SbS_4}$ containing ordered sulfur vacancies. The authors found that their system (i.e., the supercell model) is heavily *p*-doped, with the Fermi level entering into the upper valence bands.

Virtual-crystal approximation (VCA)

The second approach is to simulate doping by means of the virtual-crystal approximation (VCA) [182, 183, 184], without explicitly incorporating dopants into the host material. In this approach, one modifies the nuclear charge (denoted as Z, an integer number) of the atoms in the supercell by a small fraction ΔZ. When ΔZ is negative, this leads to excess holes in the valence (conduction) bands; when ΔZ is positive, this leads to excess electrons in the valence (conduction) bands.

The VCA approach can be easily realized in the FHI-aims calculations, and here we introduce this approach with the example discussed by Richter [183]. Consider a (charge-neutral) MgO supercell consisting of N_{Mg} magnesium atoms and N_{O} oxygen atoms ($N_{\mathrm{Mg}} = N_{\mathrm{O}}$). To realize a target hole concentration n_{h}, one needs to reduce $n_{\mathrm{h}}V$ electrons from the supercell (V denotes the volume of the supercell). This can be done by changing the nuclear charge Z_{Mg} of each magnesium atom by $\Delta Z_{\mathrm{Mg}} = -n_{\mathrm{h}}V/N_{\mathrm{Mg}}$, i.e., the nuclear charge of each magnesium atom should be set to $Z_{\mathrm{Mg}} - (n_{\mathrm{h}}V/N_{\mathrm{Mg}})$. Accordingly, the number of (valence) electrons of each magnesium atom should also be reduced by the same amount in order to observe the charge-neutrality condition. By means of this, an artificial element is created, whose nuclear charge and number of electrons are both $Z_{\mathrm{Mg}} - (n_{\mathrm{h}}V/N_{\mathrm{Mg}})$.

Similar to the description of doping with realistic point defects, the VCA approach allows for a self-consistent treatment of doping. It is suited for modeling moderate doping level resulted from point defects with delocalized states [183].

Rigid-band approximation

The above two approaches can be computationally involved if one wants to study the electrical conductivity at different doping levels. In order to alleviate the computational burden, one can approximately treat doping using the rigid-band approximation [7, 157]. This is done by adding a small number of charges to the calculated electronic band structure of an intrinsic (undoped) semiconductor. The E_F at a given temperature T is set in such a way that the net charge density equals the target doping level. For p-type doping with excessive holes,

$$n_{\mathrm{h}} - n_{\mathrm{e}} = \delta/V, \tag{3.49}$$

and for n-type doping with excessive electrons,

$$n_{\mathrm{e}} - n_{\mathrm{h}} = \delta/V, \tag{3.50}$$

where δ is a small positive number which controls the doping level.

In the rigid-band approximation, one assumes that the doping will not change the electronic band structure. Thus, such a description of doping is nothing but a shift of the Fermi level within the band gap of the intrinsic semiconductor. As a result, carrier-defect scattering is entirely missing. This approach is commonly used in *ab initio* BTE calculations of electronic transport [124, 125]. It has been suggested that the rigid-band approximation is good as long as the Fermi level (controlled by δ) lies well within the band gap [7] (probably for doping level less than $\sim 10^{18}$ cm^{-3}). This approach will be adopted in our work to make the calculations tractable.

3.4.3 Decomposition of Kubo-Greenwood formula

Following the work of Calderín *et al.* [32], we decompose Equation (3.45) into three components according to the sum over band index n:

$$\sigma(\{\mathbf{R}_I\}) = \sigma_{\text{tra}}(\{\mathbf{R}_I\}) + \sigma_{\text{deg}}(\{\mathbf{R}_I\}) + \sigma_{\text{ter}}(\{\mathbf{R}_I\}), \tag{3.51}$$

where (i) $\sigma_{\text{tra}}(\{\mathbf{R}_I\})$ denotes the intra-band contribution with $m = n$:

$$\sigma_{\text{tra}}(\{\mathbf{R}_I\}) = \frac{\pi e^2 \hbar}{3m^2 V} \sum_{\mathbf{k}} \sum_{n} (-\frac{\partial f}{\partial \epsilon})_{\epsilon=\epsilon_{n\mathbf{k}}} |\langle n\mathbf{k}|\mathbf{p}|n\mathbf{k}\rangle|^2 \frac{1}{\pi\eta}, \tag{3.52}$$

(ii) $\sigma_{\text{deg}}(\{\mathbf{R}_I\})$ denotes the degenerate-state contribution with $m \neq n$ and $\epsilon_{m\mathbf{k}} = \epsilon_{n\mathbf{k}}$:

$$\sigma_{\text{deg}}(\{\mathbf{R}_I\}) = \frac{\pi e^2 \hbar}{3m^2 V} \sum_{\mathbf{k}} \sum_{n} \sum_{\substack{m \neq n \\ \epsilon_{m\mathbf{k}} = \epsilon_{n\mathbf{k}}}} (-\frac{\partial f}{\partial \epsilon})_{\epsilon=\epsilon_{n\mathbf{k}}} |\langle m\mathbf{k}|\mathbf{p}|n\mathbf{k}\rangle|^2 \frac{1}{\pi\eta}, \tag{3.53}$$

and (iii) $\sigma_{\text{ter}}(\{\mathbf{R}_I\})$ denotes the inter-band contribution[9] with $m \neq n$ and $\epsilon_{m\mathbf{k}} \neq \epsilon_{n\mathbf{k}}$:

$$\sigma_{\text{ter}}(\{\mathbf{R}_I\}) = \frac{\pi e^2 \hbar}{3m^2 V} \sum_{\mathbf{k}} \sum_{n} \sum_{\substack{m \neq n \\ \epsilon_{m\mathbf{k}} \neq \epsilon_{n\mathbf{k}}}} \frac{f(\epsilon_{n\mathbf{k}}) - f(\epsilon_{m\mathbf{k}})}{\epsilon_{m\mathbf{k}} - \epsilon_{n\mathbf{k}}} |\langle m\mathbf{k}|\mathbf{p}|n\mathbf{k}\rangle|^2 \frac{1}{\pi\eta} \frac{\eta^2}{(\epsilon_{m\mathbf{k}} - \epsilon_{n\mathbf{k}})^2 + \eta^2}. \tag{3.54}$$

Here we note that the terms “intra-band contribution" and “inter-band contribution" usually refer to the electronic band structure of the primitive cell. For convenience, we adopt these concepts, despite the fact that the simulation cells in KG calculations are supercells. In the KG formula, the wavevectors $\mathbf{k}$ refer to the Brillouin zone of the supercell, and the momentum matrix elements $\langle m\mathbf{k}|\mathbf{p}|n\mathbf{k}\rangle$ are diagonal in $\mathbf{k}$. The Fermi derivatives in Equation (3.52) and (3.53) can be written as [97, 13],

$$(-\frac{\partial f}{\partial \epsilon})_{\epsilon=\epsilon_{n\mathbf{k}}} = \frac{1}{k_B T} f_{n\mathbf{k}} (1 - f_{n\mathbf{k}}), \tag{3.55}$$

which are nonzero only for partially occupied states.

Clearly, both the $\sigma_{\text{tra}}(\{\mathbf{R}_I\})$ and $\sigma_{\text{deg}}(\{\mathbf{R}_I\})$ depend inversely on broadening parameter η. If one replaces $\hbar/\eta$ by τ, then it follows that the $\sigma_{\text{tra}}(\{\mathbf{R}_I\})$ has the same algebraic structure as the BTE in the constant RTA [see Equation (3.6)]. The behavior of $\sigma_{\text{ter}}(\{\mathbf{R}_I\})$ can be qualitatively understood in terms of a simple two-level system: By increasing η and thus the degree of mixing of the two levels, the $\sigma_{\text{ter}}(\{\mathbf{R}_I\})$ of the two-level system

---

[9] Note that in the KG formula, indirect inter-band transitions between different $\mathbf{k}$ points are not allowed.

is expected to increase first, then be nearly stable, and decrease finally.

3.4.4 Code implementation: FHI-kubo

The evaluation of Equation (3.45) is a postprocessing of first-principles material parameters. Its code implementation is straightforward, since it is generally easy to access Kohn-Sham eigenvalues $\epsilon_{n\mathbf{k}}$ and momentum matrix elements $\langle m\mathbf{k}|\mathbf{p}|n\mathbf{k}\rangle$ from typical solid-state DFT codes (e.g., FHI-aims). We have developed a computer code, named FHI-kubo, which is a set of Python scripts for postprocessing the DFT material parameters for a single atomic configuration $\{\mathbf{R}_I\}$ and evaluating the $\sigma(\{\mathbf{R}_I\})$ for this sample. Figure 3.1 depicts our whole workflow of performing *ab initio* KG calculations, as explained in the following:

(i) *ai*MD simulations at finite temperature are performed using the FHI-aims code and monitored by the FHI-vibes code. The FHI-vibes code, which is developed by Knoop *et al.* [185], has many useful tools for e.g. creating supercells and picking samples from a MD trajectory.

(ii) For each of the samples collected, a static DFT calculation using a dense $\mathbf{k}$-mesh provides the $\epsilon_{n\mathbf{k}}$ and $\langle m\mathbf{k}|\mathbf{p}|n\mathbf{k}\rangle$; Due to the need of using dense $\mathbf{k}$-point sampling, it is not a good idea to compute these quantities “on the fly" in MD simulations. The calculated $\epsilon_{n\mathbf{k}}$ and $\langle m\mathbf{k}|\mathbf{p}|n\mathbf{k}\rangle$ are stored in binary files. Note that in FHI-aims calculations, the momentum-matrix elements are actually $\langle \psi_{m\mathbf{k}}|\nabla|\psi_{n\mathbf{k}}\rangle$.

(iii) The FHI-kubo code reads the stored quantities, and uses them to evaluate Equation (3.45) for $\sigma(\{\mathbf{R}_I\})$. A number of computational parameters can be specified, including broadening parameter η, free-carrier doping level, and band-gap scissor shift, etc. Since $\langle m\mathbf{k}|\mathbf{p}|n\mathbf{k}\rangle$ are diagonal in $\mathbf{k}$ space, the postprocessing of different $\mathbf{k}$ points are independent of each other and can be fully parallelized. This is implemented by using the MPI4py module [186] and by following the $\mathbf{k}$-point parallelization scheme as implemented in FHI-aims. Owing to this, the FHI-kubo code is very efficient in both reading data and computation. Finally, the calculated electrical conductivities and other useful quantities are written into a text file.

In the above process, the *ai*MD simulations and the static DFT calculation of $\epsilon_{n\mathbf{k}}$ and $\langle m\mathbf{k}|\mathbf{p}|n\mathbf{k}\rangle$ dominate the computational cost, which are computationally very expensive for large supercells. In contrast, the computational cost of the postprocessing KG calculation is minor. This is the reason why we develop a stand-alone computer code for the postprocessing, as it can re-use the DFT material parameters whenever the postprocessing settings need to be changed. We note that the KG formula has also been implemented for use with plane-wave electronic-structure calculations [32].

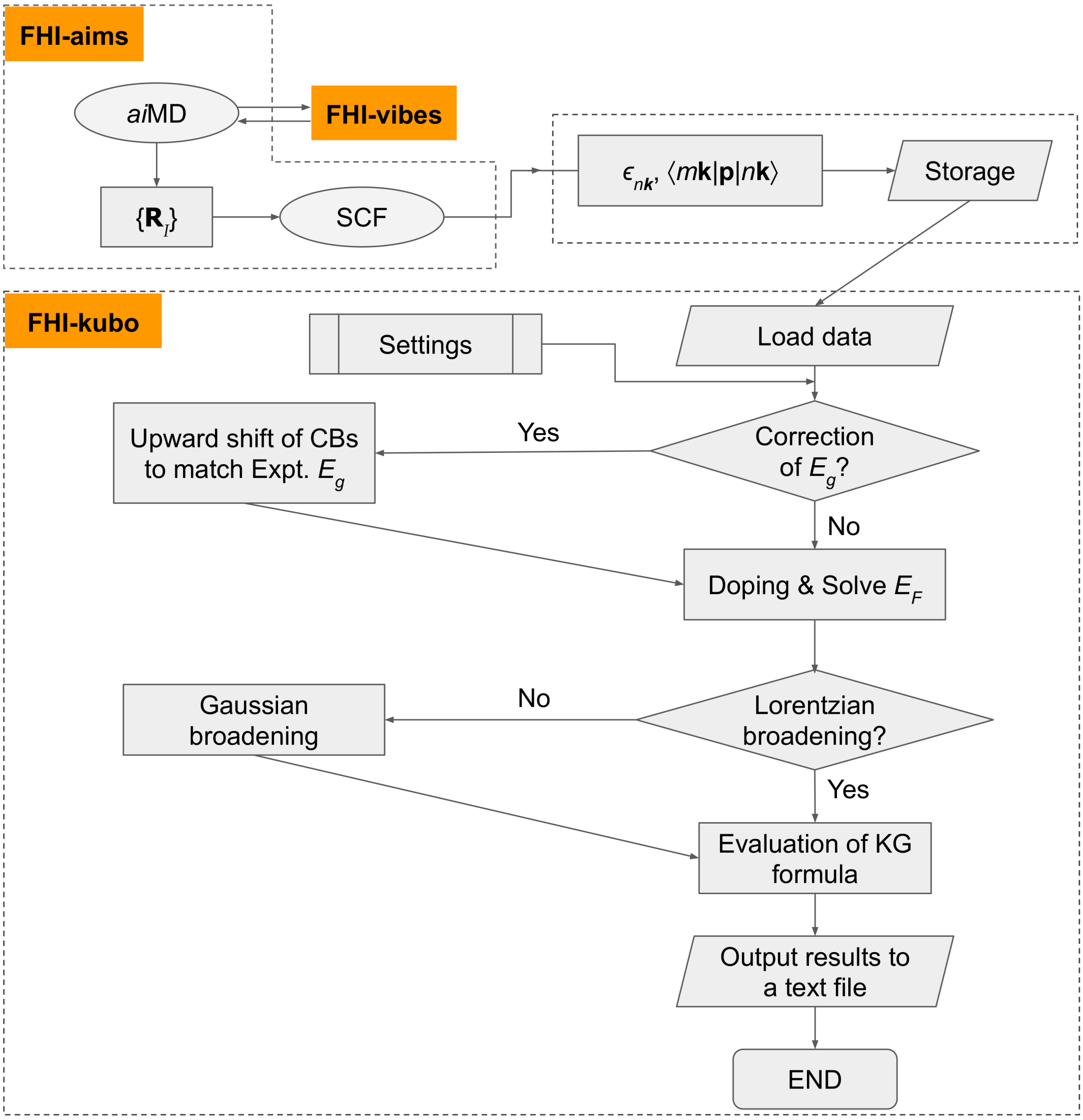

Figure 3.1: Workflow of our electrical conductivity calculations which involve three codes: FHI-aims, FHI-vibes, and FHI-kubo, as explained in the text.

4 Electrical conductivity of harmonic crystal silicon

This chapter, as our first attempt to apply the *ab initio* KG approach to study the electrical conductivity of crystalline materials, considers the prototypical semiconductor silicon (Si) at $T = 300$ K, for which extensive, high-quality literature data are available. Si is known to be a very harmonic crystal [15, 16], and therefore it is an example where the *ab initio* BTE approach works well [157]. Since little is known about *ab initio* KG calculations for crystalline materials, by focusing on the electrical conductivity of intrinsic Si, we provide a detailed convergence study of the relevant calculational parameters, such as **k**-point sampling, broadening parameter (η), number of *ai*MD samples, and supercell size. After elucidating the best practices for choosing these parameters and addressing the identified numerical difficulties, we compute the electrical conductivities of both *p*- and *n*-type Si at different doping levels, and compare our calculations with experiment and with *ab initio* BTE calculations in the literature.

4.1 Computational details

All DFT calculations in this chapter were done with the FHI-aims code using the "light" basis set of Si and the LDA functional [54], without considering spin-orbital coupling (SOC). First, *ai*MD simulations were carried out in the canonical (NVT) ensemble using a time step of 4 fs and a Langevin thermostat [102] at 300 K. They were performed (separately) in the $2 \times 2 \times 2$ (64-atom), $3 \times 3 \times 3$ (216-atom), $4 \times 4 \times 4$ (512-atom), and $5 \times 5 \times 5$ (1000-atom) cubic supercells (constructed out of the conventional cell of Si), using $3 \times 3 \times 3$, $2 \times 2 \times 2$, Γ-only, and Γ-only **k**-meshes, respectively. In the MD simulations, the density convergence criterion was set to 10^{-6} eV/Å^3 for both the $2 \times 2 \times 2$ and $3 \times 3 \times 3$ supercells, and 10^{-5} eV/Å^3 for both the $4 \times 4 \times 4$ and $5 \times 5 \times 5$ supercells (see test calculations in Section A.2.1 in the Appendix). For the $2 \times 2 \times 2$ and $3 \times 3 \times 3$ supercells, an initial period of 4 ps was used for thermal equilibration, and this duration was reduced to 2 ps for the $4 \times 4 \times 4$ and $5 \times 5 \times 5$ supercells due to the computational cost. For a given supercell size, after equilibration, the atomic configuration of the supercell was sampled every 50 time steps (i.e., 200 fs). This sampling time interval was shown to lead to uncorrelated samples (see Figure A.2). The MD samplings were accelerated by using 5, 4, 4, and 2 independent and equally long trajectories for the $2 \times 2 \times 2$, $3 \times 3 \times 3$, $4 \times 4 \times 4$, and $5 \times 5 \times 5$ supercells, respectively. The number of collected samples for each supercell size will be detailed in Section 4.3. Second, the KG calculation was carried out for each sample, which involves two steps: (i) A static DFT calculation with denser **k**-point sampling was performed to compute the Kohn-Sham eigenvalues $\epsilon_{n\mathbf{k}}$ and momentum-matrix elements $\langle m\mathbf{k}|\mathbf{p}|n\mathbf{k}\rangle$. In this calculation, the SCF convergence criteria for the density, sum of eigenvalues, and total energy were set to 10^{-6} eV/Å^3, 10^{-4} eV, and 10^{-6} eV, respectively, and the **k**-point samplings will be detailed in Section 4.2.1. (ii) Using the DFT material parameters, the electrical conductivity in this sample was computed by evaluating Equation (3.45) as implemented in our FHI-kubo code. More computational details can be found in later sections.

thermal lattice expansion of Si

Here we present the calculated lattice constant of Si at $T = 0$ and 300 K. The zero-T lattice constant is obtained by an usual structural relaxation of the unit cell of Si. Since the electrical transport properties of materials are largely influenced by temperature, it is important to take into account the thermal lattice expansion, which is purely an anharmonic effect [33]. Our computation of the lattice constant of Si at 300 K is based on a "quasi-NPT" method as detailed in Appendix A.2.3 (This method also involves structural relaxation).

Table 4.1: Calculated lattice constant of Si, compared to experimental value [187, 188]. In the table, “Relaxation" means an usual DFT-LDA structural relaxation; “Extrapolation" means extrapolating the DFT-LDA relaxed (0 K) lattice constant to 300 K using the measured thermal expansion coefficients [187].

	Lattice constant (Å)			
T (K)	Relaxation	Quasi-NPT	Extrapolation	Expt.
0	5.417	-	-	5.422
300	-	5.424	5.421	5.431

In Table 4.1 we see that the quasi-NPT method captures the thermal lattice expansion of Si. The calculated lattice constants are slightly smaller than the experimental values, which is expected for LDA. For comparison, we have also extrapolated the DFT-LDA zero-T lattice constant to 300 K using the measured thermal expansion coefficients (detailed in Appendix A.2.3), and find that the extrapolation is in good agreement with the quasi-NPT method (see Table 4.1). The thermal lattice expansion is rather small, suggesting that Si is a very harmonic material at 300 K. Our later electrical conductivity calculations for Si at 300 K will be based on the lattice constant obtained with the quasi-NPT method.

4.2 Convergence of the KG calculation

Our *ab initio* electrical conductivity calculations based on a combination of *ai*MD and the KG formula [in the form of Equation (3.45)] involve a number of calculational parameters: (i) In *ai*MD simulations, we need to consider the MD trajectory length which determines the number of samples (i.e., atomic configurations). (ii) In the KG calculation for a single sample, we need to consider the **k**-point sampling of the Brillouin zone, energy window (in other words, number of bands), broadening parameter (η, which is for the Lorentzian functions in the KG formula), and basis-set size. (iii) Furthermore, we also need to consider the supercell size. A proper choice of these parameters and addressing possible numerical issues are prerequisites for obtaining reliable results for the electrical conductivity. In addition, the underestimation of the band gaps by DFT-LDA is expected to cause large systematic error in the calculated electrical conductivities when comparing with experimental data.

In this section, by focusing on the electrical conductivity of intrinsic Si at 300 K, we investigate the convergence of the KG calculation with respect to **k**-point sampling, energy window, broadening parameter, and basis-set size, and overcome the band-gap problem. To this end, we take two MD (300 K) samples as examples: One is a $2 \times 2 \times 2$ supercell and the other is a $4 \times 4 \times 4$ supercell. We note that in this section, there is no sample mean and $T = 300$ K is for Fermi-Dirac distributions. Also, because the computational parameters are largely interdependent, several of them have to be discussed together in some situations. The convergence with respect to number of MD samples and supercell size will be discussed in Section 4.3 and 4.4, respectively.

4.2.1 k-point convergence

We first examine the convergence of the electrical conductivity with respect to the **k**-point sampling of the Brillouin zone. In the evaluation of Equation (3.45), the Brillouin-zone integration is carried out by replacing the continuous integral with the summation over a regularly spaced mesh of $n \times n \times n$ points, generated according to the Monkhorst-Pack scheme. At this stage the DFT-LDA band gaps are not corrected.

Figure 4.1 shows the calculated intrinsic electrical conductivities, which have been separated for holes and electrons, in the $2 \times 2 \times 2$ supercell and in the $4 \times 4 \times 4$ supercell[1] as a function of Γ-centered **k**-point sampling. These results are obtained with $\eta = 10$ meV (which is just an example). We see that the $20 \times 20 \times 20$ and $10 \times 10 \times 10$ **k**-meshes can yield **k**-point converged electrical conductivities for the $2 \times 2 \times 2$ and $4 \times 4 \times 4$ supercells, respectively. The convergence is well within 0.5%[2]. Obviously, the **k**-point convergence is tied to the supercell size; that is to say, the $20 \times 20 \times 20$ **k**-mesh

---

[1] Again we stress that in this entire section, we use only one MD sample of the $2 \times 2 \times 2$ supercell and one MD sample of the $4 \times 4 \times 4$ supercell. There is no sample mean.

[2] Similar **k**-point convergence was guaranteed in predictive *ab initio* BTE calculations for Si [157].

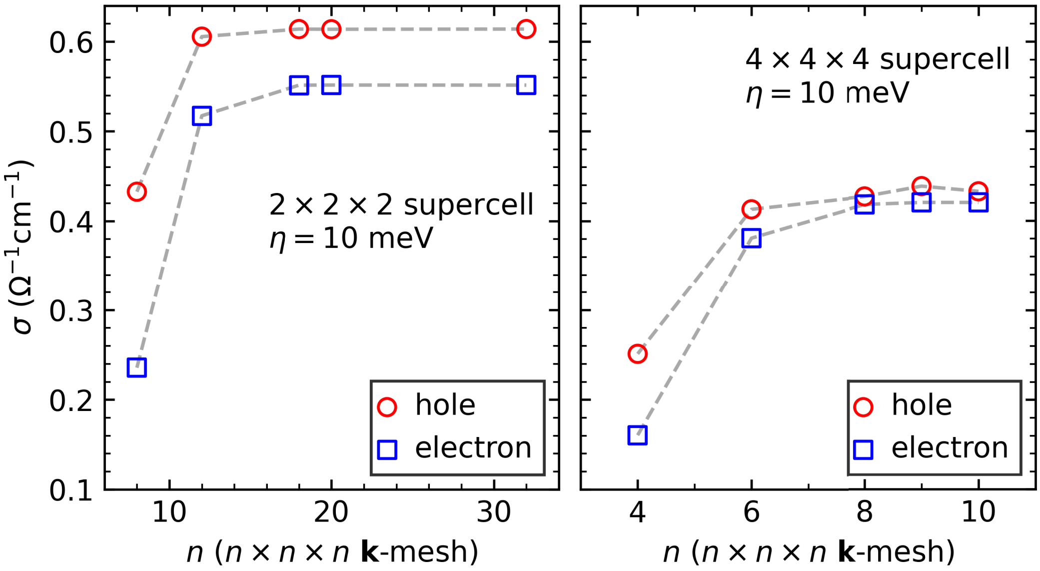

Figure 4.1: Calculated electrical conductivities, for both the holes and electrons, in the $2 \times 2 \times 2$ supercell and in the $4 \times 4 \times 4$ supercell of intrinsic Si at 300 K as a function of **k**-point sampling (of the Brillouin zone of the supercells). The broadening parameter (η) is set to 10 meV, and the DFT-LDA band gaps are not corrected. The dashed lines are a guide to the eye.

for the $2 \times 2 \times 2$ supercell and the $10 \times 10 \times 10$ **k**-mesh for the $4 \times 4 \times 4$ supercell are of the same density of **k**-point sampling, which is easily understood from the Brillouin-zone folding.

The importance of using dense **k**-point sampling in electronic transport calculations for semiconductors has been shown in previous *ab initio* BTE calculations [157]. For intrinsic Si at 300 K, the Fermi level (E_F) lies in the band gap, and the carriers are confined within a narrow energy range near the band extrema. Therefore, the **k**-point sampling must be fine in order to precisely determine the Fermi level (see Figure 4.2) and thus to capture the tails of the Fermi-Dirac distribution. In Figure 4.1, we note that the calculated hole and electron conductivities exhibit similar **k**-point convergence behavior. This is because the current results are for intrinsic Si, for which the Fermi level is given by $n_\mathrm{h} = n_\mathrm{e}$, i.e., both the upper valence bands and lower conduction bands are equally important in determining the position of the Fermi level. For a intrinsic semiconductor, the Fermi level can be estimated by $E_F = \frac{1}{2}E_g + \frac{1}{2}k_B T \ln(\frac{N_\mathrm{V}}{N_\mathrm{C}})$, where N_V and N_C are the effective density of states of the valence and conduction bands, respectively, and E_g is the band gap [111]. The precise determination of the Fermi level requires that N_V, N_C, and E_g are precisely determined.

The convergence of **k**-sampling is expected to be dependent on the broadening pa-

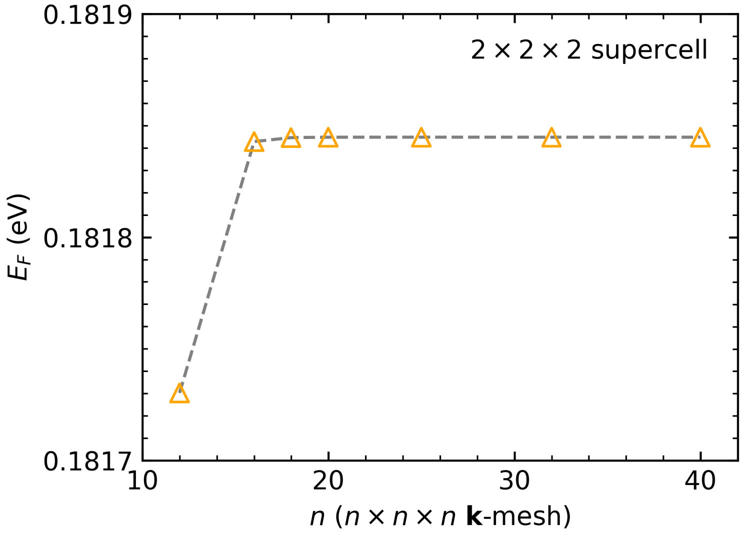

Figure 4.2: Calculated Fermi level (referenced to the VBM) for the $2 \times 2 \times 2$ supercell of intrinsic Si at 300 K as a function of **k**-point sampling. The DFT-LDA band gaps are not corrected. Note that the span of the y-axis is only 0.2 meV. The dashed line is a guide to the eye.

rameter (η). This can be understood from a related quantity, the density of states (DOS). As shown in Figure 4.3, which is for the $2 \times 2 \times 2$ supercell, the DOS calculated with the $20 \times 20 \times 20$ **k**-mesh and $\eta = 20$ meV has discrete peaks. These unphysical peaks reflect that the eigenvalues $\epsilon_{n\mathbf{k}}$ are discrete with respect to **k**, and can be eliminated using denser **k**-point samplings, e.g., the $32 \times 32 \times 32$ **k**-mesh. However, when η is decreased to 10 meV, the $32 \times 32 \times 32$ **k**-mesh becomes insufficient to provide a smooth DOS. Since η in principle should be as small as possible, the DOS results indicate that upon decreasing η to a new value, one needs to increase the **k**-point sampling accordingly. Unlike the DOS case, the **k**-point convergence of the electrical conductivity is largely independent of η, as shown in Figure 4.4 (an additional test is given in the Appendix, Section A.2.4). But, the **k**-point converged electrical conductivities depend strongly on η, suggesting that a careful choice of η has to be made. We will come back to this issue in Subsection 4.2.3. It is now clear that for a given supercell size and η value, **k**-point converged electrical conductivities can be achieved. We note that the **k**-point convergence of the electrical conductivity is faster than that of the DOS. This is understood from that the DOS is an energy-resolved spectral property, while the electrical conductivity given by Equation (3.45) involves an additional sum over the band index and is thus an integrated spectral property.

The above discussion allows us to decide the **k**-meshes for performing KG calculations for Si at 300 K. As listed in Table 4.2, we will use $20 \times 20 \times 20$, $14 \times 14 \times 14$,

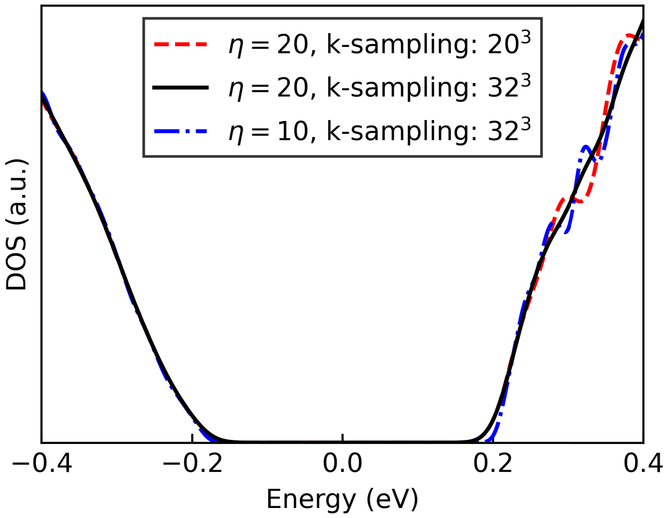

Figure 4.3: Calculated DOS for the $2 \times 2 \times 2$ supercell of Si, using: (i) $20 \times 20 \times 20$ **k**-mesh and broadening parameter $\eta = 20$ meV (red dashed line), (ii) $32 \times 32 \times 32$ **k**-mesh and $\eta = 20$ meV (black solid line), and (iii) $32 \times 32 \times 32$ **k**-mesh and $\eta = 10$ meV (blue dash-dotted line). The energy zero is at the Fermi level, and the displayed range is $[-0.4, 0.4]$ eV for visual clarity.

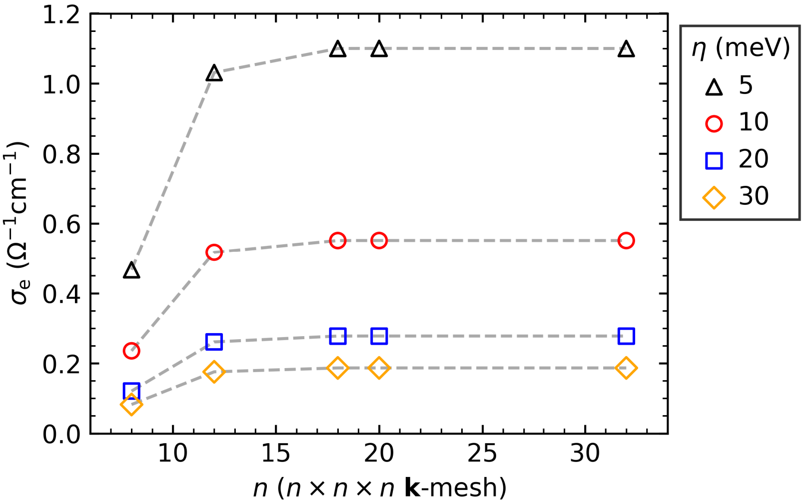

Figure 4.4: Calculated electron conductivity (σ_e) in the $2 \times 2 \times 2$ supercell of intrinsic Si at 300 K as a function of **k**-point sampling, for different choices of the broadening parameter (η). The DFT-LDA band gap is not corrected. The dashed lines are a guide to the eye.

$10 \times 10 \times 10$, and $7 \times 7 \times 7$ **k**-meshes for the $2 \times 2 \times 2$, $3 \times 3 \times 3$, $4 \times 4 \times 4$, and $5 \times 5 \times 5$ supercells, respectively. Unfortunately, we are unable to maintain the same **k**-point density for these supercell sizes. For example, in order to obtain the same **k**-point density as the $20 \times 20 \times 20$ **k**-mesh for the $2 \times 2 \times 2$ supercell, we need to use a $8 \times 8 \times 8$ **k**-mesh for the $5 \times 5 \times 5$ supercell, but this exceeds our computational capacities. Indeed, since the KG calculation is performed in supercells, the dense **k**-point sampling required makes the calculation very demanding, especially when using large supercells (see further discussion in Subsection 4.2.5).

Table 4.2: Chosen **k**-meshes for performing KG calculations in the Si supercells.

Supercell size	**k**-mesh
$2 \times 2 \times 2$	$20 \times 20 \times 20$
$3 \times 3 \times 3$	$14 \times 14 \times 14$
$4 \times 4 \times 4$	$10 \times 10 \times 10$
$5 \times 5 \times 5$	$7 \times 7 \times 7$

4.2.2 Convergence with energy window

Here, we briefly mention the convergence of the electrical conductivity with respect to the energy window which determines the number of electronic bands to be included in the KG calculation. It is found that this convergence is rapidly achieved with a small energy window, i.e., a few hundred meV below the valence-band maximum (VBM) and above the conduction-band minimum (CBM). This is because for intrinsic Si at 300 K, thermally-excited charge carriers are confined within a narrow energy range (typically a few $k_{\mathrm{B}}T$) near the band extrema. Also for this reason, one should use a larger energy window when the temperature and/or doping level become higher. For safety and consistency, we suggest simply using a large energy window as this parameter is not the primary cause of the computational cost.

4.2.3 Choice of the broadening parameter

We proceed to address the issue related to the choice of the broadening parameter (η) raised in Subsection 4.2.1. As discussed in Section 3.4.1, Equation (3.45) containing Lorentzian functions $\frac{1}{\pi\eta}\frac{\eta^2}{(\epsilon_{m\mathbf{k}}-\epsilon_{n\mathbf{k}})^2+\eta^2}$ with finite η has to be used for practical KG calculations, because the Kohn-Sham energy levels of a finite-size supercell are discrete [with respect to band index n (at each $\mathbf{k}$ point)]. The value of η should be large compared to the average level spacing, in order to recover the quasi-continuous single-particle energy spectrum in the thermodynamic limit (corresponding to an infinitely large supercell) [167]. In the work of Alfè *et al*. [34], for a given supercell, η is set to the average level spacing of this supercell. In the work of Nomura and MacDonald [177], the authors computed the electrical conductivity of disordered graphene at 0 K by evaluating the KG formula at a large number of η values. In this study, the electrical conductivity has only the inter-band contribution. Nomura and MacDonald found that the electrical conductivity is a maximum when η corresponds to $\sim \delta E$ (the level spacing at the Fermi level), and used this maximum as the result for the electrical conductivity. More detailed discussion of these works can be found in Section 3.4.1.

Because it is difficult to estimate the average level spacing, we follow the work of Nomura and MacDonald to define a strategy to determine an appropriate value for η. Although in our study the electrical conductivity is not limited to the inter-band contribution, we determine the value of η based purely on the inter-band contribution versus η. Below, we present a test of this strategy. For this, we take again the two MD samples used in Subsection 4.2.1: one is a $2 \times 2 \times 2$ supercell and the other is a $4 \times 4 \times 4$ supercell, and perform KG calculations at a large number of η values using $20 \times 20 \times 20$ and $10 \times 10 \times 10$ $\mathbf{k}$-meshes, respectively.

In Figure 4.5 we plot the calculated electrical conductivities as a function of η, for both holes and electrons in both supercells. The electrical conductivities have been decomposed into intra-band, degenerate-state, and inter-band contributions, according to Equations (3.52)-(3.54). Due to thermally induced symmetry breaking, the contribution from degenerate states[3] is zero for both supercells (thus not shown). As seen in Figure 4.5, e.g., the hole conductivity in the $2 \times 2 \times 2$ supercell, the intra-band contribution is much larger than the inter-band contribution (for the η range displayed). The intra- and inter-band contributions exhibit distinct behaviors: (i) The intra-band contribution is inversely proportional to η, which diverges as $\eta \to 0$ and vanishes for $\eta \to \infty$; (ii) The inter-band contribution shows a concave behavior, which peaks at some intermediate value of η and vanishes for either $\eta \to 0$ or $\eta \to \infty$ (similar behavior was found in Ref. [177]). There are also clear differences in the plots for the inter-band contribution versus η between the two supercells: (i) The curves for the $4 \times 4 \times 4$ supercell are steeper along with stronger peaks compared to those for the $2 \times 2 \times 2$ supercell; (ii) In the case of the $2 \times 2 \times 2$ supercell, the maxima of the curves for the holes and electrons are located at $\eta = 64$ and 53 meV, respectively, while they are moved to smaller η values of 17 and 20 meV in the case of the $4 \times 4 \times 4$ supercell.

We give a qualitative explanation for the observed behavior of inter-band contribution. Without loss of generality, we focus on the inter-band contribution to the hole conductivity in the $4 \times 4 \times 4$ supercell. In this case, the inter-band contribution arises from (direct) inter-band transitions between the upper valence-band levels[4]. When us-

---

[3] We consider that two energy levels are degenerate when their spacing is smaller than 10^{-6} eV.

[4] For the electrical conductivity, only the upper valence bands and lower conduction bands matter.

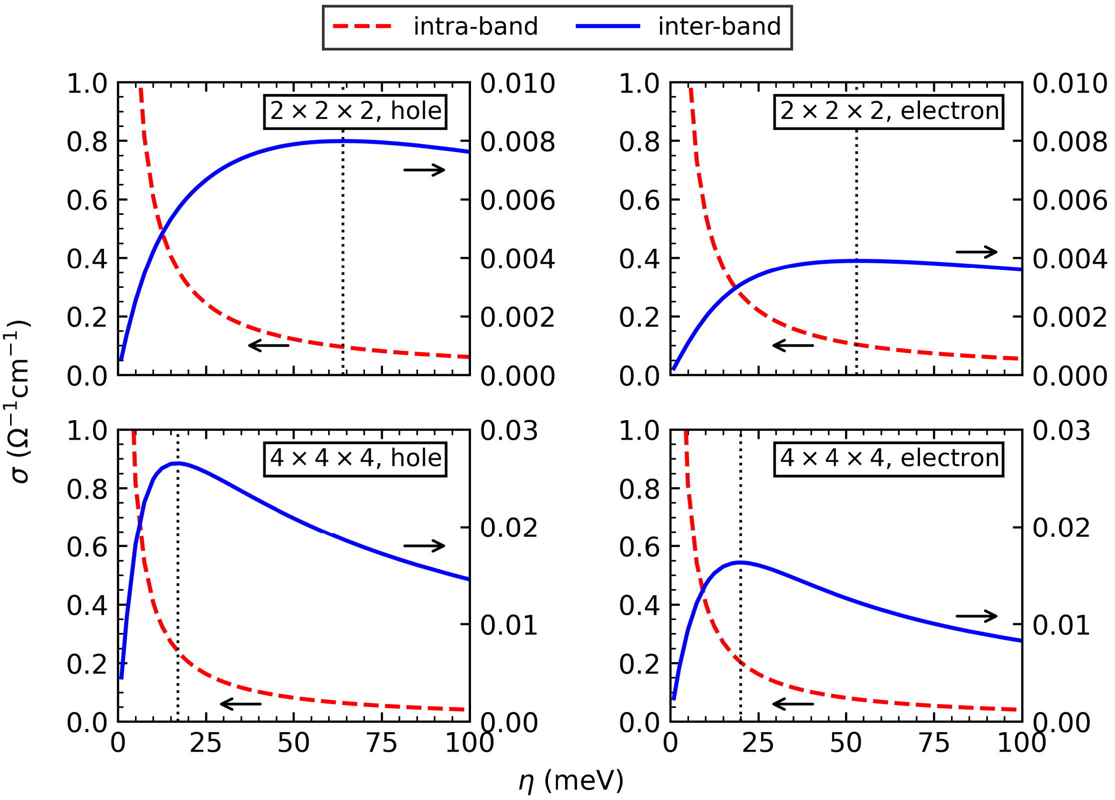

Figure 4.5: Calculated electrical conductivities for the holes and electrons in the $2 \times 2 \times 2$ supercell and in the $4 \times 4 \times 4$ supercell of intrinsic Si at 300 K as a function of broadening parameter (η). The (full) electrical conductivities have been decomposed into intra-band contribution (dashed red line) and inter-band (solid blue line) contribution. In each subplot, the left and right y-axes are for the intra-band and inter-band contributions, respectively. Note the different scales of the y-axes in each subplot and between different subplots. The vertical dotted line denotes the maximum of the inter-band contribution versus η. In the upper right subplot, the full electron conductivity at $\eta = 5$, 10, 20, and 30 meV have been shown in Figure 4.4 at the $20 \times 20 \times 20$ **k**-mesh.

ing a too small η (e.g., 5 meV), the Lorentzian broadening is not sufficient to make the upper valence-band levels describe a quasi-continuous energy spectrum. As a consequence, the inter-band transitions are suppressed, leading to underestimated inter-band contribution. When using a too large η (e.g., 75 meV), the Lorentzian broadening does make the upper valence-band levels describe a quasi-continuous energy spectrum, but the broadening is overdone. As a consequence, the inter-band transitions between the neighboring levels become less important, resulting in underestimated inter-band contribution. It is thus clear that for $\eta \sim 17$ meV (mentioned above), the Lorentzian broadening makes the upper valence-band levels represent a quasi-continuous energy spectrum as in the thermodynamic limit, yielding both numerically stable and physically reasonable result for the inter-band contribution. This implies that: (i) The average level spacing of the upper valence bands in the $4 \times 4 \times 4$ supercell is close to 17 meV; (ii) The maximum of the inter-band contribution versus η, which appears at $\eta = 17$ meV, is probably the optimal estimate of the inter-band contribution to the hole conductivity in the $4 \times 4 \times 4$ supercell, and accordingly, $\eta = 17$ meV is probably the appropriate choice of η. To verify this, we have estimated the average level spacing of the upper valence bands at the Γ-point and found that it is 12 meV. As a further check, we also estimate the average level spacing of the upper valence bands in the $2 \times 2 \times 2$ supercell and find that it is 59 meV, which is comparable to $\eta = 64$ meV (mentioned above). These results suggest that the behavior of the inter-band contribution versus η reflects the average level spacing of the supercell, and that the choice of η is required to be related to the supercell size (at least when the supercell is not sufficiently large).

Optimal-η scheme

The above discussion suggests that for a given supercell, an appropriate choice of η can be found as follows: compute the inter-band contribution (to the electrical conductivity) as a function of η, and take the η value at which the inter-band contribution is a maximum. By means of this, η is no longer an adjustable parameter, but is decided by the supercell size, or to be more precise, by the average level spacing of the Kohn-Sham energy levels of the supercell. We refer to the choice of η in this way as the "optimal-η scheme" in the following of the thesis. The chosen η value will be used to evaluate Equation (3.45) for the (full) electrical conductivity. Since the upper valence bands and lower conduction bands usually have different level spacings, η will be different for the hole and electron conductivities.

It might be argued that the optimal-η scheme is not reasonable, because in this scheme the choice of η is based purely on the inter-band contribution versus η. We recognize this, and that the validity of the optimal-η scheme is required to be checked. Yet, the optimal-η scheme is physically motivated, i.e., its goal is to recover the thermodynamic limit which is not captured by finite-size supercell calculations. More importantly, it opens up a new possibility to discuss the η problem, given that one of the main purposes of this thesis is to describe the difficulties of a numerical implementation of the *ab initio* KG approach for crystalline solids.

We note that the **k**-meshes listed in Table 4.2 guarantee a satisfactory **k**-point convergence for the inter-band contribution to the electrical conductivity (see Section A.2.4). The first application of the optimal-η scheme is found in Section 4.3.

Choice of broadening parameter in *ab initio* BTE calculations

We can gain additional insight into the choice of η from previous calculations of electronic transport coefficients using the *ab initio* BTE approach. In BTE calculations, the e-ph relaxation time $\tau_{n\mathbf{k}}$ of the Kohn-Sham eigenstate $|n\mathbf{k}\rangle$ is given by Equation (3.7), in which the delta functions[5] $\delta(\epsilon_{n\mathbf{k}} \pm \hbar\omega_{\mathbf{q}\nu} - \epsilon_{m\mathbf{k}+\mathbf{q}})$ need to be replaced by Lorentzian (or Gaussian) functions with an appropriate value of η. Unlike the KG calculation which uses the supercell approach, the BTE calculation is based on the unit cell of the perfect crystal and requires an additional $\mathbf{q}$-point sampling to describe the e-ph interaction. These two approaches can nevertheless be connected: A supercell implicitly defines a $\mathbf{q}$-mesh with the same size as that of the supercell (elucidated in Section 2.5.2). In the BTE calculation, one usually starts from a certain η value (which is a constant for all bands and $\mathbf{k}$ points) and $\mathbf{q}$-mesh size, and monitors the convergence behavior of the results by decreasing η and increasing the $\mathbf{q}$-mesh size [189, 190, 170]. When η is sufficiently small (typically a few meV) and $\mathbf{q}$-mesh size is sufficiently large (typically on the order of $100 \times 100 \times 100$), stable results can be obtained [189, 190, 170]. As shown in FIG. S2(a) of Poncé *et al.* [157], if one decreases η while keeping the $\mathbf{q}$-mesh sampling fixed, the results diverge as $\propto 1/\eta$ for $\eta \to 0$.

In view of the above, it is clear that the choice of η must be small enough and at the same time compatible with the $\mathbf{q}$-point sampling. It also implies that η as small as a few meV cannot be used in our KG calculations, because our simulated supercells are very small. The dense $\mathbf{q}$-mesh required in BTE calculations implies that supercell-size convergence is likely to be a crucial issue in our KG calculations (see Section 4.4).

4.2.4 Correction of DFT band gaps

The electrical conductivity of a material depends largely on the band gap of the material. This is exemplified by the empirical law used in experiment to describe the temperature dependence of the electrical conductivity of an intrinsic semiconductor [191]:

$$\sigma(T) = A(T)e^{-\frac{E_g(0)}{2k_BT}}, \tag{4.1}$$

where $E_g(0)$ is the zero-T band gap, and the prefactor $A(T)$ accounts for the temperature effects (e.g., the temperature renormalization of the electronic band structure [192]). Equation (4.1) indicates that in electrical conductivity calculations, the results will be significantly overestimated if the band gap is severely underestimated by (semi)local DFT. Indeed, our DFT-LDA calculated electrical conductivities for intrinsic Si at 300 K reported in the previous subsections are around five orders of magnitude larger than the experimental value ($3.33 \times 10^{-6}\ \Omega^{-1}\text{cm}^{-1}$ [193]).

---

[5] The delta functions in the KG formula are of the form $\delta(\epsilon_{n\mathbf{k}} - \epsilon_{m\mathbf{k}})$, without explicit phonon frequencies.

The severe underestimation of the band gaps can be largely corrected by performing hybrid-functional theory or *GW* calculations, which, however, are associated with high computational cost (especially for supercell calculations). The main purpose of this thesis is to implement and analyze the *ab initio* KG approach to the calculation of the electrical conductivity of crystalline materials, assuming that accurate quasiparticle energies and wave functions will be provided by e.g. *GW* calculations in the future. Therefore, in this work we perform conventional DFT calculations using (semi)local xc functionals. In the following, we discuss how to deal with the DFT band-gap problem.

Our strategy for addressing the band-gap problem in our electrical conductivity calculations is to rigidly shift the conduction bands upwards by a constant energy Δ (while keeping the valence-band positions unchanged):

$$E_g^{\mathrm{cor}} = E_g^{\mathrm{LDA}} + \Delta, \tag{4.2}$$

where E_g^{cor} denotes the corrected band gap. This is the so-called "scissor operator" approach, which was widely used in first-principles calculations of point defects in solids [52, 194]. For a given material, we define Δ as the difference between the DFT-LDA band gap of the equilibrium structure at 0 K, $E_g^{\mathrm{LDA,\,eq}}(0\,\mathrm{K})$, and the experimental band gap at 0 K, $E_g^{\mathrm{Expt}}(0\,\mathrm{K})$; that is,

$$\Delta = E_g^{\mathrm{Expt}}(0\,\mathrm{K}) - E_g^{\mathrm{LDA,\,eq}}(0\,\mathrm{K}). \tag{4.3}$$

The Δ defined in this way estimates the underestimation of the band gap by DFT LDA. For Si, $E_g^{\mathrm{Expt}}(0\,\mathrm{K})$ is 1.17 eV [195], and our calculated $E_g^{\mathrm{LDA,\,eq}}(0\,\mathrm{K})$ is 0.503 eV, and thus $\Delta = 0.667$ eV. For a given material, we assume that Δ is a constant, regardless of the supercell size and thermal atomic displacements in the supercell. In case the $E_g^{\mathrm{Expt}}(0\,\mathrm{K})$ is not available, one can perform a *GW* calculation on the equilibrium structure at 0 K. It is worth mentioning that Δ may also be estimated based on finite-T band gaps with the temperature renormalization (see Zacharias *et al.* [192] and references therein). A particular advantage of the non-self-consistent scissor operator is that it adds no computational cost. In addition, this scheme is based on the rigid-band approximation which will used for simulating free-carrier doping in our work.

Let us take the $2 \times 2 \times 2$ supercell used in the previous subsections as an example. The DFT-LDA band gap of this supercell is 0.391 eV, so after the scissor shift, the band gap is enlarged to be 1.057 eV. Also, the intrinsic Fermi level, which originally lies at 0.182 eV (referenced to the VBM), is raised to 0.515 eV. Figure 4.6 shows the intrinsic electrical conductivities[6] of the holes and electrons as a function of the Fermi-level position, with and without the scissor correction to the band gap. To help explain the results illustrated in this figure, we note that: (i) For a rigid band structure, varying the Fermi

---

[6] These results are calculated using $20 \times 20 \times 20$ $\mathbf{k}$-mesh and with the η parameter set to 10 meV.

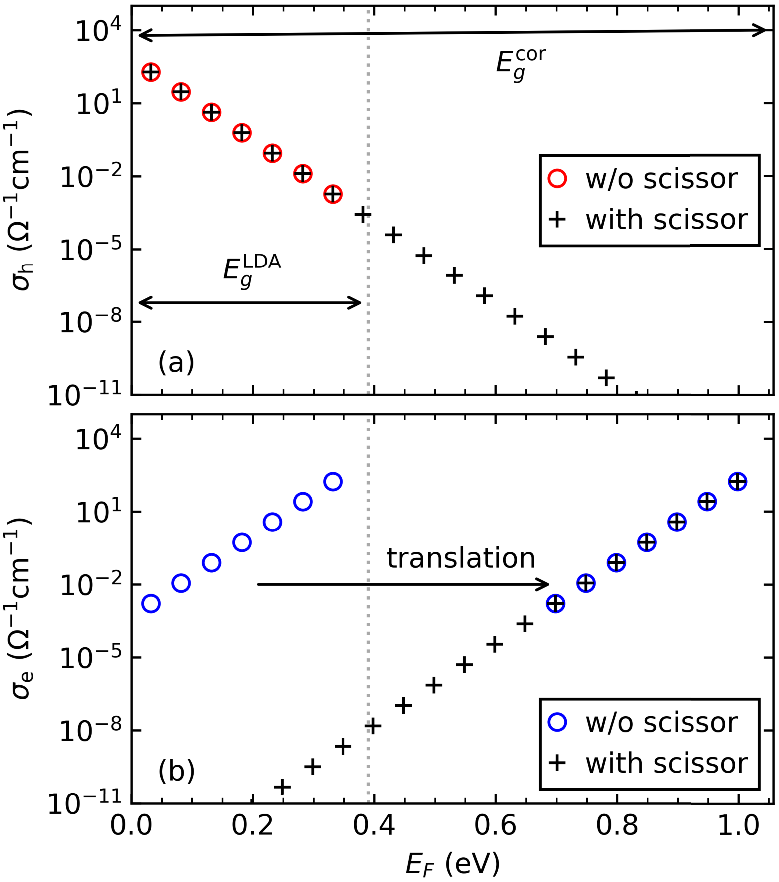

Figure 4.6: Calculated electrical conductivities of (a) holes and (b) electrons in the 2 × 2 × 2 supercell of intrinsic Si at 300 K as a function of Fermi level, with and without the scissor correction to the band gap. E_g^{LDA} and E_g^{cor} denote the DFT-LDA band gap and the gap with scissor correction, respectively. The Fermi level is referenced to the VBM. The “translation" means that we shift the plot for the electron conductivity (before band gap correction) along the x-axis together with the conduction bands when correcting the band gap. Note the logarithmic scale of the y-axes.

level away from the intrinsic Fermi-level position is equivalent to introducing free-carrier doping; (ii) When the Fermi level lies inside the band gap (i.e., non-degenerate doping), both the carrier concentration and electrical conductivity in the logarithmic scale are linear functions of the Fermi level [196]. In Figure 4.6, we see that: (i) When the Fermi level is fixed (e.g., at 0.182 eV), an upward shift in the conduction bands has no impact on the hole conductivity, while the electron conductivity becomes negligibly small; (ii) By contrast, if the Fermi level is also shifted upwards by the correction Δ, the band-gap correction then has no impact on the electron conductivity, while the hole conductivity becomes negligibly small. As a result of the band-gap correction, the calculated (total) intrinsic electrical conductivity drops from 0.19 to $4.79 \times 10^{-7}\ \Omega^{-1}\text{cm}^{-1}$, now in similar order of magnitude to the experimental value. This shows that the "scissor operator" approach can significantly reduce the error due to the band-gap underestimation. Interestingly, Figure 4.6 also implies that when the Fermi level is located near the VBM (or CBM), where the hole conductivity and electron conductivity differ by several orders of magnitude, we do not need to deal with the band-gap problem if we include in the result only the electrical conductivity of the majority carriers. This is a result of the simulation of doping in the rigid-band approximation.

4.2.5 Basis-set convergence

In this work we use the “light" basis sets for all the DFT calculations. However, in FHI-aims, the “tight" basis sets are recommended which, compared to the “light" ones, provide more reliable results but are also computationally more expensive. In this subsection we perform test calculations with the “tight" basis set of Si to check whether the “light" basis set of Si produce reliable electrical conductivity results.

With the “tight" basis set, the LDA-relaxed lattice constant of Si is 5.404 Å, which is slightly smaller than the value of 5.417 Å for the “light" basis set. Based on these two lattice constants, we have constructed two $2 \times 2 \times 2$ (64-atom) Si supercells with the nuclei at the ideal positions[7], and compute the intrinsic carrier concentrations and electrical conductivities in these two supercells using the respective basis sets. For the KG calculations, the **k**-point sampling is $20 \times 20 \times 20$, $T = 300$ K, and $\eta = 10$ meV (which is just an example). As shown in Table 4.3, the DFT-LDA band gap[8] given by the "light" basis set is 47 meV larger than that given by the “tight" basis set. As a result, the intrinsic carrier concentration, hole conductivity, and electron conductivity given by the “light" basis set are all smaller (about 2.5 times) than those given by the “tight" basis set. From this comparison, it seems that the electrical conductivity calculations using the "light" basis set are not converged.

Interestingly, we find that by enlarging the band gaps of the two supercells to 1.17 eV using the “scissor operator" approach, the two basis sets give very close results, as shown in Table 4.3. This finding suggests that the “light" and “tight" basis sets produce nearly identical electronic band structures (at least the upper valence bands and lower conduction bands) for Si, except the band-gap values. Otherwise, the intrinsic carrier concentration, which depends sensitively on the electronic eigenvalues, would be noticeably different even after the band-gap correction. We also note that the DFT

---

[7] Keeping the nuclei at ideal positions is conveniently for comparing the impact of basis sets.

[8] Here the band-gap values are obtained from the DFT calculation using $20 \times 20 \times 20$ **k**-mesh.

Table 4.3: Band gaps (E_g), intrinsic carrier concentrations (n_{i}), hole conductivities (σ_{h}), and electron conductivities (σ_{e}) in the ideal $2 \times 2 \times 2$ supercells of Si at 300 K, calculated using both the "light" and "tight" basis sets, with and without the scissor correction to the band gaps.

Basis set	E_g (eV)	n_{i} (cm^{-3})	σ_{h} ($\Omega^{-1}\mathrm{cm}^{-1}$)	σ_{e} ($\Omega^{-1}\mathrm{cm}^{-1}$)
"light"	0.503	1.89×10^{15}	0.114	0.221
"tight"	0.456	4.62×10^{15}	0.273	0.570
"light"	1.17 (scissor)	4.77×10^{9}	2.87×10^{-7}	5.58×10^{-7}
"tight"	1.17 (scissor)	4.73×10^{9}	2.79×10^{-7}	5.84×10^{-7}

quantities needed in the KG calculation are essentially derivative quantities, i.e., Fermi-function derivatives $(\partial f/\partial\epsilon)_{\epsilon_{n\mathbf{k}}}$ and momentum-matrix elements $\langle m\mathbf{k}|\mathbf{p}|n\mathbf{k}\rangle$ (which are gradients of wave functions). These derivative quantities computed with the "light" basis set have been sufficiently converged.

In a second test, we consider again the MD sample of the $2 \times 2 \times 2$ supercell used in the previous subsections. The geometry (both the cell length and atomic coordinates) of this supercell is fully obtained from the LDA calculation with the "light" basis set. We perform KG calculations in this supercell using both the "light" and "tight" basis set[9]. The LDA band gap given by the "light" basis set is 30 meV larger than that given by the "tight" basis set. For the KG calculations, we fix the Fermi level at 0.1 eV above the VBM, and compare the hole conductivities. We find that the "light" and "tight" basis sets produce very close results for the hole conductivity, 14.46 and 14.11 $\Omega^{-1}\mathrm{cm}^{-1}$, respectively. This indicates that the upper valence bands given by the two basis sets are nearly identical. Similar basis-set convergence can be found for the electron conductivity by setting the Fermi level close to the CBM.

The above two tests suggest that the "light" basis set can provide reliable results for the electrical conductivity. Nevertheless, the band-gap underestimation needs to be corrected using the "scissor operator" approach when computing the intrinsic electrical conductivities, and this is always done in our later calculations.

Computational cost

At the end of this section, we explain why in this work we choose not to use the "tight" basis set of Si. The reason is the high computational cost in the KG calculation, which

---

[9] The other settings are the same as in the first test.

is performed in supercells and requires dense **k**-point sampling. For example, our KG calculation in the $2 \times 2 \times 2$ supercell with a $20 \times 20 \times 20$ **k**-mesh, is carried out using four computer nodes[10]. When using the "light" basis set of Si, the computing time is 11 minutes and the peak run-time memory is 27 GB (per node, the same in the following); by contrast, when using the "tight" basis set of Si, the computing time and peak run-time memory are increased to 90 minutes and 72 GB, respectively. The memory quickly becomes a bottleneck as supercell size increases. For instance, in order to perform the KG calculation in the $5 \times 5 \times 5$ (1000-atom) supercell with a $7 \times 7 \times 7$ **k**-mesh and "light" basis set, we need to use 512 nodes to share the memory, and the peak run-time memory is 190 GB, almost exceeding the maximally allowed memory (192 GB). The peak run-time memory occurs when performing the real-space integration to compute the momentum-matrix elements, since this involves also basis-function gradients. For a given material, we need to perform the KG calculation for a series of supercell sizes (in order for finite-size scaling). For a given supercell size, we need to perform the KG calculation for a large number of *ai*MD samples that are collected from *ai*MD simulations for several tens of picoseconds. Apparently, the computational cost is enormous. So far, our discussion is limited to Si, which is a simple material. The computational cost will be much heavier for materials consisting of heavy elements, which is the case for SnSe studied in the next chapter.

From the above discussion, we conclude that (i) currently it is computationally infeasible to use the "tight" basis sets for a systematic *ab initio* KG study on crystalline solids, and (ii) the "light" basis sets are good enough to provide reliable results for the electrical conductivity at a reduced computational cost, and enables using large supercells.

---

[10] Each node consists of two Intel Xeon Gold 6148 processors (Skylake, 20 cores @ 2.4 GHz). See https://docs.mpcdf.mpg.de

4.3 Convergence with number of MD samples

In the last section we considered only one MD sample of the Si supercells at 300 K. Within the *ab initio* KG approach, the electrical conductivity should be evaluated as an arithmetic mean over a sufficiently large number of MD samples. Starting from this section, we report the electrical conductivities estimated by sample means. For this, from *ai*MD simulations at 300 K, we have generated $N_\mathrm{s} = 655$, 404, 204, and 100 samples for the $2 \times 2 \times 2$, $3 \times 3 \times 3$, $4 \times 4 \times 4$, and $5 \times 5 \times 5$ supercells, respectively. In this section, we compute the intrinsic electrical conductivity at 300 K in these supercells, and examine whether the samples collected lead to a good statistical convergence.

The computational details of the evaluation of Equation (3.45) in this section are as follows. The **k**-point samplings are listed in Table 4.2. The LDA band gaps are corrected by a scissor operator of 0.667 eV. Note that the calculation of the intrinsic electrical conductivity is not trivial, as the band gap is an important parameter. For all simulated supercells, the sample-averaged, scissor-corrected band gaps underestimate the experimental value by about 60 meV, leading to an overestimation of the intrinsic carrier concentration by a factor of slightly more than two (see Table A.1 in the Appendix). To further analyze the η problem, we consider two different ways of choosing η: The first one is to use $\eta = 20$ meV (an intermediate η value albeit arbitrary) for all the KG calculations for all four supercells; The second one is to use supercell-size-dependent η values determined with the optimal-η scheme (detailed later).

Results for $\eta = 20$ meV

All the electrical conductivity results reported in this part are obtained with $\eta = 20$ meV, regardless of the supercell size and carrier type (hole or electron). For each supercell size, we plot in Figure 4.7 the hole conductivity $\sigma_\mathrm{h}(\{\mathbf{R}_I\})$ and electron conductivity $\sigma_\mathrm{e}(\{\mathbf{R}_I\})$ for each individual sample[11], and their cumulative moving averages (CMAs):

$$\mathrm{CMA}_{\langle N \rangle} = \frac{1}{N} \sum_{i=1}^{N} \sigma(\{\mathbf{R}_I\}_i), \tag{4.4}$$

where the index i labels the i-th sample, and N will grow from 1 to N_s. When $N = N_\mathrm{s}$, Equation (4.4) becomes Equation (3.44) and gives the sample mean over N_s samples. As can be seen in Figure 4.7, for a given supercell size, both $\sigma_\mathrm{h}(\{\mathbf{R}_I\})$ and $\sigma_\mathrm{e}(\{\mathbf{R}_I\})$ vary from one sample to another, and their CMAs become gradually stable as more samples are included. Besides, as the supercell size increases, the fluctuation of both $\sigma_\mathrm{h}(\{\mathbf{R}_I\})$ and $\sigma_\mathrm{e}(\{\mathbf{R}_I\})$ is readily reduced, and so does the CMAs. This reflects a reduction of finite-size effects with increasing supercell size.

---

[11] $\{\mathbf{R}_I\}$ denotes a generic atomic configuration.

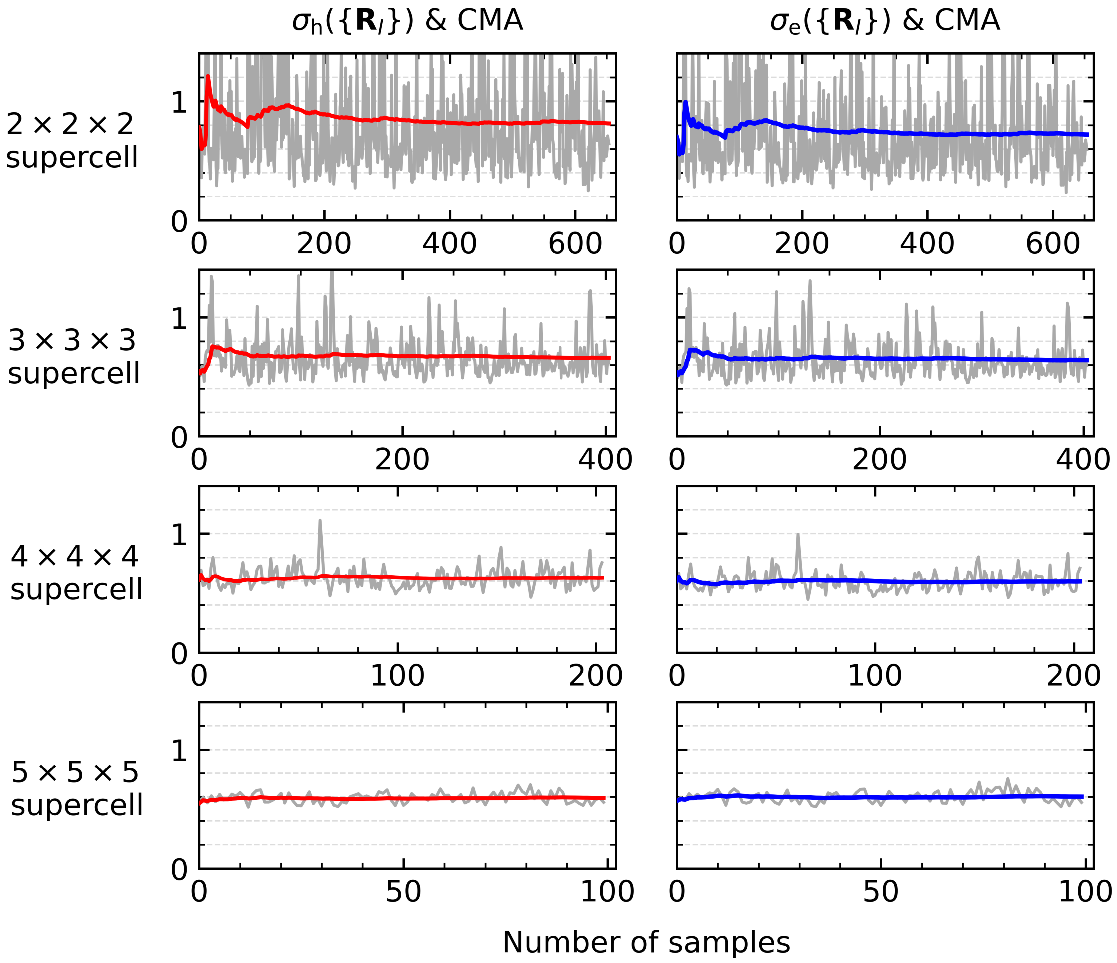

Figure 4.7: Convergence of electrical conductivity with respect to number of MD samples, for different supercells of intrinsic Si at 300 K. The left and right panels of the plot are for holes and electrons, respectively. All the electrical conductivity results are computed with broadening parameter $\eta = 20$ meV. Dark-gray thin lines: $\sigma_{h/e}(\{\mathbf{R}_I\})$ for an individual sample $\{\mathbf{R}_I\}$. Red/blue thick lines: cumulative moving averages (CMAs). The y-axes show the electrical conductivities in units of $10^{-6}\ \Omega^{-1}\text{cm}^{-1}$.

For each supercell size, we list in Table 4.4 the hole conductivity which is estimated by the mean of $\sigma_h(\{\mathbf{R}_I\})$, and the electron conductivity which is estimated by the mean of $\sigma_e(\{\mathbf{R}_I\})$. To quantify the statistical convergence of the electrical conductivities, we present also the standard error of the mean[12] (SEM). As shown in Table 4.4, for each of

---

[12] The SEM informs us the extent to which the sample mean approaches the true mean [197, 198].

our simulated supercells, the SEM is rather small compared to the sample mean, indicating a good statistical convergence. Our results suggest that it is not a big problem to converge the electrical conductivity of Si at 300 K with respect to number of MD samples, even though Si at 300 K is a highly harmonic system [15, 16]. Harmonic systems are thought to be poorly ergodic, as explained in Section 2.5.2.

Table 4.4: Hole conductivity (σ_{h}) and electron conductivity (σ_{e}) in the supercells of intrinsic Si at 300 K. The electrical conductivity and its statistical convergence are estimated by the sample mean and standard error of the mean (SEM), respectively. All the electrical conductivity results are computed with broadening parameter $\eta = 20$ meV. The values of the electrical conductivity and SEM are in units of $10^{-6}\ \Omega^{-1}\mathrm{cm}^{-1}$.

		Hole		Electron	
Supercell size	# samples	σ_{h}	SEM	σ_{e}	SEM
$2 \times 2 \times 2$	655	0.81	0.020	0.72	0.016
$3 \times 3 \times 3$	404	0.66	0.008	0.64	0.007
$4 \times 4 \times 4$	204	0.63	0.006	0.60	0.005
$5 \times 5 \times 5$	100	0.59	0.004	0.60	0.005

In addition, we note that: (i) For small supercells (e.g., the $2 \times 2 \times 2$ supercell), achieving good statistical convergence requires using a large number of samples, though the KG calculation for an individual sample is computationally cheap; (ii) By contrast, for large supercells (e.g., the $5 \times 5 \times 5$ supercell), while much less samples are needed to achieve good statistical convergence, the KG calculation for a single sample is computationally expensive. It is important to ensure good statistical convergence for all the supercells simulated, in order not to add uncertainty to the finite-size scaling (to be discussed in Section 4.4). In case of restricted computational resources, we suggest that one sets a target statistical convergence at the very beginning, starts performing KG calculations upon the MD sampling starts, and consistently monitors the statistical error to check whether the target convergence is reached. This could help achieve the target convergence with a minimum number of samples.

Results for the optimal-η scheme

The electrical conductivity results presented in this part are computed with the η values determined according to the optimal-η scheme. To be more specific, the value of η for each supercell size and a given carrier type (hole or electron) is found in the following way. We compute the inter-band contribution to the hole/electron conductivity in each MD sample at a large number of η values. Then, we compute the sample mean[13] of the inter-band contribution at each η value, and plot the sample-averaged inter-band contribution as a function of η, as shown in Figure 4.8. Finally, we take the η value which corresponds to the maximum of the plot. The chosen η values are listed in Table 4.5, where we see that: (i) For a given supercell size, the η value is different for holes and electrons, suggesting that the upper valence bands and lower conduction bands have different level spacings; (ii) For a given carrier type, the η values decrease as the supercell size increases, indicating that the level spacings are reduced with the increase of the supercell size.

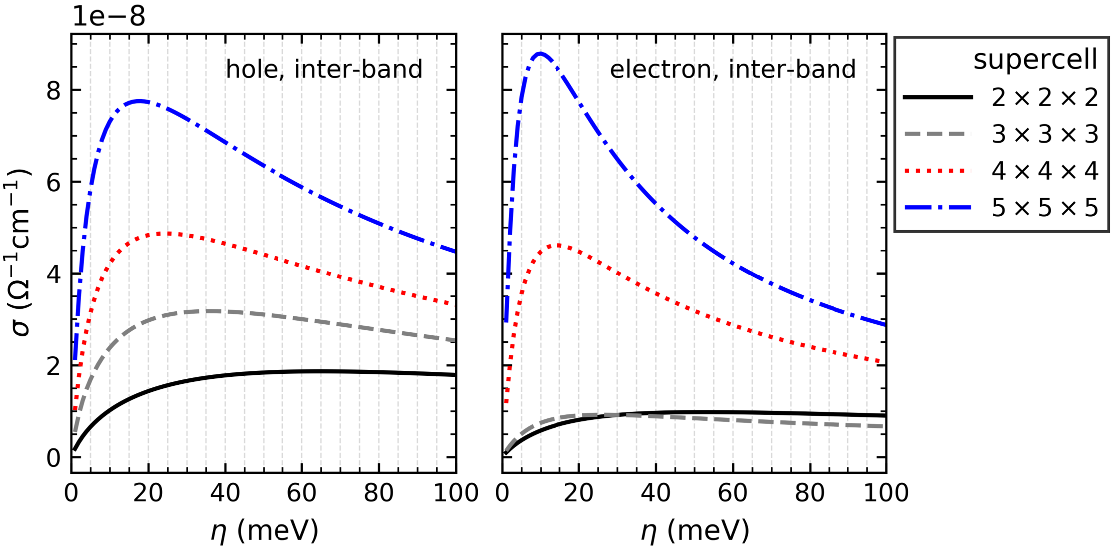

Figure 4.8: Sample-average inter-band contribution to the electrical conductivity as a function of broadening parameter (η), for the holes (left) and electrons (right) in the supercells of intrinsic Si at 300 K. Each curve has been averaged over the respective collected MD samples. Note the scale of the y-axes.

For each supercell size, in Figure 4.9 we plot $\sigma_{\rm h}(\{\mathbf{R}_I\})$ and $\sigma_{\rm e}(\{\mathbf{R}_I\})$ for each individual sample and their CMAs. A qualitative comparison of Figures 4.7 and 4.9 shows that the extent of fluctuations of $\sigma_{\rm h/e}(\{\mathbf{R}_I\})$ are seemingly different for different η values. The final electrical conductivities estimated by the sample means are listed in Table 4.6.

---

[13] In principle, for a given supercell size, η should be sample specific, because the level spacings are different in different MD samples. However, we find that for a few samples of the $2 \times 2 \times 2$ supercell and of the $3 \times 3 \times 3$ supercell, the inter-band contribution decreases monotonically as η increases, due to the presence of nearly degenerate Kohn-Sham energy levels in these samples. In this case, it is not possible to find the optimal η value, and as a result we choose to use the sample mean of the inter-band contribution to avoid this difficulty.

Let us take the hole conductivity in the $2 \times 2 \times 2$ supercell as an example. We have computed it with both $\eta = 20$ and 65 meV, and the results are 0.81 and 0.26 (in units of $10^{-6}\ \Omega^{-1}\text{cm}^{-1}$), respectively. The difference of these two results is mainly due to the intra-band contribution that is inversely proportional to η. In addition, it is easy to see that the ratio of the SEM to the sample mean hardly changes with η, suggesting very similar statistical convergence for different η values.

Table 4.5: The η values determined with the optimal-η scheme. They correspond to the maxima of the respective curves in Figure 4.8. η_h and η_e are for the hole and electron conductivities, respectively.

Supercell size	η_h (meV)	η_e (meV)
$2 \times 2 \times 2$	65	53
$3 \times 3 \times 3$	36	26
$4 \times 4 \times 4$	24	14
$5 \times 5 \times 5$	18	10

Table 4.6: Same as Table 4.4 but the electrical conductivity results are computed with the respective η values as listed in Table 4.5. Both the electrical conductivities and SEMs are in units of $10^{-6}\ \Omega^{-1}\text{cm}^{-1}$.

		Hole		Electron	
Supercell size	# samples	σ_h	SEM	σ_e	SEM
$2 \times 2 \times 2$	655	0.26	0.006	0.28	0.006
$3 \times 3 \times 3$	404	0.38	0.004	0.50	0.006
$4 \times 4 \times 4$	204	0.53	0.005	0.84	0.008
$5 \times 5 \times 5$	100	0.65	0.005	1.14	0.009

In the next section we will use the electrical conductivity results in Tables 4.4 and 4.6 to discuss supercell-size convergence.

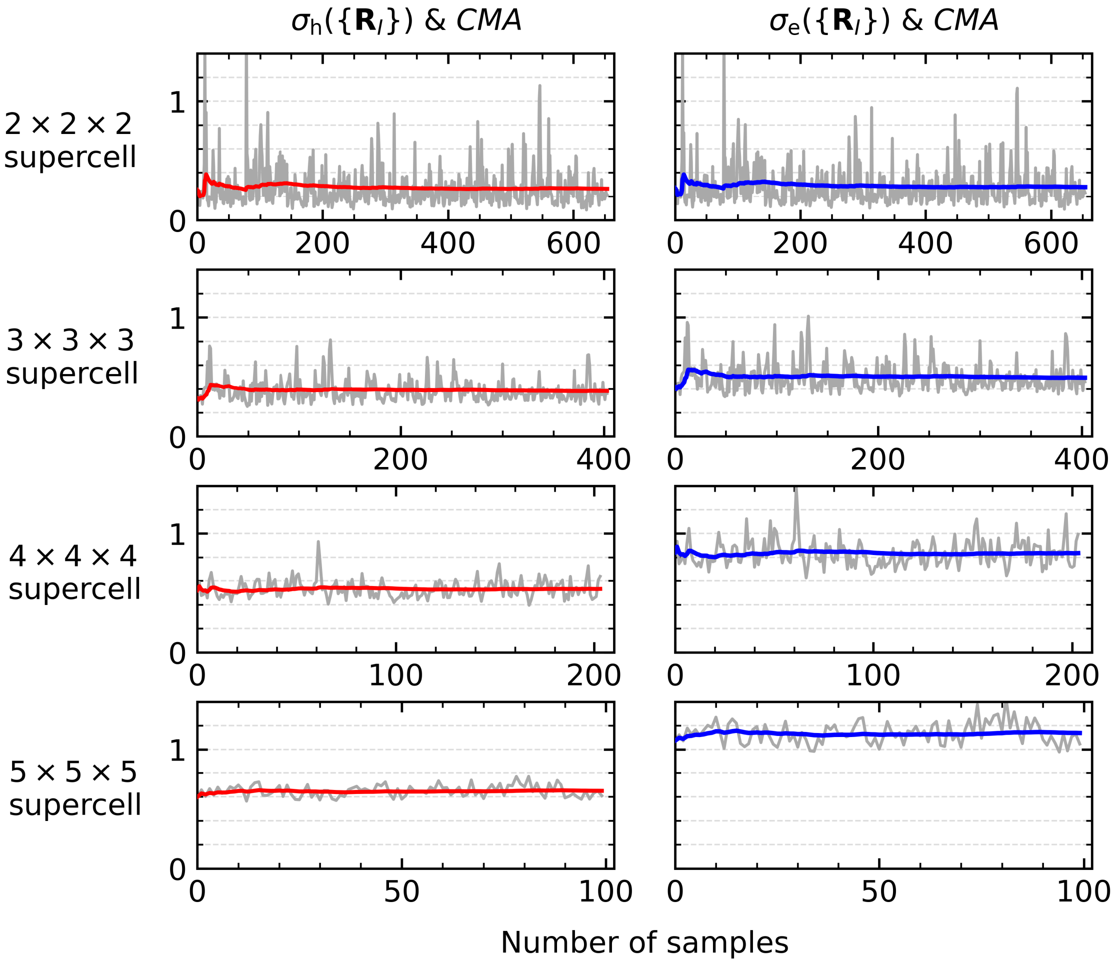

Figure 4.9: Same as Figure 4.7 but the electrical conductivity results are computed with the η values as listed in Table 4.5. The y-axes show the electrical conductivities in units of $10^{-6}\ \Omega^{-1}\mathrm{cm}^{-1}$.

4.4 Supercell-size convergence

Ab initio calculations of the electrical conductivity of crystalline solids within the KG approach in principle have to be done in the thermodynamic limit, i.e., using a sufficiently large supercell. However, for Si, the $5 \times 5 \times 5$ (1000-atom) supercell is the largest supercell we can afford and guarantee satisfactory $\mathbf{k}$-point convergence. In this section, we investigate the convergence of our electrical conductivity calculations with respect to supercell size, based on the electrical conductivity results for intrinsic Si at 300 K presented in Tables 4.4 and 4.6.

Figure 4.10 shows our calculated electrical conductivities as a function of inverse supercell length. We see that the electrical conductivities (especially those for the electrons) in the four supercells are systematically smaller than the experimental values, exhibiting significant supercell finite-size errors. The finite-size effects in our calculations (including the *ai*MD simulations) can be understood from two aspects. From the point of view of phonons, long-wavelength phonons (those with wavevectors $\mathbf{q} \to 0$) are entirely missing in our simulated supercells. Further, these supercells are too small to describe phonons with long mean free paths (MFPs). As a very harmonic system, Si at 300 K has about half of its thermal conductivity contributed from phonons with MFPs longer than one micron [104]. From the point of view of electrons, our simulated supercells cannot describe charge carriers with long MFPs. *Ab initio* BTE studies[14] [127, 199] found that the hole and electron MFPs of Si at 300 K are in the range $5-55$ and $15-110$ nm, respectively. Based on the fact that the electron MFPs are (on average) longer than hole MFPs, we can understand why for each of the supercells the electron conductivity shows larger finite-size effects compared to the hole conductivity.

The finite-size supercell calculations are inadequate for a proper description of the e-ph dynamics in Si and ultimately the electronic transport. The long MFPs of both the charge carriers and phonons in Si suggest that Si is probably the most challenging test system for the *ab initio* KG approach.

Under the two different ways of choosing η, the electrical conductivities show opposite behavior with respect to the supercell size (Figure 4.10). In the case of the common choice $\eta = 20$ meV, both the hole and electron conductivities decrease with increasing supercell size, and they are comparable at each supercell size. Experiment [193], however, shows that for intrinsic Si at 300 K, the electron conductivity is about two times larger than the hole conductivity. This implies that using such a common η is not appropriate for our simulated supercells (physically they are very small simulation cells). In contrast, in the case of the optimal-η scheme, we see that (i) both the hole and electron conductivities increase with increasing supercell size, approaching the experimental values, and (ii) although the hole and electron conductivities in the $2 \times 2 \times 2$ (64-atom)

---

[14] Often MFPs data are obtained from BTE calculations, and there is usually a large scatter in the calculated MFPs data from different calculations (one can compare Ref. [127] and [199]).

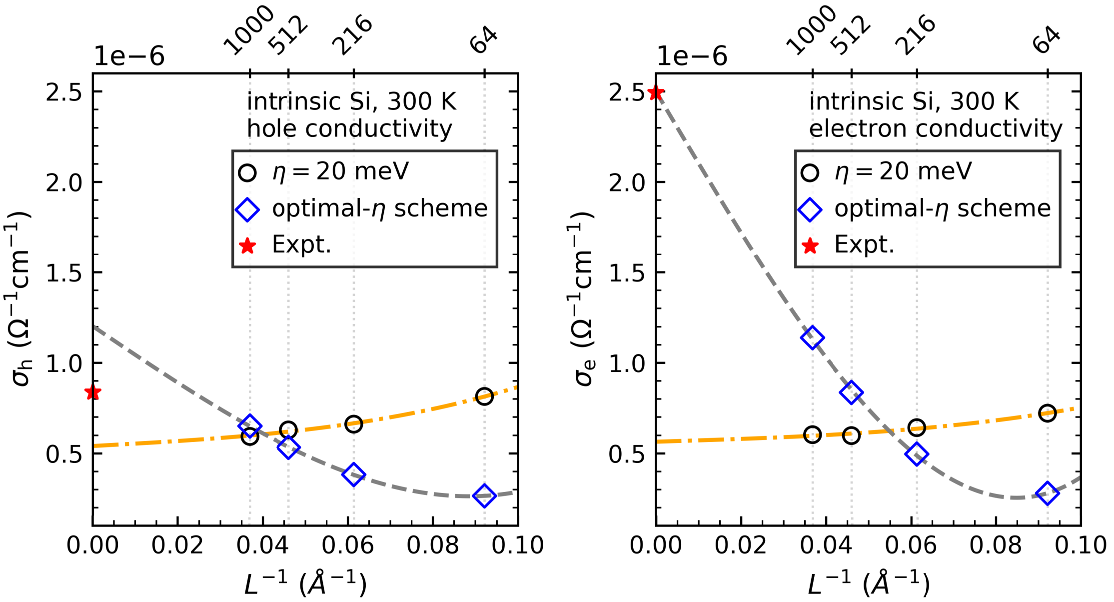

Figure 4.10: Hole conductivity (left panel) and electron conductivity (right panel) versus inverse supercell length ($1/L$), for intrinsic Si at 300 K. There are two groups of calculated results: (i) The first group of results (denoted by black circles) are obtained with broadening parameter $\eta = 20$ meV for both the holes and electrons for all four supercells; (ii) The second group of results (denoted by blue diamonds) are obtained with the η values determined with the optimal-η scheme [as listed in Table 4.5, the η values vary with the supercell size and carrier type]. The finite-size results are fitted with $\sigma(\infty) + a_1/L + a_3/L^3$ [$\sigma(\infty)$, a_1 and a_3 are free parameters], as illustrated by the gray dashed lines and orange dash-dotted lines. Experimental results are from Green [193]. Direct comparison with *ab initio* BTE calculations is not available. Compared to the scales of the axes, the statistical errors are smaller than the symbols and thus not shown. The upper x-axes indicate the number of atoms of the four supercells.

supercell are very close, the electron conductivity becomes increasingly larger than the hole conductivity as the supercell size increases, showing a correct trend.

Finite-size scaling

We have used the finite-size scaling method to deduce the electrical conductivity in the thermodynamic limit. As in first-principles studies of point defects in solids (see e.g. the work of Castleton *et al.* [178] and Lany *et al.* [200]), the finite-size scaling involves two steps. (i) First, we compute the electrical conductivities for a series of supercell sizes with the same cell shape (as we have done). For cubic system like Si, the supercells are preferably constructed to be cubic. (ii) Second, we fit the finite-size results $\sigma(L)$ (L denotes the supercell length and L^3 the volume) to a polynomial in $1/L$, usually:

$$\sigma(L) = \sigma(\infty) + \frac{a_1}{L} + \frac{a_2}{L^2} + \frac{a_3}{L^3} + \dots, \tag{4.5}$$

where a_1, a_2, $a_3, \dots$, and $\sigma(\infty)$ are free parameters to be determined; $\sigma(\infty)$ being the extrapolated electrical conductivity in the limit of an infinitely large supercell.

By testing we find that the polynomial in the form of $\sigma(\infty) + a_1/L + a_3/L^3$ gives a high-quality fit of our finite-size results, as shown in Figure 4.10. In the case of the optimal-η scheme, the extrapolated intrinsic electrical conductivities are $\sigma_\text{h} = 1.20 \times 10^{-6}\ \Omega^{-1}\text{cm}^{-1}$ and $\sigma_\text{e} = 2.51 \times 10^{-6}\ \Omega^{-1}\text{cm}^{-1}$. We compare them to the experimental data ($\sigma_\text{h} = 0.84 \times 10^{-6}\ \Omega^{-1}\text{cm}^{-1}$ and $\sigma_\text{e} = 2.49 \times 10^{-6}\ \Omega^{-1}\text{cm}^{-1}$ [193]), given that *ab initio* BTE calculations on intrinsic Si are not available. It is found that the extrapolated electron conductivity is in excellent agreement with experiment, while the extrapolated hole conductivity is about 43% above the experimental value. In this comparison, we note that there is an error cancellation in our calculations to account for an overestimation of the intrinsic carrier concentrations (see Table A.1).

For the finite-size results that are all evaluated at $\eta = 20$ meV, we find a rather large discrepancy between our extrapolated and experimental electron conductivity. This discrepancy cannot be eliminated by simply adjusting η to e.g. 5 meV, as it will lead to unreasonable results for the hole conductivity.

The pros and cons of the finite-size scaling method are briefly discussed as follows. This method can in principle provide accurate extrapolated results for the limit of an infinitely large supercell, without the need to analyze the finite-size effects in detail [200]. However, obtaining a high-quality fit (thus an accurate size extrapolation) requires that (i) the remaining errors (e.g., statistical errors) are small in the finite-size results, and (ii) sufficiently many and sufficiently large supercells are computed. The latter is a challenging task for KG calculations which require dense **k**-point sampling. For Si, we can employ the $5 \times 5 \times 5$ (1000-atom) supercell, simply because Si is a simple material and also we are able to access more than 20,000 CPU cores for a single DFT calculation[15]. When only a few supercell sizes are studied (as in our work), it will be difficult to assess the precision of the extrapolated results, due to the lack of physical insight. In Figure 4.10, it can be seen that the extrapolated electrical conductivities will change slightly if we leave out the data for the $2 \times 2 \times 2$ supercell (which is a too small simulation cell) and apply a linear extrapolation. Overcoming the shortcomings of the finite-size scaling method is beyond the scope of this thesis.

We summarize the recipe for improving supercell-size convergence of *ab initio* KG

---

[15] This is still an usual amount of computational resources for a single DFT calculation today.

calculations: (i) performing calculations for at least three (better four) supercell sizes using supercell-size-dependent η values determined with the optimal-η scheme, (ii) defining an appropriate fit function [based on Equation (4.5)], and (iii) extrapolation to the limit of an infinitely large supercell. If computational resources allow, we suggest using supercells as large as possible, because this is the physical way to reduce the uncertainties in the finite-size scaling. Obtaining physically meaningful results following the proposed recipe depends on the validity of the optimal-η scheme, which is currently still questionable. Yet, our predicted electrical conductivities for intrinsic Si at 300 K compare reasonably well with experiment.

Up to now, we have completed the *ab initio* KG calculations of the electrical conductivities in intrinsic Si at 300 K. After presenting the electrical conductivities for both *p*- and *n*-type Si at 300 K in the next section, we will comment on the main problems in our calculations.

4.5 Electrical conductivity of doped Si at 300 K

In this section we further explore the *ab initio* KG approach by applying it to calculate the electrical conductivity of both p- and n-doped Si at 300 K.

The computational details of the evaluation of Equation (3.45) in this section are as follows. First of all, we simulate free-carrier doping using the rigid-band approximation (introduced in Section 3.4.2). That is, in the postprocessing step of the KG calculation, the Fermi level is set such that the net carrier density $n_\mathrm{h} - n_\mathrm{e}$ (or $n_\mathrm{e} - n_\mathrm{h}$) equals the desired doping level. This is done separately for each of the 655, 404, 204, and 100 samples of the $2 \times 2 \times 2$, $3 \times 3 \times 3$, $4 \times 4 \times 4$, and $5 \times 5 \times 5$ supercells, respectively. For the sake of a convenient comparison, we consider several experimental doping levels at 300 K (see Ref. [201] with boron for p-type doping and phosphorous for n-type doping): (i) p-type doping with 1.325×10^{14}, 4.670×10^{15}, 5.646×10^{16}, 2.744×10^{17}, and 4.06×10^{18} cm^{-3}; (ii) n-type doping with 4.769×10^{14}, 4.739×10^{15}, 3.261×10^{16}, 9.137×10^{16}, and 4.921×10^{17} cm^{-3}. By simulating doping using the rigid-band approximation, impurity scattering is entirely absent. In addition, this approximation leads to the same carrier concentration for all the samples. This is different from the case of intrinsic Si, where the carrier concentration varies from one sample to another (as a result of band-gap fluctuation). As before, the **k**-point samplings used are listed in Table 4.2. The LDA band gaps are corrected with a scissor operator of 0.667 eV. In fact, here we do not need to consider the band-gap problem (explained in Section 4.2.4). The η values are determined with the optimal-η scheme and given in Table A.2, and they are very close to those in Table 4.5. The electrical conductivities in the limit of an infinitely large supercell are obtained from finite-size scaling. As in the case of intrinsic Si, we fit the finite-size results with $\sigma(\infty) + a_1/L + a_3/L^3$, which is found to yield high-quality fits (as exemplified in Figure A.4).

Of particular importance is to assess the overall convergence of our calculations. Since Si is a very harmonic system where the *ab initio* BTE approach works well, this can be done by comparing our calculations with the *ab initio* BTE calculations[16] by Ma *et al.* [127] and Poncé *et al.* [157]. For this, we introduce the relevant computational details of these two BTE studies, but focus only on their calculations at the LDA level and without SOC (as in our calculations). In these two BTE studies, the DFPT calculations of phonons and e-ph matrix elements were based on the crystalline unit cell[17] using a $6 \times 6 \times 6$ **q**-mesh. A noteworthy difference is that Ma *et al.* solved the BTE using an iterative method, while Poncé *et al.* solved the BTE in the relaxation-time approx-

---

[16] There are also two earlier BTE studies for n-doped Si: Li [124] and Fiorentini *et al.* [125].

[17] Ma *et al.* and Poncé *et al.* used the LDA and experimental lattice constants, respectively. Poncé *et al.* compared the carrier mobilities (LDA results without SOC) for both LDA-relaxed and experimental structures, and found close results. For the data of Poncé *et al.*, we refer to those for the experimental structure, since we consider thermal lattice expansion.

imation (RTA)[18]. The former does not assume the RTA, and is therefore, in principle, more accurate than the latter (we do not assume the RTA in our calculations). These two BTE studies reported phonon-limited hole and electron mobilities, by simulating weakly doped Si using the rigid-band approximation. We transform their mobility data to electrical conductivities using the relation $\sigma = ep\mu_\mathrm{h}$ for p-doping and $\sigma = en\mu_\mathrm{e}$ for n-doping (where e, p, n, μ_h, and μ_e denote the elementary charge, hole concentration, electron concentration, hole mobility, and electron mobility, respectively).

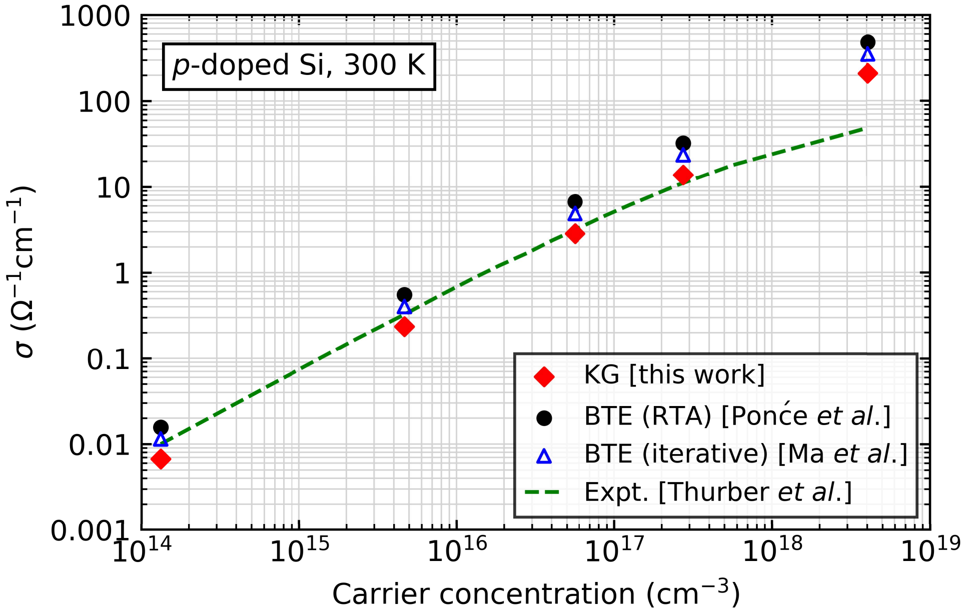

Figure 4.11: Electrical conductivity as a function of carrier concentration for p-doped Si at 300 K. The BTE-iterative results and BTE-RTA results are derived from the hole mobilities reported by Ma *et al*. [127] and Poncé *et al*. [157], respectively. All the numerical results are at the LDA level of theory and without considering SOC. The LDA band-gap problem is not important here, due to the use of the rigid-band approximation for simulating free-carrier doping. The experimental data are from Thurber *et al*. [201]. Note that both the x and y axes are on a logarithmic scale.

Figure 4.11 compares our results for the electrical conductivity of p-doped Si at 300 K with the literature data. At the carrier concentration of 1.325×10^{14} cm^{-3} (low-doping regime), where the electronic transport is mainly limited by e-ph scattering, our result is 33% smaller than the experimental data [201] (we recall that we overestimate the hole

---

[18] Both studies reported BTE-iterative and BTE-RTA results, but only a few of these results are at the LDA level without SOC.

conductivity of intrinsic Si, due to overestimation of the intrinsic carrier concentrations. This overestimation does not exist here). Given that only e-ph scattering is accounted for in our electrical conductivity calculations, our results should be larger than the experimental data (which gradually become saturated with increasing doping level as a result of increased impurity scattering). Therefore, the seemingly good agreement between our calculations and experiment at the moderate doping level of $\sim 10^{17}$ cm^{-3} just reflects the absence of impurity scattering in our calculations.

For Si at 300 K, our KG calculations should give results nearly identical to those of the iterative solution of the BTE by Ma *et al.* [127] (as introduced above), given that (i) Si at 300 K is a very harmonic system and (ii) both calculations are performed at the same level of theory (i.e., LDA without SOC) and treat doping using the rigid-band approximation. This, however, is not the case, as can be seen in Figure 4.11. Our results are noticeably smaller than the BTE-iterative results of Ma *et al.* At the carrier concentration of 1.325×10^{14} cm^{-3}, the BTE-iterative result of Ma *et al.* is in excellent agreement with experiment.

Similar conclusions can be drawn for the *n*-doped case (Figure 4.12). We see that at the carrier concentration of 4.769×10^{14} cm^{-3} (low-doping regime), our result is noticeably smaller (about 50%) than both the experimental and the BTE results.

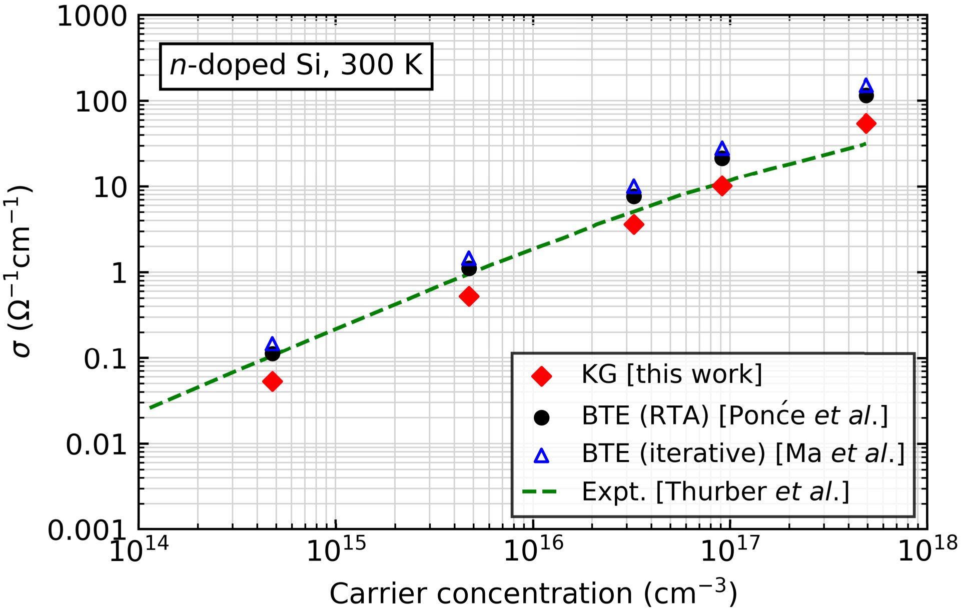

Figure 4.12: Electrical conductivity as a function of carrier concentration for *n*-doped Si at 300 K. The BTE-iterative results and BTE-RTA results are deduced from the electron mobilities reported by Ma *et al.* [127] and Poncé *et al.* [157], respectively. Other description of the data can be found in Figure 4.11.

The large discrepancy between our results and the results of *ab initio* BTE calculations suggests that our KG calculations for Si fall short of convergence. This can be mainly attributed to the η problem and the issue of supercell-size convergence in our calculations. First, the necessary introduction of an η parameter in the evaluation of the KG formula introduces a significant uncertainty in our determination of the electrical conductivity for each of the supercells and ultimately for the limit of an infinitely large supercell (via finite-size scaling). Second, the supercell-size convergence is very challenging, since in Si both the charge carriers and phonons have long MFPs. From a computational standpoint, the limited size of the simulation supercells has hindered us so far from obtaining many insights into these two issues. While there are other sources of error, including the errors associated with the "light" basis set of Si and with the number of MD samples, we believe that they are much less significant compared to the η problem and the issue of supercell-size convergence, in view of the convergence tests for basis set and number of MD samples in the previous sections. The rigid-band approximation and the band-gap problem should in principle not contribute to the observed discrepancy. This is because both our calculations and the BTE calculations describe doping within the rigid-band approximation, and in this situation the band-gap problem requires no particular attention. However, we note that the BTE calculations involve only a single unit cell, but our calculations for each supercell involve a number of atomic configurations.

4.6 Summary

In this chapter we explored, improved, and assessed the *ab initio* KG approach to compute the electrical conductivity of Si at 300 K.

We have performed a detailed convergence study of our electrical conductivity calculations in the $N \times N \times N$ ($N = 2,\ 3,\ 4,$ and 5) cubic supercells of intrinsic Si at 300 K, and have defined strategies to address the identified numerical problems. These resulted in the following findings and understanding:

(1) The convergence with respect to **k**-point sampling is challenging, because the carriers are confined in a narrow energy range near the band extrema. To achieve good **k**-point convergence, it is necessary to use $n \times n \times n$ **k**-mesh with $n \times L$ (L is the supercell length) larger than 200 Å. The convergence of **k**-point sampling is insensitive to the broadening parameter (η). The dense **k**-mesh required makes the supercell-based KG calculation very demanding.

(2) When computing the intrinsic electrical conductivities, the severe underestimation of the band gaps by DFT-LDA cause errors of several orders of magnitude. This problem can be largely solved by using a “scissor operator" approach, considering that it is currently computationally infeasible to perform hybrid-functional theory or *GW* calculations. In the case of a moderate/high free-carrier doping simulated using the rigid-band approximation, the band-gap problem requires no particular attention if one includes in the result only the electrical conductivity of the majority carriers.

(3) Compared to the “tight" basis set, the “light" basis set can deliver reliable electrical conductivity calculations at a reduced computational cost.

(4) The convergence with respect to number of *ai*MD samples is not a big problem, but it is computationally expensive for large supercells. This statistical convergence should be carefully ensured for all the supercells simulated, in order not to affect the subsequent finite-size scaling.

(5) The finite-size supercell calculations pose two severe problems. One is the necessary introduction of a broadening parameter (η), due to the discrete Kohn-Sham energy levels. The electrical conductivity results depend strongly on η, and this introduces a significant uncertainty in our quantitative determination of the electrical conductivity in each of the supercells. We have discussed an optimal-η scheme to determine η: compute the inter-band contribution to the electrical conductivity as a function of η, and take the η value at which the inter-band contribution is a maximum. The chosen η value reflects the Kohn-Sham level spacings of the supercell. We recognize that the validity of the optimal-η scheme is currently uncertain. The supercell-size convergence is not achieved even for the $5 \times 5 \times 5$ (1000-atom) supercell. This second problem is understood by the fact that the MFPs of both the charge carriers and phonons in Si at 300 K well exceed the size of our simulated supercells. We have used the finite-size scaling method with a polynomial function $\sigma(\infty) + a_1/L + a_3/L^3$ to deduce the electrical conductivities in the limit of an infinitely large supercell.

With these efforts, we have computed the electrical conductivities of both intrinsic and doped Si at 300 K. It is found that at the LDA level of theory the calculated electrical conductivities are in reasonable agreement (to within about 50%) with experimental data. However, our results do not agree well with previous *ab initio* BTE calculations at the same level of theory, suggesting that our strategies for dealing with the η problem and the issue of supercell-size convergence need to be improved.

In future developments of the *ab initio* KG approach, if Si is considered as a test system, we suggest focusing on Si at room temperature in the low-doping regime, in which case the uncertainties in the electrical conductivity results due to the band-gap problem, the neglect of impurity scattering, and the rigid-band approximation are small. While the DFT eigenvalues and eigenfunctions are approximate quantities, we do not suggest investigating the effect of different DFT xc functionals on the KG calculations for Si before the η problem and the issue of supercell-size convergence are convincingly solved. Indeed, previous *ab initio* BTE studies [124, 125, 127, 157] have shown that the LDA functional is good enough to describe the electronic transport in Si.

5 Electrical conductivity of anharmonic crystal SnSe

Ab initio KG calculations of the electrical conductivity naturally account for lattice anharmonicity and is therefore a promising approach for studying anharmonic materials. An interesting question is whether the numerical problems identified in our calculations for the very harmonic crystal Si are less severe for anharmonic crystals in which phonons typically have short MFPs [202]. In this chapter, we apply the *ab initio* KG approach to study the electrical conductivity of SnSe, a strongly anharmonic crystal with high thermoelectric performance. We present a detailed convergence study on the **k**-point sampling, broadening parameter, number of samples, and supercell size. Then, we compute the electrical conductivities at 300 K and at 523 K, and assess our results by comparing them with experiment and previous *ab initio* BTE calculations.

5.1 Introduction

Tin selenide (SnSe) is a layered semiconductor [depicted in Figure 5.1(a)] in which individual atomic layers are held together by van der Waals (vdW) interactions. The crystal has the orthorhombic space group *Pnma* below about 800 K [203, 204]. SnSe features highly anisotropic bonding: (i) Within a two-atom-thick atomic layer that is perpendicular to the crystallographic a-axis, each Sn atom is covalently bonded to three neighboring Se atoms forming a puckered structure; (ii) The three bonds, of which one is slightly shorter than the other two, take up the $5p^2$ valence electrons of Sn, leaving the lone-pair $5s^2$ valence electrons of Sn^{2+} (nominal valence) oriented towards the adjacent layers [205]. The crystal lattice of SnSe is very "soft", as evidenced by its low Debye temperatures of 154 K and 345 K [206]. As a consequence of the anisotropic bonding, the electronic band structure of SnSe exhibits strong anisotropy along different directions of the Brillouin zone [see Figure 5.1(b)]. Both the valence- and conduction-band edges are characterized by highly dispersive valleys, while the highest valence band along the Γ-X line is rather flat (or localized) and deep in energy. The band gap of SnSe is indirect, with the valence-band maximum (VBM) located on the Γ-Z line and the conduction-band minimum (CBM) on the Γ-Y line. Due to the low symmetry of the crystal structure, the degree of band degeneracy around both the VBM and CBM is rather low [207]. Both the upper valence bands and lower conduction bands are mainly composed of the Sn $5p$ orbitals and the Se $4p$ orbitals [see Figure 5.1(b)].

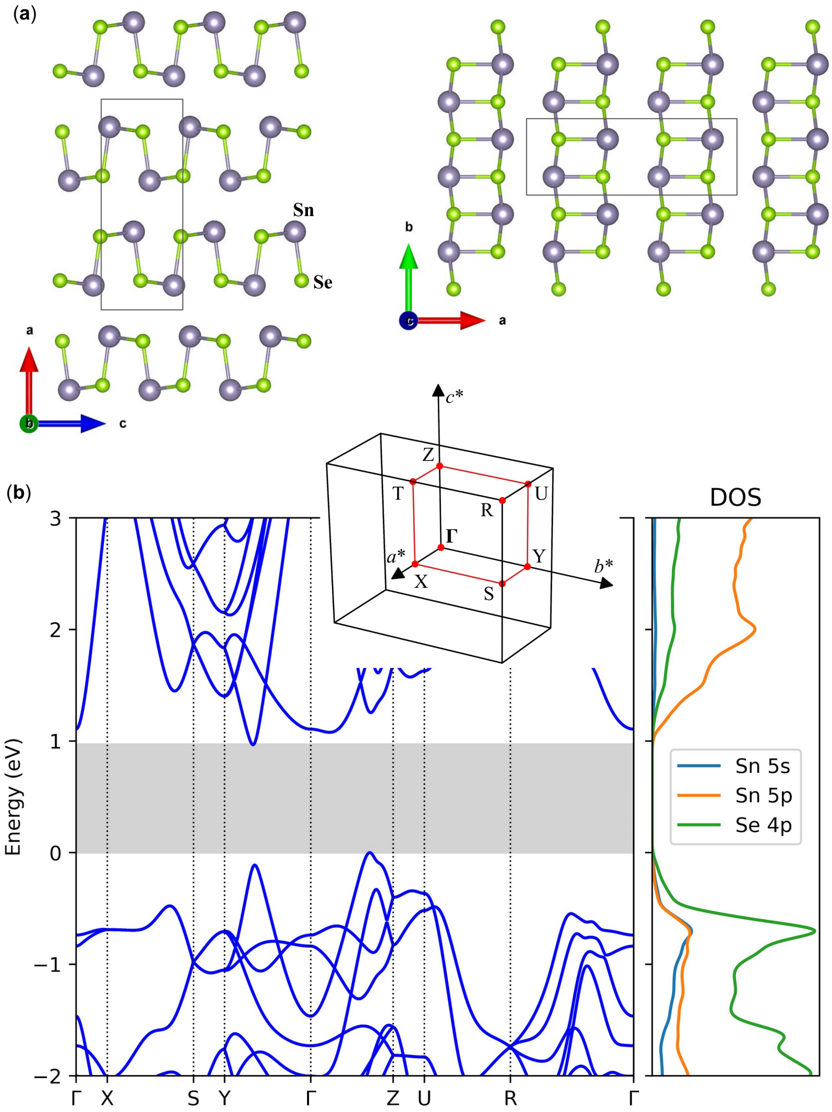

Figure 5.1: Crystal structure and electronic band structure of SnSe in the orthorhombic phase. (a) Perspective views of the atomic structure along the crystallographic b and c axes, respectively. The black border indicates the crystalline unit cell consisting of eight atoms, with the room-temperature lattice constants $a = 11.502$ Å, $b = 4.153$ Å, and $c = 4.445$ Å [203]. This subplot is created using the VESTA program [208]. (b) Band structure and (partial) density of states (DOS) calculated using the GGA PBEsol functional. The PBEsol band gap has been enlarged to match the experimental band gap (about 0.9 eV at room temperature [209]) as illustrated by the shaded area. The inset depicts the Brillouin zone with high-symmetry points and lines.

In the search for high-efficiency, environmentally friendly thermoelectric materials, SnSe has recently gained significant attention, since Zhao *et al.* [210, 179] reported remarkably large figure-of-merit values in both the as-grown *p*-type and Na-doped *p*-type single-crystal SnSe samples. The outstanding thermoelectric performance of SnSe has been attributed to a combination of the extraordinary heat and charge transport properties of this material [211, 210, 179]. (i) First, SnSe has an ultra-low intrinsic lattice thermal conductivity, due to strong lattice anharmonicity associated with the very "soft" (puckered and layered) crystal structure. The mean free paths (MFPs) of major heat-carrying phonon modes in SnSe are found to be very short and comparable to the unit-cell lattice parameters [18, 212]. (ii) Second, SnSe can be heavily doped *p*-type with hole concentrations up to the order of 10^{20} cm^{-3}. (iii) Third, SnSe shows a large enhancement of the thermoelectric transport at high hole doping levels where the Fermi level enters into the energetically close-lying valence-band valleys [see Figure 5.1(b)]. SnSe exemplifies that puckered layered crystal structure is an important material feature for the discovery of novel thermoelectric materials.

Figure 5.2 summarizes some of the reported electrical conductivity results of SnSe in the literature. As can be seen, the experimental data [210, 211] are highly anisotropic; that is, the electrical conductivity along the *a* axis (corresponding to the interlayer hole transport) is much smaller than those along the *b* and *c* axes (corresponding to the in-plane hole transport). In addition, the electrical conductivities fall with increasing temperature (up to 550 K). These observations have been quantitatively reproduced by the *ab initio* BTE calculations of Caruso *et al.* [24], achieved by accounting simultaneously for (i) the thermal lattice expansion (experimental crystal structure at each temperature was used to compute the electronic band structure) and (ii) the temperature-dependent renormalization of hole relaxation times [temperature effects were accounted for via the Fermi-Dirac and Bose-Einstein occupation factors; see Equation (3.7)]. However, in the work of Caruso *et al.*, the e-ph calculations were based on the harmonic phonons for the DFT-relaxed crystal structure at 0 K. Future *ab initio* BTE calculations on SnSe will be required to include (i) more anharmonic effects (e.g., the thermal shift of phonon frequencies) and (ii) higher-order e-ph coupling effects (e.g., the temperature-dependent renormalization of the electron eigenvalues, which was found to be pronounced in SnSe [24]). This remains a very challenging task mainly because of the computational complexity associated with the e-ph calculations [31]. This difficulty is solved automatically by the *ab initio* KG approach, which, through *ai*MD, naturally accounts for all anharmonic effects and does not require a perturbative treatment of the coupling between electrons and lattice vibrations.

This chapter is mainly devoted to assessing whether the *ab initio* KG approach can provide reliable results for the electrical conductivity of SnSe. We will focus on *p*-doped SnSe, and our results will be analyzed in terms of the unusual crystal structure, electronic band structure, and anharmonic lattice dynamics of SnSe as reviewed above.

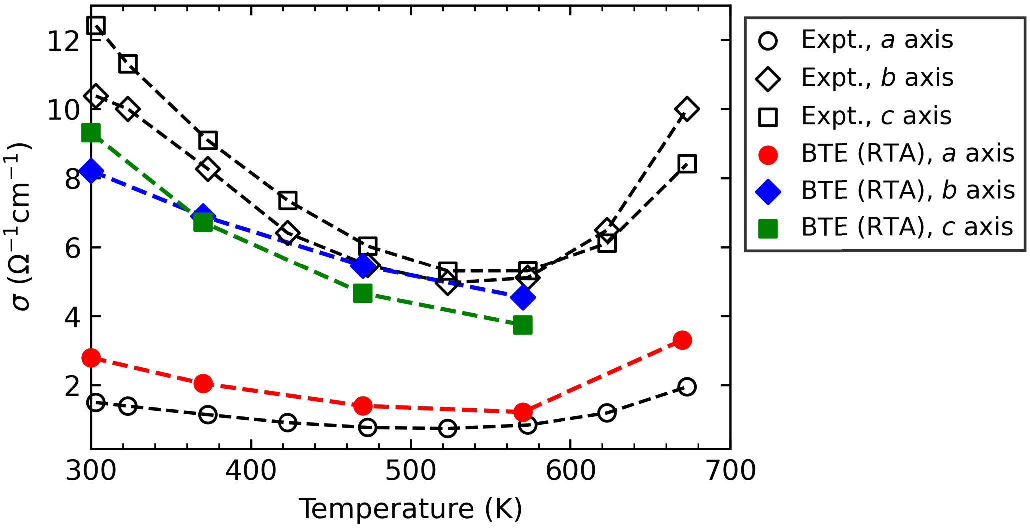

Figure 5.2: Literature results for the electrical conductivity of p-doped SnSe as a function of temperature. The experimental data are adapted from the work of Zhao *et al.* [210, 211], and are for single-crystal SnSe samples (which are p-doped as grown) along the crystallographic axes a, b, and c. The numerical results are adapted from the work of Caruso *et al.* [24], who performed *ab initio* BTE calculations in the relaxation-time approximation (RTA). In this BTE study, the authors used a constant hole concentration of 4.5×10^{17} cm^{-3} for different temperatures. The dashed lines are a guide to the eye.

5.2 Computational details

General settings. All DFT calculations in this chapter were done with the FHI-aims code using the "light" basis sets of Sn and Se and the PBEsol functional [63]. The PBEsol functional lacks long-range vdW interactions [213]; this was not corrected in the present study, as in previous *ab initio* BTE studies (e.g., Ref. [21, 24]). The SCF convergence criteria for the density, sum of eigenvalues, and total energy were set to 10^{-6} eV/Å^3, 10^{-4} eV, and 10^{-6} eV, respectively. These basic settings were kept in all following calculations, except a few small changes for the *ai*MD simulations.

Equilibrium lattice constants. In structural-relaxation calculations for determining the equilibrium geometry of SnSe, atomic forces were minimized to below 10^{-4} eV/Å. The thermal lattice expansion at 300 K was described using the quasi-NPT method (introduced in Section A.2.3). Previous studies found that SnSe exhibits negative thermal expansion along the c axis [203, 214, 215]. This behavior cannot be reproduced by the quasi-NPT method, so we determined the lattice constants of SnSe at 523 K by extrapolating the calculated lattice constants at 300 K to 523 K, using the experimental thermal expansion coefficients [215]. Our calculated lattice constants are listed in Table 5.1. The DFT-GGA study of the phase transition of SnSe by Dewandre *et al.* [204] showed that including the long-range vdW corrections does not affect the interlayer significantly. As mentioned before, Caruso *et al.* [24] considered thermal lattice expansion by employing at each temperature the experimental crystal structure.

Table 5.1: Calculated lattice constants of SnSe. The lattice constants at 0, 300, and 523 K are determined by direct structural relaxation, the quasi-NPT method, and extrapolation, respectively. Note that the lattice constant along the crystallographic a axis is much longer than those along the b and c axes. In parentheses we list the previous PBEsol data at 0 K [207], and the experimental data at 300 K and 523 K [203].

T (K)	a_0 (Å)	b_0 (Å)	c_0 (Å)
0	11.568 (11.396)	4.183 (4.147)	4.377 (4.369)
300	11.635 (11.502)	4.196 (4.153)	4.404 (4.450)
523	11.706 (11.571)	4.222 (4.190)	4.379 (4.429)

AiMD simulations. Supercells with different sizes were constructed and grouped into two subsets: $N \times 4 \times 4$ ($N = 1$, 2, and 3) and $2 \times N \times N$ ($N = 2$, 3, 4, and 5). *Ai*MD simulations were performed (separately) in these supercells in the NVT ensemble using a time step of 4 fs and a Langevin thermostat at 300 K. The $\mathbf{k}$-meshes used are listed in Table 5.2. In the MD simulations, only the density convergence was checked, and this criterion was reduced to 5×10^{-6} eV/Å^3 for the $3 \times 4 \times 4$ and $2 \times 5 \times 5$ supercells. After an initial period of $4 - 5$ ps for equilibration, atomic configurations were sampled every 50 time steps until a sufficiently large number of samples were created (see discussion in Section 5.3.2). The MD simulations were also performed at 523 K. The FHI-vibes code [185] was used for the MD simulations.

KG calculations. For each MD sample, a two-step KG calculation was performed. (i) First, a static DFT calculation using dense $\mathbf{k}$-mesh (see Section 5.3.1) was carried out to evaluate the Kohn-Sham eigenvalues $\epsilon_{n\mathbf{k}}$ and momentum-matrix elements $\langle m\mathbf{k}|\mathbf{p}|n\mathbf{k}\rangle$. (ii) Second, with the DFT material parameters, the electrical conductivity of this sample was computed using Equation (3.45) as implemented in our FHI-kubo code. More computational details can be found in later sections.

It is important to note that the electrical conductivity of SnSe is anisotropic. The x, y, and z components of the electrical conductivity can be evaluated by including in the KG calculation only the momentum-matrix elements in the x, y, and z directions, respectively. From now on we use σ_x, σ_y, and σ_z to denote the electrical conductivity in the x, y, and z directions, respectively (corresponding to the orthorhombic crystallographic *a*, *b*, and *c* axes). In this work, we focus on the x and z components of the electrical conductivity of p-doped SnSe.

Table 5.2: Two groups of supercells used in our electrical conductivity calculations for p-doped SnSe at 300 K. The listed details include supercell sizes, number of atoms, and **k**-meshes used in the *ai*MD simulations.

Supercell size	# atoms	**k**-mesh (for MD)
Group-I (for σ_x)		
$1 \times 4 \times 4$	128	$2 \times 2 \times 2$
$2 \times 4 \times 4$	256	$2 \times 2 \times 2$
$3 \times 4 \times 4$	384	$1 \times 2 \times 2$
Group-II (for σ_z)		
$2 \times 2 \times 2$	64	$2 \times 4 \times 4$
$2 \times 3 \times 3$	144	$2 \times 2 \times 2$
$2 \times 4 \times 4$	256	$2 \times 2 \times 2$
$2 \times 5 \times 5$	400	$2 \times 2 \times 2$

Comments on supercell size

As discussed in the last chapter on Si, the electrical conductivity in the limit of an infinitely large supercell can be obtained via finite-size scaling. Usually, we prefer using a series of supercells in the shape of $N \times N \times N$ with $N = 2,\ 3,\ 4,$ and 5. However, because the component elements of SnSe are not light, the supercell size quickly becomes computationally intractable. The KG calculation in the $4 \times 4 \times 4$ (512-atom) supercell is not allowed by our computational resources, unless an underconverged **k**-mesh is used for this supercell. This poses an additional difficulty for studying the anisotropic electrical conductivity of SnSe, and we have to choose appropriate supercell sizes. When computing the σ_x, the supercells must be large enough in both the y and z directions. Our computation of the σ_x is based on the $N \times 4 \times 4$ supercells, which are reasonably large in both the y and z directions, and moreover, our computational resources allow for $N = 1,\ 2,$ and 3. This will provide three data points for finite-size scaling. Similarly, our computation of the σ_z uses the $2 \times N \times N$ ($N = 2,\ 3,\ 4,$ and 5) supercells, which contain four SnSe atomic layers in the x direction. These explain why the $N \times 4 \times 4$ ($N = 1,\ 2,$ and 3) supercells and the $2 \times N \times N$ ($N = 2,\ 3,\ 4,$ and 5) supercells are used in our electrical calculations. Note that the $2 \times 4 \times 4$ supercell is employed for computing both the σ_x and σ_z.

5.3 Convergence of the electrical conductivity in *p*-doped SnSe at 300 K

In this section, by focusing on the x and z components of the anisotropic electrical conductivity of SnSe at 300 K, we present a convergence study with respect to the **k**-point sampling, broadening parameter (η), number of samples, and supercell size. Experimentally it was found that the single-crystal SnSe sample grown at 300 K is intrinsically p-type with a hole doping level of 3×10^{17} cm^{-3} [210, 211]. We simulate this hole doping using the rigid-band approximation (see Section 3.4.2), i.e., the Fermi level (of each MD sample) is set under the condition $n_\text{h} - n_\text{e} = 3 \times 10^{17}$ cm^{-3}. The PBEsol band gaps are corrected with a scissor shift of 0.659 eV, which is the difference between the PBEsol band gap (0.311 eV) and experimental band gap at 0 K (0.97 eV [209]).

5.3.1 k-point convergence

We begin by examining the convergence with respect to **k**-point sampling. For this, we take a sample of the $2 \times 2 \times 2$ supercell as an example, and perform KG calculations in this supercell using two different (Γ-centered) **k**-point samplings: $n \times 30 \times 30$ (i.e., **k**-mesh with varying size in the k_x direction) and $10 \times 30 \times n$ (i.e., **k**-mesh with varying size in the k_z direction). In addition, we consider two different η values, 20 and 30 meV, to show the influence of η on the **k**-point convergence.

Let us consider first the electrical conductivity in the x direction (i.e., σ_x). For the σ_x calculated at $\eta = 30$ meV, we see in Figure 5.3 that good **k**-point convergence[1] can be obtained using a **k**-mesh with the size of 8 and 25 in the k_x and k_z directions, respectively. This result should not be interpreted as that the σ_x converges much faster with respect to the **k**-point sampling in the k_x direction than in the k_z direction, because the cell length in the x direction is about 2.6 times longer than that in the z direction. It is interesting to note that although the σ_x is related to the momentum-matrix elements in the x direction, its convergence depends also critically on the sampling in the k_z direction. This is because the VBM of SnSe is on the Γ-Z line of the Brillouin zone[2] (see Figure 5.1), so the **k**-point sampling in the k_z direction plays a key role in determining the Fermi-level position (according to the condition mentioned above). In Figure 5.3, we further find that the **k**-point convergence hardly changes when η is decreased to 20 meV. But, the **k**-point converged σ_x are drastically different for $\eta = 20$ meV and $\eta = 30$ meV, suggesting that it is crucial to choose an appropriate value of η. We come back to this issue in the next subsection.

Consider then the electrical conductivity in the z direction (i.e., σ_z). In Figure 5.4, we see that the σ_z converges very quickly as a function of the sampling in the k_x direction.

---

[1] This has been further confirmed with a $16 \times 40 \times 40$ **k** mesh.

[2] The qualitative analysis is based on the electronic band structure of the equilibrium geometry of SnSe.

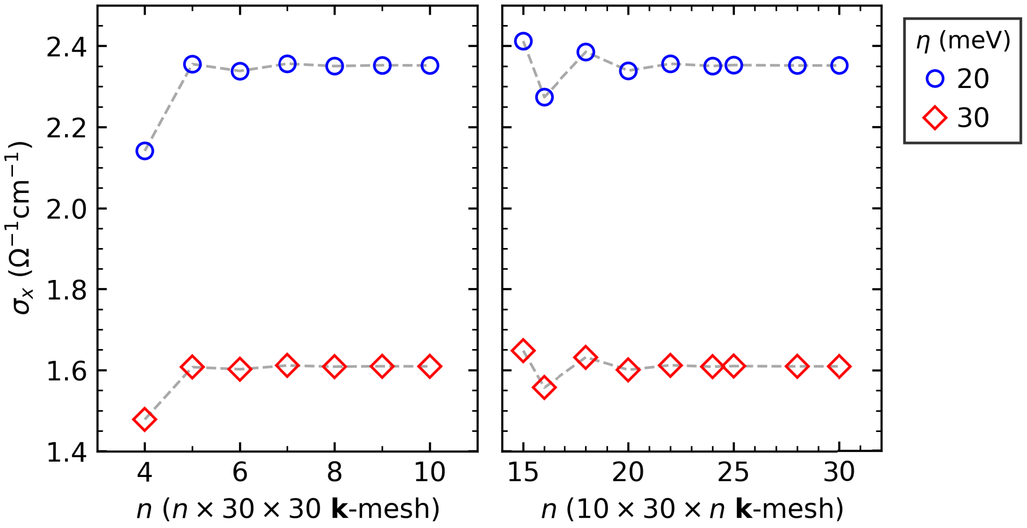

Figure 5.3: The x-component electrical conductivity (σ_x) in the $2 \times 2 \times 2$ supercell as a function of n for a $n \times 30 \times 30$ **k**-point sampling (left panel) and for a $10 \times 30 \times n$ **k**-point sampling (right panel), with two different choices of the broadening parameter ($\eta = 20$ and 30 meV). The results are for p-doped SnSe at 300 K. The gray dashed lines are a guide to the eye.

This is understood by the fact that the valence bands along the k_x direction are deep in energy and therefore play a negligible role in determining the σ_z. By contrast, the σ_z converges much more slowly with respect to the sampling in the k_z direction, and good **k**-point convergence can be obtained using a **k**-mesh with the size of 25 in this direction. This is expected, since the highest valence band along the Γ-Z line, on which the VBM is located, is highly dispersive (see Figure 5.1).

In addition, the **k**-point convergence of both the σ_x and σ_z with respect to the sampling in the k_y direction is faster than in the k_z direction (as shown in the Appendix, Figure A.5). This is understood from that the VBM in the k_y direction is lower (about 50 meV) than the global VBM (see Figure 5.1).

The above discussion suggests that when analyzing the **k**-point convergence of the electrical conductivity of an anisotropic material, one should keep in mind the material's electronic band-structure features, including: (i) the energy positions and dispersion of the band edges along each reciprocal-space direction; (ii) the **k** locations of the VBM and CBM. This is especially so for materials having a indirect band gap and highly dispersive band edges, e.g., the currently studied SnSe.

In our later calculations, we will use a $10 \times 30 \times 30$ **k**-mesh to compute the electrical conductivities in the $2 \times 2 \times 2$ supercell. This **k**-point sampling is equivalent to the $20 \times 60 \times 60$ **k**-mesh used in the BTE calculations for the SnSe unit cell (i.e., the $1 \times 1 \times 1$ cell)

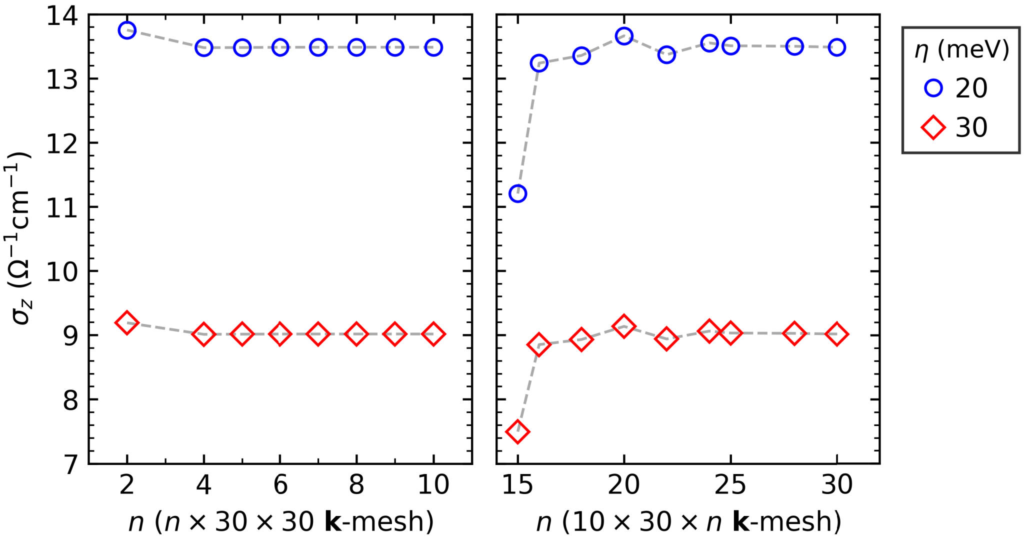

Figure 5.4: The z-component electrical conductivity (σ_z) in the $2 \times 2 \times 2$ supercell as a function of n for a $n \times 30 \times 30$ **k**-point sampling (left panel) and for a $10 \times 30 \times n$ **k**-point sampling (right panel), with two different choices of the broadening parameter ($\eta = 20$ and 30 meV). The results are for p-doped SnSe at 300 K. The gray dashed lines are a guide to the eye.

Table 5.3: Chosen **k**-meshes for performing KG calculations in the SnSe supercells.

Supercell size	**k**-mesh
Group-I (for σ_x)	
$1 \times 4 \times 4$	$20 \times 15 \times 15$
$2 \times 4 \times 4$	$10 \times 15 \times 15$
$3 \times 4 \times 4$	$7 \times 15 \times 15$
Group-II (for σ_z)	
$2 \times 2 \times 2$	$10 \times 30 \times 30$
$2 \times 3 \times 3$	$10 \times 20 \times 20$
$2 \times 4 \times 4$	$10 \times 15 \times 15$
$2 \times 5 \times 5$	$10 \times 12 \times 12$

by Caruso *et al.* [24], and can be conveniently scaled with the size of our other simulated supercells, as shown in Table 5.3. For instance, the scaling leads to the $3 \times 4 \times 4$ supercell with a $7 \times 15 \times 15$ **k**-mesh, $2 \times 5 \times 5$ supercell with a $10 \times 12 \times 12$ **k**-mesh, or even $4 \times 4 \times 4$ supercell with a $5 \times 15 \times 15$ **k**-mesh. For the $3 \times 4 \times 4$ supercell with a $7 \times 15 \times 15$ **k**-mesh and the $2 \times 5 \times 5$ supercell with a $10 \times 12 \times 12$ **k**-mesh, the calculations are very demanding. And, as mentioned earlier, the $4 \times 4 \times 4$ supercell with a $5 \times 15 \times 15$ **k**-mesh is beyond our computational capabilities (a memory problem). For this supercell, the largest **k**-mesh size we can afford is $5 \times 6 \times 6$, which is insufficient. This is why the $4 \times 4 \times 4$ supercell is not studied. Our chosen **k**-meshes can guarantee a good **k**-point convergence of the electrical conductivities in the respective supercells. In addition, there is no need to worry about the influence of η on the **k**-point convergence (an additional test is given in the Appendix, Section A.3.2).

5.3.2 Broadening parameter and number of MD samples

In this subsection, we discuss the choice of η which is a crucial numerical parameter in the evaluation of Equation (3.45). For ease of discussion, we also examine the convergence with respect to the number of MD samples. Through the *ai*MD simulations at 300 K, we have generated (i) 160, 125, 75 samples for the $N \times 4 \times 4$ supercell with $N = 1$, 2, and 3, respectively, and (ii) 250, 200, 100, and 44 samples for the $2 \times N \times N$ supercell with $N = 2$, 3, 4, and 5, respectively. Note that the $N \times 4 \times 4$ and $2 \times N \times N$ supercells are used for calculating the σ_x and σ_z of *p*-doped SnSe at 300 K, respectively. The KG calculations are performed using the **k**-meshes listed in Table 5.3.

Choice of broadening parameter

We have considered two different ways for choosing η. First, we describe how we determine the value of η with the optimal-η scheme (described in Section 4.2.3). This scheme is to use the η value that maximizes the inter-band contribution (to the electrical conductivity) for computing the (full) electrical conductivity.

Following the optimal-η scheme, we show in Figure 5.5 for each of our simulated supercells the calculated sample-averaged inter-band contribution (to the electrical conductivity) versus η. Note that the results in Figure 5.5(a) are the inter-band σ_x in the $N \times 4 \times 4$ ($N = 1$, 2, and 3) supercells, and those in Figure 5.5(b) are the inter-band σ_z in the $2 \times N \times N$ ($N = 2$, 3, 4, and 5) supercells. As can be seen, for all the supercells (except the $2 \times 2 \times 2$ supercell), the inter-band contribution versus η shows a concave behavior and exhibits a maximum when η is about 30 meV. This behavior is due to the discreteness of Kohn-Sham energy levels in the finite-size supercell calculations (see Section 4.2.3). We note that the inter-band contribution to σ_z in the $2 \times 2 \times 2$ supercell increases very slowly with η and its maximum is at very large η [not fully displayed in Figure 5.5(b)], implying that for this supercell the upper valence bands along the Γ-Z direction have rather large level spacings. This is understood by noticing that the highest valence band along the Γ-Z line is highly dispersive. In view of this, the

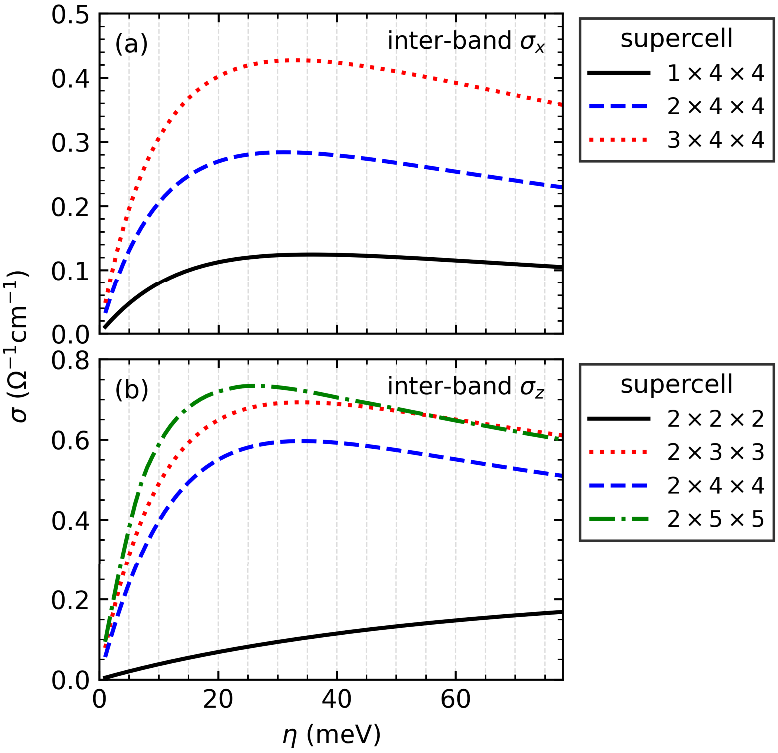

Figure 5.5: Sample-averaged inter-band contribution to the (a) σ_x and (b) σ_z as a function of broadening parameter (η), for different SnSe supercells. The inter-band σ_x are for the $N \times 4 \times 4$ ($N = 1,\ 2,$ and 3) supercells; the inter-band σ_z are for the $2 \times N \times N$ ($N = 2,\ 3,\ 4,$ and 5) supercells. Note the different scales of the y axes in the two graphs. The results are for p-doped SnSe at 300 K and calculated using the **k**-meshes listed in Table 5.3.

$2 \times 2 \times 2$ supercell is a too small simulation cell for computing the σ_z. The low degree of band degeneracy around the VBM [207] might be an additional factor that prevents the $2 \times 2 \times 2$ supercell from having small level spacings.

Table 5.4 lists the η values that correspond to the maxima of the curves in Figure 5.5. We find that for the $2 \times 4 \times 4$ supercell, the determined η values are slightly different for σ_x and σ_z, indicating the anisotropy of SnSe. Consider the $N \times 4 \times 4$ supercells (for σ_x). The η value for the $3 \times 4 \times 4$ supercell is slightly larger than that for the $2 \times 4 \times 4$ supercell, seemingly suggesting that the average level spacing of the upper valence-band levels is larger for $3 \times 4 \times 4$ supercell than for the $2 \times 4 \times 4$ supercell. This contradicts our intuition at the first sight, but can be understood from that the lattice vibrational modes allowed in these two supercells are very different (due to the different supercell size in the x direction), and so are their impact on the electron eigenvalues. From the point of view of the thermodynamic limit, neither the $2 \times 4 \times 4$ supercell nor the $3 \times 4 \times 4$ supercell can be viewed as a large simulation cell, though computationally both are large systems. Consider then the $2 \times N \times N$ supercells. On the whole, the η value is reduced when the size N is increased from 2 to 5. The η value for the $2 \times 3 \times 3$ and $2 \times 4 \times 4$ supercells are the same, in contrast to our expectation. In addition, the η value for the $2 \times 2 \times 2$ supercell is very large, which makes us question whether it is reasonable to use this supercell as a simulation cell. Yet, the $2 \times 2 \times 2$ supercell will still be included in our calculations.

Table 5.4: The η values determined with the optimal-η scheme. They correspond to the maxima of the respective curves in Figure 5.5. Two groups of supercells: *Group*-I is for computing the σ_x; *Group*-II is for computing the σ_z.

Supercell size	# samples	η (meV)
Group-I (for σ_x)		
$1 \times 4 \times 4$	160	36
$2 \times 4 \times 4$	125	31
$3 \times 4 \times 4$	75	33
Group-II (for σ_z)		
$2 \times 2 \times 2$	250	207
$2 \times 3 \times 3$	200	34
$2 \times 4 \times 4$	125	34
$2 \times 5 \times 5$	44	26

The supercell-size-dependent η values given in Table 5.4 will be used to calculate the electrical conductivities in the respective supercells. Figure 5.5 also suggests that it is sensible to take $\eta = 30$ meV as a common choice for all the supercells simulated. Thus, our second way for choosing η is to simply use $\eta = 30$ meV, irrespective of the supercell size and direction. In addition, another two η values, 10 and 50 meV, will be used as such common choices. The resulted comparison will help us check the validity of the optimal-η scheme.

Statistical convergence

We now compute the electrical conductivities in our simulated supercells. This is done for each of the collected MD samples, by evaluating Equation (3.45) with the respective η values given in Table 5.4. In the left panels of Figure 5.6, for each of the $N \times 4 \times 4$ ($N = 1$, 2, and 3) supercells, we show the $\sigma_x(\{\mathbf{R}_I\})$ and its cumulative moving average

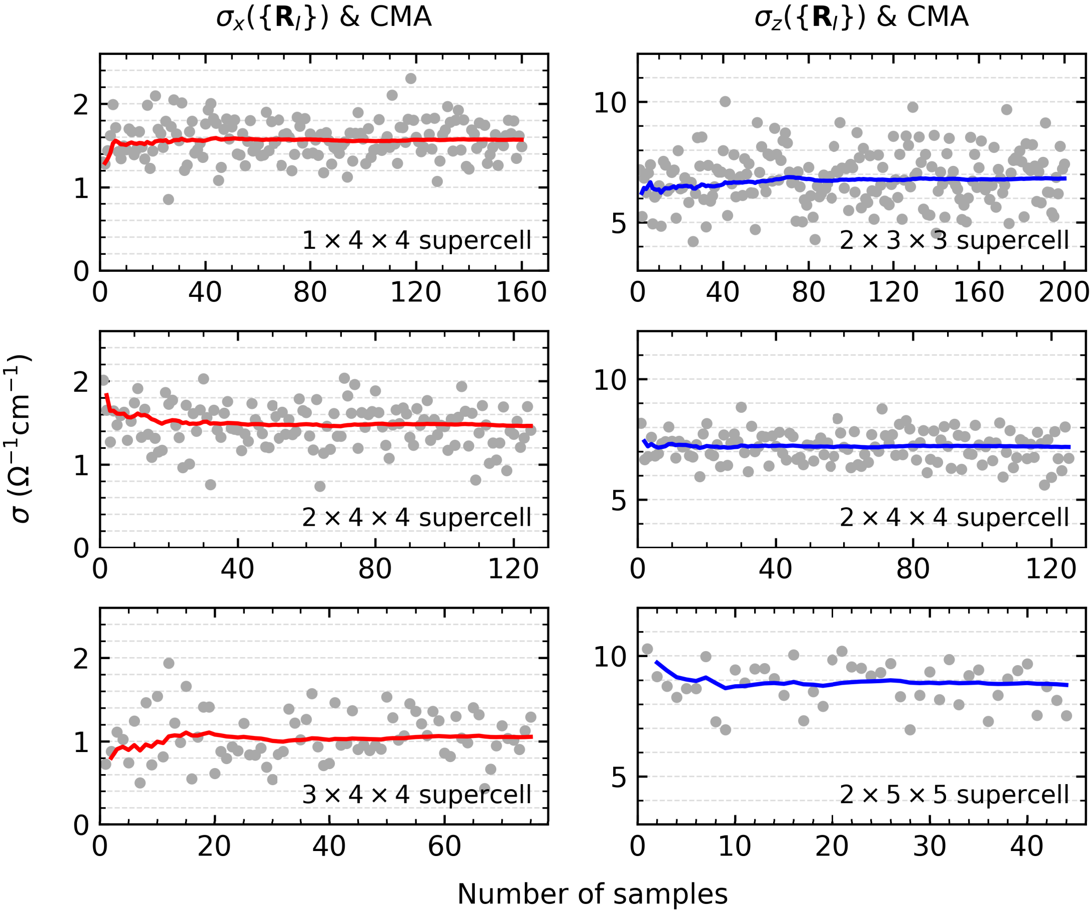

Figure 5.6: Convergence of electrical conductivity with respect to number of MD samples. Left panels: σ_x in the $N \times 4 \times 4$ ($N = 1,\ 2,$ and 3) supercells. Right panels: σ_z in the $2 \times N \times N$ ($N = 3,\ 4,$ and 5) supercells. Gray dots: $\sigma_{x/z}(\{\mathbf{R}_I\})$ for an individual MD sample ($\{\mathbf{R}_I\}$ denotes the atomic configuration). For instance, in the graph for σ_x in the $1 \times 4 \times 4$ supercell, there are 160 gray dots, each of which corresponds to a MD sample. The data points follow the time order of the MD simulations. Red and blue lines: cumulative moving average (CMA) of $\sigma_{x/z}(\{\mathbf{R}_I\})$. The results are for p-doped SnSe at 300 K, and calculated using the $\mathbf{k}$-meshes listed in Table 5.3 and with the η values listed in Table 5.4. Note the different scales of y-axes in the left and right panels.

(CMA); in the right panels, for each of the $2 \times N \times N$ ($N = 3,\ 4,$ and 5) supercells, we plot the $\sigma_z(\{\mathbf{R}_I\})$ and its CMA. For convenience of plotting, the results for the $2 \times 2 \times 2$ supercell are shown in Figure A.9 in the Appendix.

It can be seen qualitatively that for each supercell, the $\sigma_{x/z}(\{\mathbf{R}_I\})$ varies from one sample to another, and its CMA becomes gradually stable as the number of samples is increased. Relatively stable CMA, namely acceptable convergence with respect to number of samples, is achieved with about 50 samples, for most cases shown in the figure. There is no sign of reducing fluctuation of $\sigma_{x/z}(\{\mathbf{R}_I\})$ as the supercell size increases, unlike what was observed in the last chapter on Si. For instance, the extent of fluctuation of $\sigma_x(\{\mathbf{R}_I\})$ in the $2 \times 4 \times 4$ and $3 \times 4 \times 4$ supercells looks comparable. This may be understood as follows: SnSe is a soft material, so even for the large supercells, thermal atomic fluctuation with large displacements can occur in the MD simulations, leading to a large variation of the electrical conductivity.

Table 5.5 presents the electrical conductivities calculated in the supercells. These values are the sample means corresponding to the end points of the respective CMA curves displayed in Figure 5.6. As can be seen, the results for σ_z are much larger than those for σ_x, in line with experimental findings (see Figure 5.2). The statistical convergence of the results has been quantified by the standard error of the mean (SEM). We can see that the SEMs are small enough compared to the respective sample means, and that the ratio of the SEM to the sample mean is generally smaller than 2%. For σ_x in the $3 \times 4 \times 4$ supercell, the statistical error is a little large, suggesting that more MD samples are needed to improve the precision. Although we try to limit the ratio of the SEM to the sample mean to within 1%, this is not achieved due to the high computational cost[3]. Since SnSe is a material whose component elements are not light[4], the KG calculation in the $3 \times 4 \times 4$ (384-atom) and $2 \times 5 \times 5$ (400-atom) supercells is very demanding, making it challenging to compute many samples for these two supercells. Yet, we find that for σ_z in the $2 \times 5 \times 5$ supercell, a satisfactory statistical convergence has been achieved with less than 50 samples.

It should be mentioned that our results for different supercells are obtained with a different number of MD samples (here we limit our discussion to either σ_x or σ_z). This does not mean that we ignore the consistency. Instead, in our experience, it is often the case that for different supercell sizes we have to use a different number of samples, in order to achieve a similar statistical convergence of the electrical conductivity. Usually, smaller supercells require a larger number of samples. This can be seen from the quantitative error analysis for σ_z in the $2 \times N \times N$ supercells (see Table 5.5).

Besides, we have evaluated the electrical conductivities at three common choices $\eta = 10, 30$, and 50 meV. As an example, we present in Table 5.6 the results calculated at $\eta = 30$ meV [see Figure A.8 for $\sigma_{x/z}(\{\mathbf{R}_I\})$]. By comparing the last columns of Table 5.6 and Table 5.5, we see that the ratio of the SEM to the sample mean hardly changes with η. This indicates that the statistical convergence is decided by the number of samples. In

---

[3] Reducing the statistical error by including more MD samples is a slow process $\sim 1/\sqrt{N_{\text{sample}}}$ [52].

[4] As a comparison, SnSe and Si both have a conventional cell containing 8 atoms, but the number of electrons of SnSe is 3 times of that of Si.

next subsection, the electrical conductivity results in Tables 5.5 and 5.6 as well as those evaluated at $\eta = 10$ and 50 meV will be used to discuss the supercell-size convergence.

Table 5.5: Sample-averaged electrical conductivities in different SnSe supercells: σ_x in the $N \times 4 \times 4$ ($N = 1, 2,$ and 3) supercells; σ_z in the $2 \times N \times N$ ($N = 2, 3, 4,$ and 5) supercells. The results are for p-doped SnSe at 300 K and with the doping level of 3×10^{17} cm^{-3}, and calculated using the **k**-meshes listed in Table 5.3 and with the η values listed in Table 5.4. The statistical convergence is estimated by the SEM.

Supercell size	# samples	$\sigma_{x/z}$ (Ω^{-1}cm^{-1})	SEM (Ω^{-1}cm^{-1})	SEM/σ
Group-I (for σ_x)				
$1 \times 4 \times 4$	160	1.57	0.018	1.16%
$2 \times 4 \times 4$	125	1.46	0.023	1.58%
$3 \times 4 \times 4$	75	1.05	0.034	3.26%
Group-II (for σ_z)				
$2 \times 2 \times 2$	250	1.41	0.011	0.82%
$2 \times 3 \times 3$	200	6.82	0.078	1.14%
$2 \times 4 \times 4$	125	7.19	0.056	0.78%
$2 \times 5 \times 5$	44	8.80	0.137	1.55%

Table 5.6: Same as Table 5.5 but for the common choice $\eta = 30$ meV.

Supercell size	# samples	$\sigma_{x/z}$ (Ω^{-1}cm^{-1})	SEM (Ω^{-1}cm^{-1})	SEM/σ
Group-I (for σ_x)				
$1 \times 4 \times 4$	160	1.86	0.022	1.16%
$2 \times 4 \times 4$	125	1.50	0.024	1.60%
$3 \times 4 \times 4$	75	1.11	0.038	3.40%
Group-II (for σ_z)				
$2 \times 2 \times 2$	250	8.31	0.092	1.10%
$2 \times 3 \times 3$	200	7.64	0.089	1.17%
$2 \times 4 \times 4$	125	8.06	0.064	0.79%
$2 \times 5 \times 5$	44	7.73	0.119	1.54%

5.3.3 Supercell-size convergence

The electrical conductivity results presented in the last subsection now enable us to discuss the convergence with respect to the supercell size. The discussion below will also include (i) a comparison of the results for the different choices of η and (ii) a comparison of our results with experiment and previous *ab initio* BTE calculations. We discuss the experimental data for single-crystal SnSe samples of Zhao *et al*. [210, 211] and the BTE results of Caruso *et al*. [24], Li *et al*. [216], and Ma *et al*. [21].

Before proceeding, we summarize the relevant computational details of the above-mentioned BTE studies, which will help explain the differences in the numerical results. These studies were all done at the PBE level (Ma *et al*. employed a G_0W_0 correction to the DFT-PBE eigenvalues; we use instead PBEsol). Caruso *et al*. and Ma *et al*. both used the experimental crystal structure, while Li *et al*. used PBE-relaxed structure. In these studies, phonons and e-ph matrix elements were computed using DFPT. As mentioned in the Introduction, the DFPT calculations of Caruso *et al*. were done for the PBE-relaxed structure[5]. Caruso *et al*. and Li *et al*. both solved the BTE in the relaxation-time approximation (RTA). While Ma *et al*. also provided BTE-RTA calculations, the authors' focus was on an iterative solution of the BTE (which does not assume the RTA). It is worth noting that these studies employed different **k**- and **q**-meshes not only in the solution of BTE but also in the DFPT calculations[6] (as detailed in the Appendix, Table A.3). Caruso *et al*. reported temperature-dependent electrical conductivities, assuming a constant hole concentration of 4.5×10^{17} cm^{-3} for different temperatures. Li *et al*. presented electrical conductivities at 300 K as a function of hole concentration. Ma *et al*. reported temperature-dependent hole mobilities[7]. Hole doping was simulated using the rigid-band approximation, and hence (carrier-)defect scattering is entirely absent (as in our study). Note that defect scattering does exist in real single-crystal SnSe samples, which are unintentionally p-doped by Sn vacancies [217].

We also note here that all the electrical conductivity results discussed in this subsection are for p-type SnSe at 300 K and at the corresponding experimental hole doping level of 3×10^{17} cm^{-3} (this value was actually measured at 303 K) [210, 211]. For comparison, we (i) reduce the BTE results of Caruso *et al*. by 1.5 times and (ii) transform the mobility data of Ma *et al*. to electrical conductivities using the relation $\sigma = e\mu_\mathrm{h}n_\mathrm{h}$, where μ_h and n_h are the hole mobility and hole concentration, respectively (here $n_\mathrm{h} = 3 \times 10^{17}$ cm^{-3}).

---

[5] This is understandable since Caruso *et al*. considered a number of temperatures. Performing DFPT calculations for the crystal structure at each temperature is a formidable task.

[6] Interpolation of DFPT e-ph matrix elements on coarse **k**- and **q**-meshes to fine meshes was made in the solution of the BTE.

[7] In the work of Ma *et al*., temperature dependence was investigated with the experimental crystal structure at 300 K (i.e., only one crystal structure was used in the DFPT calculations). In addition, Ma *et al*. performed a test calculation of the 300 K hole mobilities at three different hole concentrations (1.57×10^{14}, 7.49×10^{15}, and 3.56×10^{17} cm^{-3}), and found the identical results.

Convergence of the σ_x with respect to the supercell size in the x direction

In Figure 5.7, we have plotted our calculated x-component electrical conductivities (σ_x) in the $N \times 4 \times 4$ ($N = 1,\ 2,$ and 3) supercells, as a function of $1/L_x$ (the inverse supercell length in the x direction).

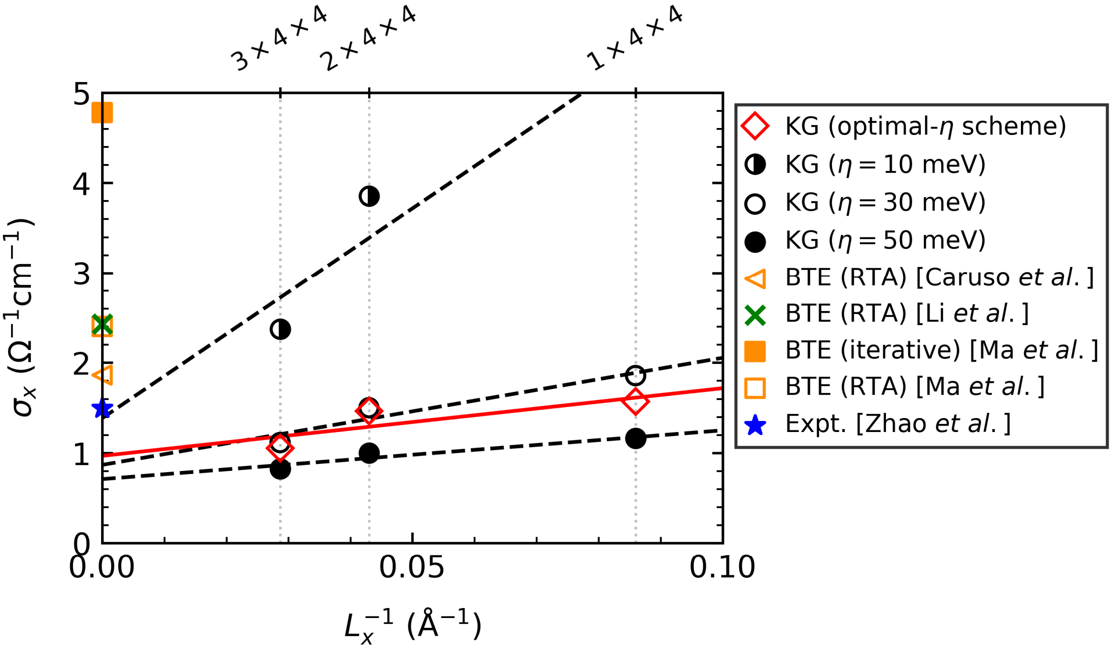

Figure 5.7: The x-component electrical conductivity (σ_x) as a function of $1/L_x$ (the inverse supercell size in the x direction). Our results are obtained from KG calculations in the $N \times 4 \times 4$ ($N = 1,\ 2,$ and 3) supercells, using different choices of broadening parameter (η): supercell-size-dependent η values (determined with the optimal-η scheme; listed in Table 5.4); Three different common choices (10, 30, and 50 meV). Our results are fitted with $\sigma_x(L_x = \infty) + a_1/L_x$, as indicated by the red solid line and black dashed lines. Literature data are included for comparison: experimental result of Zhao *et al.* [210, 211]; BTE-RTA results (obtained from solution of the BTE in the RTA) of Caruso *et al.* [24], Li *et al.* [216], and Ma *et al.* [21]; BTE-iterative results (obtained from iterative solution of the BTE) of Ma *et al.* [21]. All the data displayed in this graph are for p-doped SnSe at 300 K and with the doping level of 3×10^{17} cm^{-3}. The result of Caruso *et al.*, which is originally for the doping level of 4.5×10^{17} cm^{-3}, has been reduced by 1.5 times.

As can be seen, the σ_x obtained from the $1 \times 4 \times 4$ supercell calculations is in good agreement with experiment [Here and below, unless specified otherwise, we refer to our results for the optimal-η scheme, i.e., the data points marked by red diamonds)]. This indicates that the $1 \times 4 \times 4$ supercell, which contains two SnSe atomic layers in the x direction, provides a satisfactory description of the hole transport in the x direction. This observation can be understood in terms of the short MFPs of both the holes and phonons in SnSe in the x direction. First, as reported in Ref. [21], the hole MFPs in SnSe are in the range of $1 - 13$ nm, which are (on average) much shorter than in Si $(5 - 55$ nm) [127]. While to our knowledge there is no information available on the hole MFPs of SnSe in a specific direction, it can be speculated that the hole MFPs are short in the x direction, given that (i) the layered crystal structure of SnSe constitutes a barrier for the interlayer hole transport in the x direction, and (ii) the highest valence band along the Γ-X line is rather dispersionless (i.e., localized hole states). Second, because of the puckered layered crystal structure and strong lattice anharmonicity, the lattice vibrations in SnSe are localized irrespective of the spatial direction. Previous heat transport studies found that in SnSe at 300 K heat is mainly carried by phonons with MFPs on the order of nanometers (~ 0.84 nm reported by Xiao *et al.* [18] and $1 - 30$ nm by Guo *et al.* [212]), which are much shorter than those in Si at 300 K (longer than 1 micron [104]). From these two aspects, we can understand why the $1 \times 4 \times 4$ supercell seems adequate to accommodate the hole carriers and lattice vibrational modes that dominate the hole transport in the x direction. Similarly, the $2 \times 4 \times 4$ supercell is found to give a very satisfactory description of the interlayer hole transport. However, the σ_x shows a noticeable decrease (slightly less than 30%) when going from the $2 \times 4 \times 4$ supercell to the $3 \times 4 \times 4$ supercell. This is entirely unexpected, but may be understood from that the allowed lattice vibrational modes in the $3 \times 4 \times 4$ supercell are very different from those in the $2 \times 4 \times 4$ supercell.

Fitting the σ_x in the $N \times 4 \times 4$ ($N = 1$, 2, and 3) supercells with the polynomial function[8] $\sigma_x(L_x = \infty) + a_1/L_x$ and extrapolating to infinite L_x (i.e., $1/L_x \to 0$), we obtain our final result for the σ_x, 0.97 $\Omega^{-1}\text{cm}^{-1}$, which is about 35% below the experimental value of 1.5 $\Omega^{-1}\text{cm}^{-1}$ [210, 211]. The quality of the fit is not very good (see the red solid line in Figure 5.7; note the large scale of the y-axis), for the reason mentioned above. We expect that the fit quality will get improved by including the σ_x in the $4 \times 4 \times 4$ supercell whose calculation is, however, not affordable.

From Figure 5.7, we further see that the finite-size σ_x for the common choice $\eta = 30$ meV (marked by black empty circles) are very close to those for the optimal-η scheme. This is simply because the η values determined with the optimal-η scheme are close to 30 meV (see Table 5.4, for the σ_x). Thus, these two η choices result in very close extrapolated σ_x. Let us focus now on the results for the three common choices of η (all black circles). We see that the finite-size σ_x increase as η varies from 50 to 30 meV, and that the increase is more pronounced as η varies from 30 to 10 meV. In the case of $\eta = 10$ meV, although the extrapolated value looks very close to the experimental value, the

---

[8] By observing the data, including higher-order terms of $1/L_x$ will give very wrong results.

fit quality is rather poor, so the extrapolated value is not reliable. We believe that our simulation supercells are not large enough to allow η to be as small as 10 meV.

We comment on the BTE reference data in Figure 5.7. (i) First, they scatter widely, but are all larger than the experimental value which correctly reflects the absence of defect scattering. (ii) Second, the BTE-RTA results of Li *et al*. [216] and of Ma *et al.* [21] agree well with each other (despite that Li *et al*. and Ma *et al.* used different lattice parameters and that Ma *et al.* used a G_0W_0 correction to the DFT-PBE eigenvalues), but they are different from the one of Caruso *et al.* [24]. We tentatively interpret this in terms of the coarse **q**-meshes in their e-ph calculations. As detailed in Table A.3, for the DFPT calculations, Li *et al*. and Ma *et al.* used $3 \times 3 \times 3$ and $3 \times 6 \times 6$ **q**-meshes, with the same **q**-point sampling in the k_x direction. In contrast, Caruso *et al.* used a $2 \times 4 \times 4$ **q**-mesh (which is equivalent to the $2 \times 4 \times 4$ supercell in our KG calculations). (iii) Third, in the work of Ma *et al.*, the BTE-RTA result is much closer to the experimental value compared to the BTE-iterative result. This contradicts the expectation that the BTE-iterative result should be more accurate than the BTE-RTA result.

Because SnSe is a very anharmonic crystal, whether these BTE results can be used as a good reference for assessing the convergence of our KG calculations is questionable. This is even more so considering the large scatter in the BTE results. Nevertheless, our extrapolated σ_x (for the optimal-η scheme) is noticeably smaller than the BTE results (even the one of Caruso *et al.*).

Convergence of the σ_z with respect to the supercell size in the z direction

In Figure 5.8, we have plotted our calculated z-component electrical conductivities (σ_z) in the $2 \times N \times N$ ($N = 2,\ 3,\ 4,$ and 5) supercells, as a function of $1/L_z$ (the inverse supercell length in the z direction).

Let us first look at our calculated results for the optimal-η scheme. As can be seen, the finite-size σ_z (marked by red diamonds) are systematically smaller than the experimental value. This is the case for the $2 \times 5 \times 5$ supercell (the largest SnSe supercell that we can afford), not to mention the smaller supercells which suffer from very large finite-size effects. The slow supercell-size convergence of the σ_z is not unexpected. As mentioned before, the hole MFPs of SnSe are in the range of $1 - 13$ nm [21]. While the hole MFPs in a specific direction are unknown, the hole MFPs in the z direction are probably (on average) the longest among all three directions, considering that (i) the hole transport in the z direction is within the SnSe atomic layers, and (ii) the highest valence band of SnSe along the Γ-Z line (on which the VBM is located) is highly dispersive (i.e., delocalized states). In fact, the hole MFPs must be long within the SnSe atomic layers, otherwise SnSe will not possess the known superior thermoelectric performance. As a result, even the $2 \times 5 \times 5$ supercell (whose L_z is about 2.3 nm) is inadequate for describing the hole transport in the z direction. Note that due to the strong lattice anharmonicity, the phonon MFPs are short irrespective of the spatial direction [18, 212].

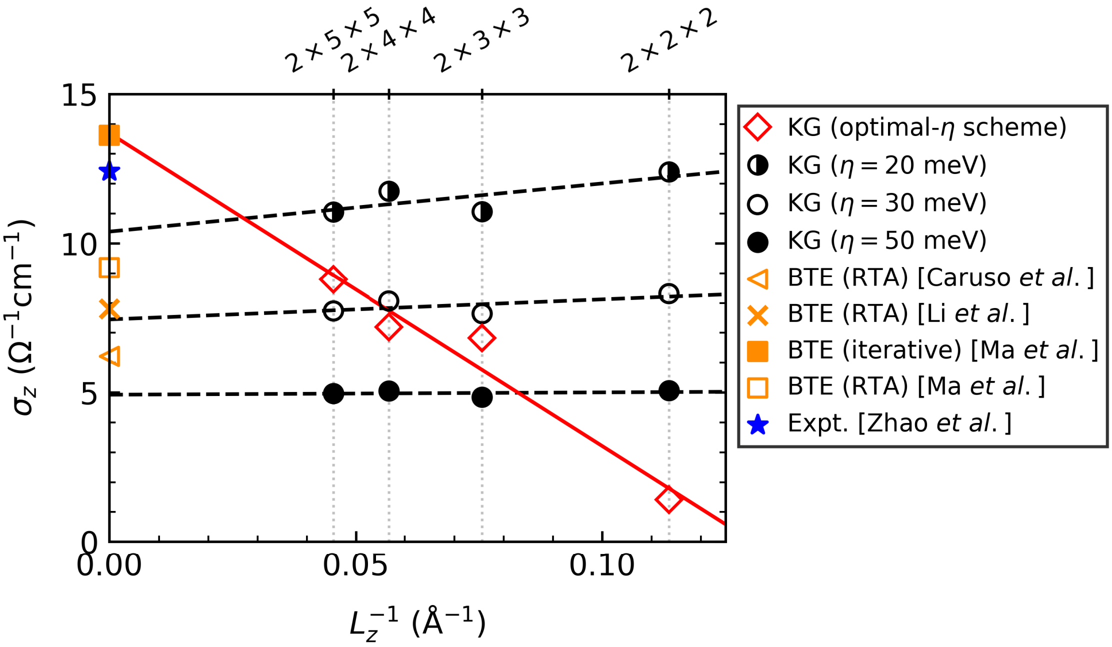

Figure 5.8: The z-component electrical conductivity (σ_z) as a function of $1/L_z$ (the inverse supercell size in the z direction). Our results are obtained from KG calculations in the $2 \times N \times N$ ($N = 2$, 3, 4, and 5) supercells, using different choices of broadening parameter (η): supercell-size-dependent η values (determined with optimal-η scheme; listed in Table 5.4); Three different common choices (20, 30, and 50 meV). Our results are fitted with $\sigma_z(L_z = \infty) + a_1/L_z$, as indicated by the red solid line and black dashed lines. Other description of the data (including the literature data) in this graph is the same as in Figure 5.7 and not repeated here.

Thus, we conclude that even for strongly anharmonic crystal with short phonon MFPs, the convergence of KG calculations with respect to supercell size will be slow if the associated charge-carrier MFPs are long. Since materials with long charge-carrier MFPs are usually preferred in thermoelectric and (opto)electronic applications, the supercell-size convergence is expected to be a common issue in *ab initio* calculations of the electrical conductivity within the KG approach.

The observed slow supercell-size convergence necessitates the use of the finite-size scaling method to deduce the σ_z in the thermodynamic limit. As illustrated by the red solid line in Figure 5.8, fitting the σ_z in the $2 \times N \times N$ ($N = 2$, 3, 4, and 5) supercells with the polynomial function $\sigma(L_z = \infty) + a_1/L_z$ and extrapolating to infinite L_z (i.e., $1/L_z \to 0$), we obtain our final result for the σ_z, 13.69 Ω^{-1}cm^{-1}. This value is about

10% above the experimental value of 12.4 $\Omega^{-1}\text{cm}^{-1}$ [210, 211]. We note that the σ_z in the $2 \times N \times N$ supercells increase as N is increased from 2 to 5, and this is largely due to that the η values decrease with the increase of N (see Table 5.4). It should be mentioned that the σ_z for the $2 \times 2 \times 2$ supercell is evaluated with a very large η value. If we leave out the $2 \times 2 \times 2$ supercell, the extrapolated value will be slightly smaller than the experimental value.

Figure 5.8 (black circles) shows our calculated σ_z versus L_z for the three common choices of η (here $\eta = 20$ meV instead of 10 meV is considered, as the latter leads to very large σ_z values). At the common choice $\eta = 50$ meV, the results are nearly independent of L_z, but obviously this supercell-size convergence does not make sense. At the two smaller η values, the finite-size σ_z show a decreasing trend with increasing L_z (i.e., $1/L_z \to 0$), unlike the case of the optimal-η scheme.

From Figure 5.8, we see that the BTE reference data for the σ_z are widely scattered. They are noticeably smaller than the experimental data, except for the BTE-iterative result of Ma *et al.* [21] which, unlike for the σ_x, is in good agreement with experiment. Unlike for the σ_x, the BTE-RTA result for the σ_z of Caruso *et al.* [24] deviates significantly from experiment. The three BTE-RTA results for the σ_z do not agree with each other. Again, we attribute this difference to the fact that Caruso *et al.*, Li *et al.* [216], and Ma *et al.* used $2 \times 4 \times 4$, $3 \times 3 \times 3$, and $3 \times 6 \times 6$ **q**-meshes in the DFPT calculations, respectively (see Table A.3). These coarse **q**-meshes result in a quite different **q**-point sampling e.g. in the k_z direction, but for this no convergence test was reported. Our extrapolated σ_z (for the optimal-η scheme) agrees well with the BTE-iterative result of Ma *et al*. Despite this, we refrain from assessing the convergence of our calculations in terms of this comparison, given the wide scatter of the BTE results.

Convergence with respect to the supercell size in other directions

Our calculations of the σ_x using the $N \times 4 \times 4$ ($N = 1$, 2, and 3) supercells and of the σ_z using the $2 \times N \times N$ ($N = 2$, 3, 4, and 5) supercells offer us the best compromise between accuracy and computational cost. Despite this, we still need to check (i) whether the size of the $N \times 4 \times 4$ supercells in the y and z directions is sufficient for describing the hole transport in the x direction, and (ii) whether the size of the $2 \times N \times N$ supercells in the x direction is sufficient for describing the hole transport in the z direction. These are addressed below. For the necessary parameter η, we consider both the optimal-η scheme and the common choice $\eta = 30$ meV.

In Figure 5.9, we compare the σ_x calculated in the $N \times 4 \times 4$ supercell with that in the $N \times 5 \times 5$ supercell ($N = 1$ and 2). Figure 5.9(a) shows the finite-size σ_x for the optimal-η scheme[9]. We see that (i) the $1 \times 4 \times 4$ and $1 \times 5 \times 5$ supercell calculations

---

[9] For the $1 \times 5 \times 5$ supercell, we generate 126 samples from *ai*MD simulations at 300 K. The η values determined with the optimal-η scheme are 55 and 39 meV for evaluating the σ_x in the $1 \times 5 \times 5$ and $2 \times 5 \times 5$ supercells, respectively. Other σ_x results can be found in Tables 5.5 and 5.6.

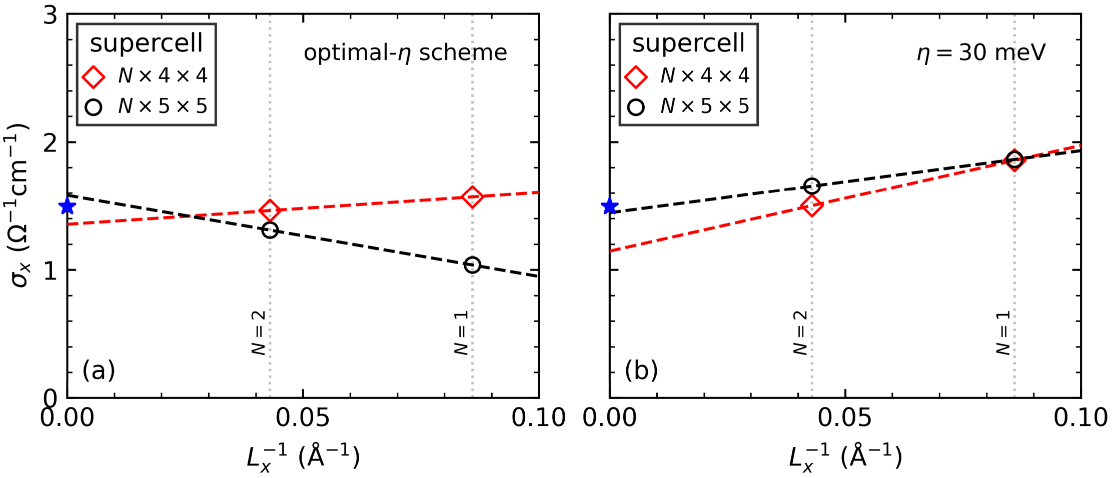

Figure 5.9: Calculated σ_x in the $N \times 4 \times 4$ and $N \times 5 \times 5$ ($N = 1$ and 2) supercells. The σ_x are computed with: (a) the η values determined with the optimal-η scheme (see main text); and (b) $\eta = 30$ meV. All the results are for *p*-doped SnSe at 300 K and with the doping level of 3×10^{17} cm^{-3}. The results for the $N \times 4 \times 4$ supercells are already displayed in Figure 5.7. Due to insufficient amount of data points, the red and black dashed lines are a guide to the eye. The experimental result of Zhao *et al.* [210, 211] is marked by blue star.

yield quite different σ_x (evaluated at $\eta = 36$ and 55 meV, respectively), and (ii) the $2 \times 4 \times 4$ and $2 \times 5 \times 5$ supercell calculations give close σ_x (evaluated at $\eta = 31$ and 39 meV, respectively). Figure 5.9(b) shows the results that are all evaluated at $\eta = 30$ meV. We see that, for both $N = 1$ and 2, the $N \times 4 \times 4$ and $N \times 5 \times 5$ supercell calculations produce very close σ_x.

Second, we compare the σ_z calculated in the $1 \times N \times N$ supercell with that in the $2 \times N \times N$ supercell ($N = 4$ and 5). From Figure 5.10(a), which shows the finite-size σ_z for the optimal-η scheme[10], we see that (i) the $1 \times 4 \times 4$ and $2 \times 4 \times 4$ supercell calculations yield different σ_z (evaluated at $\eta = 46$ and 34 meV, respectively), and (ii) the $1 \times 5 \times 5$ and $2 \times 5 \times 5$ supercell calculations give quite different σ_z (evaluated at $\eta = 39$ and 26 meV, respectively). Figure 5.10(b) shows the results that are all evaluated at $\eta = 30$ meV. We see that, for both $N = 4$ and 5, the $1 \times N \times N$ and $2 \times N \times N$ supercell calculations produce very close σ_z.

The present test shows that when using the η values determined with the optimal-η scheme, the convergence of the electrical conductivity in one direction with respect to the supercell size in other directions seems not systematic, due to the dependence of η

---

[10] The η values determined with the optimal-η scheme are 46 and 39 meV for evaluating the σ_z in the $1 \times 5 \times 5$ and $2 \times 5 \times 5$ supercells, respectively.

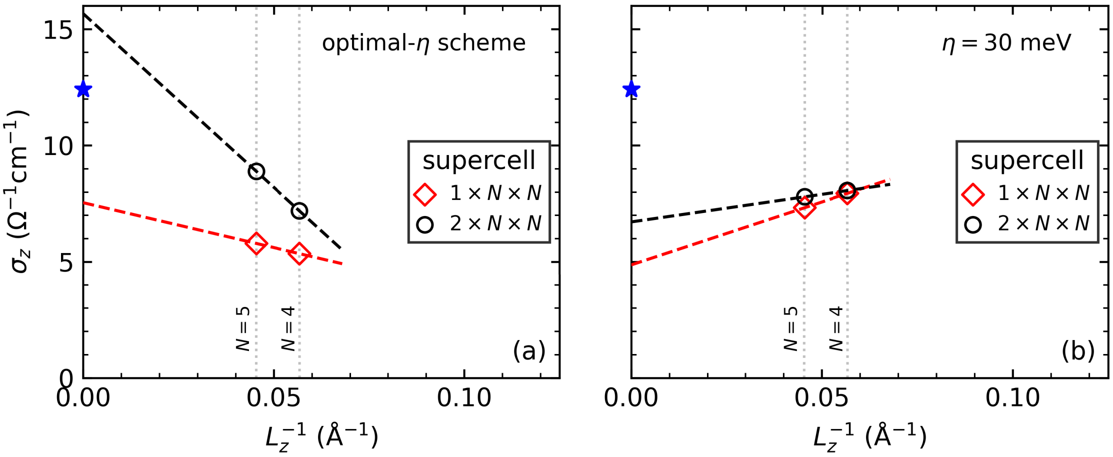

Figure 5.10: Calculated σ_z in the $1 \times N \times N$ and $2 \times N \times N$ ($N = 4$ and 5) supercells. The σ_z are computed with: (a) the η values determined with the optimal-η scheme (see main text); and (b) $\eta = 30$ meV. All the results are for p-doped SnSe at 300 K and with the doping level of 3×10^{17} cm^{-3}. The results for the $2 \times N \times N$ supercells are already displayed in Figure 5.8. Due to insufficient amount of data points, the red and black dashed lines are a guide to the eye. The experimental result of Zhao *et al.* [210, 211] is marked by blue star.

on the supercell size in this scheme. Thus, there are large uncertainties in our results for the σ_x and σ_z as reported in Figures 5.7 and 5.8 (those at the optimal-η scheme). In contrast, systematic convergence behavior is seen at the common choice $\eta = 30$ meV, but we add that this behavior will no longer be seen if we adjust η to smaller values (e.g., 20 meV). Because of the large uncertainties associated with η, at present it is not possible to make a conclusive analysis of the supercell-size convergence based on the results in the present test. Essentially, this difficulty is due to the very limited size of our supercells. To aim for a conclusive analysis, future work will be required to compute the σ_x in the $N \times 6 \times 6$ ($N = 1$ and 2) supercells and the σ_z in the $3 \times N \times N$ ($N = 4$ and 5) supercells (both are currently computationally infeasible).

5.4 Electrical conductivity of *p*-doped SnSe at 523 K

In this section we perform *ab initio* KG calculations of the electrical conductivity in SnSe at 523 K. Experimentally it was found that the single-crystal SnSe sample prepared at 523 K is intrinsically p-type with a hole doping level of 3.16×10^{17} cm^{-1} [210, 211]. Due to the high computational cost, here we consider only the x component of the electrical conductivity, and the calculations are performed in the $N \times 4 \times 4$ ($N = 1$, 2, and 3) supercells using the respective $\mathbf{k}$-meshes as listed in Table 5.3.

In Table 5.7, we present for each of the three supercells: (i) the number of samples generated from the *ai*MD simulations at 523 K, (ii) the value of η determined with the optimal-η scheme, (ii) the σ_x result which is the sample mean of the $\sigma_x(\{\mathbf{R}_I\})$ for individual samples, and (iv) the statistical convergence estimated by SEM. For each supercell, we find that the η value is quite large compared to the one in the 300 K case (Table 5.4). This implies that the spacings of Kohn-Sham energy levels are larger at 523 K than at 300 K. Besides, for each supercell, the statistical convergence is found to be slower compared to the 300 K case (Table 5.5). This can be understood by the fact that the MD simulations explore a larger subspace of the PES at higher temperature.

Table 5.7: The size of the supercells simulated, number of collected *ai*MD samples, η values (determined with the optimal-η scheme) in our calculations of the σ_x in p-doped SnSe at 523 K. The electrical conductivities are estimated by the sample means, and their statistical convergence is quantified by standard error of the mean (SEM).

Supercell	# samples	η (meV)	σ_x (Ω^{-1}cm^{-1})	SEM/σ_x
$1 \times 4 \times 4$	200	78	0.52	1.44%
$2 \times 4 \times 4$	125	50	0.55	2.43%
$3 \times 4 \times 4$	75	49	0.43	3.62%

Figure 5.11 shows the calculated σ_x for the three supercells. We see a noticeable decrease of the σ_x when going from the $2 \times 4 \times 4$ supercell to the $3 \times 4 \times 4$ supercell (similar to what we have observed at 300 K). With a simple linear fit and extrapolation to infinitely large L_x, we obtain our final result for the σ_x, 0.45 Ω^{-1}cm^{-1}. The finite-size and the extrapolated σ_x are smaller compared to the calculations at 300 K (see Figure 5.7). This is consistent with the experimental observation [210, 211] that the electrical conductivity of SnSe falls as temperature increases (see Figure 5.2;up to 550 K).

Our extrapolated σ_x is about 40% below the experimental value of 0.74 Ω^{-1}cm^{-1} measured at 523 K [210, 211]. By contrast, the BTE-RTA result for the σ_x reported by

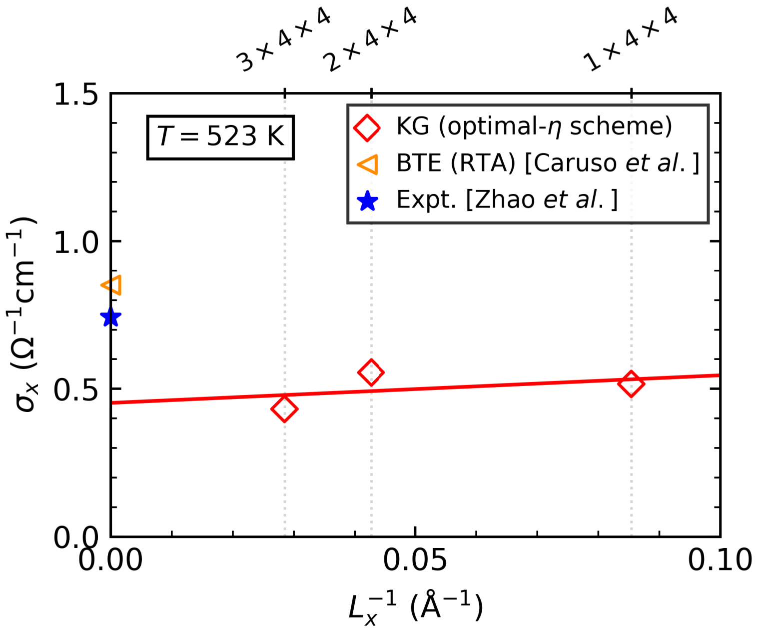

Figure 5.11: The x-component electrical conductivity (σ_x) as a function of $1/L_x$ (the inverse supercell size in the x direction), for SnSe at 523 K and with the hole doping level of 3.16×10^{17} cm^{-3}. The finite-size results are fitted with $\sigma_x(L_x = \infty) + a_1/L_x$. Literature data are included for comparison: experimental result from Zhao *et al.* [210, 211]; *ab initio* BTE calculations in the RTA from Caruso *et al.* [24].

Caruso *et al.*[11] [24] agrees much better with experiment and, moreover, is larger than the experimental value (similar to the 300 K case). We discuss this difference in the ability to compare with experiment in the next section.

---

[11] The BTE result for the σ_x at 523 K is not directly available from the work of Caruso *et al.*, but we estimate it from FIG. 3 of this reference.

5.5 Discussion

We add some remarks on what we have learned from Sections 5.3.3 and 5.4.

First, when comparing the electrical conductivity results of KG and BTE calculations, it is important to pay attention to (i) the size of the supercell used in KG calculations and (ii) the size of the DFPT **q**-mesh used for computing phonons and e-ph matrix elements in BTE calculations. This is especially so when such sizes are very limited, in which case the calculated results might even depend on whether the size is an even or odd number. We have seen that in our KG calculations of the σ_x, the $2 \times 4 \times 4$ supercell calculations yield results closer to the experimental data than the $3 \times 4 \times 4$ supercell calculations[12]. In the BTE calculations of the σ_x, Caruso *et al.* [24], Li *et al.* [216], and Ma *et al.* [21] used $2 \times 4 \times 4$, $3 \times 3 \times 3$, and $3 \times 6 \times 6$ **q**-meshes in the DFPT calculations, respectively (see Table A.3). These DFPT **q**-meshes, which are very coarse e.g. in the k_x direction, describe different phonon modes, and therefore provide different starting points for interpolating the e-ph matrix elements to fine meshes for the solution of the BTE. By looking at these **q**-point samplings especially in the k_x direction, we may understand why the BTE-RTA results for the σ_x by Li *et al.* and Ma *et al.* agree with each other but different from the one by Caruso *et al.* (Figure 5.8). A careful convergence test with respect to the DFPT **q**-mesh is needed to verify this speculation.

The above discussion implies that our finite-size scaling of the σ_x in the $N \times 4 \times 4$ ($N = 1,\ 2,$ and 3) supercells will not lead to improved supercell-size convergence (as we have already seen). To quantitatively reproduce the σ_x results of Caruso *et al.*, we may need to check the finite-size scaling of the σ_x in the $1 \times 4 \times 4$, $2 \times 4 \times 4$, and $4 \times 4 \times 4$ supercells, without considering the $3 \times 4 \times 4$ supercell. It should be pointed out that such a selection of supercells is not necessary (and should not be done) if sufficiently many and sufficiently large supercells can be computed. We expect a better understanding of the η problem and the issue of supercell-size convergence when KG calculations in the $4 \times 4 \times 4$ supercell become possible.

Second, a quantitative and predictive calculation of the electronic transport coefficients in SnSe may be a challenging task in view of the widely scattered BTE results. We think that the calculation of the σ_x in p-doped SnSe is a good test case for discussing the predictive power of the *ab initio* BTE approach to anharmonic crystals. In future developments of the *ab initio* KG approach, if SnSe is considered as a test system, we suggest focusing on the σ_x in p-doped SnSe at 300 K.

Third, we can now shed light on the question of whether strong lattice anharmonicity facilitates the supercell-size convergence of KG calculations. Our study of SnSe shows that the supercell-size convergence is not only determined by the lattice vibrations, but also by the charge carriers. While we do find that the $1 \times 4 \times 4$ supercell provides a satisfactory description of the hole transport in the x direction, this is built on that both

---

[12] Here and in the following we refer to our results in the case of the optimal-η scheme.

the holes and phonons in SnSe probably have short MFPs in the x direction. In contrast, the supercell-size convergence of the σ_z is slow, because the hole MFPs in the z direction well exceed the size of our simulation supercells. These bring us to the conclusion that in the theoretical description of electronic transport in crystalline solids, one should keep in mind two aspects: charge carriers and lattice vibrations. This is different from the study of heat transport (i.e., thermal conductivity) in crystalline solids, where lattice anharmonicity plays a dominant role [218].

Lastly, we have not discussed the uncertainties in the experimental data. This is because (i) the experimental electrical conductivities discussed in the previous sections were measured for single-crystal SnSe samples [210, 211] and (ii) our considered temperatures are well below the phase-transition temperature of SnSe (about 800 K). Yet, we notice that SnSe is a compound whose component elements are prone to volatilize especially at high temperature [217, 219].

5.6 Summary

In this chapter we explored and assessed the *ab initio* KG approach by applying it to study the anisotropic electrical conductivity of the anharmonic material SnSe.

By focusing on the x and z components of the electrical conductivity in p-doped SnSe at 300 K, new insights have been obtained:

(i) The $\mathbf{k}$-point convergence of the electrical conductivity is related to the highly anisotropic valence bands. The convergence of the σ_x depends critically on the $\mathbf{k}$-point sampling in the k_z direction, since the VBM is on the Γ-Z line. On the contrary, the σ_z converges very quickly with respect to the $\mathbf{k}$-point sampling in the k_x direction, because the valence bands in the k_x direction are deep in energy.

(ii) The anisotropic nature of SnSe poses an additional challenge in addressing the issue of supercell-size convergence with the finite-size scaling method. To achieve a good compromise between accuracy and computational cost, we compute the σ_x using the $N \times 4 \times 4$ ($N = 1$, 2, and 3) supercells, which are reasonably large in both the y and z directions and provide three data points for performing finite-size scaling to deduce the σ_x in the limit $L_x \to \infty$. In a similar spirit, the $2 \times N \times N$ ($N = 2$, 3, 4, and 5) supercells are employed to calculate the σ_z.

For p-doped SnSe at 300 K, it is found that both the $1 \times 4 \times 4$ and $2 \times 4 \times 4$ supercell calculations yield σ_x results in good agreement with experiment. This is attributed to that the holes and phonons both probably have short MFPs in the x direction. In contrast, the σ_z obtained from the $2 \times 5 \times 5$ supercell calculations suffers from considerable finite-size effects, and this is understood from the probably long hole MFPs in the z direction. With the optimal-η scheme and the finite-size scaling method, our final results for the σ_x and σ_z are in reasonable agreement with experiment. However, the large uncertainties due to the η problem and the issue of supercell-size convergence remain. The comparison of our results with previous *ab initio* BTE calculations is somewhat hindered by the wide scatter of the BTE results.

We have not achieved a systematic study on the temperature dependence of the electrical conductivity of SnSe, though we have calculated the σ_x of SnSe at 523 K. Realizing high thermoelectric performance in SnSe requires both high temperatures and heavily p-type doping [210, 179], but we are unable at this time to apply the KG approach to these cases due to the high computational cost.

6 Conclusions and outlook

6.1 Conclusions

Motivated by the quest for a first-principles approach to reliably predict the electrical conductivity in anharmonic materials, in this thesis we described the *ab initio* KG approach to the calculation of the electrical conductivity of crystalline solids, and explored a numerical implementation of this approach for two very different systems: the harmonic crystal Si and anharmonic crystal SnSe.

Starting from the Kubo's theory of linear response, we introduced the KG formula, and established the connection with electronic-structure calculations including *ai*MD simulations of lattice vibrations in the supercell approach. Practical aspects such as the methods to account for carrier doping were also discussed.

The case study for Si at 300 K revealed that a number of numerical difficulties need to be overcome in order to obtain reliable results for the electrical conductivity from *ab initio* KG calculations. First, the evaluation of the KG formula requires a dense **k**-point sampling of the Brillouin zone, which places a high demand on computational resources and severely limits the size of supercells. Second, due to the high computational cost, currently the calculations are only feasible at the LDA/GGA level, at which the severe underestimation of band-gaps significantly overestimates the electrical conductivity. This problem is largely corrected by the “scissor operator" approach without additional computational cost. Third, in order to make the calculations tractable, the “light" basis set of Si should be used but nevertheless the resulting electrical conductivities are very close to those obtained with the “tight" basis set. Fourth, carrier doping is simulated within the rigid-band approximation in order to reduce the computational cost. Despite these efficient strategies, we are only able to calculate supercells up to 1000 Si atoms. Fifth, due to discrete Kohn-Sham energy levels in the finite-size supercell calculations, a broadening parameter (η) has to be introduced in the evaluation of the KG formula. It is found that the calculated electrical conductivities depend strongly on the choice of η, which introduces a significant uncertainty in the quantitative calculation of the electrical conductivity. An “optimal-η scheme" is discussed to determine the appropriate value of η, by making the choice of η reflect the average level spacing of the supercell. Sixth, the calculations suffer from considerable finite-size effects, which is understood by the fact that the (typical) MFPs of the charge carriers and phonons in Si well exceed the size of our supercells (or more generally the size possible with first-principles calculations). The finite-size scaling method is used to extrapolate the electrical conductivities calculated in the $N \times N \times N$ ($N = 2, 3, 4,$ and 5) cubic supercells to the limit of an infinitely large supercell. Lastly, while the convergence of the calculations with respect to the number of *ai*MD samples is not a big problem, it is computationally expensive for the large supercells.

With these efforts, our KG calculations at the LDA level yield electrical conductivities that are in reasonable agreement with experiment. The discrepancy is within about 50%, for both intrinsic and doped Si at 300 K. For doped Si, we also compared with previous *ab initio* BTE calculations which work well for the very harmonic crystal Si. It is found that our results do not agree well with previous BTE results obtained at the same level of theory. This suggests that our strategies for dealing with the η problem and the issue of supercell-size convergence need to be improved.

The case study for the layered semiconductor SnSe shows very similar numerical difficulties as in the case of Si, so the defined strategies were applied to this case study. For SnSe, it is rather challenging to address the issue of supercell-size convergence, because of the anisotropic electrical conductivity and that the $4 \times 4 \times 4$ (512-atom) supercell is computationally unfeasible. As a result, we computed the x-component electrical conductivity (σ_x) using the $N \times 4 \times 4$ ($N = 1, 2,$ and 3) supercells, which are reasonably large in both the y and z directions and provide three values of σ_x for finite-size extrapolation in the x (i.e., interlayer) direction. Similarly, the z-component electrical conductivity (σ_z) was computed using the $2 \times N \times N$ ($N = 2, 3, 4,$ and 5) supercells.

Our calculated results (at the GGA-PBEsol level) for the σ_x and σ_z of p-doped SnSe at 300 K are in reasonable agreement with the experimental data. However, the large uncertainties due to the η problem and the issue of supercell-size convergence remain. Comparison with previous *ab initio* BTE calculations is elusive because of the wide scatter of the BTE results. Still, it indicates that our KG calculations so far provide no improved predictive power over existing BTE calculations, despite the highly anharmonic nature of SnSe. The same conclusions hold for our calculated results for the σ_x of p-doped SnSe at 523 K.

Despite the limited size of the supercells and the large uncertainty associated with η, the case study for SnSe provides an insight into the influence of lattice anharmonicity on the convergence of KG calculations. That is, while the supercell-size convergence can benefit from the short phonon MFPs due to strong lattice anharmonicity, this convergence is also determined by the MFPs of charge carriers.

From the two case studies, we conclude that more expertise needs to be acquired on how to deal with the η problem and the issue of supercell-size convergence before the *ab initio* KG approach can be applied for quantitative and predictive calculations of the electrical conductivity of crystalline materials.

6.2 Outlook

Our work is a first step towards a reliable numerical implementation of the *ab initio* KG approach for crystalline materials. From what we have learned, we think that the following efforts are needed in the future developments of this framework.

First, the primary effort should be put on addressing the η problem and the issue of supercell-size convergence. To this end, it is necessary to have an in-depth comparison of KG and BTE calculations of the electrical conductivity. We suggest the following recipe. One performs (i) KG calculations in a $N \times N \times N$ supercell and (ii) BTE calculations in the unit cell using a $N \times N \times N$ $\mathbf{q}$-mesh (here interpolation of the e-ph matrix elements to fine $\mathbf{q}$-mesh must not be done in the solution of the BTE). All other computational settings such as the lattice constants, xc functional, basis set, broadening parameter (η), and $\mathbf{k}$-point sampling should be the same in the two calculations. The $\mathbf{k}$-point sampling should be tightly converged, and the KG calculations should be well converged with respect to the number of MD samples. Then, one compares the electrical conductivity results $\sigma^{\mathrm{KG}}(N)$ and $\sigma^{\mathrm{BTE}}(N)$. For the highly harmonic crystal Si at 300 K, $\sigma^{\mathrm{KG}}(N)$ and $\sigma^{\mathrm{BTE}}(N)$ should, in principle, be (nearly) identical. If this is case, insight into the η problem will be gained. In another test, one considers e.g. the σ_x in p-doped SnSe at 300 K, and investigates convergence of the difference $\sigma^{\mathrm{KG}}(N) - \sigma^{\mathrm{BTE}}(N)$ with respect to the size N. If $\sigma^{\mathrm{KG}}(N) - \sigma^{\mathrm{BTE}}(N)$ can be converged for not too big N, the electrical conductivity can then be computed as:

$$\sigma = \sigma^{\mathrm{BTE}}(N \to \infty) + \sigma^{\mathrm{KG}}(N) - \sigma^{\mathrm{BTE}}(N) \tag{6.1}$$

Where $\sigma^{\mathrm{BTE}}(N \to \infty)$ is the result obtained from fully converged BTE calculations with a fine $\mathbf{q}$-mesh. Equation (6.1) defines $\sigma^{\mathrm{KG}}(N) - \sigma^{\mathrm{BTE}}(N)$ as a correction to $\sigma^{\mathrm{BTE}}(N \to \infty)$. This scheme combines the advantage of the BTE approach with that of the KG approach: (i) The BTE approach can account for the charge-carriers and phonons with long MFPs albeit within the harmonic approximation and perturbation theory in the e-ph interaction; (ii) The KG approach naturally accounts for lattice anharmonicity to all orders albeit limited by the size of supercells. Thus, Equation (6.1) provides an anharmonic correction to BTE calculations.

Second, in order to make larger-supercell calculations possible, it is crucial to reduce the computational cost due to the dense $\mathbf{k}$-point sampling. For this, it is necessary to go beyond the Monkhorst-Pack scheme that generates a regularly spaced $\mathbf{k}$-mesh, given that the charge carriers in semiconductors are typically distributed near the band extrema. Previous BTE studies have shown that the $\mathbf{k}$-point convergence can be accelerated using quasirandom grids with a densified sampling near the band extrema (see, e.g., Ref. [157]). If one prefers the Monkhorst-Pack scheme, a simple linear interpolation of the electronic eigenvalues and momentum-matrix elements from a relatively coarse grid to a fine grid can be performed. The linear interpolation has been used to interpolate the e-ph matrix elements in *ab initio* BTE calculations (see, e.g., Ref. [124]; Wannier interpolation [89, 100] is more commonly used but complex). In KG calculations, the linear interpolation is expected to be simple, because thermal atomic displacements in the supercell eliminate band degeneracies and different **k**-points do not couple.

Besides, since *ai*MD simulations are typically limited to system sizes of a few hundred atoms and time scales of tens of picoseconds, neural network based schemes are being actively developed to substantially overcome this limitation while at the same time retaining the *ai*MD accuracy [220, 221, 222].

Third, more case studies are needed to enhance the understanding of the role of lattice anharmonicity in electronic transport in crystalline solids. The metal-halide perovskites are such interesting systems, as they are found to exhibit strong lattice anharmonicity and even dynamic disorder at room temperature [19, 20].

Improving the predictive power of *ab initio* description of electronic transport in crystalline solids is an active area of research, though the current focus is on the *ab initio* BTE approach. Here we introduce some recent topics and advances in this research area. First, efforts are being made to study complex materials, such as metal-halide perovskites [22, 23], transition-metal oxides [223], and organic molecular crystals [31, 224]. These studies have revealed the critical role of higher-order electron-phonon interactions (e.g., multiphonon processes, temperature-dependent renormalization of the electronic band structure) in understanding the electronic transport properties of complex materials. Second, efforts are being devoted to push the accuracy of the *ab initio* BTE approach to its limits, e.g., by using the *GW* correction of DFT eigenvalues and including spin-orbital coupling [225, 127, 157]. It is worth noting that while the e-ph matrix elements are usually computed at the DFPT level, the recently developed *GW* perturbation theory (*GW*PT) gives access to e-ph matrix elements at the *GW* level [226]. Third, attention is being paid to a long-standing challenge — *ab initio* calculations of carrier-defect interactions. This is crucial for studying the electronic transport in realistic doped semiconductors. First-principles approach to this problem has existed for more than a decade [227, 228]: perturbative calculations of electron-defect interaction matrix elements $\langle \psi_{n\mathbf{k}} | (V_\mathrm{d} - V_\mathrm{ref}) | \psi_{m\mathbf{k}'} \rangle$ (where V_d and V_ref are the crystal potential in the defect and pristine supercells, respectively). However, due to the high computational cost, so far carrier-defect scattering is usually treated using semi-empirical models [125, 157]. The recent progress in this direction is to develop specialized numerical techniques to make such calculations tractable [229]. It is straightforward to account for realistic point defects in *ab initio* KG calculations, which are based on the supercell approach (commonly used for first-principles calculations of point defects in crystalline solids [52]). Finally, a good news for this research area is the looming “exascale computing" with an unprecedented amount of computational power [230].

A Appendix

A.1 Kubo's identity

Here we give a proof of the "Kubo's identity" [131, 231] for a physical observable O:

$$[\varrho_0, O] = i\hbar \int_0^\beta \varrho_0 \dot{O}(-i\hbar\lambda) d\lambda, \tag{A.1}$$

where $\dot{O}$ is the time derivative of O at $t = 0$, i.e.,

$$\frac{dO}{dt} = \frac{1}{i\hbar}[O, H], \tag{A.2}$$

and $\dot{O}(-i\hbar\lambda)$ is a Heisenberg operator with an imaginary time $t = -i\hbar\lambda$, following

$$O(t) = e^{iH_0 t/\hbar} O e^{-iH_0 t/\hbar}. \tag{A.3}$$

First,

$$\begin{aligned} e^{\beta H} O e^{-\beta H_0} - O &= \int_0^\beta \frac{d}{d\lambda}[e^{\lambda H_0} O e^{-\lambda H_0}] \\ &= \int_0^\beta (\frac{d}{d\lambda} e^{\lambda H_0}) O e^{-\lambda H_0} + e^{\beta H} O (\frac{d}{d\lambda} e^{-\lambda H_0})] \\ &= \int_0^\beta [e^{\lambda H_0} H_0 O e^{-\lambda H_0} - e^{\lambda H_0} O H_0 e^{-\lambda H_0}] d\lambda \\ &= \int_0^\beta e^{\lambda H_0} [H_0, O] e^{-\lambda H_0} d\lambda. \end{aligned} \tag{A.4}$$

Second,

$$\begin{aligned} e^{\beta H} O e^{-\beta H_0} - O &= e^{\beta H} O e^{-\beta H_0} - e^{\beta H} e^{-\beta H_0} O \\ &= e^{\beta H} [O, e^{-\beta H_0}]. \end{aligned} \tag{A.5}$$

Then we get,

$$\begin{aligned}[O, e^{-\beta H_0}] &= e^{-\beta H_0} \int_0^\beta e^{\lambda H_0}[H, O]e^{-\lambda H_0} d\lambda \\ &= i\hbar e^{-\beta H_0} \int_0^\beta e^{\lambda H_0} \dot{O} e^{-\lambda H_0} d\lambda \\ &= i\hbar e^{-\beta H_0} \int_0^\beta \dot{O}(-i\hbar\lambda) d\lambda, \end{aligned} \tag{A.6}$$

which is just the Kubo's identity by noticing $\varrho_0 = e^{-\beta H_0}/\mathrm{Tr}\{e^{-\beta H_0}\}$.

A.2 Supplementary data for the study of silicon

A.2.1 Convergence of atomic forces in MD simulations

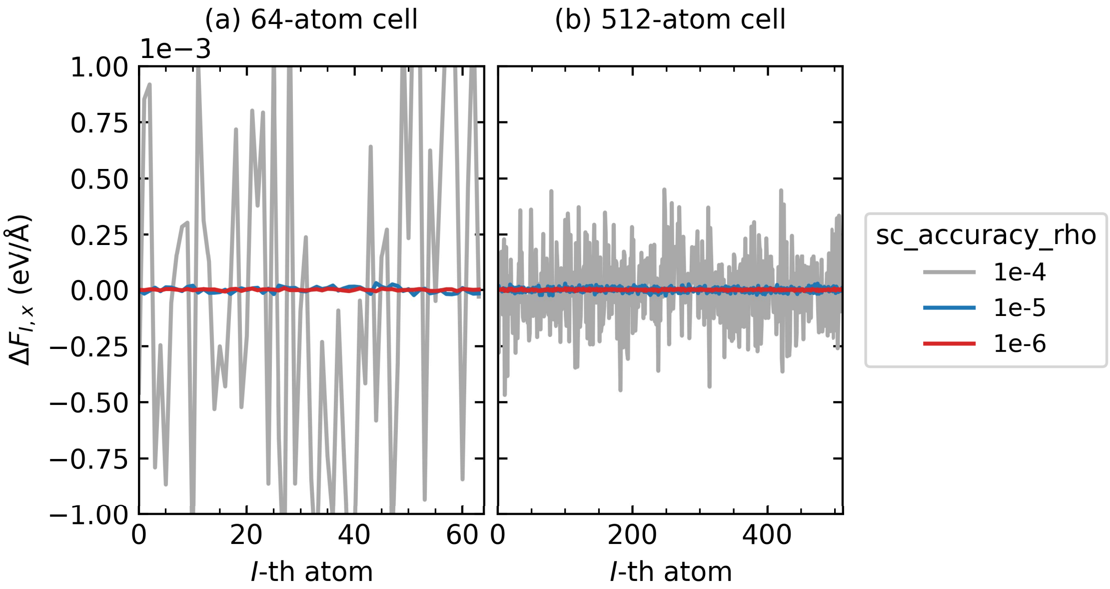

Figure A.1: Convergence of atomic forces for different density convergence criteria: 1e-4, 1e-5, 1e-6 eV/Å^3 (specified by the “sc_accuracy_rho" tag in the FHI-aims standard input file control.in). (a) 64-atom supercell calculated with a $3 \times 3 \times 3$ $\mathbf{k}$-point mesh. (b) 512-atom supercell calculated with a Γ-only $\mathbf{k}$-point mesh. Here the atomic forces are reported as a difference to those for the case of 1e-8 eV/Å^3 (for this reference, the convergence criterion for the atomic forces is also set and is 10^{-4} eV/Å).

In *ai*MD simulations, each time step involves a SCF calculation, at the end of which the atomic forces are computed and used for updating the MD trajectory. In Figure A.1, we show that converged atomic forces can be guaranteed by checking only the density convergence criterion, which is the most important SCF convergence criterion in the FHI-aims calculations. Based on this test, we set the density convergence criterion to 10^{-6} eV/Å^3 for both the 64- and 216-atom supercells, and to 10^{-5} eV/Å^3 for both the 512- and 1000-atom supercells.

A.2.2 Uncorrelated samples

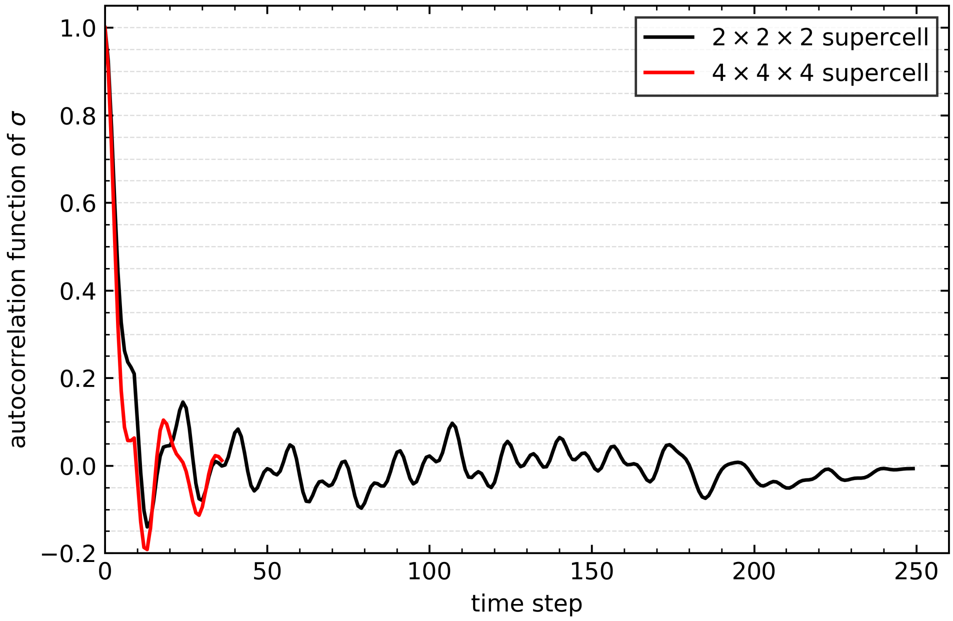

Figure A.2: Autocorrelation function of the electrical conductivity along a *ai*MD trajectory. Each time step is 4 fs.

In order to generate a set of uncorrelated samples from *ai*MD simulations, it is important to collect samples regularly with a sufficiently large sampling time interval. To see how many time steps are needed to guarantee that two samples (or snapshots) can be viewed as uncorrelated, we calculate the autocorrelation function of the electrical conductivity for both the $2 \times 2 \times 2$ and $4 \times 4 \times 4$ supercells (The electrical conductivities are calculated using $20 \times 20 \times 20$ and $10 \times 10 \times 10$ **k**-meshes, respectively, and broadening parameter $\eta = 20$ meV). As shown in Figure A.2, the correlation is lost very fast, and a sampling time interval of 10 time steps (i.e., 40 fs) is sufficient for the samples being uncorrelated. By weighing the computational cost and for safety, we choose to use a sampling time interval of 50 time steps (i.e., 200 fs).

A.2.3 thermal lattice expansion

We describe how to determine the lattice constant of Si at 300 K using the “quasi-NPT" method as implemented in the FHI-vibes code [185]. This method has two steps.

In the first step, we evaluate the internal pressure of the zero-T (DFT-LDA optimized) equilibrium structure of Si when it is at 300 K. To this end, we perform *ai*MD-NVT simulations at 300 K in a $2 \times 2 \times 2$ (64-atom) cubic supercell, which is constructed based on the zero-T lattice constant. The total MD time length is 10 ps, of which the last 8 ps period is used for computing the stress tensor, i.e., internal pressure [232]. The internal pressure at 300 K is calculated to be 0.0023 eV/Å^3, suggesting that the zero-T structure tends to expand at 300 K. Test calculation using a $3 \times 3 \times 3$ (216-atom) supercell yields a very similar value of pressure. This is expected, as the lattice anharmonicities are generally short-range interactions.

In the second step, we perform again structural relaxation but this time the unit cell is under an external hydrostatic pressure (denoted as p_{ext}), thus requiring minimizing the enthalpy [232]:

$$H_f(p_{\text{ext}}) = E_{\text{tot}}(V) + p_{\text{ext}}V, \tag{A.7}$$

where $E_{\text{tot}}(V)$ is the DFT total energy, and V the unit-cell volume. Here, the p_{ext} is negative and has the same absolute value as the computed internal pressure in the first step. In the structural relaxation, atomic forces were required to be less than 10^{-4} eV/Å. By means of this, we obtain the lattice constant of Si at 300 K, as shown in Table 4.1 in the main text. Using the calculated thermally expanded lattice constant, we repeat the first step, and find that the internal pressure becomes negligibly small.

To verify the “quasi-NPT" method, we have also estimated the lattice constant at 300 K using extrapolation based on the empirical formula [187]:

$$a(T) = a_0[\int_0^T \alpha(T)dT + 1], \tag{A.8}$$

where α is the temperature-dependent thermal expansion coefficient, and a_0 the zero-T lattice constant. In experiment, Equation (A.8) was used to fit the temperature-dependent lattice constant of Si, and $\alpha(300\text{K}) = 2.57 \times 10^{-6}$ K^{-1} [187]. Here we use the DFT-LDA optimized lattice constant (5.417 Å) as the a_0 to derive the lattice constant at 300 K. The extrapolated lattice constant is shown in Table 4.1 in the main text.

In Chapter 5, the lattice constants of SnSe at 300 K and at 523 K are determined using the “quasi-NPT" method and the extrapolation method, respectively. For the former, we did not do the calculation ourselves, but instead we obtain the lattice-constant data from the NOMAD repository (Florian Knoop, not yet published).

A.2.4 k-point convergence and broadening parameter

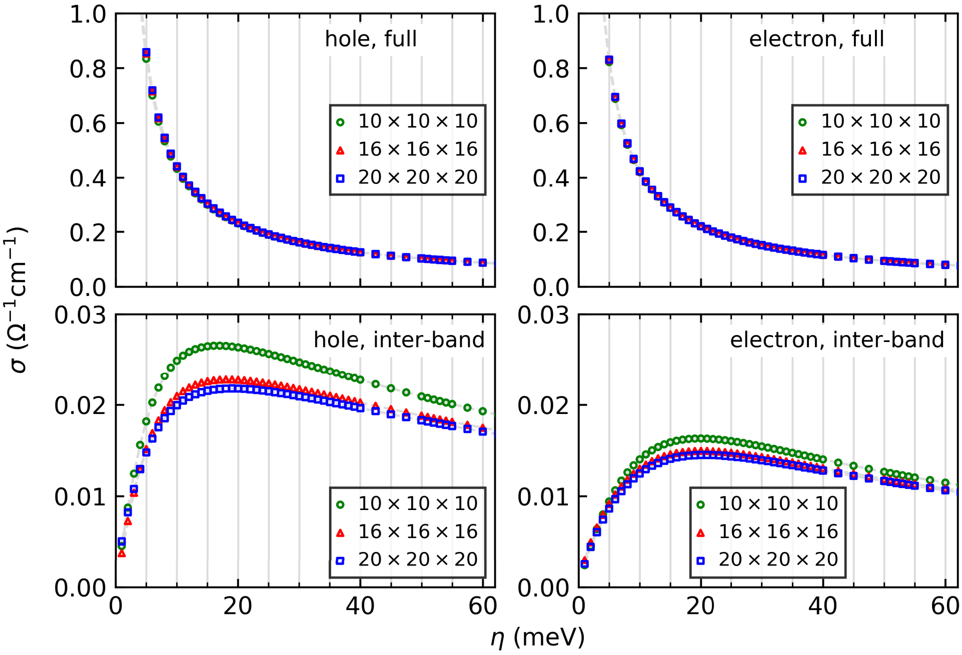

Figure A.3: The hole and electron electrical conductivities (upper panels) and their inter-band contributions (lower panels) in the $4 \times 4 \times 4$ supercell as a function of broadening parameter (η), for different **k**-point samplings. “full" means that the electrical conductivity is not decomposed into its constituent terms. The results are for intrinsic Si at 300 K. Note the different scales of the y-axes. The dashed lines and grids are a guide to the eye.

We have further checked how the broadening parameter (η) affects the **k**-point convergence, following the discussion in Section 4.2.1 in the main text. The $4 \times 4 \times 4$ supercell used in Section 4.2.1 and 4.2.3 in the main text is studied here. We focus on whether the $10 \times 10 \times 10$ **k**-mesh can produce reliable results for the electrical conductivity in the $4 \times 4 \times 4$ supercell, and how η affects this.

The upper subplots of Figure A.3 show that the **k**-point convergence of the (full) electrical conductivity is well achieved with the $10 \times 10 \times 10$ **k**-mesh and largely independent of η. This conclusion also holds for the $2 \times 2 \times 2$ supercell (not displayed).

The lower subplots of Figure A.3 show that the inter-band contribution constitutes only a very small portion of the full electrical conductivity, and its **k**-point convergence depends on η. With the $10 \times 10 \times 10$ **k**-mesh, the inter-band contribution (especially for the hole conductivity) is slightly underconverged. The largest underconvergence is at the η value where the inter-band contribution is a maximum. Despite the small underconvergence, the maximum of the inter-band contribution given by the 10 × 10 × 10 **k**-mesh and given by the denser **k**-meshes are located at nearly the same η value. In the optimal-η scheme, we take the η value which maximizes the inter-band contribution. In this respect, the 10 × 10 × 10 **k**-mesh is good enough, since it has precisely located the η value we want. We also find that the 20 × 20 × 20 **k**-mesh fully converges the inter-band contribution to the electrical conductivity in the 2 × 2 × 2 supercell (not displayed). The case of the 5 × 5 × 5 supercell is not checked, simply because **k**-mesh denser than 7 × 7 × 7 (which is used for this supercell) is computationally unfeasible.

A.2.5 Intrinsic Si: Band gaps and carrier concentrations

Table A.1: Band gaps (E_g) and intrinsic carrier concentrations (n_i) in the supercells of intrinsic Si at 300 K. They are estimated by the sample means. The LDA band gaps have been corrected with a scissor operator of 0.667 eV. At 300 K, the measured band gap and intrinsic carrier concentration are 1.1242 eV and 1.07×10^{10} cm^{-3}, respectively [193].

Supercell size	# samples	E_g (eV)	n_i (cm^{-3})
2 × 2 × 2	655	1.0595	2.5715×10^{10}
3 × 3 × 3	404	1.0629	2.2035×10^{10}
4 × 4 × 4	204	1.0743	2.1983×10^{10}
5 × 5 × 5	100	1.0758	2.2128×10^{10}

A.2.6 Doped Si: Broadening parameter and finite-size scaling

Table A.2 presents our chosen η values for the electrical conductivity calculations in hole- and electron-doped Si at 300 K. Note that the free-carrier doping is simulated using the rigid-band approximation, as detailed in the main text. Compared to the η values listed in Table 4.5 for intrinsic Si, the η values are hardly changed by the doping, except for the 2 × 2 × 2 supercell. In addition, for the 3 × 3 × 3 supercell, the η value is 35 meV when the hole concentration is 4.06×10^{18} cm^{-3}. In our KG calculations, we see this kind of problem in the case of small supercells, i.e., 2 × 2 × 2 and 3 × 3 × 3. These two supercells are far from being a good approximation to the thermodynamic limit. However, we still include them in the finite-size scaling, since we do not have a convincing reason to leave them out.

In the case of intrinsic Si, we have employed the polynomial in the form of $\sigma(\infty) + a_1/L + a_3/L^3$ ($1/L$ denotes the inverse supercell length) to perform the finite-size scaling. Now we check whether this polynomial form can still produce good fit in the presence of carrier doping. To this end, we take two of our considered hole densities as examples, which are $n_\mathrm{h} = 1.325 \times 10^{14}$ and 4.06×10^{18} cm^{-3}. Figure A.4 shows the finite-size scalings of the calculated electrical conductivity results for these two hole doping levels. We find that for both cases, the polynomial form $\sigma(\infty) + a_1/L + a_3/L^3$ provides good fit quality. In fact, we have done tests for all considered doping levels for both hole and electron conductivities.

Table A.2: The η values determined with the optimal-η scheme. The η_h are used for computing the hole conductivities in hole-doped Si at 300 K; the η_e are used for computing the electron conductivities in electron-doped Si at 300 K.

Supercell size	η_h (meV)	η_e (meV)
$2 \times 2 \times 2$	55	50
$3 \times 3 \times 3$	34	26
$4 \times 4 \times 4$	24	14
$5 \times 5 \times 5$	18	10

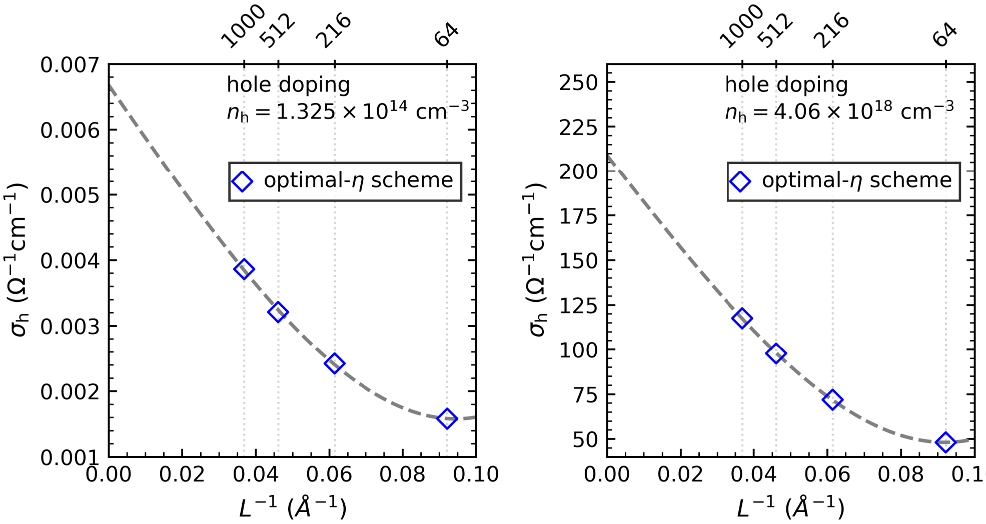

Figure A.4: Finite-size scaling of the calculated electrical conductivities in the supercells of hole-doped Si at 300 K. Two hole doping levels, $n_\mathrm{h} = 1.325 \times 10^{14}$ and 4.06×10^{18} cm^{-3}, are considered. The polynomial function in the form of $\sigma(\infty) + a_1/L + a_3/L^3$ is used as the fit function.

A.3 Supplementary data for the study of SnSe

A.3.1 Convergence of k-point sampling in the y direction

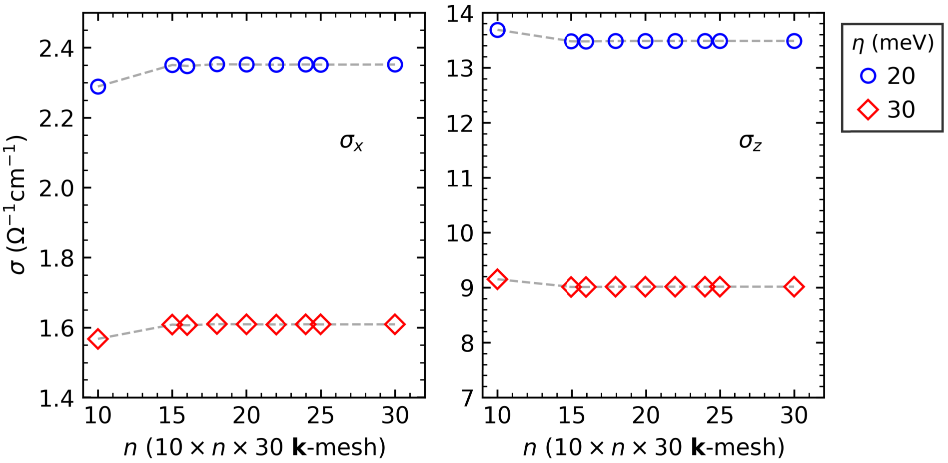

Figure A.5: Left panel: the x-component electrical conductivity (σ_x) in the $2 \times 2 \times 2$ supercell as a function of n for a $10 \times n \times 30$ **k**-point sampling; Right panel: the z-component electrical conductivity (σ_z) in the $2 \times 2 \times 2$ supercell as a function of n for a $10 \times n \times 30$ **k**-point sampling. The results are for hole-doped SnSe at 300 K. The gray dashed lines are a guide to the eye.

A.3.2 k-point convergence and broadening parameter

We have also checked the influence of η on the **k**-point convergence of the electrical conductivity and its inter-band contribution. For this, we consider the $2 \times 4 \times 4$ supercell as it is used in computing both the σ_x and σ_z. We take a random sample of the $2 \times 4 \times 4$ supercell as an example, and perform KG calculations using different **k**-meshes, including the $10 \times 15 \times 15$ mesh listed in Table 5.3.

Figure A.6(a) shows that the **k**-point convergence of the σ_x in the $2 \times 4 \times 4$ supercell is well achieved with the $10 \times 15 \times 15$ **k**-mesh and independent of η (over the η range displayed). With the $10 \times 15 \times 15$ **k**-mesh, the inter-band contribution to σ_x shows very satisfactory **k**-point convergence, as seen in Figure A.6(b). Similar conclusions can be draw from Figure A.7(a) for the σ_z and from Figure A.7(b) for the inter-band contribution to σ_z. These additional tests suggest that there is generally no need to worry about the influence of η on the **k**-point convergence of the electrical conductivity. This is especially so considering that we use the sample-averaged inter-band contribution in determining the value of η with the optima-η scheme.

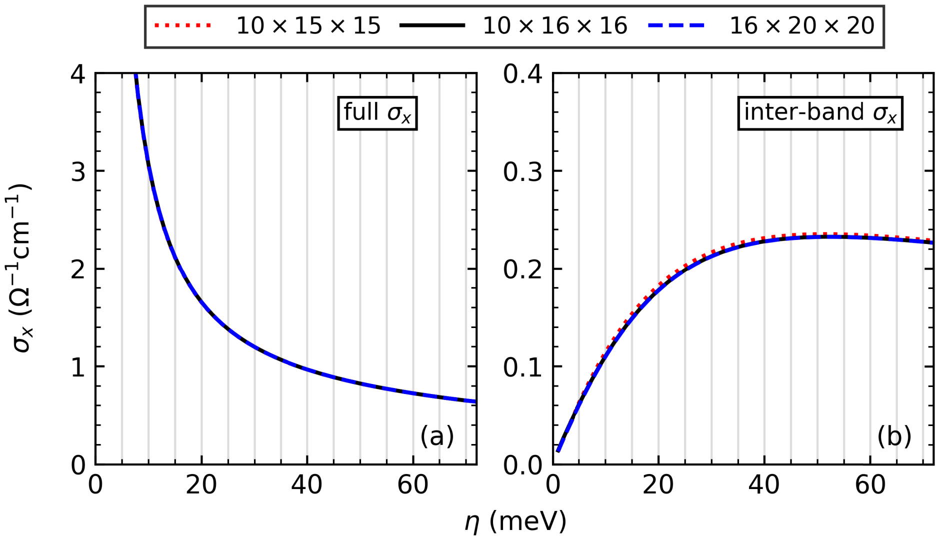

Figure A.6: The σ_x (left) and its inter-band contribution (right) in the $2 \times 4 \times 4$ supercell versus the broadening parameter (η), for three different **k**-meshes: $10 \times 15 \times 15$, $10 \times 16 \times 16$, and $16 \times 20 \times 20$. “full" means that the electrical conductivity is not decomposed into its constituent terms. The results are for hole-doped SnSe at 300 K. Note the different scales of the y-axes. The gray grids are a guide to the eye.

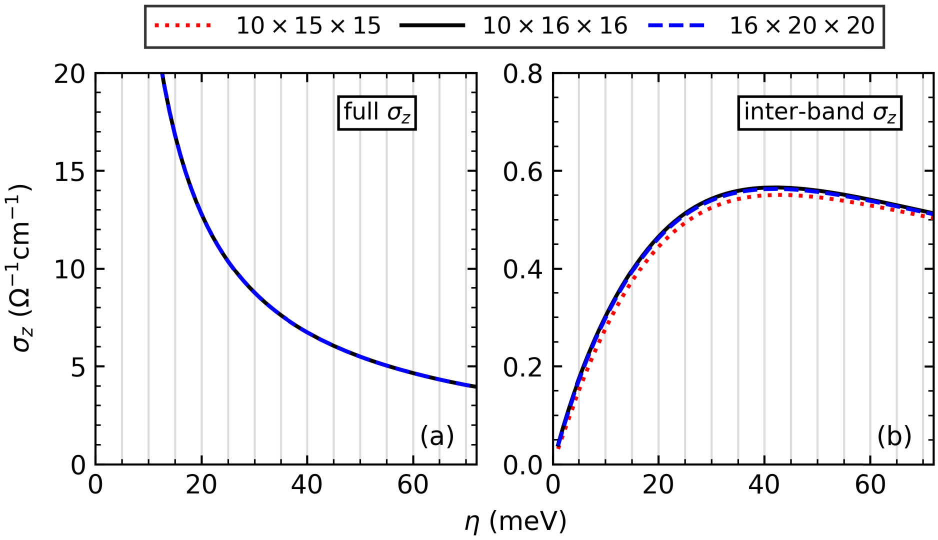

Figure A.7: Same as Figure A.6, but for the σ_z and its inter-band contribution.

A.3.3 Statistical convergence for two cases

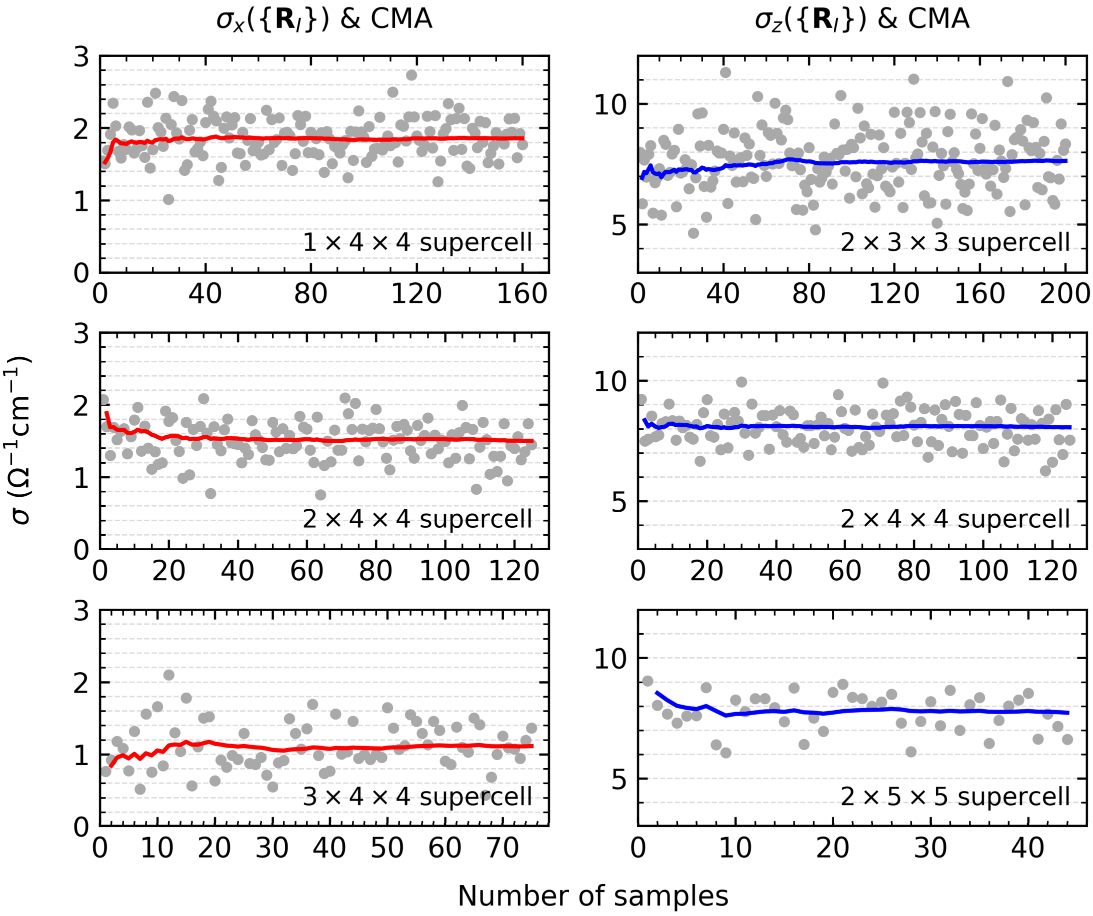

Figure A.8: Same as Figure 5.6 in the main text but for the common choice $\eta = 30$ meV. Note the different scales of the y-axes in the left and right panels. Also note that the scales of the y-axes in the left panels are different from those in Figure 5.6.

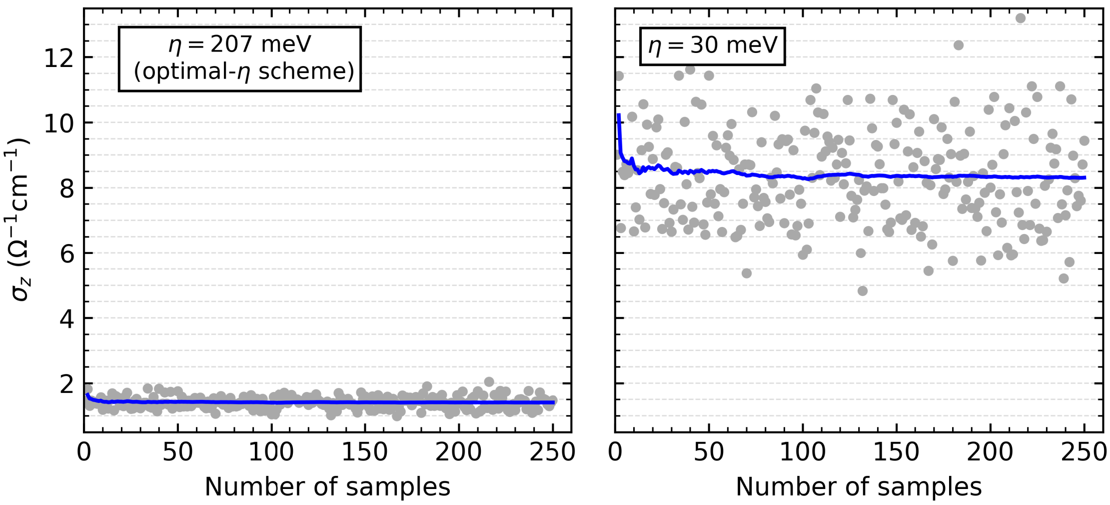

Figure A.9: Convergence of the z-component electrical conductivity with respect to the number of samples, for the $2 \times 2 \times 2$ (64-atom) supercell. Left panel: results calculated at $\eta = 207$ meV (determined with the optimal-η scheme). Right panel: results calculated at $\eta = 30$ meV. Gray dots: $\sigma_z(\{\mathbf{R}_I\})$ for individual samples ($\{\mathbf{R}_I\}$ denotes the atomic configuration). The results are for hole-doped SnSe at 300 K, and calculated using the $\mathbf{k}$-meshes listed in Table 5.3. Blue lines: cumulative moving average (CMA).

A.3.4 k- and q-point samplings in previous BTE studies

Table A.3: The **k**- and **q**-meshes used in the *ab initio* BTE calculations of the electronic transport in SnSe reported in literature. In these studies, the e-ph matrix elements on the coarse grids in the DFPT calculations were interpolated to the fine grids in the solution of the BTE.

Purpose	**k**-mesh	**q**-mesh
DFPT e-ph calculations		
Caruso *et al.* [24]	$4 \times 8 \times 8$	$2 \times 4 \times 4$
Li *et al.* [216]	$6 \times 6 \times 6$	$3 \times 3 \times 3$
Ma *et al.* [21]	$3 \times 6 \times 6$	$3 \times 6 \times 6$
Solution of the BTE		
Caruso *et al.* [24]	$20 \times 60 \times 60$	88,942 random points
Li *et al.* [216]	$40 \times 40 \times 40$	$25 \times 25 \times 25$
Ma *et al.* [21]	$36 \times 96 \times 96$	$36 \times 96 \times 96$

Bibliography

[1] Hideo Hosono and Kazushige Ueda. Transparent conducting oxides. In Springer Handbook of Electronic and Photonic Materials, page 1391. Springer, 2017.

[2] Milton Ohring. Engineering materials science, page 561. Elsevier, 1995.

[3] Brian S Mitchell. An introduction to materials engineering and science for chemical and materials engineers. John Wiley & Sons, 2004.

[4] Otfried Madelung. Semiconductors-basic data. Springer Science & Business Media, 2012.

[5] Akira Uedono, Shoichiro Tanigawa, Ryoichi Suzuki, Hideaki Ohgaki, and Tomohisa Mikado. Defects in heavily phosphorus-doped Si epitaxial films probed by monoenergetic positron beams. Japanese journal of applied physics, 33(11R): 6286, 1994.

[6] Jun-ichi Nishizawa, Hideo Otsuka, Shigenobu Yamakoshi, and Katsuhiko Ishida. Nonstoichiometry of Te-doped GaAs. Japanese Journal of Applied Physics, 13(1): 46, 1974.

[7] T. J. Scheidemantel, C. Ambrosch-Draxl, T. Thonhauser, J. V. Badding, and J. O. Sofo. Transport coefficients from first-principles calculations. Phys. Rev. B, 68: 125210, Sep 2003.

[8] Claudia Draxl and Matthias Scheffler. Big Data-Driven Materials Science and Its FAIR Data Infrastructure. Handbook of Materials Modeling: Methods: Theory and Modeling, pages 49–73, 2020.

[9] Claudia Draxl and Matthias Scheffler. The NOMAD laboratory: from data sharing to artificial intelligence. Journal of Physics: Materials, 2(3):036001, 2019.

[10] Prashun Gorai, Vladan Stevanović, and Eric S Toberer. Computationally guided discovery of thermoelectric materials. Nature Reviews Materials, 2(9):1–16, 2017.

[11] Donald T Morelli. Thermoelectric materials. In Springer Handbook of Electronic and Photonic Materials, page 1379. Springer, 2017.

[12] Marco Bernardi. First-principles dynamics of electrons and phonons. The European Physical Journal B, 89(11):239, 2016.

[13] Samuel Poncé, Wenbin Li, Sven Reichardt, and Feliciano Giustino. First-principles calculations of charge carrier mobility and conductivity in bulk semiconductors and two-dimensional materials. Reports on Progress in Physics, 83 (3):036501, 2020.

[14] Feliciano Giustino. Electron-phonon interactions from first principles. Reviews of Modern Physics, 89(1):015003, 2017.

[15] Florian Knoop, Thomas AR Purcell, Matthias Scheffler, and Christian Carbogno. Anharmonicity measure for materials. Physical Review Materials, 4(8):083809, 2020.

[16] Dennis S Kim, O Hellman, N Shulumba, Claire N Saunders, Jiao YY Lin, Hillary L Smith, JE Herriman, Jennifer L Niedziela, Douglas L Abernathy, Chen W Li, et al. Temperature-dependent phonon lifetimes and thermal conductivity of silicon by inelastic neutron scattering and ab initio calculations. Physical Review B, 102(17): 174311, 2020.

[17] Chen W Li, Jiawang Hong, Andrew F May, Dipanshu Bansal, Songxue Chi, Tao Hong, Georg Ehlers, and O Delaire. Orbitally driven giant phonon anharmonicity in SnSe. Nature Physics, 11(12):1063–1069, 2015.

[18] Yu Xiao, Cheng Chang, Yanling Pei, Di Wu, Kunling Peng, Xiaoyuan Zhou, Shengkai Gong, Jiaqing He, Yongsheng Zhang, Zhi Zeng, et al. Origin of low thermal conductivity in SnSe. Physical Review B, 94(12):125203, 2016.

[19] Christian Gehrmann and David A Egger. Dynamic shortening of disorder potentials in anharmonic halide perovskites. Nature communications, 10(1):1–9, 2019.

[20] Marcelo A Carignano, S Assa Aravindh, Iman S Roqan, Jacky Even, and Claudine Katan. Critical fluctuations and anharmonicity in lead iodide perovskites from molecular dynamics supercell simulations. The Journal of Physical Chemistry C, 121(38):20729–20738, 2017.

[21] Jinlong Ma, Yani Chen, and Wu Li. Intrinsic phonon-limited charge carrier mobilities in thermoelectric SnSe. Physical Review B, 97(20):205207, 2018.

[22] Samuel Poncé, Martin Schlipf, and Feliciano Giustino. Origin of low carrier mobilities in halide perovskites. ACS Energy Letters, 4(2):456–463, 2019.

[23] Chelsea Q Xia, Jiali Peng, Samuel Poncé, Jay B Patel, Adam D Wright, Timothy W Crothers, Mathias Uller Rothmann, Juliane Borchert, Rebecca L Milot,

Hans Kraus, et al. Limits to electrical mobility in lead-halide perovskite semiconductors. The Journal of Physical Chemistry Letters, 12:3607–3617, 2021.

[24] Fabio Caruso, Maria Troppenz, Santiago Rigamonti, and Claudia Draxl. Thermally enhanced Fröhlich coupling in SnSe. Physical Review B, 99(8):081104, 2019.

[25] Jin-Jian Zhou, Olle Hellman, and Marco Bernardi. Electron-phonon scattering in the presence of soft modes and electron mobility in SrTiO3 perovskite from first principles. Physical review letters, 121(22):226603, 2018.

[26] Gabriel Antonius, Yang-Hao Chan, and Steven G Louie. Polaron spectral properties in doped ZnO and SrTiO3 from first principles. Physical Review Research, 2 (4):043296, 2020.

[27] Göran Grimvall, Blanka Magyari-Köpe, Vidvuds Ozoliņš, and Kristin A Persson. Lattice instabilities in metallic elements. Reviews of Modern Physics, 84(2):945, 2012.

[28] Olle Hellman and Igor A Abrikosov. Temperature-dependent effective third-order interatomic force constants from first principles. Physical Review B, 88 (14):144301, 2013.

[29] Bartomeu Monserrat, ND Drummond, and RJ Needs. Anharmonic vibrational properties in periodic systems: energy, electron-phonon coupling, and stress. Physical Review B, 87(14):144302, 2013.

[30] Nien-En Lee, Jin-Jian Zhou, Hsiao-Yi Chen, and Marco Bernardi. Ab initio electron-two-phonon scattering in GaAs from next-to-leading order perturbation theory. Nature communications, 11(1):1–7, 2020.

[31] Florian Brown-Altvater, Gabriel Antonius, Tonatiuh Rangel, Matteo Giantomassi, Claudia Draxl, Xavier Gonze, Steven G Louie, and Jeffrey B Neaton. Band gap renormalization, carrier mobilities, and the electron-phonon self-energy in crystalline naphthalene. Physical Review B, 101(16):165102, 2020.

[32] Lucas Calderin, Valentin V Karasiev, and Samuel B Trickey. Kubo-Greenwood electrical conductivity formulation and implementation for projector augmented wave datasets. Computer Physics Communications, 221:118–142, 2017.

[33] Stefano Baroni, Stefano De Gironcoli, Andrea Dal Corso, and Paolo Giannozzi. Phonons and related crystal properties from density-functional perturbation theory. Reviews of Modern Physics, 73(2):515, 2001.

[34] Dario Alfè, Monica Pozzo, and Michael P Desjarlais. Lattice electrical resistivity of magnetic bcc iron from first-principles calculations. Physical Review B, 85(2): 024102, 2012.

[35] Martin French and Thomas R Mattsson. Thermoelectric transport properties of molybdenum from ab initio simulations. Physical Review B, 90(16):165113, 2014.

[36] Richard M. Martin. Electronic Structure: Basic Theory and Practical Methods. Cambridge University Press, 2004. doi: 10.1017/CBO9780511805769.003.

[37] Robert O Jones and Olle Gunnarsson. The density functional formalism, its applications and prospects. Reviews of Modern Physics, 61(3):689, 1989.

[38] Mike C Payne, Michael P Teter, Douglas C Allan, TA Arias, and ad JD Joannopoulos. Iterative minimization techniques for ab initio total-energy calculations: molecular dynamics and conjugate gradients. Reviews of modern physics, 64 (4):1045, 1992.

[39] P Haynes. Linear-scaling methods in ab initio quantum-mechanical calculations. PhD thesis, University of Cambridge, 1998.

[40] P. Hohenberg and W. Kohn. Inhomogeneous electron gas. Phys. Rev., 136:B864–B871, Nov 1964.

[41] W. Kohn and L. J. Sham. Self-consistent equations including exchange and correlation effects. Phys. Rev., 140:A1133–A1138, Nov 1965.

[42] John P Perdew et al. Understanding band gaps of solids in generalized Kohn-Sham theory. Proceedings of the National Academy of Sciences, 114(11):2801–2806, 2017.

[43] J. P. Perdew and Alex Zunger. Self-interaction correction to density-functional approximations for many-electron systems. Phys. Rev. B, 23:5048–5079, May 1981.

[44] John P Perdew, Robert G Parr, Mel Levy, and Jose L Balduz Jr. Density-functional theory for fractional particle number: derivative discontinuities of the energy. Physical Review Letters, 49(23):1691, 1982.

[45] James F Janak. Proof that $\partial E/\partial n_i = \varepsilon_i$ in density-functional theory. Physical Review B, 18(12):7165, 1978.

[46] C Göransson, Weine Olovsson, and Igor A Abrikosov. Numerical investigation of the validity of the Slater-Janak transition-state model in metallic systems. Physical Review B, 72(13):134203, 2005.

[47] John Clarke Slater. The self-consistent field for molecules and solids, volume 4. McGraw-Hill, 1974.

[48] N David Mermin. Thermal properties of the inhomogeneous electron gas. Physical Review, 137(5A):A1441, 1965.

[49] BG Walker, C Molteni, and N Marzari. Ab initio molecular dynamics of metal surfaces. Journal of Physics: Condensed Matter, 16(26):S2575, 2004.

[50] Aron J Cohen, Paula Mori-Sánchez, and Weitao Yang. Challenges for density functional theory. Chemical reviews, 112(1):289–320, 2012.

[51] John P Perdew and Karla Schmidt. Jacob's ladder of density functional approximations for the exchange-correlation energy. In AIP Conference Proceedings, volume 577, pages 1–20. American Institute of Physics, 2001.

[52] Christoph Freysoldt, Blazej Grabowski, Tilmann Hickel, Jörg Neugebauer, Georg Kresse, Anderson Janotti, and Chris G Van de Walle. First-principles calculations for point defects in solids. Reviews of modern physics, 86(1):253, 2014.

[53] David M Ceperley and Berni J Alder. Ground state of the electron gas by a stochastic method. Physical Review Letters, 45(7):566, 1980.

[54] John P. Perdew and Yue Wang. Accurate and simple analytic representation of the electron-gas correlation energy. Phys. Rev. B, 45:13244–13249, Jun 1992.

[55] Olle Gunnarsson and Bengt I Lundqvist. Exchange and correlation in atoms, molecules, and solids by the spin-density-functional formalism. Physical Review B, 13(10):4274, 1976.

[56] Philipp Haas, Fabien Tran, and Peter Blaha. Calculation of the lattice constant of solids with semilocal functionals. Physical Review B, 79(8):085104, 2009.

[57] Guo-Xu Zhang, Anthony M Reilly, Alexandre Tkatchenko, and Matthias Scheffler. Performance of various density-functional approximations for cohesive properties of 64 bulk solids. New Journal of Physics, 20(6):063020, 2018.

[58] John P Perdew. Density functional theory and the band gap problem. International Journal of Quantum Chemistry, 28(S19):497–523, 1985.

[59] John P Perdew, Kieron Burke, and Matthias Ernzerhof. Generalized gradient approximation made simple. Physical review letters, 77(18):3865, 1996.

[60] Xin Xu and William A Goddard III. The extended Perdew-Burke-Ernzerhof functional with improved accuracy for thermodynamic and electronic properties of molecular systems. The Journal of chemical physics, 121(9):4068–4082, 2004.

[61] John P. Perdew, Kieron Burke, and Matthias Ernzerhof. Generalized gradient approximation made simple. Phys. Rev. Lett., 77:3865–3868, 1996.

[62] Elliott H Lieb and Stephen Oxford. Improved lower bound on the indirect coulomb energy. International Journal of Quantum Chemistry, 19(3):427–439, 1981.

[63] John P. Perdew, Adrienn Ruzsinszky, Gábor I. Csonka, Oleg A. Vydrov, Gustavo E. Scuseria, Lucian A. Constantin, Xiaolan Zhou, and Kieron Burke. Restoring the density-gradient expansion for exchange in solids and surfaces. Phys. Rev. Lett., 100:136406, 2008.

[64] Pedro Borlido, Thorsten Aull, Ahmad W Huran, Fabien Tran, Miguel AL Marques, and Silvana Botti. Large-scale benchmark of exchange-correlation functionals for the determination of electronic band gaps of solids. Journal of chemical theory and computation, 15(9):5069–5079, 2019.

[65] John P Perdew, Matthias Ernzerhof, and Kieron Burke. Rationale for mixing exact exchange with density functional approximations. The Journal of chemical physics, 105(22):9982–9985, 1996.

[66] Stewart J Clark and John Robertson. Screened exchange density functional applied to solids. Physical Review B, 82(8):085208, 2010.

[67] T Körzdörfer and Stephan Kümmel. Single-particle and quasiparticle interpretation of kohn-sham and generalized kohn-sham eigenvalues for hybrid functionals. Physical Review B, 82(15):155206, 2010.

[68] Jochen Heyd, Gustavo E Scuseria, and Matthias Ernzerhof. Hybrid functionals based on a screened coulomb potential. The Journal of chemical physics, 118(18): 8207–8215, 2003.

[69] Aliaksandr V Krukau, Oleg A Vydrov, Artur F Izmaylov, and Gustavo E Scuseria. Influence of the exchange screening parameter on the performance of screened hybrid functionals. The Journal of chemical physics, 125(22):224106, 2006.

[70] John P Perdew and Mel Levy. Physical content of the exact Kohn-Sham orbital energies: band gaps and derivative discontinuities. Physical Review Letters, 51 (20):1884, 1983.

[71] L. J. Sham and M. Schlüter. Density-functional theory of the energy gap. Phys. Rev. Lett., 51:1888–1891, Nov 1983.

[72] Paula Mori-Sánchez, Aron J Cohen, and Weitao Yang. Localization and delocalization errors in density functional theory and implications for band-gap prediction. Physical review letters, 100(14):146401, 2008.

[73] LJ Sham and M Schlüter. Density-functional theory of the band gap. Physical Review B, 32(6):3883, 1985.

[74] Paula Mori-Sánchez, Aron J Cohen, and Weitao Yang. Many-electron self-interaction error in approximate density functionals. The Journal of chemical physics, 125(20):201102, 2006.

[75] Marios Zacharias and Feliciano Giustino. Theory of the special displacement method for electronic structure calculations at finite temperature. Physical Review Research, 2(1):013357, 2020.

[76] Joachim Paier, Robin Hirschl, Martijn Marsman, and Georg Kresse. The perdew–burke–ernzerhof exchange-correlation functional applied to the G2-1 test set using a plane-wave basis set. The Journal of chemical physics, 122(23):234102, 2005.

[77] Larry A Curtiss, Krishnan Raghavachari, Paul C Redfern, and John A Pople. Assessment of gaussian-2 and density functional theories for the computation of enthalpies of formation. The Journal of Chemical Physics, 106(3):1063–1079, 1997.

[78] Volker Blum, Ralf Gehrke, Felix Hanke, Paula Havu, Ville Havu, Xinguo Ren, Karsten Reuter, and Matthias Scheffler. Ab initio molecular simulations with numeric atom-centered orbitals. Computer Physics Communications, 180(11):2175–2196, 2009.

[79] José M Soler, Emilio Artacho, Julian D Gale, Alberto García, Javier Junquera, Pablo Ordejón, and Daniel Sánchez-Portal. The siesta method for ab initio order-N materials simulation. Journal of Physics: Condensed Matter, 14(11):2745, 2002.

[80] Jürg Hutter, Marcella Iannuzzi, Florian Schiffmann, and Joost VandeVondele. cp2k: atomistic simulations of condensed matter systems. Wiley Interdisciplinary Reviews: Computational Molecular Science, 4(1):15–25, 2014.

[81] Andris Gulans, Stefan Kontur, Christian Meisenbichler, Dmitrii Nabok, Pasquale Pavone, Santiago Rigamonti, Stephan Sagmeister, Ute Werner, and Claudia Draxl. Exciting: a full-potential all-electron package implementing density-functional theory and many-body perturbation theory. Journal of Physics: Condensed Matter, 26(36):363202, 2014.

[82] Ville Havu, Volker Blum, Paula Havu, and Matthias Scheffler. Efficient O(N) integration for all-electron electronic structure calculation using numeric basis functions. Journal of Computational Physics, 228(22):8367–8379, 2009.

[83] Bernard Delley. High order integration schemes on the unit sphere. Journal of computational chemistry, 17(9):1152–1155, 1996.

[84] Vyacheslav Ivanovich Lebedev and DN Laikov. A quadrature formula for the sphere of the 131st algebraic order of accuracy. In Doklady Mathematics, volume 59, pages 477–481. Pleiades Publishing, Ltd., 1999.

[85] Georg Kresse and Jürgen Furthmüller. Efficiency of ab-initio total energy calculations for metals and semiconductors using a plane-wave basis set. Computational materials science, 6(1):15–50, 1996.

[86] Jouko Lehtomäki, Jingrui Li, and Patrick Rinke. Boron doping in gallium oxide from first principles. Journal of Physics Communications, 4(12):125001, 2020.

[87] Christian Carbogno, Kristian Sommer Thygesen, Björn Bieniek, Claudia Draxl, Luca M Ghiringhelli, Andris Gulans, Oliver T Hofmann, Karsten W Jacobsen, Sven Lubeck, Jens Jørgen Mortensen, et al. Numerical quality control for dft-based materials databases. arXiv preprint arXiv:2008.10402, 2020.

[88] Sebastian Kokott, Sergey V Levchenko, Patrick Rinke, and Matthias Scheffler. First-principles supercell calculations of small polarons with proper account for long-range polarization effects. New Journal of Physics, 20(3):033023, 2018.

[89] Nicola Marzari, Arash A Mostofi, Jonathan R Yates, Ivo Souza, and David Vanderbilt. Maximally localized Wannier functions: Theory and applications. Reviews of Modern Physics, 84(4):1419, 2012.

[90] Hendrik J Monkhorst and James D Pack. Special points for Brillouin-zone integrations. Physical review B, 13(12):5188, 1976.

[91] Franz Knuth. Strain and Stress: Derivation, Implementation, and Application to Organic Crystals. PhD thesis, Freie Universität Berlin, 2015.

[92] Honghui Shang, Christian Carbogno, Patrick Rinke, and Matthias Scheffler. Lattice dynamics calculations based on density-functional perturbation theory in real space. Computer Physics Communications, 215:26–46, 2017.

[93] Claudia Ambrosch-Draxl and Jorge O Sofo. Linear optical properties of solids within the full-potential linearized augmented planewave method. Computer physics communications, 175(1):1–14, 2006.

[94] Bartomeu Monserrat. Electron–phonon coupling from finite differences. Journal of Physics: Condensed Matter, 30(8):083001, 2018.

[95] K Kunc and Richard M Martin. Ab initio force constants of GaAs: A new approach to calculation of phonons and dielectric properties. Physical Review Letters, 48(6):406, 1982.

[96] Jonathan M Skelton, Stephen C Parker, Atsushi Togo, Isao Tanaka, and Aron Walsh. Thermal physics of the lead chalcogenides PbS, PbSe, and PbTe from first principles. Physical Review B, 89(20):205203, 2014.

[97] Felix Bloch. Über die quantenmechanik der elektronen in kristallgittern. Zeitschrift für Physik, 52(7):555–600, Jul 1929.

[98] Pui K Lam, Michel M Dacorogna, and Marvin L Cohen. Self-consistent calculation of electron-phonon couplings. Physical Review B, 34(8):5065, 1986.

[99] Xavier Gonze and J-P Vigneron. Density-functional approach to nonlinear-response coefficients of solids. Physical Review B, 39(18):13120, 1989.

[100] Feliciano Giustino, Marvin L Cohen, and Steven G Louie. Electron-phonon interaction using Wannier functions. Physical Review B, 76(16):165108, 2007.

[101] Barbara Kirchner, Philipp J di Dio, and Juerg Hutter. Real-world predictions from ab initio molecular dynamics simulations. Multiscale Molecular Methods in Applied Chemistry, pages 109–153, 2011.

[102] Mark Tuckerman. Statistical mechanics: theory and molecular simulation. Oxford University Press, 2010.

[103] Michael P Allen and Dominic J Tildesley. Computer simulation of liquids. Oxford University Press, 2017.

[104] Keivan Esfarjani, Gang Chen, and Harold T Stokes. Heat transport in silicon from first-principles calculations. Physical Review B, 84(8):085204, 2011.

[105] Alan JH McGaughey and Jason M Larkin. Predicting phonon properties from equilibrium molecular dynamics simulations. Annual Review of Heat Transfer, 17, 2014.

[106] Julia Wiktor, Ursula Rothlisberger, and Alfredo Pasquarello. Predictive determination of band gaps of inorganic halide perovskites. The journal of physical chemistry letters, 8(22):5507–5512, 2017.

[107] Chang L Tien and John H Lienhard. Statistical thermodynamics/revised printing. wdch, 1979.

[108] Gabriel Antonius, Samuel Poncé, E Lantagne-Hurtubise, Gabriel Auclair, Xavier Gonze, and Michel Côté. Dynamical and anharmonic effects on the electron-phonon coupling and the zero-point renormalization of the electronic structure. Physical Review B, 92(8):085137, 2015.

[109] Feliciano Giustino, Steven G Louie, and Marvin L Cohen. Electron-phonon renormalization of the direct band gap of diamond. Physical review letters, 105(26): 265501, 2010.

[110] EB Davies and H Spohn. Open quantum systems with time-dependent hamiltonians and their linear response. Journal of Statistical Physics, 19(5):511–523, 1978.

[111] Charles Kittel and Paul McEuen. Introduction to solid state physics, volume 8. Wiley New York, 1976.

[112] Ryogo Kubo. Brownian motion and nonequilibrium statistical mechanics. Science, 233(4761):330–334, 1986.

[113] Paul Drude. Zur elektronentheorie der metalle. Annalen der physik, 306(3):566–613, 1900.

[114] Raymond A Serway and John W Jewett. Physics for scientists and engineers. Cengage learning, 2018.

[115] John J Quinn and Kyung-Soo Yi. Free electron theory of metals. In Solid State Physics, pages 83–112. Springer, 2018.

[116] Daniel Gall. Electron mean free path in elemental metals. Journal of Applied Physics, 119(8):085101, 2016.

[117] Manuel Cardona and Y Yu Peter. Fundamentals of semiconductors. Springer, 2005.

[118] Arnold Sommerfeld. Zur elektronentheorie der metalle auf grund der fermischen statistik. Zeitschrift für Physik, 47(1-2):1–32, 1928.

[119] Philip B Allen and William H Butler. Electrical conduction in metals. Phys. Today, 31(12), 1978.

[120] John Bardeen. Electrical conductivity of metals. Journal of Applied Physics, 11 (2):88–111, 1940.

[121] Philip B Allen. Electrical conductivity. The Physics Teacher, 17(6):362–366, 1979.

[122] PB Allen. Electron transport. Contemporary Concepts of Condensed Matter Science, 2:165–218, 2006.

[123] Kristen Kaasbjerg, Kristian S Thygesen, and Karsten W Jacobsen. Phonon-limited mobility in n-type single-layer MoS2 from first principles. Physical Review B, 85 (11):115317, 2012.

[124] Wu Li. Electrical transport limited by electron-phonon coupling from Boltzmann transport equation: An ab initio study of Si, Al, and MoS2. Physical Review B, 92 (7):075405, 2015.

[125] Mattia Fiorentini and Nicola Bonini. Thermoelectric coefficients of n-doped silicon from first principles via the solution of the Boltzmann transport equation. Physical Review B, 94(8):085204, 2016.

[126] Alireza Faghaninia, Joel W Ager III, and Cynthia S Lo. Ab initio electronic transport model with explicit solution to the linearized Boltzmann transport equation. Physical Review B, 91(23):235123, 2015.

[127] Jinlong Ma, Arun S Nissimagoudar, and Wu Li. First-principles study of electron and hole mobilities of Si and GaAs. Physical Review B, 97(4):045201, 2018.

[128] Krishnendu Ghosh and Uttam Singisetti. Ab initio calculation of electron–phonon coupling in monoclinic β-Ga2O3 crystal. Applied Physics Letters, 109 (7):072102, 2016.

[129] Thibault Sohier, Davide Campi, Nicola Marzari, and Marco Gibertini. Mobility of two-dimensional materials from first principles in an accurate and automated framework. Physical Review Materials, 2(11):114010, 2018.

[130] Martin Schlipf, Samuel Poncé, and Feliciano Giustino. Carrier lifetimes and polaronic mass enhancement in the hybrid halide perovskite CH3NH3PbI3 from multiphonon Fröhlich coupling. Physical review letters, 121(8):086402, 2018.

[131] Ryogo Kubo. Statistical-mechanical theory of irreversible processes. I. General theory and simple applications to magnetic and conduction problems. Journal of the Physical Society of Japan, 12(6):570–586, 1957.

[132] John Bertrand Johnson. Thermal agitation of electricity in conductors. Physical review, 32(1):97, 1928.

[133] Harry Nyquist. Thermal agitation of electric charge in conductors. Physical review, 32(1):110, 1928.

[134] JF Qu, SP Benz, H Rogalla, WL Tew, DR White, and KL Zhou. Johnson noise thermometry. Measurement Science and Technology, 30(11):112001, 2019.

[135] Ryogo Kubo. The fluctuation-dissipation theorem. Reports on progress in physics, 29(1):255, 1966.

[136] Herbert B Callen and Theodore A Welton. Irreversibility and generalized noise. Physical Review, 83(1):34, 1951.

[137] W Kohn and JM Luttinger. Quantum theory of electrical transport phenomena. Physical Review, 108(3):590, 1957.

[138] Robert Zwanzig. Time-correlation functions and transport coefficients in statistical mechanics. Annual Review of Physical Chemistry, 16(1):67–102, 1965.

[139] Gerald D Mahan. Many-particle physics. Springer Science & Business Media, 2013.

[140] J. M. Luttinger. Transport Theory, pages 157–193. Springer US, Boston, MA, 1968.

[141] Wo Shockley. Hot electrons in germanium and Ohm's law. The Bell System Technical Journal, 30(4):990–1034, 1951.

[142] Christian Carbogno, Rampi Ramprasad, and Matthias Scheffler. Ab initio Green-Kubo approach for the thermal conductivity of solids. Physical review letters, 118(17):175901, 2017.

[143] Alper T Celebi, Seyed Hossein Jamali, André Bardow, Thijs JH Vlugt, and Othonas A Moultos. Finite-size effects of diffusion coefficients computed from molecular dynamics: a review of what we have learned so far. Molecular Simulation, pages 1–15, 2020.

[144] Werner Ebeling and Igor Sokolov. Statistical thermodynamics and stochastic theory of nonequilibrium systems, volume 8. World Scientific Publishing Company, 2005.

[145] Bernhard Altaner, Matteo Polettini, and Massimiliano Esposito. Fluctuation-dissipation relations far from equilibrium. Physical review letters, 117(18):180601, 2016.

[146] GV Chester and A Thellung. On the electrical conductivity of metals. Proceedings of the Physical Society, 73(5):745, 1959.

[147] An-Ban Chen, Gideon Weisz, and Arden Sher. Temperature dependence of the electron density of states and dc electrical resistivity of disordered binary alloys. Physical Review B, 5(8):2897, 1972.

[148] James Dufty, Jeffrey Wrighton, Kai Luo, and SB Trickey. On the Kubo-Greenwood model for electron conductivity. Contributions to Plasma Physics, 58(2-3):150–154, 2018.

[149] Noëlle Pottier. Physique statistique hors d'équilibre. EDP Sciences, 2021.

[150] Jørgen Rammer. Quantum transport theory of electrons in solids: A single-particle approach. Reviews of Modern Physics, 63(4):781, 1991.

[151] DA Greenwood. The Boltzmann equation in the theory of electrical conduction in metals. Proceedings of the Physical Society, 71(4):585, 1958.

[152] Bastian Holst, Martin French, and Ronald Redmer. Electronic transport coefficients from ab initio simulations and application to dense liquid hydrogen. Physical Review B, 83(23):235120, 2011.

[153] Emmanouil Stylianos Kioupakis. Quasiparticle calculations for solids and molecules. University of California, Berkeley, 2008.

[154] Patrick Rinke, Abdallah Qteish, Jörg Neugebauer, Christoph Freysoldt, and Matthias Scheffler. Combining GW calculations with exact-exchange density-functional theory: an analysis of valence-band photoemission for compound semiconductors. New Journal of Physics, 7(1):126, 2005.

[155] Dorothea Golze, Marc Dvorak, and Patrick Rinke. The GW compendium: A practical guide to theoretical photoemission spectroscopy. Frontiers in chemistry, 7:377, 2019.

[156] Mark S Hybertsen and Steven G Louie. Electron correlation in semiconductors and insulators: Band gaps and quasiparticle energies. Physical Review B, 34(8): 5390, 1986.

[157] Samuel Poncé, Elena R Margine, and Feliciano Giustino. Towards predictive many-body calculations of phonon-limited carrier mobilities in semiconductors. Physical Review B, 97(12):121201, 2018.

[158] Samuel Poncé, Debdeep Jena, and Feliciano Giustino. Hole mobility of strained GaN from first principles. Physical Review B, 100(8):085204, 2019.

[159] Wenbin Li and Feliciano Giustino. Many-body renormalization of the electron effective mass of InSe. Physical Review B, 101(3):035201, 2020.

[160] J Vorberger, KU Plageman, and R Redmer. The structure in warm dense carbon. High Energy Density Physics, 35:100737, 2020.

[161] Mandy Bethkenhagen, Bastian BL Witte, Maximilian Schörner, Gerd Röpke, Tilo Döppner, Dominik Kraus, Siegfried H Glenzer, Philip A Sterne, and Ronald Redmer. Carbon ionization at gigabar pressures: An ab initio perspective on astrophysical high-density plasmas. Physical Review Research, 2(2):023260, 2020.

[162] A Ravasio, M Bethkenhagen, J-A Hernandez, A Benuzzi-Mounaix, F Datchi, M French, M Guarguaglini, F Lefevre, S Ninet, R Redmer, et al. Metallization of shock-compressed liquid ammonia. Physical Review Letters, 126(2):025003, 2021.

[163] Pier Luigi Silvestrelli and Alberto Ambrosetti. Liquid-glass transition in monoatomic vanadium: A first-principles study. Physical Review B, 99(9):094201, 2019.

[164] TA Abtew, Mingliang Zhang, and DA Drabold. Ab initio estimate of temperature dependence of electrical conductivity in a model amorphous material: Hydrogenated amorphous silicon. Physical Review B, 76(4):045212, 2007.

[165] Rajarshi Sinha-Roy, Antonin Louiset, Magali Benoit, and Lionel Calmels. Electronic structure and conductivity of off-stoichiometric and Si-doped Ge2Sb2Te5 crystals from multiple-scattering theory. Physical Review B, 99(24):245124, 2019.

[166] Cono Di Paola, Francesco Macheda, Savio Laricchia, Cedric Weber, and Nicola Bonini. First-principles study of electronic transport and structural properties of Cu12Sb4S13 in its high-temperature phase. Physical Review Research, 2(3): 033055, 2020.

[167] Rudolf Peierls. Some simple remarks on the basis of transport theory. In Transport Phenomena, pages 1–33. Springer, 1974.

[168] Heidi Reinholz, G Röpke, S Rosmej, and R Redmer. Conductivity of warm dense matter including electron-electron collisions. Physical Review E, 91(4):043105, 2015.

[169] SF Edwards. A new method for the evaluation of electric conductivity in metals. Philosophical Magazine, 3(33):1020–1031, 1958.

[170] Guillaume Brunin, Henrique Pereira Coutada Miranda, Matteo Giantomassi, Miquel Royo, Massimiliano Stengel, Matthieu J Verstraete, Xavier Gonze, Gian-Marco Rignanese, and Geoffroy Hautier. Phonon-limited electron mobility in Si, GaAs, and GaP with exact treatment of dynamical quadrupoles. Physical Review B, 102(9):094308, 2020.

[171] James A McLennan Jr. Statistical mechanics of the steady state. Physical review, 115(6):1405, 1959.

[172] Maxim Trushin, Janik Kailasvuori, John Schliemann, and AH MacDonald. Finite conductivity minimum in bilayer graphene without charge inhomogeneities. Physical Review B, 82(15):155308, 2010.

[173] MP Desjarlais, JD Kress, and LA Collins. Electrical conductivity for warm, dense aluminum plasmas and liquids. Physical Review E, 66(2):025401, 2002.

[174] Monica Pozzo, Michael P Desjarlais, and Dario Alfe. Electrical and thermal conductivity of liquid sodium from first-principles calculations. Physical Review B, 84(5):054203, 2011.

[175] Lars Stixrude, Roberto Scipioni, and Michael P Desjarlais. A silicate dynamo in the early earth. Nature communications, 11(1):1–5, 2020.

[176] Jonathan R. Yates, Xinjie Wang, David Vanderbilt, and Ivo Souza. Spectral and fermi surface properties from Wannier interpolation. Phys. Rev. B, 75:195121, May 2007.

[177] Kentaro Nomura and Allan H MacDonald. Quantum transport of massless Dirac fermions. Physical review letters, 98(7):076602, 2007.

[178] Christopher WM Castleton, A Höglund, and Susanne Mirbt. Density functional theory calculations of defect energies using supercells. Modelling and Simulation in Materials Science and Engineering, 17(8):084003, 2009.

[179] Li-Dong Zhao, Gangjian Tan, Shiqiang Hao, Jiaqing He, Yanling Pei, Hang Chi, Heng Wang, Shengkai Gong, Huibin Xu, Vinayak P Dravid, et al. Ultrahigh power factor and thermoelectric performance in hole-doped single-crystal SnSe. Science, 351(6269):141–144, 2016.

[180] Johannes Boy, Martin Handwerg, Rüdiger Mitdank, Zbigniew Galazka, and Saskia F Fischer. Charge carrier density, mobility, and Seebeck coefficient of melt-grown bulk ZnGa2O4 single crystals. AIP Advances, 10(5):055005, 2020.

[181] Klaus Ellmer. Past achievements and future challenges in the development of optically transparent electrodes. Nature Photonics, 6(12):809–817, 2012.

[182] Matthias Scheffler. Lattice relaxations at substitutional impurities in semiconductors. Physica B+C, 146(1-2):176–186, 1987.

[183] Norina Richter. Charged point defects in oxides – a case study of MgO bulk and surface F centers. PhD thesis, Technische Universität Berlin, 2013.

[184] Norina A Richter, Sabrina Sicolo, Sergey V Levchenko, Joachim Sauer, and Matthias Scheffler. Concentration of vacancies at metal-oxide surfaces: Case study of MgO (100). Physical review letters, 111(4):045502, 2013.

[185] Florian Knoop, Matthias Scheffler, Christian Carbogno, et al. FHI-vibes: Ab initio vibrational simulations. Journal of Open Source Software, 5(56):2671, 2020.

[186] Lisandro Dalcín, Rodrigo Paz, and Mario Storti. Mpi for python. Journal of Parallel and Distributed Computing, 65(9):1108–1115, 2005.

[187] Yasumasa Okada and Yozo Tokumaru. Precise determination of lattice parameter and thermal expansion coefficient of silicon between 300 and 1500 k. Journal of applied physics, 56(2):314–320, 1984.

[188] Roberto Peverati and Donald G Truhlar. Performance of the M11-L density functional for bandgaps and lattice constants of unary and binary semiconductors. The Journal of chemical physics, 136(13):134704, 2012.

[189] Jin-Jian Zhou and Marco Bernardi. Ab initio electron mobility and polar phonon scattering in GaAs. Physical Review B, 94(20):201201, 2016.

[190] Binyuan Zhang, Mingfeng Zhu, Zhe Liu, Fei Guo, and Yisong Zheng. Temperature-dependent electron-phonon spectral function and the intrinsic resistivity of a metal: A case study of monolayer Ti2N. Physical Review B, 102(16): 165402, 2020.

[191] J. H. Racette. Intrinsic electrical conductivity in silicon carbide. Phys. Rev., 107: 1542–1544, 1957.

[192] Marios Zacharias, Matthias Scheffler, and Christian Carbogno. Fully anharmonic nonperturbative theory of vibronically renormalized electronic band structures. Physical Review B, 102(4):045126, 2020.

[193] Martin A Green. Intrinsic concentration, effective densities of states, and effective mass in silicon. Journal of Applied Physics, 67(6):2944–2954, 1990.

[194] G. A. Baraff and M. Schlüter. Migration of interstitials in silicon. Phys. Rev. B, 30: 3460–3469, 1984.

[195] Simon M Sze and Kwok K Ng. Physics of semiconductor devices. John wiley & sons, 2006.

[196] Bart Van Zeghbroeck. Principles of electronic devices. University of Colorado, 2011.

[197] Alan Grossfield, Paul N Patrone, Daniel R Roe, Andrew J Schultz, Daniel W Siderius, and Daniel M Zuckerman. Best practices for quantification of uncertainty and sampling quality in molecular simulations. Living journal of computational molecular science, 1(1), 2018.

[198] Peter Nagele. Misuse of standard error of the mean (SEM) when reporting variability of a sample. a critical evaluation of four anaesthesia journals. British Journal of Anaesthesia, 90(4):514–516, 2003.

[199] Bo Qiu, Zhiting Tian, Ajit Vallabhaneni, Bolin Liao, Jonathan M Mendoza, Oscar D Restrepo, Xiulin Ruan, and Gang Chen. First-principles simulation of electron mean-free-path spectra and thermoelectric properties in silicon. EPL (Europhysics Letters), 109(5):57006, 2015.

[200] Stephan Lany and Alex Zunger. Assessment of correction methods for the band-gap problem and for finite-size effects in supercell defect calculations: Case studies for ZnO and GaAs. Physical Review B, 78(23):235104, 2008.

[201] W. R. Thurber, R. L. Matthias, Y. M. Liu, and J. J. Filliben. The relationship between resistivity and dopant density for phosphorus-and boron-doped silicon, volume 400. US Department of Commerce, National Bureau of Standards, 1981.

[202] Tian Lan and Zhaoyan Zhu. Renormalized phonon microstructures at high temperatures from first-principles calculations: methodologies and applications in studying strong anharmonic vibrations of solids. Advances in Condensed Matter Physics, 2016, 2016.

[203] K Adouby, C Perez-Vicente, JC Jumas, R Fourcade, and A Abba Touré. Structure and temperature transformation of SnSe. Stabilization of a new cubic phase Sn4Bi2Se7. Zeitschrift für Kristallographie-Crystalline Materials, 213(6):343–349, 1998.

[204] Antoine Dewandre, Olle Hellman, Sandip Bhattacharya, Aldo H Romero, Georg KH Madsen, and Matthieu J Verstraete. Two-step phase transition in SnSe and the origins of its high power factor from first principles. Physical review letters, 117(27):276601, 2016.

[205] Aron Walsh and Graeme W Watson. Influence of the anion on lone pair formation in Sn(II) monochalcogenides: a DFT study. The Journal of Physical Chemistry B, 109(40):18868–18875, 2005.

[206] Srinivasa Rao Popuri, Michaël Pollet, Rodolphe Decourt, ML Viciu, and Jan-Willem G Bos. Evidence for hard and soft substructures in thermoelectric SnSe. Applied Physics Letters, 110(25):253903, 2017.

[207] Yong Lu, Fa-wei Zheng, Yu Yang, Ping Zhang, and Dong-Bo Zhang. Phase stabilities of Cmcm and Pnma SnSe studied by phonon quasiparticle approach. Physical Review B, 100(5):054304, 2019.

[208] Koichi Momma and Fujio Izumi. Vesta 3 for three-dimensional visualization of crystal, volumetric and morphology data. Journal of applied crystallography, 44 (6):1272–1276, 2011.

[209] Martin Parenteau and Cosmo Carlone. Influence of temperature and pressure on the electronic transitions in SnS and SnSe semiconductors. Physical Review B, 41 (8):5227, 1990.

[210] Li-Dong Zhao, Shih-Han Lo, Yongsheng Zhang, Hui Sun, Gangjian Tan, Ctirad Uher, Christopher Wolverton, Vinayak P Dravid, and Mercouri G Kanatzidis. Ultralow thermal conductivity and high thermoelectric figure of merit in SnSe crystals. Nature, 508(7496):373–377, 2014.

[211] Li-Dong Zhao, Cheng Chang, Gangjian Tan, and Mercouri G Kanatzidis. SnSe: a remarkable new thermoelectric material. Energy & Environmental Science, 9(10): 3044–3060, 2016.

[212] Ruiqiang Guo, Xinjiang Wang, Youdi Kuang, and Baoling Huang. First-principles study of anisotropic thermoelectric transport properties of IV-VI semiconductor compounds SnSe and SnS. Physical Review B, 92(11):115202, 2015.

[213] Guo-Xu Zhang, Alexandre Tkatchenko, Joachim Paier, Heiko Appel, and Matthias Scheffler. Van der waals interactions in ionic and semiconductor solids. Physical review letters, 107(24):245501, 2011.

[214] Dipanshu Bansal, Jiawang Hong, Chen W Li, Andrew F May, Wallace Porter, Michael Y Hu, Douglas L Abernathy, and Olivier Delaire. Phonon anharmonicity and negative thermal expansion in snse. Physical Review B, 94(5):054307, 2016.

[215] Heribert Wiedemeier and Frank J Csillag. The thermal expansion and high temperature transformation of SnS and SnSe. Zeitschrift für Kristallographie-Crystalline Materials, 149(1-2):17–29, 1979.

[216] Shouhang Li, Zhen Tong, and Hua Bao. Resolving different scattering effects on the thermal and electrical transport in doped SnSe. Journal of Applied Physics, 126(2):025111, 2019.

[217] Ganbat Duvjir, Taewon Min, Trinh Thi Ly, Taehoon Kim, Anh-Tuan Duong, Sunglae Cho, SH Rhim, Jaekwang Lee, and Jungdae Kim. Origin of p-type characteristics in a SnSe single crystal. Applied Physics Letters, 110(26):262106, 2017.

[218] Michele Simoncelli, Nicola Marzari, and Francesco Mauri. Unified theory of thermal transport in crystals and glasses. Nature Physics, 15(8):809–813, 2019.

[219] Min Jin, Jun Jiang, Rongbin Li, Xianghu Wang, Yunxia Chen, Yuqi Chen, and Jiayue Xu. Thermoelectric properties of pure SnSe single crystal prepared by a vapor deposition method. Crystal Research and Technology, 54(6):1900032, 2019.

[220] Linfeng Zhang, Jiequn Han, Han Wang, Roberto Car, and E Weinan. Deep potential molecular dynamics: a scalable model with the accuracy of quantum mechanics. Physical review letters, 120(14):143001, 2018.

[221] Simon Batzner, Tess E Smidt, Lixin Sun, Jonathan P Mailoa, Mordechai Kornbluth, Nicola Molinari, and Boris Kozinsky. SE(3)-equivariant graph neural networks for data-efficient and accurate interatomic potentials. arXiv preprint arXiv:2101.03164, 2021.

[222] Manyi Yang, Luigi Bonati, Daniela Polino, and Michele Parrinello. Using metadynamics to build neural network potentials for reactive events: the case of urea decomposition in water. Catalysis Today, 2021.

[223] Jin-Jian Zhou, Jinsoo Park, Iurii Timrov, Andrea Floris, Matteo Cococcioni, Nicola Marzari, and Marco Bernardi. Electron-phonon interactions in transition metal oxides in the framework of DFT+U. arXiv preprint arXiv:2102.06840, 2021.

[224] Benjamin Chang, Jin-Jian Zhou, Nien-En Lee, and Marco Bernardi. Polaronic electron transport in a naphthalene crystal from first principles. Bulletin of the American Physical Society, 2021.

[225] Véronique Brousseau-Couture, Xavier Gonze, and Michel Cote. Influence of spin-orbit coupling and Rashba interaction on the electron-phonon renormalized electronic energy levels. Bulletin of the American Physical Society, 65, 2020.

[226] Zhenglu Li, Gabriel Antonius, Meng Wu, H Felipe, and Steven G Louie. Electron-phonon coupling from ab initio linear-response theory within the GW method: Correlation-enhanced interactions and superconductivity in $\mathrm{Ba}_{1-x}\mathrm{K}_x\mathrm{BiO3}$. Physical review letters, 122(18):186402, 2019.

[227] OD Restrepo, K Varga, and ST Pantelides. First-principles calculations of electron mobilities in silicon: Phonon and Coulomb scattering. Applied Physics Letters, 94(21):212103, 2009.

[228] Vincenzo Lordi, Paul Erhart, and Daniel Åberg. Charge carrier scattering by defects in semiconductors. Physical Review B, 81(23):235204, 2010.

[229] I-Te Lu, Jin-Jian Zhou, and Marco Bernardi. Efficient ab initio calculations of electron-defect scattering and defect-limited carrier mobility. Physical Review Materials, 3(3):033804, 2019.

[230] Paolo Giannozzi, Oscar Baseggio, Pietro Bonfà, Davide Brunato, Roberto Car, Ivan Carnimeo, Carlo Cavazzoni, Stefano De Gironcoli, Pietro Delugas, Fabrizio Ferrari Ruffino, et al. Quantum espresso toward the exascale. The Journal of chemical physics, 152(15):154105, 2020.

[231] AL Kuzemsky. Electronic transport in metallic systems and generalized kinetic equations. International Journal of Modern Physics B, 25(23n24):3071–3183, 2011.

[232] Franz Knuth, Christian Carbogno, Viktor Atalla, Volker Blum, and Matthias Scheffler. All-electron formalism for total energy strain derivatives and stress tensor components for numeric atom-centered orbitals. Computer Physics Communications, 190:33–50, 2015.

Declaration

I declare that I have completed the thesis independently using only the aids and tools specified. I have not applied for a doctor's degree in the doctoral subject elsewhere and do not hold a corresponding doctor's degree. I have taken due note of the Faculty of Mathematics and Natural Sciences PhD Regulations, published in the Official Gazette of Humboldt-Universität zu Berlin no. 42/2018 on 11/07/2018.